TIME-RESOLVED AND STEADY-STATE INVESTIGATIONS OF CARRIER DYNAMICS AT THE SEMICONDUCTOR/LIQUID INTERFACE

Thesis by

Christopher Neil Kenyon

In Partial Fulfillment of the Requirements

for the Degree of

Doctor of Philosophy

California Institute of Technology

Pasadena, California

1997

(Submitted September 13, 1996)

Acknowledgments

I must confess to being somewhat daunted by the task of writing the infamous Acknowledgments page. There are many people whom I would like to thank and it is unsettling to know that any omissions will be on display in the library for years to come. I'll partially indemnify myself by naming only those people whom I wish to acknowledge professionally.

I am grateful to my advisor Prof. Nathan Lewis for providing me the opportunity to work in his research group. I won't offer any humorous remarks regarding our Fearless Leader since I don't think I can improve on those made by the cast of characters from Stanford who were in the group way back when. If you want a good laugh, read their acknowledgments. However, members of that same group also never fail to state their appreciation for Nate's intelligence and scientific rigor. I echo that sentiment. Put simply, if you choose to work in the Lewis Group, expect to have the limits of your patience tested, and expect to emerge a far better scientist.

To the extent that graduate school is supposed to be an educational experience, I made few choices as intelligent as electing to work under Dr. Jay Winkler in the BILRC. In addition to suffering an innumerable number of questions from me, he teamed up with Dr. Max Bachrach (who solved many of my programming dilemmas) to create that unmistakably cheerful working environment in the laser center.

I have been fortunate to have the privilege of working with several very talented individuals during my graduate career. When I first joined the group, Dr. Gail Ryba patiently introduced me to the world of lasers and semiconductors, and I truly enjoyed and benefited from that learning period. Later on, I embarked on a highly productive collaboration with Dr. Ming Tan. I don't feel boastful in saying that on a given day, we were unstoppable. Most recently I have worked with Dr. Olaf Krüger and am indebted to him for helping to transform lots of unresolved questions into definitive answers. Finally, Dr. Stephen Doig showed up towards the end and showed me that its never too late to learn

a few new tricks. I would also like to thank the Lewis Group as a whole. The group has a considerably different character than when I first joined but change is a necessary thing. I think there is a good crop in place at the moment and I wish them all the best.

Outside of the laboratory, six years in southern California has produced some excellent adventures. There has been a great group of people who have accompanied (and educated) me during climbing, skiing, and mountaineering forays. These experiences and the friendships which have grown out of them have been an incredibly rewarding part of my life here. I have also enjoyed the camaraderie of a number of people at Caltech who were willing to occasionally step out and have a beer (maybe two) with me. As a group, they embody the saying that it is quality and not quantity that counts.

I have also benefited from the presence in Los Angeles of a group of friends from my undergraduate days who have offered a (how should I put this) continual broadening of the often myopic perspective that life at Caltech can produce. A Friday evening dash out to the "909 Club" and all its reincarnations has frequently provided a welcome respite to graduate school. My own living arrangements have also provided me with a place to relax and to both my roommates and those who were honorary residents - Cheers! I'll miss the simple times in the 'hood.

Lastly, I will break the self-imposed anonymity clause and identify my parents as deserving of my sincerest gratitude. Their continual support throughout my time as a graduate student is more remarkable to me than any scientific principle in this thesis.

Abstract

Fundamental investigations of carrier transport and charge transfer at the semiconductor/liquid interface are presented. The application of both steady-state and time-resolved methods to these studies is discussed.

Small signal photocurrent transients have been measured for n-Si/CH_3OH-dimethylferrocene $(Me_2Fc)^{+/0}$/Pt and n-Si/Au/CH_3OH-$Me_2Fc^{+/0}$/Pt interfaces. The photocurrent transients for these interfaces decayed in <10 μs, and were limited by the series resistance of the cell in combination with the space charge capacitance of the semiconductor. An equivalent circuit model is presented and physically justified in order to explain this behavior, and to elucidate the conditions under which photocurrent transients at semiconductor electrodes can be expected to yield information regarding the faradaic charge transfer rate across the semiconductor/liquid interface. To provide additional support for the equivalent circuit representation, transient photocurrent responses are also presented for n-Si/Pt/NaOH(aq)/$Ni(OH)_2$/Ni, n-TiO_2/NaOH(aq)/$Ni(OH)_2$/Ni and n-TiO_2/NaOH(aq)-$Fe(CN)_6^{3-/4-}$/$Ni(OH)_2$/Ni contacts.

Studies are reported on the behaviors of thin, nearly intrinsically doped Si electrodes having interdigitated n^+ and p^+ back contact points. An analysis of the factors governing the photocurrent directionality and photovoltage in these samples is presented. Additionally the back contact geometry has been exploited to perform measurements of the open circuit potential of either electrons or holes while the other carrier type was under electrical control. In combination with current density-voltage measurements of carriers passing through the back contact points, these data allowed a comparison of the behavior of a given carrier type when generated by an applied bias (i.e., as majority carriers) relative to their behavior when generated with band gap illumination of the solid (as minority carriers). The results have been used to validate certain key predictions of the quasi-Fermi level concept in photoelectrochemistry. In addition, digital simulations that include two-dimensional representations of the charge density distribution and of the current fluxes in

the solid have been utilized to provide a quantitative understanding of the observed experimental behavior.

The application of time-resolved photoluminescence to the study of InP interfaces is described. Photoluminescence decay profiles for etched n-type and p-type InP have been recorded. These data provide support for a bulk-recombination limited PL lifetime in p-InP, while that of n-InP is evidenced to be dominated by radiative recombination. Additional PL decay data are reported for a series of InP/liquid contacts. InP/CH_3CN junctions having $Me_2Fc^{+/0}$, decamethylferrocene$^{+/0}$ ($Me_{10}Fc^{+/0}$), methyl viologen $(MV)^{2+/+}$, and cobaltocene $(CoCp_2)^{+/0}$ as acceptor species have been studied. Quantitative information on the rate constant for charge transfer could not be obtained from these studies, but upper limits are suggested, and promising systems for further study are identified.

Table of Contents

List of Figures

Chapter 1.

Chapter 2.

Chapter 3.

List of Tables

General Introduction and Overview

This thesis describes studies of carrier transport and charge transfer at the semiconductor/electrolyte interface. While the work presented herein is strictly fundamental in nature, interest in studying semiconductor/liquid contacts has historically been generated by their potential applications. Applications include the conversion of solar energy to electricity or chemical fuel,[1-3] waste water remediation using colloidal semiconductors,[4,5] and novel organic syntheses.[6] Additional impetus for studies of semiconductor/liquid interfaces is provided by the possibility of obtaining information on controlling the electrical properties of semiconductor surfaces, which is of critical importance to the microelectronics industry.[7]

The most mature of the applications listed above is the use of semiconductor/liquid junctions in solar energy conversion schemes. It is the topic of several books[8-10] and an extensive review literature which can be found in recent surveys by Koval and Howard[11] and by Tan et al.[12] Although there has been many studies examining the operation of semiconductor electrodes in photoelectrochemical cells, several fundamental questions remain unresolved. The three chapters of this thesis are unified as being investigations of these basic issues.

The first and third chapters describe efforts relevant to the study of charge transfer at the semiconductor/liquid interface. Rate constants for this process are an area of active experimental interest, and are the focus of an ongoing theoretical debate.[11,13,14] Despite the considerable effort invested in its examination, the amount of reliable kinetic data which exists on the transfer of an electron (or hole) in a semiconductor to a molecular species in

solution is limited.[11,15] This is especially conspicuous when the work is viewed in comparison with the extensive data available for metal electrodes.[11]

Along with a relative lack of experimental rate constant measurements, the theoretical description of electron transfer at semiconductor electrodes has not attained the level of sophistication that has been realized for charge transfer at metal electrodes,[16,17] and in homogeneous condensed media.[18,19] Details of the rate constant are typically evaluated in the context of classical theories set forth by Marcus and Gerischer.[20,21] Although these approaches have been successful in explaining much of the available data, they have recently been criticized as being inappropriate descriptions of the semiconductor/electrolyte interface.[22] This controversy underscores the need for more experimental data for comparison with theoretical predictions.

It is apparent that there are difficulties associated with the measurement of charge transfer rate constants at semiconductor/liquid interfaces. However, this difficulty is not suggested by the simple bimolecular rate law describing the flux due to electron transfer from a semiconductor to acceptor species in solution,[13]

$$J = k_{et}(n_s - n_{so})[A] \qquad (1.1)$$

In eq 1.1, n_s is the concentration of electrons at the surface (cm^{-3}), n_{so} is the equilibrium surface electron concentration, [A] is the concentration of acceptors in solution (cm^{-3}), and k_{et} is the electron transfer rate constant which has units of $cm^4\ sec^{-1}$, giving J the correct units of flux ($cm^{-2}\ sec^{-1}$). Since n_s exhibits a known dependence on bias, and carrier flux across an interface can be measured as current, eq 1.1 suggests that current-voltage measurements could be used to determine the electron transfer rate constant. While this is true under some circumstances, there are a number of mechanisms which can determine the rate of carrier transport across the semiconductor/liquid interface, and if direct electron transfer is not the dominant of these, it cannot be measured using steady-state current-voltage techniques.[23] The predominance of a mechanism other than charge transfer is commonly manifested as a failure of the current to exhibit the predicted first order

dependence on the acceptor concentration.[24] In these instances, data can be used to establish an upper limit on k_{et} if the surface concentration of electrons can be determined (itself problematic), but a quantitative assignment of the rate constant is not possible.[25]

As direct measurement of the rate constant for charge transfer is often precluded, other experimental methods must be employed. Unfortunately, most of the techniques developed for studying charge transfer kinetics at metal electrodes cannot be applied to the semiconductor/electrolyte interface.[26] Varying the potential at a metal electrode amounts to a change in the activation energy, and consequently the rate constant, for charge transfer.[27] By varying the potential according to a prescribed waveform, information about the primary charge transfer event can often be obtained. However, this is typically not the case for depleted semiconductors, as changing the potential applied to the semiconductor affects the concentration of charge carriers at the semiconductor surface (n_s in eq 1.1), but is not expected to alter the rate constant.[13] These difficulties have motivated a search for alternative techniques, and the work of Chapters 1 and 3 addresses the application of two time-resolved optical methods to semiconductor/liquid charge transfer studies. It is seen that the numerous mechanisms which can control carrier motion in these systems is also a concern in real-time measurements.

Chapter 2 is an examination of another fundamental concept in semiconductor photoelectrochemistry, the quasi-Fermi level. The work presented is part of a larger and essentially complete project examining the behaviors of high-purity lithographically-patterned Si electrodes operated under high-level injection conditions.[28-33] Owing to the collaborative the nature of this project, it is important to acknowledge the indispensable contributions of Dr. Ming Tan and Dr. Olaf Krüger.

Quasi-Fermi levels were originally introduced by Shockley to describe the transport of electrons and holes under non-equilibrium conditions,[34] and they continue to be widely employed in semiconductor device physics.[35,36] They were applied to the description of charge transfer reactions at semiconductor/liquid interfaces by Gerischer,[37] and have been

incorporated in others theories of semiconductor photoelectrochemistry.[10] Recently there has been renewed interest in examining the behaviors of quasi-Fermi levels at semiconductor/liquid junctions. In an earlier phase of this project, the first direct and simultaneous measurement of the quasi-Fermi levels for electrons and holes at an illuminated semiconductor/liquid interface was reported.[28] The results, combined with recent work by Memming and coworkers,[38,39] highlight the utility and thermodynamic significance of quasi-Fermi levels. However, this view is not universally held, and other workers have questioned the meaning and appropriateness of the quasi-Fermi level formalism. In particular, there has been controversy on the use of quasi-Fermi levels to describe fuel-forming reactions at large band gap metal-oxide semiconductors.[40-44] Chapter 2 presents measurements and simulations of the behavior of quasi-Fermi levels under illumination and applied bias, which lend additional support to the quasi-Fermi level concept, and further the understanding of charge separation and collection events at illuminated semiconductor/liquid contacts.

As the three projects discussed in this thesis are distinct, a separate introduction is provided in Section I of each chapter. In addition, some of the key concepts relevant to the interpretation of the data are presented in Section II. More detailed information can be found in the references cited.

REFERENCES

(1) Wrighton, M.S. *Acc. Chem. Res.* **1979**, *12*, 303.

(2) Heller, A. *Acc. Chem. Res.* **1981**, *14*, 154.

(3) Lewis, N.S. *Acc. Chem. Res.* **1990**, *23*, 176.

(4) *Photocatalysis and Environment: Trends and Applications*; Schiavello, M. Ed.; NATO ASI Series C: Mathematical and Physical Sciences; Kluwer Academic: Dordrecht, 1988; Vol. 237.

(5) *Photoelectrochemistry, Photocatalysis and Photoreactors: Fundamentals and Developments.*; Schiavello, M. Ed.; NATO ASI Series C: Mathematical and Physical Science; D. Reidel: Dordrecht, 1985; Vol. 146.

(6) Fox, M.A. In *Photocatalysis: Fundamentals and Applications*; Serpone, N., Pelizzetti, E. Eds.; John Wiley & Sons: New York, 1989; p 421.

(7) Wolf, S.; Tauber, R.N. *Silicon Processing for the VLSI Era*; Lattice Press: Sunset Beach, CA, 1986.

(8) *Semiconductor Liquid Junction Solar Cells*; Heller, A. Ed.; Electrochemical Society: Princeton, NJ, 1977.

(9) Finklea, H.O. *Semiconductor Electrodes*, Studies in Physical and Theoretical Chemistry; Elsevier: New York, 1988.

(10) Pleskov, Y.V.; Gurevich, Y.Y. *Semiconductor Photolectrochemistry*; Consultants Bureau: New York, 1986.

(11) Koval, C.A.; Howard, J.N. *Chem. Rev.* **1992**, *92*, 411.

(12) Tan, M.X.; Laibinis, P.E.; Nguyen, S.T.; Kesselman, J.M.; Stanton, C.E.; Lewis, N.S. *Prog. Inorg. Chem.* **1994**, *41*, 21.

(13) Lewis, N.S. *Annu. Rev. Phys. Chem.* **1991**, *42*, 543.

(14) Memming, R. In *Electron Transfer I*; Mattay, J. Ed.; Topics in Current Chemistry; Springer-Verlag: Berlin, 1994; Vol. 169; p 105.

(15) Morrison, S.R. *Electrochemistry at Semiconductor and Oxidized Metal Electrodes*; Plenum: New York, 1980.

(16) Hale, J.M. In *Reactions of Molecules at Electrodes*; Hush, N. Ed.; Wiley: New York, 1971.

(17) Weaver, M.J. In *Comprehensive Chemical Kinetics*; Compton, R.G. Ed.; Elsevier: New York, 1987; Vol. 27; p 1.

(18) Marcus, R.A.; Sutin, N. *Biochim. Biophys. Acta* **1985**, *811*, 265 and references therein.

(19) A good introduction to recent developments in the study of electron transfer is provided by a series of review articles in *Chem. Rev.* **1992**, *92*, 411.

(20) Gerischer, H. In *Physical Chemistry: An Advanced Treatise*; Eyring, H.; Henderson, D., Yost, W. Eds.; Academic: New York, 1970; Vol. IXA; p 463.

(21) Marcus, R.A. *Annu. Rev. Phys. Chem.* **1964**, *15*, 155.

(22) Smith, B.B.; Halley, J.W.; Nozik, A.J. *Chem. Phys.* **1996**, *205*, 245.

(23) Lewis, N.S.; Rosenbluth, M. In *Photocatalysis: Fundamentals and Applications*; Serpone, N., Pelizzetti, E. Eds.; John Wiley & Sons: New York, 1989; p 45.

(24) Rosenbluth, M.L.; Lewis, N.S. *J. Am. Chem. Soc.* **1986**, *108*, 4689.

(25) Pomykal, K.E.; Fajardo, A.M.; Lewis, N.S. *J. Phys. Chem.* **1996**, *100*, 3652.

(26) Bard, A.J.; Faulkner, L.R. *Electrochemical Methods: Fundamentals and Applications*; John Wiley & Sons: New York, 1980.

(27) Peter, L.M. *Chem. Rev.* **1990**, *90*, 753.

(28) Tan, M.X.; Kenyon, C.N.; Lewis, N.S. *J. Phys. Chem.* **1994**, *98*, 4959.

(29) Tan, M.X.; Kenyon, C.N.; Wilisch, W.C.A.; Lewis, N.S. *J. Electrochem. Soc.* **1995**, *142*, L62.

(30) Tan, M.X.; Kenyon, C.N.; Krüger, O.; Lewis, N.S. *J. Phys. Chem.* submitted for publication.

(31) Krüger, O.; Kenyon, C.N.; Tan, M.X.; Lewis, N.S. *J. Phys. Chem.* submitted for publication.

(32) Kenyon, C.N.; Tan, M.X.; Krüger, O.; Lewis, N.S. *J. Phys. Chem.* submitted for publication.

(33) Tan, M.X. Ph. D. Thesis, California Institute of Technology, 1994.

(34) Shockley, W. *Electrons and Holes in Semiconductors*; Van Nostrand: New York, 1950.

(35) Fonash, S.J. *Solar Cell Device Physics*; Academic: New York, 1981.

(36) Sze, S.M. *The Physics of Semiconductor Devices*, 2nd ed.; John Wiley and Sons: New York, 1981.

(37) Gerischer, H. In *Solar Energy Conversion. Solid-State Physics Aspects*; Seraphin, B.O. Ed.; Topics in Applied Physics; Springer-Verlag: Berlin, 1979; Vol. 31; p 115.

(38) Reineke, R.; Memming, R. *J. Phys. Chem.* **1992**, *96*, 1317.

(39) Reineke, R.; Memming, R. *J. Phys. Chem.* **1992**, *96*, 1310.

(40) Williams, F.; Nozik, A.J. *Nature* **1978**, *271*, 137.

(41) Nozik, A.J. *Annu. Rev. Phys. Chem.* **1978**, *29*, 189.

(42) Gregg, B.A.; Nozik, A.J. *J. Phys. Chem.* **1993**, *97*, 13441.

(43) Kumar, A.; Santangelo, P.G.; Lewis, N.S. *J. Phys. Chem.* **1992**, *96*, 834.

(44) Shreve, G.A.; Lewis, N.S. *J. Electrochem. Soc.* **1995**, *142*, 112.

Chapter 1

An Analysis of Time Resolved Photocurrent Transients at Semiconductor/Liquid Interfaces

I. INTRODUCTION

The rate constant for charge transfer across a semiconductor/liquid interface is one of the key experimental variables in photoelectrochemistry.[1-3] To date, various methods have been used to measure this rate constant, including optical grating decays,[4,5] electro-optic sampling methods,[6] luminescence decays,[7-10] rf and microwave conductivity decays, [11,12] and transient photovoltage and photocurrent measurements.[13-34] Transient current and voltage relaxation methods are especially attractive because they are extremely sensitive, are analogous to the well-known coulostatic pulse method of conventional electrochemistry,[35-39] and can be performed at very low carrier injection levels in the semiconductor.

At present, however, there is controversy regarding the interpretation of transient photocurrent measurements at semiconductor electrodes.[40] Some workers have suggested that photocurrent decay transients contain interfacial charge transfer rate information,[19,26,30,31,33,34] while others claim that the photocurrent decay does not yield any direct information on the minority carrier charge transfer kinetics at the semiconductor/liquid interface.[41,42] To date, at least five different equivalent circuit representations have been invoked to model the transient photovoltage and photocurrent decays at various semiconductor/liquid contacts.[14,17,20,26,33,34,41,43,44] Clearly, a definitive interpretation of transient photocurrent decays at semiconductor electrodes is still lacking in the literature.

The studies described herein were stimulated by time-resolved microwave and rf conductivity measurements at Si/CH_3OH-dimethylferrocene $(Me_2Fc)^{+/0}$ interfaces.[11] These measurements indicated that photogenerated carriers persisted in the Si sample for >100 μs before undergoing either interfacial charge transfer or surface recombination.[45] Electrochemical cells can readily be constructed with RC response limitations that are shorter than 10 μs; thus, the transient photocurrent response of the n-Si/CH_3OH-$Me_2Fc^{+/0}$ interface should provide information on whether transient photocurrent measurements do,

in fact, yield information on the interfacial charge transfer kinetics at depleted semiconductor electrodes.In this chapter, the results of such transient photocurrent measurements are presented along with a physically realistic equivalent circuit that can be used to understand the data for the Si/liquid interface. To provide additional support for the equivalent circuit representation, transient photocurrent responses of n-Si/Au electrodes and of n-TiO_2 electrodes are also reported.

II. BACKGROUND

A. Capacitance of the Semiconductor/Liquid Interface

As suggested in the preceding section, this work involves equating components of photoelectrochemical cells with elements in an electrical circuit. Most of the relevant elements are discussed in Section V, but the differential capacitance associated with either side of the semiconductor/liquid interface is introduced presently. Under the experimental conditions employed in this work, expressions for both are of the form for a parallel plate capacitor in which κ is the dielectric constant of the medium, ε_o is the permittivity of free space, A is the geometric area and d is the separation of the plates.

$$C = \frac{\kappa \varepsilon_o A}{d} \tag{1.1}$$

1. Space Charge Capacitance

The first term to be considered is the capacitance of the semiconductor space charge region, C_{sc}. Figure 1.1 depicts an n-type semiconductor with a Fermi level, $\mathbf{E}_F$, placed in contact with a solution having an electrochemical potential $\mathbf{E}(A/A^-)$. The Fermi level concept is introduced in more detail in Section 2.II, but for this discussion, it is sufficient to describe it as the electrochemical potential of electrons in the solid. The energetic position of $\mathbf{E}_F$ is given by eq 1.2 were $\mathbf{E}_c$ is the energy of the conduction band edge, N_d is the dopant density, N_c is a collection of constants known as the effective density of states, k is the Boltzmann constant and T is the temperature.[46]

$$\mathbf{E}_F = \mathbf{E}_C + kT \ln\left(\frac{N_c}{N_d}\right) \tag{1.2}$$

A rearranged form of eq 1.2 illustrates that the position of $\mathbf{E}_F$ describes the equilibrium electron concentration in the conduction band, n_o.

$$n_o = N_d = N_c \exp\left(\frac{\mathbf{E}_C - \mathbf{E}_F}{kT}\right) \tag{1.3}$$

The difference between the electrochemical potentials of the two phases results in charge flow from the semiconductor to the solution. As electrons are removed from the

semiconductor, an excess positive charge density $\rho(x)$ is left in the solid. Under the depletion approximation, ionized dopant atoms are the only source of this fixed positive charge, and, therefore, an expression for $\rho(x)$ can be written in terms of the dopant concentration.[47]

$$\rho(x) = qN_d \tag{1.4}$$

The region from which electrons are withdrawn is known as the depletion or space charge region, and its extent is governed by the total amount of charge which must be removed to align $\mathbf{E}_F$ and $\mathbf{E}(A/A^-)$.[48] It is the width of this region, W, which forms the denominator in eq 1.1; thus, calculation of C_{sc} reduces to a calculation of W.

The first step is to relate the charge density in the solid to the electric field, $\mathcal{E}(x)$, using a one-dimensional form of Poisson's equation.[49]

$$\mathcal{E}(x) = \int \rho(x)dx = \frac{1}{\kappa\varepsilon_o}\int qN_d dx \tag{1.5}$$

Evaluating the integral subject to the boundary condition that $\mathcal{E}(W) = 0$ yields the following expression for the electric field.

$$\mathcal{E}(x) = \frac{qN_d}{\kappa\varepsilon_o}(x - W) \tag{1.6}$$

Integrating a second time gives the electric potential as a function of distance from the solid/liquid contact.

$$V(x) = -\int \mathcal{E}(x)dx = -\frac{qN_d}{\kappa\varepsilon_o}\int (x - W)dx \tag{1.7}$$

Defining the zero of potential to be at the solution potential, $\mathbf{E}(A/A^-)/q$, the potential at the edge of the depletion region can be expressed as:

$$V(W) = -\frac{qN_d}{2\kappa\varepsilon_o}W^2 \tag{1.8}$$

This potential is known as the built-in voltage, V_{bi}, and is readily related to the initial separation of $\mathbf{E}(A/A^-)$ and $\mathbf{E}_F$.

$$qV_{bi} = \mathbf{E}(A/A^-) - \mathbf{E}_F \tag{1.9}$$

Making this substitution for V(W) in eq 1.7 and solving for the width of the depletion region yields the following relationship.

$$W = \sqrt{\frac{2V_{bi}\kappa\varepsilon_o}{qN_d}} \tag{1.10}$$

Combining this result with the eq 1.1 gives an expression for C_{sc}.

2. Double Layer Capacitance

Having addressed the solid phase, it is necessary to examine the capacitance associated with the electrolyte. Excess positive charge in the semiconductor is balanced by a distribution of excess negative charge in solution and this combination gives rise to the double layer capacitance, C_{dl}.[35] In general, this solution-based capacitor is a complicated function of potential, concentration and several other factors, but at the high electrolyte concentrations used in the present work (1 M), it can be approximated by eq 1.11 where δ is the distance from the electrode to the plane of closest approach for ions in solution.

$$C_{dl} = \frac{\kappa\varepsilon}{\delta} \tag{1.11}$$

B. Sign Conventions

One additional point to be made is in reference to the sign conventions employed. This is a frequent source of confusion and a concerted effort has been made to consistently employ the convention shown in Figure 1.1 throughout this thesis. More positive potentials are plotted in the *negative* y direction and conversion of potentials to energies is accomplished by considering the elementary charge to be a signed quantity. The energy of a positive species (hole) increases in the negative y direction (as shown) while that of an electron increases in the positive y direction.

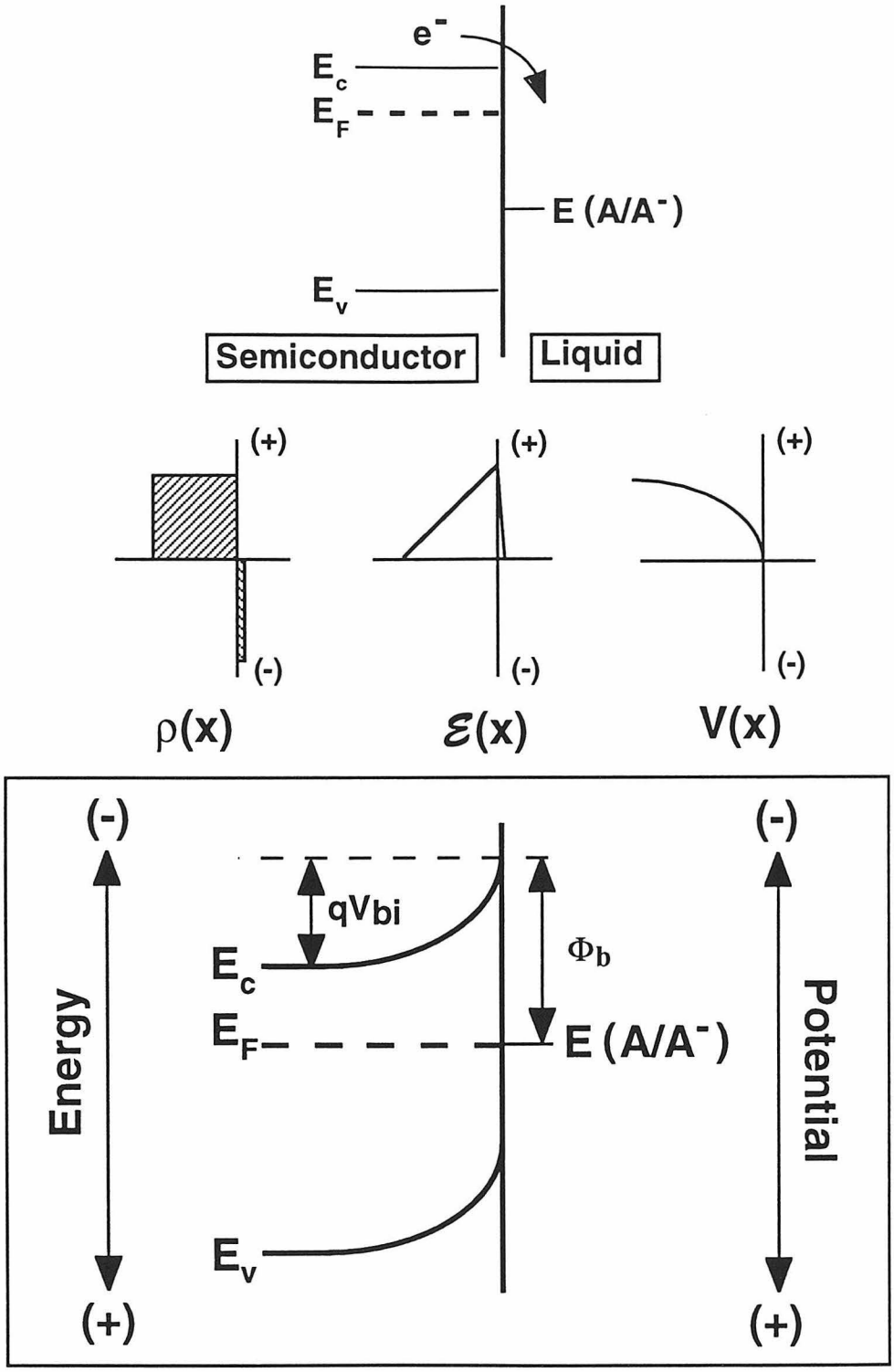

Figure 1.1: Charge equilibration at the semiconductor/liquid interface. Electron flow from the semiconductor to the solution produces the charge density, electric field and potential distribution shown. The potential gradient is represented as bending of the conduction and valence bands in the semiconductor band diagram. Φ_b is the barrier of the semiconductor/liquid contact.

III. EXPERIMENTAL

A. Materials and Preparation

The silicon wafers used in this study were n-type (phosphorus doped), (100) oriented single crystals obtained from Siltec Corp or Monsanto Co. Float zone grown, n-type 0.245 Ω-cm resistivity Si samples were supplied by Dr. R. Swanson of Sunpower, Inc.. Resistivities of these samples were determined by the four-point probe technique, and were converted to dopant densities using the data of Thurber *et al.*[50] The (001)-oriented TiO_2 samples used in this study were purchased from Atomergic Chemicals or from Commercial Crystal Laboratories, and were doped n-type by heating at 800 °C for 2.5 hours in a flow of forming gas. The dopant density of these crystals is not known accurately, but prior literature reports estimate that doping levels of $\approx 10^{19}$-10^{20} cm^{-3} are typically obtained using this procedure.[44,51,52]

Si photoelectrodes were prepared as described previously.[53] Prior to use in any experiment, n-Si electrodes were etched in 49% HF(aq) for 10-15 s, rinsed with distilled water, and blown dry in a stream of nitrogen. TiO_2 electrodes were fabricated in an identical manner, except that the TiO_2 crystals were immersed in 10% HCl(aq) for several minutes prior to forming the back ohmic contact. To clean the exposed electrode surface prior to electrochemical measurements, n-TiO_2 electrodes were immersed in 10% HCl for several minutes and were then rinsed with distilled water.

Schottky barriers were fabricated by evaporation of ~100 Å of the elemental metal (99.999% pure) onto the semiconductor surface at a base pressure of $5x10^{-5}$ torr. The steady-state current-voltage properties of all electrodes were periodically examined in the dark and under illumination to verify the integrity of the electrodes. An ELH-type tungsten halogen bulb provided the illumination for n-Si anodes, while ultraviolet light from a 150 W Xe lamp was used to illuminate the n-TiO_2 cells.

B. Solvents and Chemicals

Me_2Fc (Polysciences) was purified by sublimation, while $Me_{10}Fc$ (Strem) was used as received. The oxidized forms of the ferrocenes were prepared according to published procedures.[54] $K_3Fe(CN)_6$, $K_4Fe(CN)_6$, NaOH, and $LiClO_4$ (J.T.Baker Inc.) were used without further purification.

All studies on Si were performed in methanol (EM Science). Some initial experiments were performed to compare the effects of using CH_3OH as supplied vs. CH_3OH that had been dried over calcium hydride and then distilled from Mg. As no differences were observed, all further experiments were performed using reagent grade methanol that had not been further purified. The H_2O for TiO_2 experiments was obtained from a Barnstead Inc. deionizing column and was typically 18 MΩ-cm in resistivity, with reagent grade NaOH added to obtain the 0.50 M NaOH(aq) solutions. A 30% w/w solution of NaOD in D_2O (99+ atom% D; Aldrich) was used as received and was diluted with D_2O (99.9 atom% D; Cambridge Isotopes Laboratory) to yield the 0.50 M NaOD-D_2O solutions.

C. Photoelectrochemical Cells and Techniques

All time-resolved experiments were performed in a custom Pyrex cell that was equipped with a quartz window, a gas inlet, and a sidearm for solution entry. The semiconductor and auxiliary electrodes were held rigidly at a separation of a few mm by a teflon stopcock containing two drilled holes. The cell was entirely enclosed by a 2 mm thick aluminum box that contained a small hole for light entry. The hole was carefully aligned with the cell window, and the entire electrode area was illuminated during an experiment. Short electrical leads were used to connect the electrodes to BNC bulkheads that had been mounted in the Al case. Short leads were also used to make connections to a potentiometer, which functioned as the variable load resistor, R_L. Shielding the cell in this manner was essential to the measurement of small signals in the presence of large noise sources, such as laser Q-switches and modelockers.

Except where noted, the counterelectrode was a ~6.25 cm^2 Pt gauze electrode. The corners of the electrode were bent around the sides and bottom of the working electrode towards the exposed semiconductor crystal face in an attempt to minimize the cell resistance. The electrode was cleaned before each experiment in a 3:1 (v/v) mixture of HNO_3 and HCl (aqua regia). The $Ni(OH)_2/Ni$ counterelectrode used in the TiO_2 experiments was made by chemical oxidation of a 6.25 cm^2 piece of Ni foil (>99% pure, Aesar).[55] To obtain reproducible results with this electrode, the Ni was freshly prepared and oxidized prior to each experiment. In 0.50 M NaOH(aq) (the solution in which the TiO_2 studies were conducted), the equilibrium potential of such $Ni(OH)_2/Ni$ electrodes varied between +0.25 and +0.28 V vs SCE, but the potential for an individual electrode was stable to within <5 mV for the duration of any given experiment.

The counterelectrode areas used in this study were much larger than those of the working electrodes, so that the impedance of the counterelectrode/electrolyte contact would make a negligible contribution to the observed photocurrent decays. The series resistance of the electrolyte was determined by replacing the working electrode with an equal area Pt foil electrode, and then using standard ac impedance methods to extract the series resistance of the cell, R_{cell}. Values of R_{cell} were generally between 20 and 120 Ω, and as expected, R_{cell} became larger when smaller working electrodes were used. In a given cell configuration, the procedures used to fabricate n-Si/Au Schottky barrier electrodes led to smaller values of R_{cell} than were observed with other electrodes studied in this work. This decrease in R_{cell} was quantified by ac impedance measurements on a Pt foil working electrode that had been subjected to the same metal evaporation procedure as was used to prepare the n-Si/Au Schottky barrier electrodes. The decreased value of R_{cell} was attributable to the evaporation procedure required to form the Schottky contact, which yielded a conducting, metallic coating over the edges of the working electrode and onto the surrounding epoxy insulation. As the counter electrode wrapped around the sides of the

working electrode, this highly conductive Au coating reduced the amount of electrolyte through which the charge had to flow, thereby decreasing R_{cell}.

D. Optical Configuration

Excitation for all experiments on n-Si was provided by a Coherent Inc. 700 Series dye laser (FWHM < 20 ps) that was synchronously pumped by the frequency doubled output of a Coherent Inc. Antares CW modelocked (76 MHz) Nd:YAG laser (Figure 1.2). The wavelength of the incident light ranged from 610-650 nm, depending on whether rhodamine-6G (Exciton) or DCM (Kodak or Exciton) was used in the dye laser. The output of the dye laser was modulated at 100 Hz using a Coherent Inc. 7220 cavity dumper triggered by a Wavetek signal generator. Excitation for experiments on n-TiO_2 was provided by the third harmonic (λ=355 nm) of a Continuum Nd:YAG regenerative amplifier seeded by the chirped fundamental output of another Coherent Antares laser. This configuration produced pulses of ~25 ps duration at a repetition rate of 10 Hz.

The incident power was reduced with neutral density filters until the photocurrent decays exhibited no change in response to an order of magnitude variation in power. Data were then recorded at the lowest power of this range. Typical input photon fluxes were 10^{10}-10^{11} photons-cm^{-2}-pulse^{-1}. These input photon fluxes produced open circuit voltage excursions (measured through a 1 MΩ input impedance, 300 MHz bandwidth oscilloscope) below 20 mV for n-Si surfaces and below 30 mV for n-TiO_2 electrodes.

E. Data Collection and Analysis

The photocurrent transients were generally monitored as a voltage drop across R_M, which was the internal 50 Ω input resistance of a Textronix Model DSA600 digitizing oscilloscope (600 MHz bandwidth at 50 Ω input impedance). The transient decays were simultaneously collected and averaged in this configuration. For TiO_2, R_M was an external 50 Ω resistor, and the voltage across this resistor was followed through the 1 MΩ input impedance of the DSA600 oscilloscope (300 MHz bandwidth at 1 MΩ input impedance). The latter configuration produced noisier signals, but was necessary to isolate the

$Ni(OH)_2/Ni$ auxiliary electrode from ground. Data were then transferred by a GPIB interface to a PC for storage. Analysis was performed on a personal computer using a non-linear least squares exponential fitting routine based on the Marquardt algorithm.

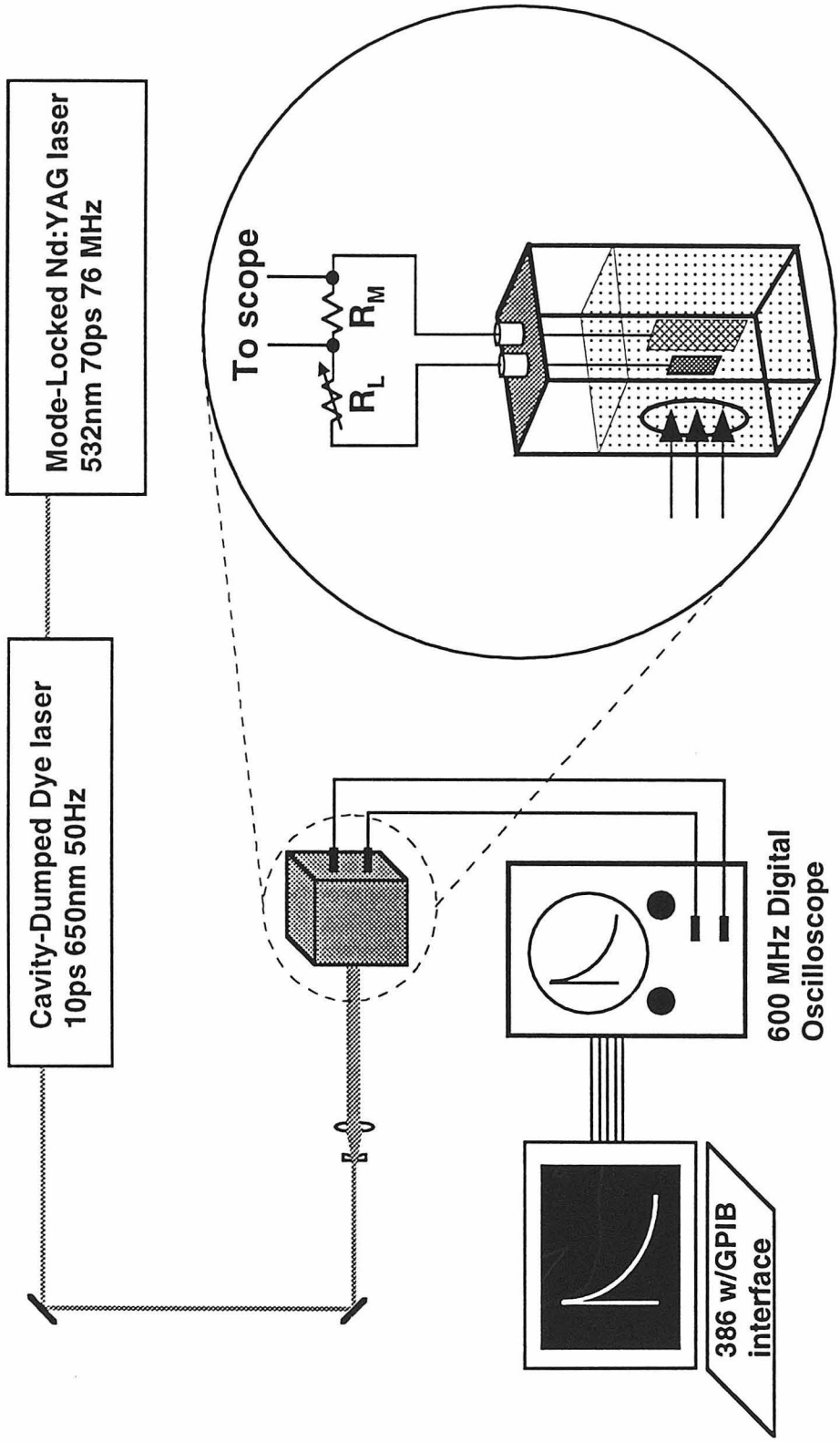

Figure 1.2: Schematic of the experimental configuration used in the photocurrent transient experiments. For experiments on TiO_2, the dye laser output was replaced by the third harmonic of a Nd:YAG regenerative amplifier.

IV. RESULTS

A. Transient Photocurrents at n-Si/CH_3OH-$Me_2Fc^{+/0}$ Interfaces

Figure 1.3 displays the photocurrent transient of the n-Si/CH_3OH-1.0 M $LiClO_4$-0.005 M Me_2Fc-0.005 M Me_2FcPF_6/Pt cell in response to a <20 ps laser pulse. Through a 50 Ω external load resistance (R_L), the decays for a 1.2 Ω-cm resistivity Si sample (dopant density, N_d= $4.2x10^{15}$ cm^{-3}) were well fit by a single exponential. As expected, τ was a function of the value of R_L (Figure 1.4). The slope of the τ vs R_L plot yielded a value for the measured areal capacitance, C_{meas}, of ≈$2.7x10^{-8}$ F-cm^{-2}, and the x-intercept of this plot yielded a value for R_{meas} (where the total resistance, R_{series}=R_{meas}+R_M+R_L) of 35 Ω.

These decay times are much shorter than those obtained in prior rf and microwave conductivity studies of Si/CH_3OH-$Me_2Fc^{+/0}$ interfaces,[11] despite the lower concentration of hole scavenger used in the present work. To address this point, the concentration of Me_2Fc was varied while the redox potential and the supporting electrolyte concentration were held constant. Within the range 0.10 M Me_2Fc - 0.005 M Me_2Fc, changes in the concentration of the redox species had negligible effect on τ. This striking result implies that τ either does not reflect the interfacial minority carrier charge transfer rate constant, or that the rate constant is independent of the donor concentration under these conditions.

The circuit elements that determined the measured value of τ can be clearly identified. R_{meas} agrees well with the independently measured value of the series resistance of the electrolyte, while the value for C_{meas} is in accord with the differential capacitance of the space charge region for a high barrier height contact at the n-Si/CH_3OH-$Me_2Fc^{+/0}$ junction.[49,56,57] Consistently, photocurrent transient measurements on the lower barrier height n-Si/CH_3OH-$Me_{10}Fc^{+/0}$ contact[57] exhibited similar behavior, but yielded values of C_{meas} that were 35-40% larger than those of the n-Si/CH_3OH-$Me_2Fc^{+/0}$/Pt system.

To verify quantitatively that C_{meas} of the n-Si/CH_3OH-$Me_2Fc^{+/0}$/Pt cell was a direct function of the semiconductor space charge capacitance, transient photocurrent

decays were collected for Si samples having a variety of doping densities. In all cases, the photocurrent transients were well-fit to single exponentials, and plots of τ vs R_L were linear. Figure 1.5 presents a plot of $\log(C_{meas})$ vs $\log(N_d)$, whereas the solid line is a fit to the known dependence of the equilibrium semiconductor depletion capacitance on dopant density (Section II):

$$\frac{C_{sc}}{A} = \sqrt{\frac{\varepsilon_s q N_d}{2(V_{bi} - \frac{kT}{q})}} = \sqrt{\frac{\varepsilon_s q N_d}{2(\phi_b - \frac{kT}{q}\ln\frac{N_c}{N_d} - \frac{kT}{q})}} \qquad (1.12)$$

with ε_s the static dielectric constant of the semiconductor and ϕ_b the barrier height of the semiconductor/liquid contact. The small correction to V_{bi} that is not present in eq 1.10 results from a more detailed treatment of the charge density in the depletion region.[49] The correlation of C_{meas} with the depletion layer capacitance expected for a high barrier height silicon/liquid junction, combined with the dependence of C_{meas} on N_d, and with the agreement between R_{meas} and the measured electrolyte series resistance, imply that τ is dominated by the series resistance of the cell and the capacitance of the semiconductor space charge region, as opposed to the impedance for minority carrier charge transfer across the semiconductor/liquid interface.

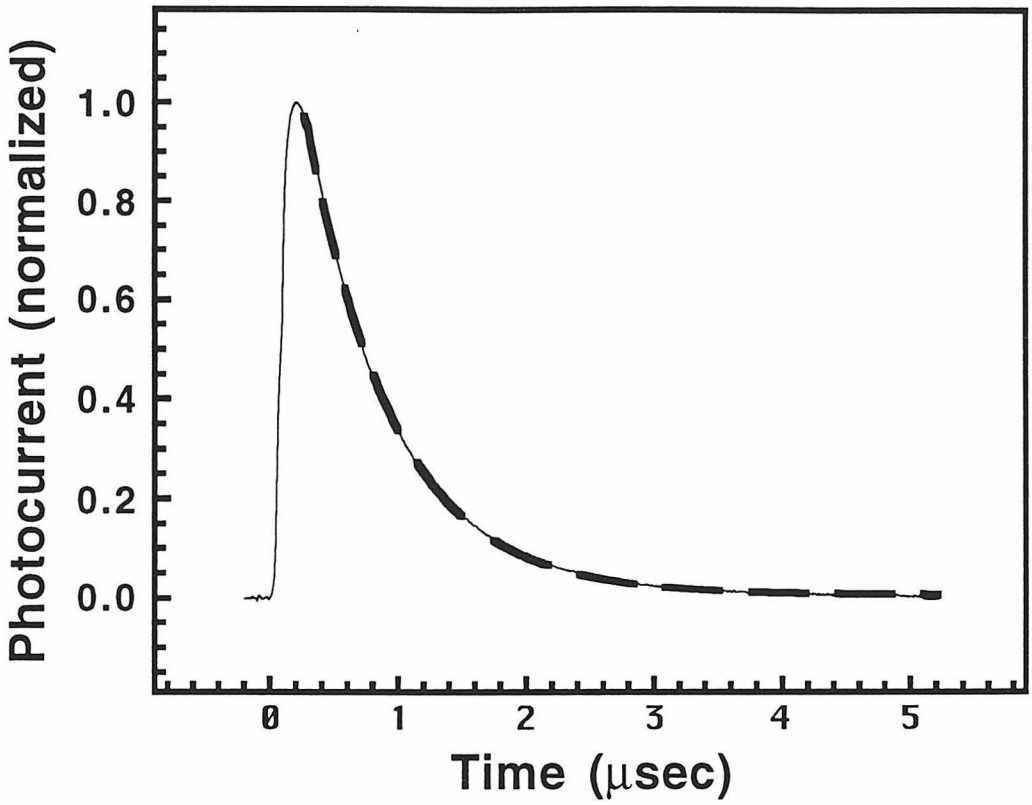

Figure 1.3: Photocurrent decay for the n-Si/CH_3OH-$LiClO_4$-$Me_2Fc^{+/0}$/Pt system. The thin line is the observed transient and the heavy dashed line represents a fit of the decay to a single exponential.

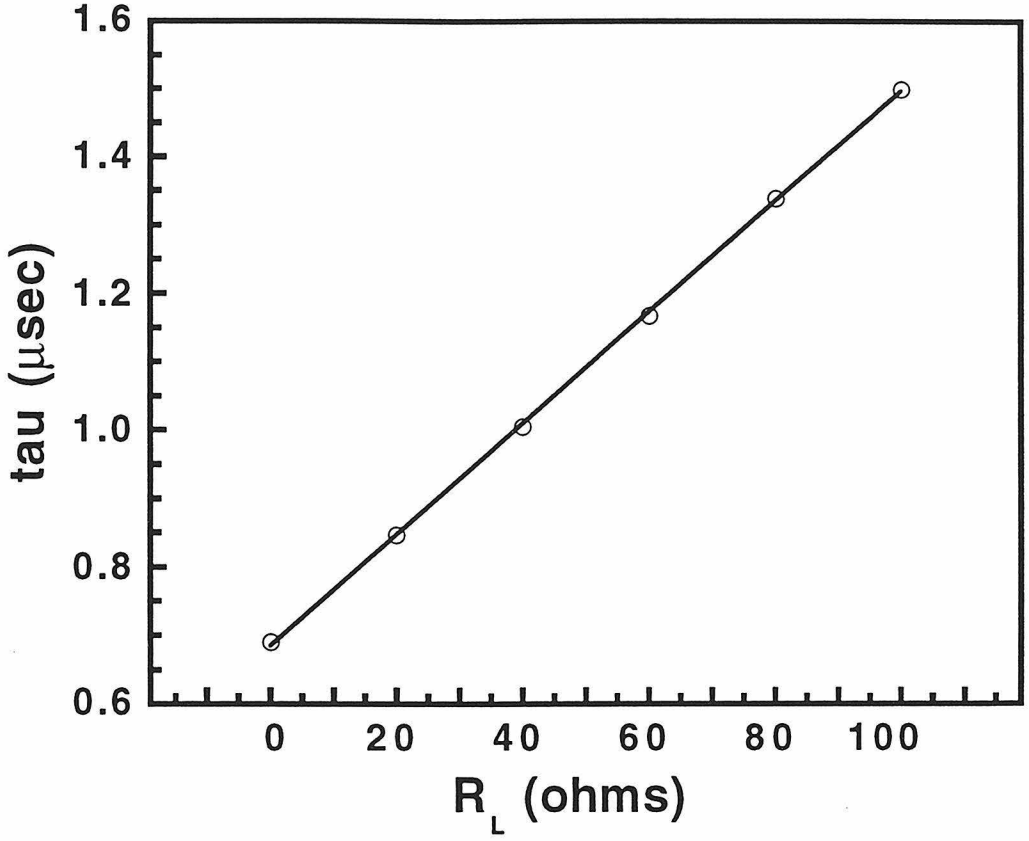

Figure 1.4: Plot of τ as a function of R_L for the n-Si/CH_3OH-$LiClO_4$-$Me_2Fc^{+/0}$/Pt system. The data are shown as open circles and the solid line is a linear fit to the data. The intercept had a value of -85 Ω when the y-axis was rescaled to start at zero μs.

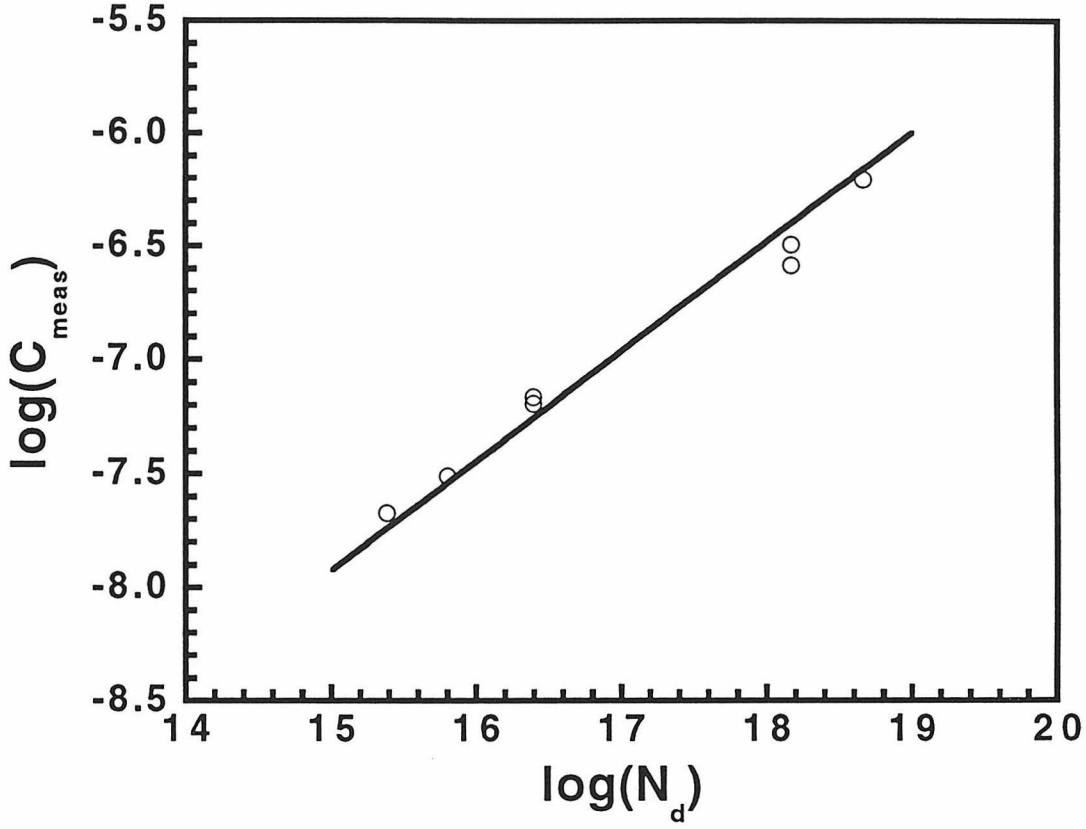

Figure 1.5: Plot of $\log(C_{sc})$ versus $\log(N_d)$. The data are shown as open circles and the solid line represents a fit to eq 1.12. A barrier height of 0.88±0.15 V for the n-Si/CH_3OH-$Me_2Fc^{+/0}$ junction was obtained from the fit to the data.

B. Transient Photocurrents at n-Si/Au/CH_3OH-$Me_2Fc^{+/0}$ Interfaces

The lack of dependence of τ on donor concentration, together with the discrepancy between the photocurrent decay times and the rf or microwave conductivity decay times, strongly suggests that the photocurrent decay kinetics in this system are insensitive to the minority carrier charge transfer rate. This important conclusion was tested further through the use of electrodes based on an n-Si/Au Schottky barrier contact.

Figure 1.6 displays the photocurrent decay data for an n-Si/Au Schottky barrier (R_L = 50 ohm) in the n-Si/Au/CH_3OH-$Me_2Fc^{+/0}$/Pt cell. Although the metallic Au overlayer would be expected to catalyze interfacial charge transfer between Si and Me_2Fc, the decay kinetics for the n-Si/Au/CH_3OH-$Me_2Fc^{+/0}$/Pt cell were very similar to those for the n-Si/CH_3OH-$Me_2Fc^{+/0}$/Pt cell. The decays were well-fit by a single exponential, and τ was a linear function of R_L (Figure 1.7). For this experiment, the slope yielded C_{meas}=3.2x10^{-8} F/cm^2, and the intercept yielded a value for R_{meas} of 20 Ω.

For a given doping density of the Si, the value of C_{meas} was higher for n-Si/Au/CH_3OH-$Me_2Fc^{+/0}$/Pt cells than for n-Si/CH_3OH-$Me_2Fc^{+/0}$/Pt cells. This behavior is in accord with the expected increase in barrier height for the n-Si/CH_3OH-$Me_2Fc^{+/0}$ contact as compared to the n-Si/Au interface.[57,58] To quantify this difference, an n-Si electrode was prepared, its area determined carefully, and the junction capacitance determined in a CH_3OH-$Me_2Fc^{+/0}$/Pt cell. A value of C_{meas}=7.05x10^{-8} F/cm^2 was obtained as the slope of the τ vs R_L plot. A Schottky barrier was then fabricated from the same electrode and the capacitance was then determined, by the same method, to be C_{meas}=8.05x10^{-8} F-cm^{-2}. The barrier height of this metal-semiconductor contact was then determined independently to be 0.83 V by analyzing the steady state I-V properties of the diode according to the thermionic emission model (Figure 1.8).[49] Multiplying this barrier height by the ratio of C_{meas} values for the liquid and Schottky contacts yielded a value of 0.95 V for the barrier height of the n-Si/CH_3OH-$Me_2Fc^{+/0}$ junction. This value is consistent with the larger open circuit voltages exhibited by n-Si/CH_3OH/$Me_2Fc^{+/0}$

contacts relative to n-Si/Au Schottky barriers, and with the "ideal" electrochemical behavior reported previously for n-Si/CH_3OH contacts.[59]

The Au overlayer was also useful because it established a fixed degree of band bending at the Si/Au contact even in the absence of a redox couple. Thus, it was possible to remove completely the redox couple from the cell and to then determine the transient decay kinetics of the system. If the minority carrier charge transfer process dominated the observed decay kinetics, extremely long decays would be expected due to the absence of deliberately added redox species in the electrolyte. However, examination of Figure 1.9 reveals that, within experimental error, the photocurrent decay dynamics for the n-Si/Au photoelectrode were not only independent of the Me_2Fc and Me_2Fc^+ concentration, but did not even require the presence of the redox couple in the solution! This observation provides a striking confirmation that photocurrent decay transients do not reflect the interfacial minority carrier charge transfer kinetics in this system.

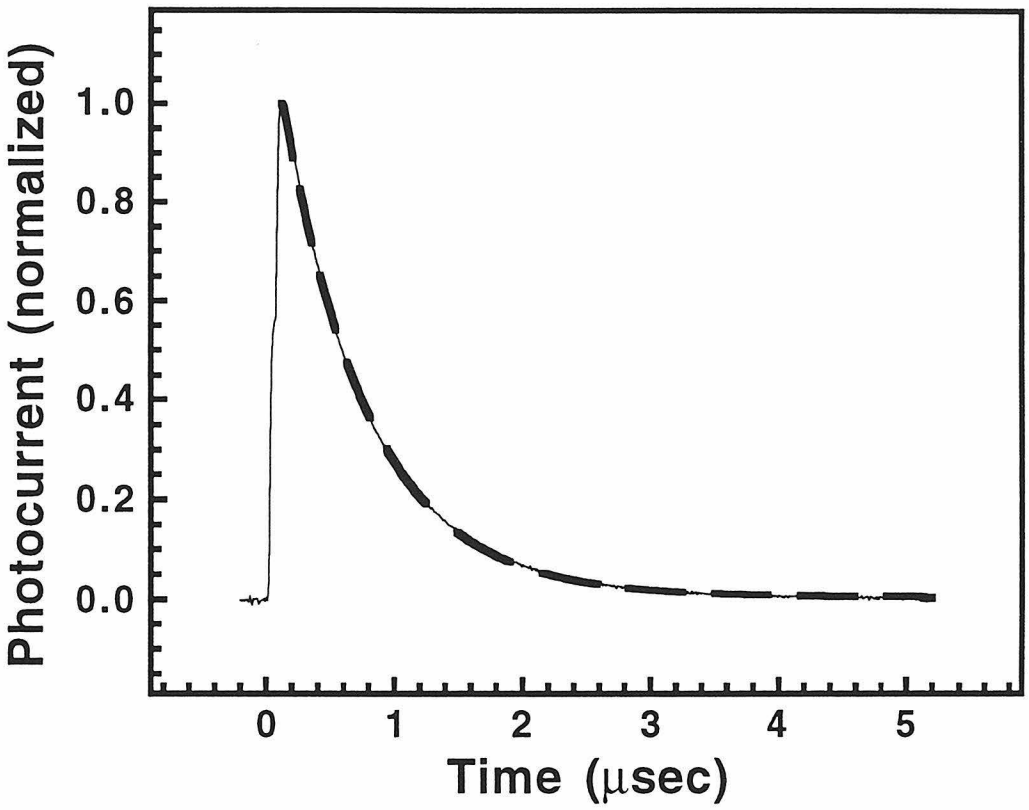

Figure 1.6: Photocurrent decay for the n-Si/Au/CH_3OH-$LiClO_4$-$Me_2Fc^{+/0}$/Pt system. The thin line is the observed transient and the heavy dashed line represents a fit of the decay to a single exponential.

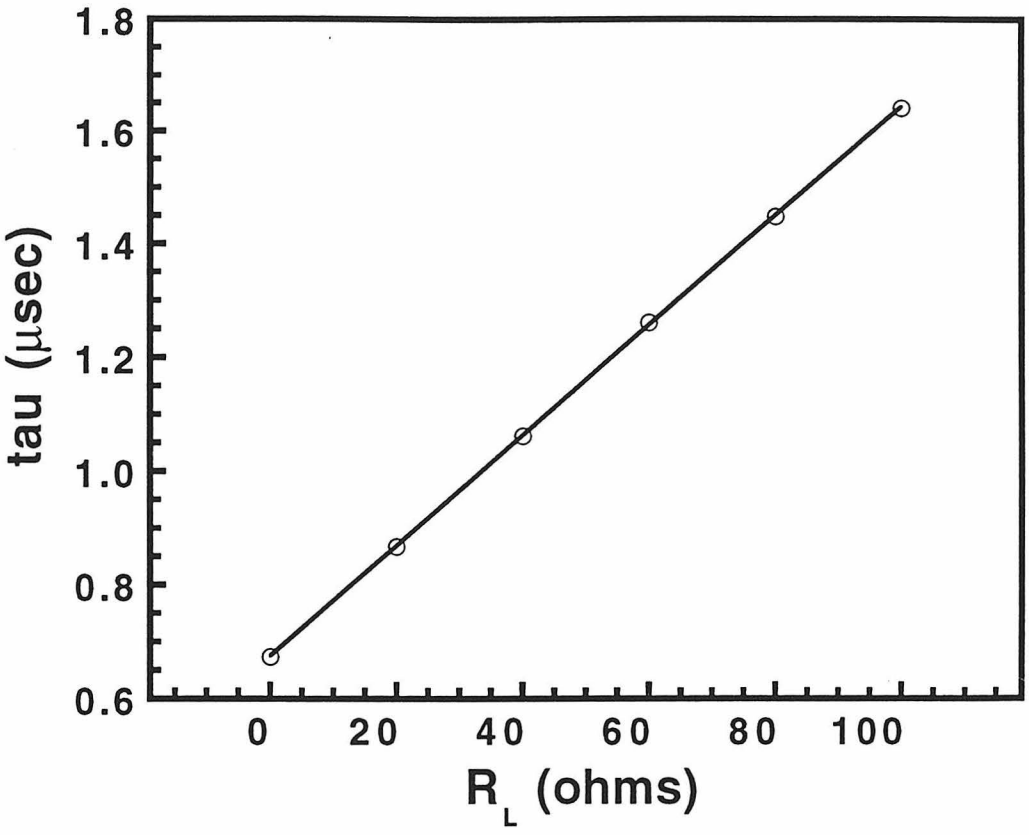

Figure 1.7: Plot of τ as a function of R_L for the n-Si/Au/CH_3OH-$LiClO_4$-$Me_2Fc^{+/0}$/Pt system. The data are shown as open circles and the solid line is a linear fit to the data.

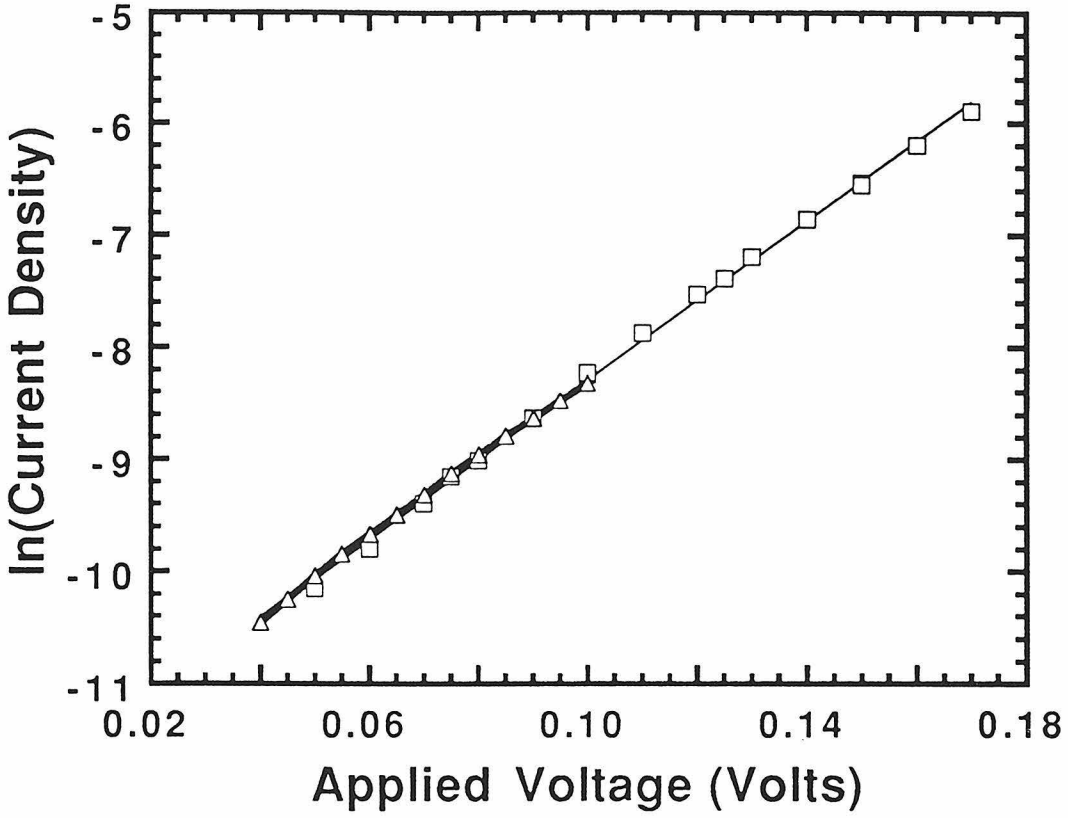

Figure 1.8: Plot of the natural logarithm of the current density as a function of the applied voltage for an n-Si/Au Schottky contact. The open symbols are the data from two independent measurements. From the y-intercepts of linear fits to these data (solid lines), a barrier height of .95 V was determined for this junction.

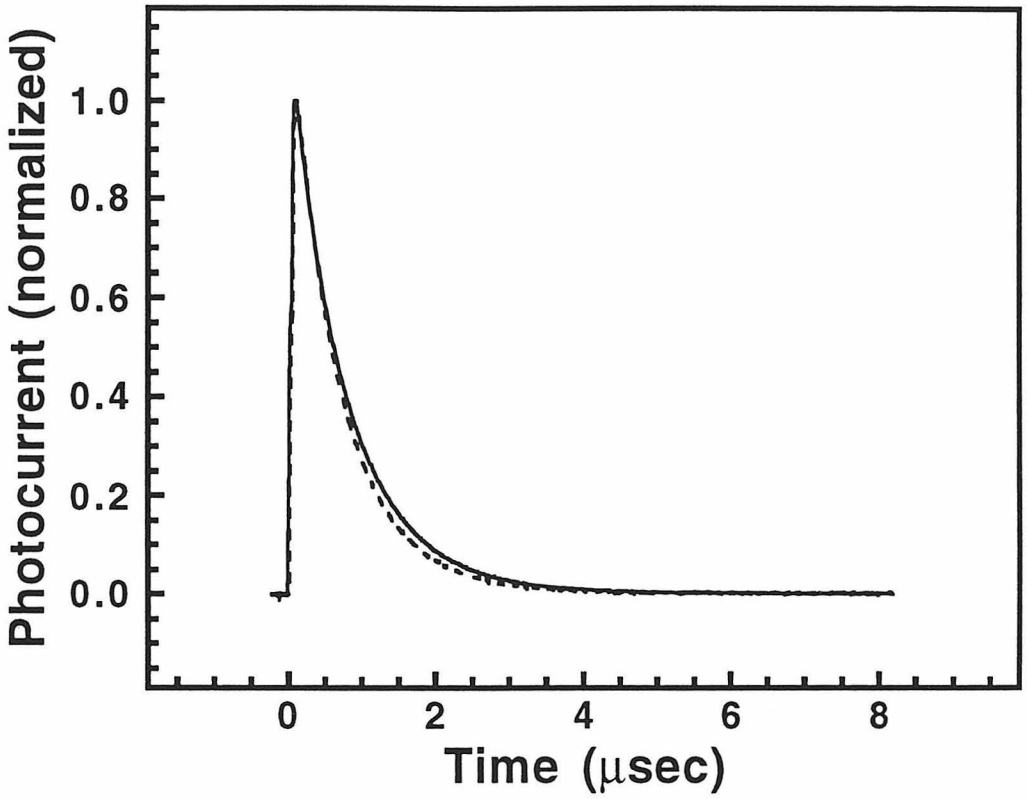

Figure 1.9: Comparison of the decays observed for the n-Si/Au/CH_3OH-$LiClO_4$/Pt cell in the presence (dashed line) and absence (solid line) of the 0.005 M Me_2Fc^+-0.005 M Me_2Fc^0 redox couple.

C. Transient Photocurrents at n-TiO_2/NaOH(aq) Interfaces

To extend this study, photocurrent transients were also recorded for n-TiO_2/NaOH(aq)/$Ni(OH)_2$/Ni cells. Prior studies of the n-TiO_2/NaOH(aq) contact have reported biexponential photocurrent decays on the 100 μs time scale.[33] Analysis of the early portion of these decays ($\tau \approx 10$ μs) has been performed to extract information on the minority carrier kinetics at the n-TiO_2/H_2O interface. This analysis appears to contradict the conclusions presented above, in which the transient photocurrent decays were of a simple form and were not sensitive to the interfacial charge transfer kinetics.

Figure 1.10 displays the transient photocurrent decays obtained in this work for the n-TiO_2/0.50 M NaOH(aq) interface. A $Ni(OH)_2$/Ni counterelectrode was used in these experiments, because it provided a well-defined, nonpolarizable counterelectrode and also effected significant band bending at the n-TiO_2/NaOH(aq) contact. No potentiostats or other electrochemical control instrumentation were required using this experimental arrangement. The photocurrent decay, measured through R_L=50 Ω, was well-fit by a biexponential. The time constant for the slower component varied in a linear fashion with changes in R_L (Figure 1.11) while that for the faster component exhibited no clear dependence on R_L, but instead fluctuated about an average value of 2.2 μs. To insure that the biexponential form did not result from the use of the $Ni(OH)_2$/Ni counterelectrode, transient photocurrents were also measured for an n-Si/Pt Schottky barrier electrode in an n-Si/Pt/NaOH(aq)/$Ni(OH)_2$/Ni cell. Through R_L=50 Ω, these electrodes yielded single exponential decays similar to those observed for the n-Si/Au/CH_3OH-$Me_2Fc^{+/0}$/Pt cell, and the decay times in the aqueous electrolyte were comparable to those obtained in the non-aqueous solvent.

To further examine the behavior of TiO_2/liquid contacts, photocurrent decays were determined for n-TiO_2/0.50 M NaOH(aq)-0.01 M $Fe(CN)_6^{3-}$ -0.001 M $Fe(CN)_6^{4-}$/Pt cells. For direct comparison to the n-TiO_2/NaOH(aq)/$Ni(OH)_2$/Ni cells, the composition of the NaOH-$Fe(CN)_6^{3-/4-}$ solution was adjusted by controlled addition of $Fe(CN)_6^{3-}$ until the

equilibrium Nernst potential of the solution was within 10 mV of the $Ni(OH)_2/Ni$ electrode potential. This procedure was adopted to avoid discrepancies between the decays for the two systems resulting solely from differences in the equilibrium values of the semiconductor depletion capacitance. It was therefore expected that this experiment would reveal whether the second time constant of the biexponential decay of n-TiO_2/NaOH(aq) contacts reflected the interfacial charge transfer dynamics, as has been suggested previously.[33] As depicted in Figure 1.12, n-TiO_2/0.50 M NaOH(aq)-$Fe(CN)_6^{3-/4-}$/Pt cells yielded photocurrent decays that were biexponential, with time constants similar to those observed for the n-TiO_2/0.50 M NaOH(aq) junction. The time constant for the longer component of the n-TiO_2/0.50 M NaOH(aq)-$Fe(CN)_6^{3-/4-}$/Pt cell varied linearly with changes in R_L (Figure 1.11), while the shorter time constant again showed no significant dependence on R_L, varying about the somewhat smaller value of 1.6 μs. The lack of any significant change in either time constant due to the presence of $Fe(CN)_6^{4-}$ indicated either that the kinetics for the oxidation of 0.0010 M $Fe(CN)_6^{4-}$ at n-TiO_2 were fortuitously very similar to those for the oxidation of 0.50 M OH^-(aq), that both reactions proceeded through a common intermediate, or that the photocurrent decay transients are relatively insensitive to the faradaic minority carrier charge transfer kinetics. These possibilities are discussed further in Section V.

Photocurrent decay transients were also collected for n-TiO_2 electrodes in contact with D_2O-0.50 M NaOD solutions. The n-TiO_2 photocurrent decays in contact with D_2O-NaOD exhibited similar characteristics to those in contact with H_2O-NaOH, in that the time constant for the longer component of the biexponential decay varied linearly with changes in R_L (Figure 1.11), while data for the shorter time constant were scattered about an average value of 2.5 μs. Whereas the faster time constants were very similar in D_2O and H_2O, the time constant for the slower component of the decay was systematically longer in heavy water than in light water. A plot of τ vs R_L revealed that this effect was due to a larger value of R_{meas} in the D_2O electrolyte (Figure 1.11), yielding a ratio of

$R_{meas}(D_2O)/R_{meas}(H_2O)$ of 1.4. This ratio is in close accord with the known higher resistivity of D_2O-0.50 M NaOD solutions relative to H_2O-0.50 M NaOH solutions. Thus, in the experimental configuration employed, the first decay component showed no identifiable isotope effect, while changes in the second component of the photocurrent decay dynamics were fully consistent with the known isotope effects on electrolyte conductivity, and did not require any further interpretation in terms of kinetic isotope effects on the interfacial charge transfer dynamics. These results, combined with the n-TiO_2/NaOH(aq)-$Fe(CN)_6^{3-/4-}$ data, therefore suggest that the photocurrent decay transients provide little, if any direct information on the faradaic minority carrier charge transfer kinetics at such semiconductor/liquid interfaces.

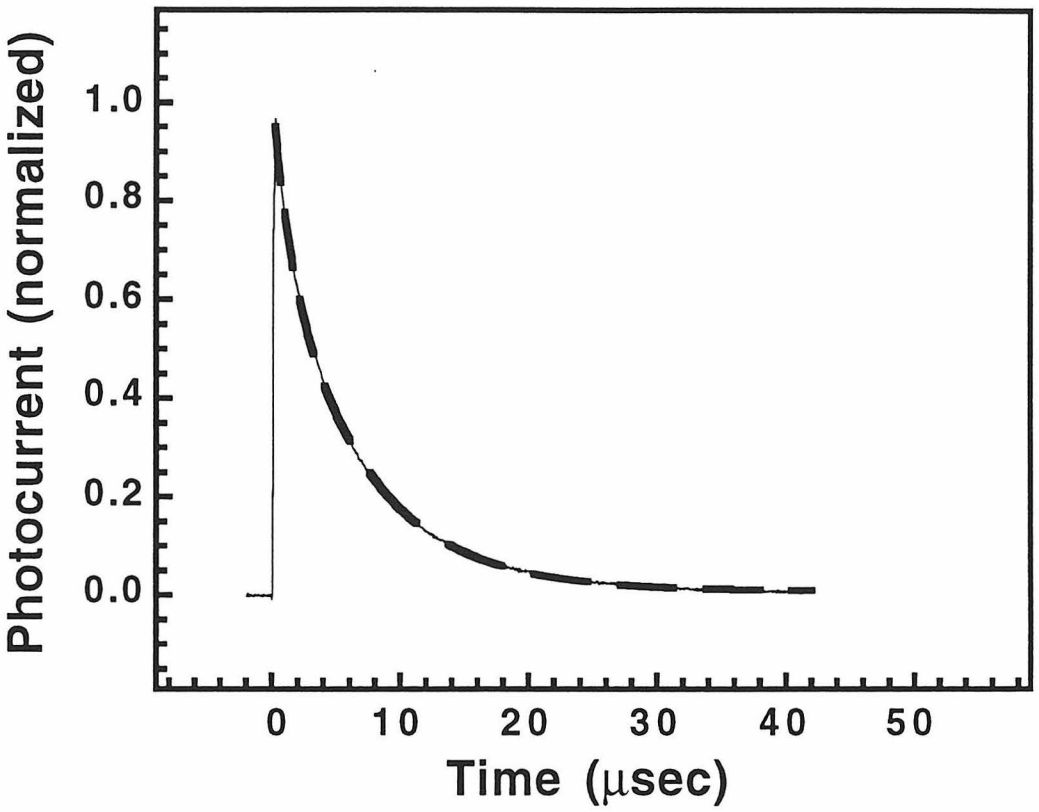

Figure 1.10: Photocurrent decay for the n-TiO_2/0.50 M NaOH(aq)/$Ni(OH)_2$/Ni system. The thin line is the observed transient and the heavy dashed line represents a fit of the data to a double exponential.

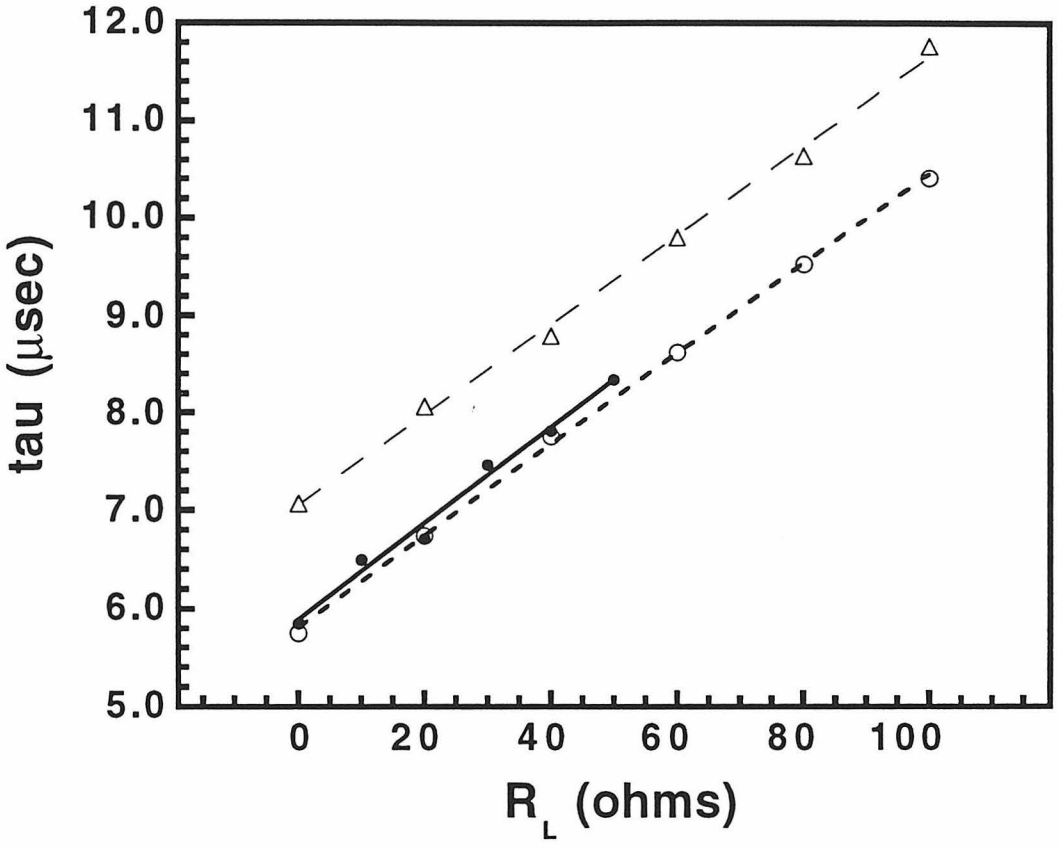

Figure 1.11: Plot of R_L vs time constant, τ, for the longer component of the biexponential photocurrent decay of n-TiO_2/liquid contacts. Filled circles are data for n-TiO_2/0.50 M NaOH-H_2O contacts; triangles are data for n-TiO_2/0.50 M NaOD-D_2O contacts, and open circles are data for n-TiO_2/0.50 M NaOH(aq)-$Fe(CN)_6^{3-/4-}$ contacts.

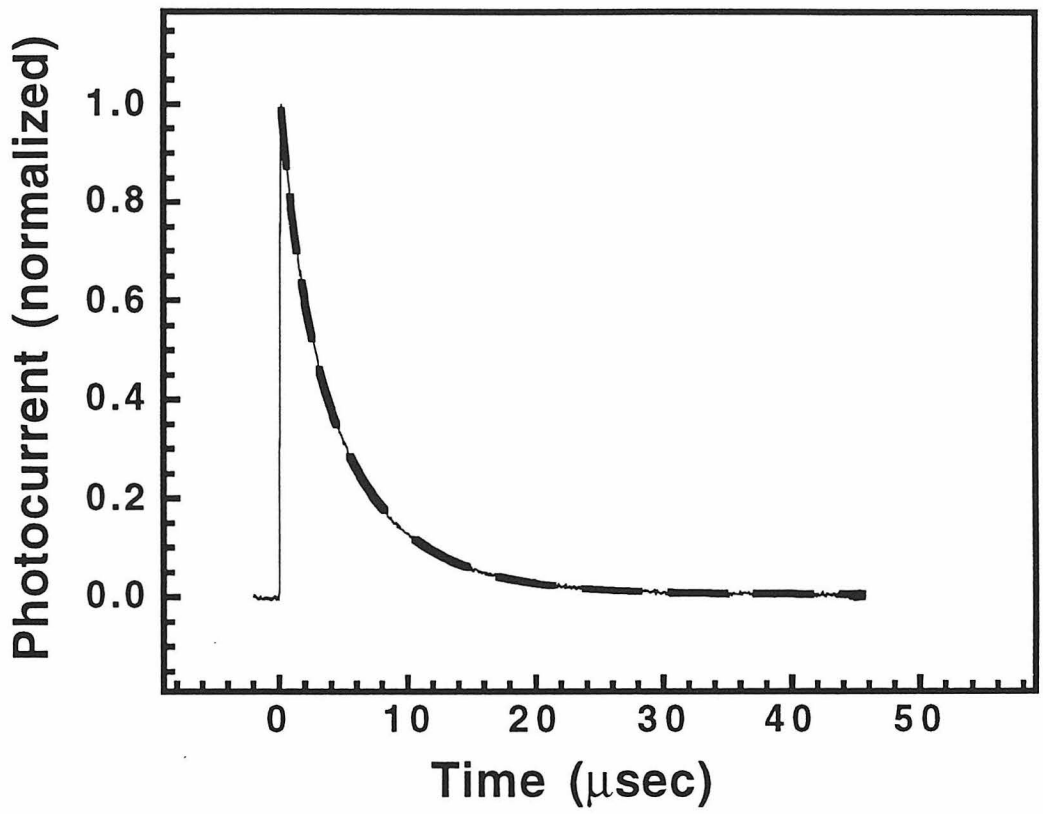

Figure 1.12: Photocurrent decay for the n-TiO_2/0.50 M NaOH(aq)-$Fe(CN)_6^{3-/4-}$/Pt system. The thin line is the observed transient while the heavy dashed line represents a fit of the data to a double exponential.

V. DISCUSSION

The results presented above clearly indicate that, under the conditions employed, the transient photocurrents of depleted Si/liquid contacts do not contain direct information concerning the interfacial minority carrier kinetics. The variety of situations explored in this work implies that this conclusion should generally apply to moderately doped, depleted semiconductor surfaces in contact with dissolved redox couples. Such transient photocurrent decay measurements are valuable as an alternative to high frequency measurements of the differential capacitance of the semiconductor/liquid contact, but generally will yield no direct information on the kinetics for faradaic charge transfer across the semiconductor/liquid junction. This stands in contrast to the situation for the metal/liquid interface or for highly doped semiconductor/liquid contacts, where current transients and coulostatic responses can contain important kinetic information.

The data and conclusions presented above can be understood more completely by reference to an equivalent circuit for the semiconductor/electrolyte/metal photoelectrochemical cell. For small perturbations in the carrier concentrations, the relevant charge transfer impedances can be linearized with respect to voltage, and the equivalent circuit describing the small signal current response can then be represented in terms of simple resistive and capacitive elements. The important capacitive elements in the cell are the differential capacitance of the semiconductor space charge region, C_{sc}, and the differential capacitance of the solution double layer adjacent to the semiconductor electrode, C_{dl}. Important resistances are the external load and measuring resistances, R_L and R_M, the collective series resistance of the electrodes and electrolyte, R_{cell}, the charge transfer resistance to minority carrier flow across the semiconductor/liquid interface, R_{ct}, and the resistance to recombination of photogenerated minority carriers in the semiconductor, R_{rec}. For simplicity, circuit elements due to surface states are neglected.[60] Also ignored are elements arising from the counterelectrode/solution interface, as its large capacitance and low resistance to charge transfer make its impedance negligibly small in the experimental

configuration employed. These elements could be included in a more complete description of the cell, but the features of the simplified equivalent circuit will suffice to explain fully the data of concern in this work.

The key to constructing a valid equivalent circuit is to obtain the physically correct connectivity between the various linearized circuit elements. There is great controversy on this approach in the literature, and even the relatively small number of resistances and capacitances retained in the simplified circuit of Figure 1.13b have been connected by several different routes in the literature.[14,17,20,26,33,34,41,43] For this reason, the equivalent circuit being forwarded herein, and the reasoning behind it, will be justified in a somewhat detailed fashion. The discussion will focus on an n-type, depleted semiconductor electrode, as this is relevant to the experimental results described above.

Figure 1.13a depicts a proposed arrangement of elements in the simplified equivalent circuit. The photocurrent generation impulse, which can be represented as a current source, is connected across the semiconductor space charge capacitance, C_{sc}. The field-induced charge separation in the semiconductor depletion region is responsible for rapidly placing charge on opposite plates of C_{sc}, and the current source then becomes an open circuit after the initial charge impulse. The charge separation process produces excess positive, minority carrier-based, charge density at the semiconductor surface. This excess positive charge is offset by excess negative charge in the electrolyte and by excess negative charge in the bulk of the semiconductor. Thus, the semiconductor space charge region, C_{sc}, and the solution double layer capacitor, C_{dl}, share a common plate and must be connected in series in the equivalent circuit.

The relevant cell resistances must also be placed into the simplified equivalent circuit. The recombination resistance, R_{rec}, represents the rate at which excess photogenerated charge carriers recombine in the semiconducting solid. Since recombination will annihilate an electron with a hole, recombination will decrease the net charge across C_{sc}. R_{rec} must therefore be placed in parallel with C_{sc}. The photogenerated

majority carriers that do not recombine internally will eventually flow through the external circuit and through the electrolyte; thus, R_M, R_L and R_{cell} must be placed in series with each other (R_{series}) and with the other pertinent circuit elements.

The critical remaining question involves the connectivity of the minority carrier charge transfer resistance, R_{ct}. Clearly, R_{ct} must be placed across C_{dl}, because carrier movement into the solution would act to shunt the excess photogenerated charge that has developed across the plates of C_{dl}. However, R_{ct} cannot be also consistently be placed across C_{sc}. Transfer of minority carriers across the solid/liquid interface will only lead to shunting of the capacitance across the semiconductor/liquid double layer, and will not shunt C_{sc}. Only recombination with majority carriers that have been separated across the space charge region can shunt C_{sc}, but this process is already contained in the simplified equivalent circuit as the element R_{rec}. The complete equivalent circuit represented in Figure 1.13a is therefore generated from this body of reasoning.

Figure 1.13b depicts this equivalent circuit in a more convenient form. Assuming that a current impulse of strength Q_0 is delivered across C_{sc}, Laplace transform methods yield the following time dependence of the current in the external circuit:[61]

$$i(t) = \frac{Q_0}{R_{series}C_{sc}}\left[K_0 e^{-\alpha_0 t} + K_1 e^{-\alpha_1 t}\right] \qquad (1.13)$$

$$-\alpha_{0,1} = -\frac{A}{2} \pm \sqrt{\frac{A}{4} - B} \qquad K_0 = \frac{\alpha_2 - \alpha_0}{\alpha_1 - \alpha_0} \qquad K_1 = \frac{\alpha_1 - \alpha_2}{\alpha_1 - \alpha_0}$$

$$A = \frac{R_{rec}R_{ct}(C_{sc} + C_{dl}) + R_{series}(\tau_1 + \tau_2)}{R_{series}\tau_1\tau_2} \qquad B = \frac{R_{rec} + R_{ct} + R_{series}}{R_{series}\tau_1\tau_2}$$

$$\alpha_2 = \frac{1}{\tau_2} \qquad \tau_1 = R_{rec}C_{sc} \qquad \tau_2 = R_{ct}C_{dl}$$

Simple multiplication of i(t) by R_M then yields the experimentally measured transient response of the cell, V(t). Note that this response is a biexponential function, as must be the case from the presence of two separable RC loops in the simplified equivalent circuit.

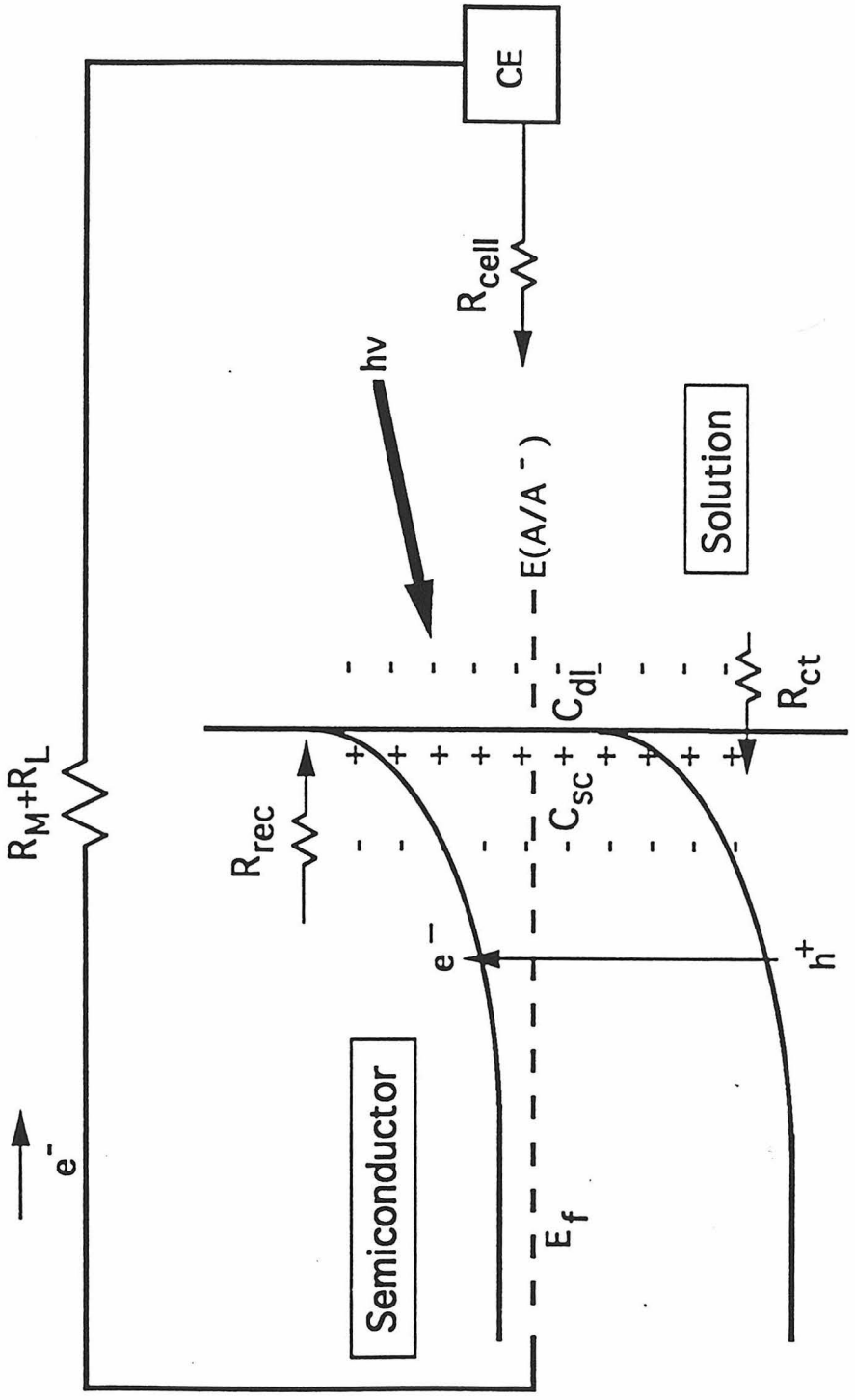
CE
R_{cell}
hν
$E(A/A^-)$
Solution
R_{ct}
C_{dl}
C_{sc}
R_{rec}
R_M+R_L
e^-
h^+
Semiconductor
E_f

Figure 1.13a

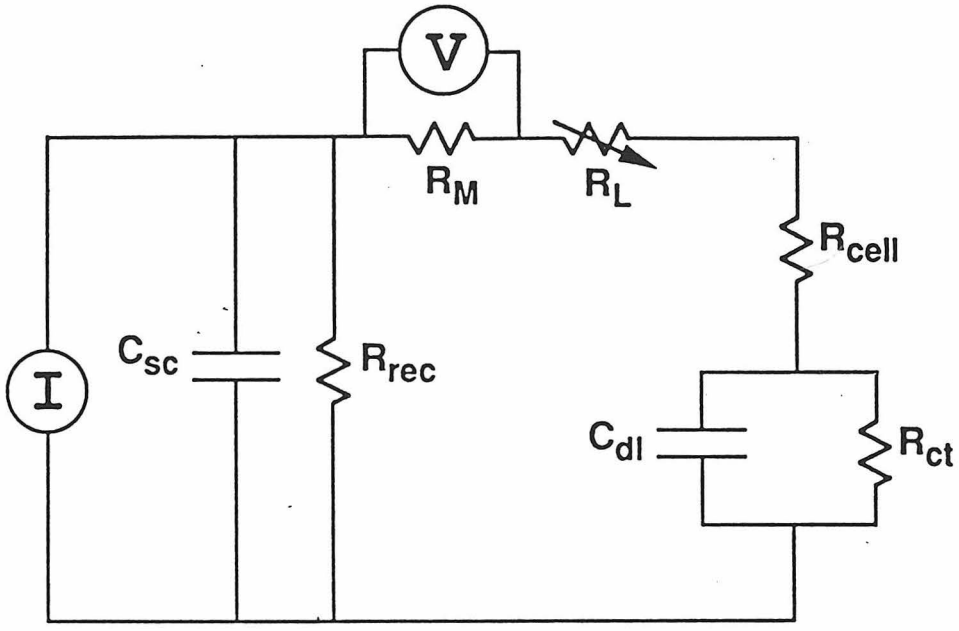

Figure 1.13b

Figure 1.13: (a) Proposed arrangement of circuit elements where an attempt has been made to associate the important elements in the simplified circuit with their physical basis in the photoelectrochemical cell. (b) Simplified equivalent circuit.

Using the circuit of Figure 1.13b and eq 1.13, the photocurrent decay experiment can be analyzed both qualitatively and quantitatively. An analysis will first be given for the situation where $C_{sc} \ll C_{dl}$, as is typically the case for moderately doped semiconductor electrodes in depletion.[35] It will be shown below that this is the key constraint which differentiates the behavior of transient currents at most semiconductor electrodes from those at metal electrodes.

The first case to be considered is where R_{rec} is very large ($R_{rec} \gg R_{series}$), as would be the case near short circuit for high quality bulk semiconductor samples used to form strongly rectifying semiconductor/liquid contacts. After charge injection into the semiconductor, rapid charge separation across C_{sc} occurs. In this early time window, the observed photocurrent reflects the internal charge motion in the solid, and is usually observed as a bandwidth-limited rise in photocurrent.[41] After charge separation, the excess photogenerated majority carriers experience a relatively high resistance to recombination in the semiconductor bulk and semiconductor space charge regions, and will then spontaneously flow through the external circuit to charge C_{dl}. This process is favorable because $C_{dl} \gg C_{sc}$, so charge flow onto C_{dl} yields a lower overall cell voltage. This charging process, due to majority carrier flow, is independent of R_{ct}, so τ (as measured across R_M) is also independent of R_{ct}.

If the minority carrier interfacial charge transfer resistance is relatively small, then C_{dl} is discharged as soon as the photogenerated excess majority carrier charge reaches the solution-based plate of C_{dl}. Under these conditions, the time constant for the photocurrent decay transient, measured through R_M, is clearly independent of R_{ct}. Alternatively, if the minority carrier interfacial charge transfer resistance is large, the excess charge will persist on C_{dl} for a significant period of time before it can flow through R_{ct} and complete the circuit. However, the time scale for this discharge process is irrelevant to the time scale for photocurrent flow through R_M; thus, even under conditions where R_{ct} is large compared to R_M, the photocurrent decay transient is predicted to be independent of the value of R_{ct}.

It is also of interest to examine the situation when the recombination resistance, R_{rec}, is small relative to R_{ct} but is still much larger than R_{series}. After excitation and subsequent charge separation across C_{sc}, the carriers will still move spontaneously to charge C_{dl}. However, the subsequent discharge process will occur predominantly by recombination in the semiconductor (through R_{rec}) as opposed to faradaic charge transfer across the semiconductor/liquid interface (through R_{ct}). The favored recombination process then leads to a current of opposite sign flowing through R_M.[20,41] For large values of R_{rec} and small ratios of C_{sc} to C_{dl}, this reverse current is of a significantly smaller magnitude and will decay with a much longer time constant than the initial majority carrier current flow.[62] Even if this portion of the decay could be observed, it would not yield direct information on the magnitude of R_{ct}, but would only yield an estimate of the ratio R_{rec}/R_{ct}.

The last case of importance to consider for $C_{sc} \ll C_{dl}$ is the situation when R_{rec} is relatively small compared to R_{series}. Under this condition, rapid recombination will occur in the semiconductor, and few photogenerated majority carriers will flow through the external circuit. The observed decay is predicted to be a single exponential for this situation as well. The current will decay with a time constant $\tau \cong R_{rec}C_{sc}$ when $R_{rec} \ll R_{series}$, and $\tau \cong 0.5\ R_{rec}C_{sc}$ when $R_{rec} \cong R_{series}$. Intermediate values of R_{rec} yield more complicated exponents, but in no case when $C_{sc} \ll C_{dl}$ does the experimentally measurable, main component of i(t) depend on R_{ct}.

The above analysis suffices to understand the behavior of the n-Si/CH_3OH contacts studied in this work. For typical depleted semiconductor/liquid contacts, the lack of dependence of i(t) on R_{ct} distinguishes photocurrent transients at semiconductor electrodes from light-induced transients at metal electrodes induced by coulostatic pulse methods. The key difference is that for a metal, the differential capacitance of the electrode far exceeds that of C_{dl}. Thus, for a metal electrode, the charge flow through an external load measures the current that shunts C_{dl}, and this current then directly yields information on R_{ct}. For

most semiconductor electrodes, however, C_{sc}«C_{dl}, so the photocurrent transient is essentially a non-faradaic charging current of C_{dl}, as opposed to a faradaic charge transfer current. An equivalent statement is that the rate of majority carrier flow through the external circuit does not yield information on the rate of minority carrier transfer across the semiconductor/liquid junction.

For such systems, this analysis therefore predicts that the only electrical circuit-based method to measure R_{ct} directly would be to place a hypothetical "voltmeter" across the electrolyte double layer adjacent to the semiconductor electrode, and thus to measure the time-dependence of the voltage across C_{dl}. Although this might be possible using a spectroscopic probe of charge movement, it is not currently feasible to perform an electrically-based measurement of this type. This equivalent circuit model is similar to some prior analyses, but is fundamentally different than others. Willig's current source model is functionally equivalent to the analysis presented herein,[41,42] as is the simplified circuit presented in the study of Sakata and Wilson.[20] One of the key features of this work is the experimental validation of the equivalent circuit model with respect to the behavior of essentially all of the key circuit elements. The experimental results described above have validated the dependences of eq 1.13 on R_{series} and C_{sc}. They have shown that τ yields essentially no information on R_{ct}, as is predicted by eq 1.13 using the known constraint that C_{sc}«C_{dl}. The photoelectrochemical stability and ideal electrical nature of n-Si/CH_3OH interfaces, combined with the comparison of Si/liquid contacts to Si/metal contacts, allows us to formulate these conclusions in a robust fashion.

Transient photocurrent measurements are thus basically equivalent to photocapacitance measurements of the semiconductor space charge region, even in the presence of faradaic charge flow across the semiconductor/liquid contact. Prior applications of similar methodology include Si/H_2O based light-addressable potentiostatic sensors[63] and light-impulse-based Mott-Schottky measurements.[64] The presence of the faradaic charge transfer process does not significantly perturb V(t), so the same principles

would be expected to apply to photoelectrochemical cells in the presence of high concentrations of redox species, such as the systems discussed in this work. This conclusion is validated by the experiments and equivalent circuit discussed above.

The arguments used to develop the equivalent circuit of Figure 1.13 also are relevant to transient photovoltage measurements of semiconductor/liquid contacts. Photovoltage transients have been interpreted by some workers to yield information on the charge transfer dynamics of semiconductor/liquid interfaces.[13-15,65] The equivalent circuit of Figure 1.13, however, also can be used to predict the photovoltage transients of such systems. R_M is simply set to 10^6 ohm (which is a typical input impedance for voltage measurements), and again i(t) is calculated. This change in the numerical value of R_M, however, does not affect the validity of the equivalent circuit of Figure 1.13 nor does it affect the validity of eq 1.13 for i(t). Thus, V(t) is not a function of R_{ct} under any common experimental conditions, provided that $C_{sc} \ll C_{dl}$. This situation has been analyzed previously by Feldberg and Gottesfeld,[66] and by Willig,[41] who have pointed out that the initial photovoltage rise across a depleted semiconductor electrode will predominantly reflect the charge separation across C_{sc}. This analysis is entirely consistent with the predictions of the equivalent circuit model and eq 1.13, as described above.

The question then arises as to whether or not a situation can be envisioned for which a faradaic contribution to the decay can be observed. Eq 1.13 predicts that when the time constants for charging and discharging of C_{dl} are comparable, both terms in the expression for i(t) will make significant contributions to the current decay transient. When $C_{sc} \ll C_{dl}$, this condition requires a very large value of R_{series}. Under these conditions, the decays occur on a very long time scale, and the currents become very small and difficult to measure. Furthermore, internal recombination in the semiconductor can become important at large values of R_{series}, because R_{series} generally will become comparable to, or larger than, R_{rec}. Additionally, the range over which R_{ct} and R_{series} can be varied independently

while still having both exponential components contribute significantly to i(t) is extremely small, further confounding attempts to extract interfacial rate information when $C_{sc} \ll C_{dl}$.

In contrast, the restrictions outlined above are significantly relaxed when C_{sc} becomes comparable to C_{dl}. This situation is applicable to typical n-TiO_2/liquid contacts, due to the high dopant concentration produced by most TiO_2 preparations and due to the large dielectric constant of TiO_2.[44] For example, for n-TiO_2 with $N_d=1x10^{20}$ cm^{-3} and a barrier height of 1.0 V, $C_{sc}=11$ $\mu F\text{-}cm^{-2}$,[67] whereas $C_{dl} \approx 20$ $\mu F\text{-}cm^{-2}$. If $R_{series}=10^2$ Ω and $R_{ct}= 10^2$ Ω, the time constant for charging C_{dl} becomes comparable to the time constant for discharging the charge across R_{ct}, and both terms of eq 1.13 may be expected to make a measurable contribution to the observed decay. The biexponential photocurrent transients observed for the n-TiO_2/NaOH(aq) interface are therefore not inconsistent with the equivalent circuit of Figure 1.13 and the analysis in eq 1.13.

Under these conditions, the photocurrent transient decay times are expected to be much longer than those of moderately doped, depleted semiconductor/liquid contacts, and the photocurrent decays would be expected to contain some information regarding the magnitude of the interfacial charge transfer rate constant. Earlier studies observing biexponential decays for the n-TiO_2/NaOH(aq) system interpreted the insensitivity of the time constant for the faster component of the decays to external circuit parameters such as R_L, along with a pronounced isotope effect on this component, as evidence for the sensitivity of this component to interfacial minority carrier charge transfer.[33] It is therefore tempting to associate the faster components observed in this work for TiO_2 in different redox solutions with the charge transfer kinetics for these contacts. However, this assertion is problematic, as the effect of changing the donor cannot be broken down simply into an effect on one decay component or the other. Additionally, the shorter component of the decay was rather insensitive to changes in the redox couple, and showed essentially no isotope effect in the experimental configuration employed. Instead, a complete circuit analysis, generally requiring additional measurements or assumptions, must be used to

extract the desired kinetic information from such experiments. For example, eq 1.13 predicts that when K_0 is of the same order of magnitude as K_1, (i.e. when both terms make measurable contributions to the decay), changing R_L is predicted to change *both* α_0 and α_1 in a systematic fashion. Therefore, the failure to observe any clear dependence on R_L of the time constant for the faster component casts doubt on any attempt to associate these time constants with the faradaic charge transfer kinetics. As some scatter was observed in the data for the faster time constants, one explanation is that the true dependence of these values on R_L was obscured by the larger error associated with measuring the relatively short component of a long biexponential decay. Another possibility, and one that merits consideration given the small range over which the faster time constants varied, is that the biexponential form for these decays is not a result of kinetic contributions, but is instead due to the pronounced frequency dependence of the dielectric constant of reductively doped TiO_2.[68,69] Unfortunately, the form of this frequency dispersion is apparently not known for highly-doped TiO_2 samples, but TiO_2 samples with resistivities of 10^5 Ω-cm have been reported to possess a relatively low dielectric constant at high frequencies, with a rapid increase in ε between 10^4 and 10^5 Hz. Such an effect would lead to a time dependence of the apparent depletion region capacitance in the 1-100 μs time domain, in accord with the form of the n-TiO_2 photocurrent decay data described herein.

In summary, a simple equivalent circuit model for photocurrent transients at depleted semiconductor/liquid contacts has been validated. This model is based on straightforward physical properties of the photoelectrochemical cell, and correctly predicts the behavior of the experimental photocurrent transients under a variety of situations. For moderately doped semiconductors in depletion at liquid contacts, the photocurrent decay dynamics will yield no direct information on the minority carrier charge transfer kinetics. In fact, the presence of a minority carrier acceptor in the solution is not even required for such current to flow, provided that the band edge positions can be stabilized for the duration of the photocurrent decay experiment. For highly doped semiconductors, some

kinetic information is potentially available from photocurrent decay data, but extraction of the interfacial charge transfer resistance from the photocurrent decay data is problematic in most situations. Even when the correct dependence of the biexponential decay on external circuit elements can be validated, uncertainties in various solution and semiconductor parameters make calculation of an accurate value for R_{ct} difficult. Transient photocurrent experiments are therefore best viewed as an alternative to electrical measurements of the differential capacitance of semiconductor/liquid contacts, and yield similar, valuable information concerning the electrostatics of semiconductor/liquid contacts.

VI. REFERENCES

(1) Koval, C.A.; Howard, J.N. *Chem. Rev.* **1992**, *92*, 411.

(2) Finklea, H.O. *Semiconductor Electrodes*, Studies in Physical and Theoretical Chemistry; Elsevier: New York, 1988.

(3) Lewis, N.S. *Annu. Rev. Phys. Chem.* **1991**, *42*, 543.

(4) Kasinski, J.J.; Gomez-Jahn, L.A.; Faran, K.J.; Gracewski, S.M.; Miller, R.J.D. *J. Chem. Phys.* **1989**, *90*, 1253.

(5) Nakabayashi, S.; Komuro, S.; Aoyagi, Y.; Kira, A. *J. Phys. Chem.* **1987**, *91*, 1696.

(6) Min, L.; Miller, R.J.D. *Appl. Phys. Lett.* **1990**, *56*, 524.

(7) Evenor, M.; Gottesfeld, S.; Harzion, Z.; Huppert, D.; Feldberg, S.W. *J. Phys. Chem.* **1984**, *88*, 6213.

(8) Rosenwaks, Y.; Thacker, B.R.; Ahrenkiel, R.K.; Nozik, A.J. *J. Phys. Chem.* **1992**, *96*, 10096.

(9) Krüger, O.; Jung, C. *Ber. Bunsenges. Phys. Chem* **1994**, *98*, 1022.

(10) Kauffman, J.F.; Balko, B.A.; Richmond, G.L. *J. Phys. Chem* **1992**, *96*, 6371.

(11) Forbes, M.D.E.; Lewis, N.S. *J. Am. Chem. Soc.* **1990**, *112*, 3682.

(12) Gmitter, T.J.; Yablonovitch, E.; Heller, A. *J. Electrochem. Soc.* **1988**, *135*, 2391.

(13) Richardson, J.H.; Perone, S.P.; Deutscher, S.B. *J. Phys. Chem.* **1981**, *85*, 341.

(14) Deutscher, S.B.; Richardson, J.H.; Perone, S.P.; Rosenthal, J.; Ziemer, J. *Faraday Discuss. Chem. Soc.* **1980**, *70*, 33.

(15) Kamat, P.V.; Fox, M.A. *J. Phys. Chem.* **1983**, *87*, 59.

(16) Frippiat, A.; Kirsch-De Mesmaeker, A.; Nasielski, J. *J. Electrochem. Soc.* **1983**, *130*, 237.

(17) Frippiat, A.; Kirsch-De Mesmaeker, A. *J. Phys. Chem.* **1985**, *89*, 1285.

(18) Karlsson, K.; Kirsch-De Mesmaeker, A. *J. Phys. Chem.* **1991**, *95*, 10681.

(19) Kawai, T.; Tributsch, H.; Sakata, T. *Chem. Phys. Lett.* **1980**, *69*, 336.

(20) Wilson, R.H.; Sakata, T.; Kawai, T.; Hashimoto, K. *J. Electrochem. Soc.* **1985**, *132*, 1082.

(21) Jaegermann, W.; Sakata, T.; Janata, E.; Tributsch, H. *J. Electroanal. Chem.* **1985**, *189*, 65.

(22) Sakata, T.; Janata, E.; Jaegermann, W.; Tributsch, H. *J. Electrochem. Soc.* **1986**, *133*, 339.

(23) Jaegermann, W. *J. Phys. Chem.* **1984**, *88*, 5309.

(24) Cook, R.L.; Dempsey, P.F.; Sammels, A.F. *J. Electrochem. Soc.* **1986**, *133*, 1821.

(25) Cook, R.L.; Dempsey, P.F.; Sammels, A.F. *J. Electrochem. Soc.* **1986**, *133*, 2287.

(26) Cook, R.L.; MacDuff, R.C.; Sammels, A.F. *J. Electrochem. Soc.* **1989**, *136*, 1468.

(27) Bitterling, K.; Willig, F. *J. Electroanal. Chem.* **1986**, *204*, 211.

(28) Bitterling, K.; Willig, F.; Decker, F. *J. Electroanal. Chem.* **1987**, *228*, 29.

(29) Harzion, Z.; Croitoru, N.; Gottesfeld, S. *J. Electrochem. Soc.* **1981**, *128*, 551.

(30) Harzion, Z.; Huppert, D.; Gottesfeld, S.; Croituru, N. *J. Electroanal. Chem.* **1983**, *150*, 571.

(31) Prybla, S.; Struve, W.S.; Parkinson, B.A. *J. Electrochem. Soc.* **1984**, *131*, 1587.

(32) Hartig, K.J.; Grabner, G.; Getoff, N.; Popkirov, G.; Kanev, S. *Ber. Bunsenges. Phys. Chem.* **1985**, *89*, 831.

(33) Norton, A.P.; Bernasek, S.L.; Bocarsly, A.B. *J. Phys. Chem.* **1988**, *92*, 6009.

(34) Ramsden, J.J.; Tóth-Boconádi, R. *J. Chem. Soc. Faraday Trans.* **1990**, *86*, 1527.

(35) Bard, A.J.; Faulkner, L.R. *Electrochemical Methods: Fundamentals and Applications*; John Wiley & Sons: New York, 1980.

(36) Barker, G.C.; Gardner, A.W.; Bottura, G. *J. Electroanal. Chem.* **1973**, *45*, 21.

(37) Richardson, J.H.; George, S.M.; Harrar, J.E.; Perone, S.P. *J. Phys. Chem.* **1978**, *82*, 1818.

(38) Richardson, J.H.; Deutscher, S.B.; Maddux, A.S.; Harrar, J.E.; Johnson, D.C.; Schmelzinger, W.L.; Perone, S.P. *J. Electroanal. Chem.* **1980**, *109*, 95.

(39) Barker, G.C.; McKeown, D.; Williams, M.J.; Bottura, G.; Concialini, V. *Faraday Discuss. Chem. Soc.* **1973**, *56*, 41.

(40) Peter, L.M. *Chem. Rev.* **1990**, *90*, 753.

(41) Willig, F. *Ber. Bunsenges. Phys. Chem.* **1988**, *92*, 1312.

(42) Willig, F.; Bitterling, K.; Charlé, K.-P.; Decker, F. *Ber. Bunsenges. Phys. Chem.* **1984**, *88*, 374.

(43) Gottesfeld, S. *Ber. Bunsenges. Phys. Chem.* **1987**, *91*, 362.

(44) Finklea, H.O. In *Semiconductor Electrodes*; Finklea, H.O. Ed.; Studies in Physical and Theoretical Chemistry; Elsevier: New York, 1988 ; Vol. 55; p 43.

(45) It should be noted that the reported time-resolved conductivity experiments are fundamentally different from the current transients being analyzed in this work. The earlier study was performed under conditions where the overall rate of charge transfer is dictated by the slower of the individual electron and hole rates (see Section 3.II), whereas it is the accessibility of only the minority carrier rate that is relevant to the present discussion.

(46) Pierret, R.F. *Semiconductor Fundamentals*, 2nd ed., Modular Series on Solid State Devices; Pierret, R.F., Neudeck, G.W. Eds.; Addison-Wesley: Reading, MA, 1988; Vol. I.

(47) Neudeck, G.W. *The PN Junction Diode*, 2nd ed., Modular Series on Solid State Devices; Neudeck, G.W., Pierret, R.F. Eds.; Addison-Wesley: Reading, MA, 1989; Vol. II.

(48) Lewis, N.S.; Rosenbluth, M. In *Photocatalysis: Fundamentals and Applications*; Serpone, N., Pelizzetti, E. Eds.; John Wiley & Sons: New York, 1989; p 45.

(49) Sze, S.M. *The Physics of Semiconductor Devices*, 2nd ed.; John Wiley and Sons: New York, 1981.

(50) Thurber, W.R.; Mattis, R.L.; Liu, Y.M.; Filliben, J.J. *J. Electrochem. Soc.* **1980**, *127*, 1807.

(51) Grant, F.A. *Rev. Mod. Phys.* **1959**, *31*, 646.

(52) Breckenridge, R.G.; Hosler, W.R. *Phys. Rev.* **1953**, *91*, 793.

(53) Gronet, C.M.; Lewis, N.S.; Cogan, G.; Gibbons, J. *Proc. Natl. Acad. Sci., USA* **1983**, *80*, 1152.

(54) Tufts, B.J.; Kumar, A.; Bansal, A.; Lewis, N.S. *J. Phys. Chem.* **1992**, *96*, 4581.

(55) Briggs, G.W.D.; Jones, E.; Wynne-Jones, W.F.K. *Trans. Faraday Soc.* **1955**, *51*, 1433.

(56) Lewis, N.S. *J. Electrochem. Soc.* **1984**, *131*, 2496.

(57) Rosenbluth, M.L.; Lewis, N.S. *J. Am. Chem. Soc.* **1986**, *108*, 4689.

(58) Rosenbluth, M.L.; Lieber, C.M.; Lewis, N.S. *Appl. Phys. Lett.* **1984**, *45*, 423.

(59) Note, however, that this method cannot be used to obtain an accurate quantitative evaluation of the barrier height for the n-Si/liquid contacts, because a relatively small error in C_{meas} produces a rather large uncertainty in the calculated value of the junction barrier height.

(60) This is a reasonable approximation for strongly reverse biased semiconductors possessing inert surfaces, but would not be appropriate when a large density of surface states are present. This inadequacy is illustrated by earlier observations of inferior surface preparations producing complicated photocurrent transients (ref. 20,29,31).

(61) Blackwell, W.A. *Introductory Network Theory*; PWS Engineering: Boston, 1985.

(62) In practice, it would be difficult to observe the reverse current under these conditions but it has been seen at low blocking bias when C_{sc} is larger and R_{rec} is expected to be smaller (ref. 20).

(63) Hafeman, D.G.; Parce, J.W.; McConnell, H.M. *Science* **1988**, *240*, 1182.

(64) Kamieniecki, E. *J. Appl. Phys.* **1983**, *54*, 6481.

(65) Perone, S.P.; Richardson, J.H.; Deutscher, S.B.; Rosenthal, J.; Ziemer, J.N. *J. Electrochem. Soc.* **1980**, *127*, 2580.

(66) Gottesfeld, S.; Feldberg, S.W. *J. Electroanal. Chem.* **1983**, *146*, 47.

(67) This capacitance was calculated using ε_s=173, but this value was obtained from literature measurements on stoichiometric rutile TiO_2. The dielectric constant of reduced rutile crystals can be much higher, making the calculated number a lower limit on C_{sc}.

(68) Lal, H.B.; Srivastava, K.G. *Can. J. Phys.* **1969**, *47*, 3.

(69) Hollander, L.E.; Castro, P.L. *J. Appl. Phys.* **1962**, *33*, 3421.

VII. APPENDIX

In this appendix, a derivation of eq 1.13 is presented following that outlined by Prof. H. Martel of Caltech. The equivalent circuit shown if Figure 1.13b is an impedive current divider and its impulse response can be conveniently solved using Laplace transforms. The ratio of the current in the external circuit, I_2, to the current, I, is given by the ratio of the impedance, Z_1, to the total impedance of the circuit.

$$H = \frac{I_2}{I} = \frac{Z_1}{Z_1 + Z_2}$$

Z_1 and Z_2, are the s-domain impedances defined by:

$$Z_1 = \frac{R_{rec}}{1 + \tau_1 s} \qquad Z_2 = R_{series} + \frac{R_{rec}}{1 + \tau_2 s}$$

$$\tau_1 = R_{rec} C_{sc} \qquad \tau_1 = R_{rec} C_{sc}$$

Insertion of these values into the expression for H gives the following relationships.

$$H = \frac{R_{rec}(1 + \tau_2 s)}{R_{rec}(1 + \tau_2 s) + R_{series}(1 + \tau_1 s)(1 + \tau_2 s) + R_{ct}(1 + \tau_1 s)}$$

$$H = \frac{R_{rec}(1 + \tau_2 s)}{(R_{rec} + R_{ct} + R_{series}) + \left[R_{rec} R_{ct}(C_{sc} + C_{dl}) + R_{series}(\tau_1 + \tau_2)\right] s + R_{series} \tau_1 \tau_2 s^2}$$

The denominator is quadratic in s, and can be rearranged into the following more convenient form.

$$H = \frac{1}{R_{series} C_{sc}} \left[\frac{s + \alpha_2}{s^2 + As + B} \right]$$

$$\alpha_2 = \frac{1}{\tau_2} \qquad A = \frac{R_{rec} R_{ct}(C_{sc} + C_{dl}) + R_{series}(\tau_1 + \tau_2)}{R_{series} \tau_1 \tau_2} \qquad B = \frac{R_{rec} + R_{ct} + R_{series}}{R_{series} \tau_1 \tau_2}$$

The roots of the denominator quadratic, $\alpha_{0,1}$, can be obtained from the quadratic equation .

$$H = \frac{1}{R_{series} C_{sc}} \left[\frac{s + \alpha_2}{(s + \alpha_0)(s + \alpha_1)} \right]$$

$$-\alpha_{0,1} = -\frac{A}{2} \pm \sqrt{\frac{A}{4} - B}$$

Partial fraction expansion of H yields the following form:

$$H = \frac{1}{R_{series}C_{sc}}\left[\frac{K_0}{(s+\alpha_0)} + \frac{K_1}{(s+\alpha_1)}\right]$$

where

$$K_0 = \frac{\alpha_2 - \alpha_0}{\alpha_1 - \alpha_0} \qquad K_1 = \frac{\alpha_1 - \alpha_2}{\alpha_1 - \alpha_0}$$

The impulse response of the circuit is the inverse Laplace transform of H. The inverse of $1/(s+\alpha)$ is $\exp(-\alpha t)$ so $L^{-1}\{H\}$ is readily obtained.

$$h(t) = \frac{1}{R_{series}C_{sc}}\left[K_0 e^{-\alpha_0 t} + K_1 e^{-\alpha_1 t}\right]$$

h(t) can be converted to eq 1.13 by multiplying by the charge contained in the impulse.

Chapter 2

Studies of Si Photoelectrodes in High-Level Injection: Quasi-Fermi Level Behavior Under Illumination and Applied Bias

I. INTRODUCTION

Recently, a novel type of semiconductor/liquid solar cell has been reported that is based on thin, high-purity Si photoelectrodes operated under high-level injection conditions.[1,2] These samples are capable of efficient charge separation and collection under conditions where minimal electric fields exist at the solid/liquid contact. In contrast, essentially all other efficient semiconductor/liquid energy conversion schemes reported to date rely critically on the presence of a strong field at the interface to effect charge separation. Another remarkable feature of these Si photoelectrodes is they permit the individual and simultaneous measurement of the electrochemical potentials of electrons and holes in the semiconductor.[3] Such information is of fundamental interest to theories of photoelectrochemistry, and is unavailable from conventional semiconductor electrodes. This chapter describes further studies of these unique Si samples.

The absence of a strong interfacial electric field at the Si/liquid contacts examined in this work is a result of the high-level injection conditions under which they are operated. In high-level injection, the number of photogenerated charge carriers exceeds the number of carriers present at equilibrium. Because these samples are nearly intrinsic (very lightly doped; $N_d = 3x10^{13}$ cm^{-3}), high-level injection conditions are attained even at moderate illumination intensities. Since a photon creates both an electron and a hole, and because the number of photogenerated carriers is large relative to the carrier concentrations at equilibrium , excess charge density in the solid is effectively screened. Poisson's equation dictates that this will minimize any electric fields existing in the solid including those at the solid/liquid contact. Consequently, charge separation in these samples cannot rely exclusively on the presence of a strong electric field at the interface. Carrier motion is driven primarily by diffusion as opposed to drift, and requires establishing and sustaining controlled gradients in the carrier concentrations across the sample. Charge separation is effected at the back of the sample through a lithographically-patterned array of degenerately n-type doped (n^+) and degenerately p-type doped (p^+) regions (Figure 2.1a). The potential

gradients existing at the interface between the nearly intrinsic bulk of the photoelectrode and the heavily doped regions result in efficient collection of electrons and rejection of holes, at the n^+ point contacts and the reverse behavior at the p^+ point contacts. It has been shown through studies of quantum yield as a function of wavelength that carriers are collected efficiently regardless of whether they are created nearly uniformly throughout the sample, or within 1μm of the solid/liquid interface, more than 100 μm away from the primary site of charge separation.[2,4]

Data has been collected for these samples in contact with four redox couples having formal potentials spanning a range greater than 1 V. These studies revealed a number of interesting and unique features of these samples that are attributable to various combinations of the thin, high-purity nature of the electrodes, the high-level illumination conditions and the array of point contacts. The most dramatic findings include: i) open circuit voltages have been obtained which are greater than the theoretical upper limit for conventional photoelectrochemical cells; ii) efficient anodic and cathodic current flow has been accomplished using a single photoelectrode/electrolyte combination by simply reversing the contact configuration; iii) it is possible to individually observe or control the electrochemical potential of one carrier type while simultaneously monitoring the electrochemical potential of the other carrier.

The free energy available from a photoelectrochemical cell is determined by the voltage measured at open circuit, V_{oc}. For a conventional semiconductor/liquid junctions operated under low-level injection conditions, the upper limit on V_{oc} is set by the Shockley diode equation:[5]

$$V_{oc} = \frac{kT}{q} \ln\left(\frac{J_{ph} L_p N_d}{q D_p n_i^2}\right) \tag{2.1}$$

where J_{ph} is the light-limited photocurrent density, L_p is the diffusion length, D_p is the diffusion coefficient of minority carriers (holes for n-type material), n_i is the intrinsic carrier concentration of the semiconductor, and all other terms have the same meaning as in

the previous chapter. The origin of the limit given by eq 2.1 is a diffusion current, induced by recombination of carriers within the semiconductor bulk, that opposes the desired photocurrent. As stated above eq 2.1 represents a theoretical maximum and most photoelectrochemical cells display photovoltages significantly lower than this limit. However, photovoltages in accord with those predicted by eq 2.1 have been obtained using n-Si electrodes in contact with CH_3OH-$Me_2Fc^{+/0}$. These previous results indicate that this semiconductor/liquid interface has such excellent electrical properties that it does not limit the photovoltage in this system. Instead, deleterious recombination processes occurring in the bulk of the semiconductor control V_{oc}. Consequently, the only way to increase V_{oc} in this system is by altering the semiconductor properties through variations in N_d and L_p.[6] While it is difficult to produce controlled variations in L_p, it is possible to vary N_d over several orders of magnitude, and, indeed, the shift in V_{oc} with changes in N_d has been studied in detail for the n-Si/$CH_3$0H-$Me_2Fc^{+/0}$ system.[7] However, there are limits to how far this approach can be pursued as other recombination mechanisms (Auger, tunneling through space charge barrier) can become significant at high dopant densities and these will inevitably lead to V_{oc} values below those given by eq 2.1.[8]

In order to circumvent the limit imposed by eq 2.1, an alternative approach is required. The use of thin, nearly intrinsic Si samples operated under high-level illumination represents such an alternative approach, and it has been successful in producing photovoltages substantially in excess of those given by the Shockley diode equation.[2,9] Section IV.2 of this chapter presents a simple and cohesive model to explain the magnitude of the photovoltages observed for these samples as a function of the energetics of the redox couple. The model is based upon fundamental carrier statistics and discussed in terms of the separation of the electron and hole quasi-Fermi levels, $E_{F,n}$ and $E_{F,p}$, respectively.

Another remarkable facet of these Si photoelectrodes is their demonstrated ability to reverse the sign of the photocurrent in response to a change in the back contact

configuration.[2] For redox couples having electrochemical potentials in the middle of the Si band gap, anodic photocurrents were observed when the n^+ point contacts were connected and the p^+ points left at open circuit, while cathodic currents were observed when the p^+ points were contacted and the n^+ point contacts were at open circuit. This is markedly different behavior that what is observed in conventional photoelectrochemical cells in which the sign of the electric field at the interface uniquely determines the sign of the photocurrent. The origin of the photocurrent directionality is also examined in this chapter and it is proposed that the results are likely applicable to other photoelectrochemical cells based on intrinsic semiconductors.

The electrical junction configuration fabricated into these samples also offers the possibility of controlling electrically the potential at, and measuring the charge carrier flux through, one collection of contacts while monitoring the electrochemical potential (at open circuit) produced at the other set of contacts. Such measurements, described in Section IV.2, have made it possible to investigate the position of the quasi-Fermi level for a given carrier type in the presence of band gap excitation of the semiconductor, under a variety of bias conditions and for a variety of redox couples in the liquid phase. These results are relevant to the controversy regarding the thermodynamic interpretation of the quasi-Fermi levels in an operating, illuminated photoelectrochemical cell and are of fundamental interest with respect to the behavior of the quasi-Fermi levels under an applied bias.[10-17] In addition to such experimental data, digital simulations of the carrier generation, transport, and recombination processes in these systems are presented. The simulations have been performed to confirm quantitatively some of the approximations advanced in this and other work,[2-4,9] and to provide insight into some unexpected aspects of the behavior of quasi-Fermi levels observed during the course of this study.

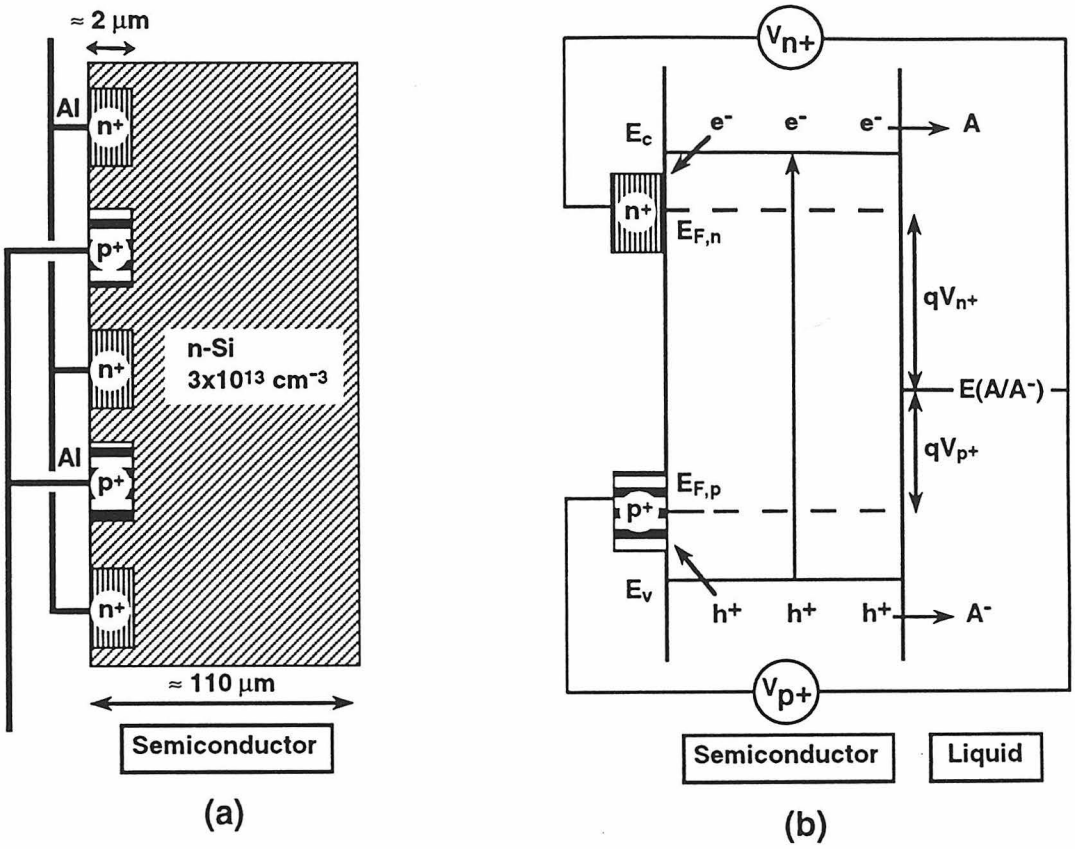

Figure 2.1: (a) Illustration of the high-purity (100-400 Ω-cm; background donor density $3x10^{13}$ cm^{-3}) lithographically-patterned Si samples employed in this work showing the n^+ and p^+ point contact array. (b) Schematic representation of the band diagram of the high-purity Si/liquid junction under high-level injection conditions. $\mathbf{E}_C$ and $\mathbf{E}_V$ represent the energies of the conduction band edge and valence band edge of the semiconductor, respectively. qV_{n+} is the energy difference measured between the n^+ point contacts and the solution electrochemical potential, $\mathbf{E}(A/A^-)$, while qV_{p+} is the energy difference measured between the p^+ point contacts and $\mathbf{E}(A/A^-)$. The voltages at the n^+ and p^+ contact points directly reflect the quasi-Fermi level positions of electrons and holes at the back of the sample, $\mathbf{E}_{F,n}(d)=qV_{n+}$ and $\mathbf{E}_{F,p}(d)=qV_{p+}$.

II. BACKGROUND

The work in this chapter is centered on the behaviors of quasi-Fermi levels at an illuminated semiconductor/liquid contact. Quasi-Fermi levels are a powerful formalism and are widely employed in semiconductor device physics to describe electron and hole motion under non-equilibrium conditions. One illustration of their utility is that knowledge of quasi-Fermi levels as a function of distance permits all carrier transport to be described by a single expression.[18]

Quasi-Fermi levels are also a fundamental concept in semiconductor photoelectrochemistry.[19] They were first used to describe charge transfer reactions at semiconductor/liquid interfaces a number of years ago, but only recently have they been investigated more quantitatively and their direct measurement reported.[3,13-15] The term "quasi-Fermi level" has a historical origin and will be used herein,[20] but is perhaps less informative than the alternative description of $\mathbf{E}_{F,n}$ and $\mathbf{E}_{F,p}$ as electrochemical potentials.[21] This description identifies the thermodynamic nature of $\mathbf{E}_{F,n}$ and $\mathbf{E}_{F,p}$ and indicates they are the sum of a term related to the concentration of the charge carrier (the chemical potential) and a contribution due to the electrical environment in which the carriers reside.[22] An additional benefit of using this terminology for $\mathbf{E}_{F,n}$ and $\mathbf{E}_{F,p}$ is the parallels it draws with the electrochemical potential $\mathbf{E}(A/A^-)$, used to describe the solution phase of a semiconductor/liquid junction.

To understand the meaning of quasi-Fermi levels, it is necessary to examine the related Fermi level concept in more detail. In Section 1.II, the Fermi level was introduced and described as the electrochemical potential of electrons in the solid. The Fermi level is an equilibrium construct and is incorporated into eq 1.3 which describes the equilibrium carrier occupancy of a non-degenerate sample. While this expression for carrier density (electrons in the conduction band) is appropriate under most equilibrium conditions, it is actually a simplification of the general relation given below,

$$n_o = \int_{E_c}^{-\infty} F(\mathbf{E}) g_c(E) d\mathbf{E} \tag{2.2}$$

where n_o is the equilibrium carrier density, $g_c(\mathbf{E})$ is the density of states per unit energy in the conduction band and $F(\mathbf{E})$ is the Fermi function which describes the occupancy of these states.[23] The integral should strictly be performed from the lower edge of the conduction band, $\mathbf{E_c}$, to the top of the band, but as $F(\mathbf{E})$ decreases quickly with increasing energy, it is acceptable to set the upper limit to the more convenient value of infinity.[18]

Near $\mathbf{E_c}$, the density of states at energy in the conduction band $\mathbf{E}$ can be approximated by eq 2.3, where $\hbar$ is Planck's constant divided by 2π.[24]

$$g_c(\mathbf{E}) = \frac{\sqrt{2(\mathbf{E} - \mathbf{E_c})}}{\pi^2 \hbar^3} (m_n^*)^{3/2} \tag{2.3}$$

The preceding equation is derived by the application of quantum principles to free-electron theory,[25] and the use of a density of states effective mass, m_n^*, to account for the interaction of electrons with the periodic potential of the lattice.[21,23]

The Fermi function is given by eq 2.4. For a collection of indistinguishable particles obeying the Pauli exclusion principle, it yields the probability that a state at energy $\mathbf{E}$ is occupied.[21]

$$F(\mathbf{E}) = \frac{1}{1 + \exp \frac{(\mathbf{E} - \mathbf{E_F})}{kT}} \tag{2.4}$$

An expression analogous to eq 2.2 can be written for the concentration of holes

$$p_o = \int_{\infty}^{E_v} (1 - F(\mathbf{E})) g_v(\mathbf{E}) d\mathbf{E} \tag{2.5}$$

where $g_v(\mathbf{E})$ is the density of states in the valence band given by an equation identical to 2.3 except that the energies are referenced to the top of the valence band and the density of states effective mass of holes, m_h^*, is employed. The function (1-$F(\mathbf{E})$) is used as the occupancy factor since a hole represents a vacant state.

The integrals shown in eqs 2.2 and 2.5 can be evaluated to yield the following:

$$n_o = N_c \frac{2}{\sqrt{\pi}} F_{1/2}\left(\frac{\mathbf{E}_c - \mathbf{E}_F}{kT}\right) \tag{2.6}$$

$$p_o = N_v \frac{2}{\sqrt{\pi}} F_{1/2}\left(\frac{\mathbf{E}_F - \mathbf{E}_v}{kT}\right) \tag{2.7}$$

where N_c and N_v are the effective density of states in the conduction and valence band, respectively, and $F_{1/2}(\eta)$ is the Fermi-Dirac integral of order 1/2.

$$N_c = 2\left(\frac{2\pi m_n^* kT}{h^2}\right)^{3/2} \tag{2.8}$$

$$N_v = 2\left(\frac{2\pi m_p^* kT}{h^2}\right)^{3/2} \tag{2.9}$$

Eqs 2.6 and 2.7 can successfully describe the carrier density for essentially any positioning of $\mathbf{E}_F$, and the Fermi-Dirac statistics underpinning them are incorporated into the semiconductor simulation package utilized in the present work. However, simplified forms can be obtained when the Fermi level is more than a few kT away from a band edge. When $\mathbf{E}_v$-3kT $\geq \mathbf{E}_F \geq \mathbf{E}_c$+3kT (argument to the Fermi function $\leq$-3), $F_{1/2}(\eta)$ can be approximated by $\sqrt{\pi}\ \exp(\eta)/2$.[24] After substitution of this approximation into eqs 2.6 and 2.7, it is seen that the electron and hole occupancies are now described by Maxwell-Boltzmann statistics.[21]

$$n_o = N_c \exp\left(-\frac{\mathbf{E}_F - \mathbf{E}_c}{kT}\right) \tag{2.10}$$

$$p_o = N_v \exp\left(-\frac{\mathbf{E}_v - \mathbf{E}_F}{kT}\right) \tag{2.11}$$

Some physical insight into this result can be obtained by considering the implications of having $\mathbf{E}_v$-3kT $\geq \mathbf{E}_F \geq \mathbf{E}_c$+3kT . Since the Fermi level is located in the band gap, the density of states at $\mathbf{E}_F$ is zero. Blakemore points out that, "Only within a few kT of $\mathbf{E}_F$ is the probability of occupancy appreciably different from zero or unity."[21] This implies that only the low probability tail of the Fermi function extends beyond $\mathbf{E}_c$; thus, only a small fraction of the available states is occupied. Therefore, the restriction imposed by the Pauli exclusion principle, that only one electron may occupy a given state, is not an important

consideration, and carrier occupancy can be described by the classical distributions of eqs 2.10 and 2.11.

Alternative expressions for eqs 2.10 and 2.11 can be obtained by considering the ideal case of an intrinsic semiconductor, a material containing essentially no impurity atoms.[24] In this type of sample, the density of holes and electrons are mutually equal to the intrinsic carrier concentration, n_i, and the position adopted by the Fermi level is referred to as the intrinsic level, $\mathbf{E}_i$. After substitution into eqs 2.10 and 2.11 of $\mathbf{E}_i$ for $\mathbf{E}_F$, and n_i for the carrier concentrations, n_o, p_o, it is possible to eliminate N_c and N_v and obtain the following relationships.[23]

$$n_o(x) = n_i \exp\left(\frac{\mathbf{E}_i - \mathbf{E}_F}{kT}\right) \tag{2.12}$$

$$p_o(x) = n_i \exp\left(\frac{\mathbf{E}_F - \mathbf{E}_i}{kT}\right) \tag{2.13}$$

In these equations, the dependence on position of the equilibrium carrier concentrations is made explicit. It arises from the spatial variation of $\mathbf{E}_i$ which, unlike the Fermi level, is not necessarily constant across a sample at equilibrium.[23] It can seen from eqs 2.12 and 2.13 that, at thermal equilibrium, the product of the electron and hole concentrations is equal to n_i^2.

While eqs 2.10-2.13 are appropriate under most equilibrium conditions, they cannot be used to describe the situation when excess carriers are generated in the sample by light or bias. The is because it is no longer possible to describe the occupancy of electrons and holes with the single electrochemical potential, $\mathbf{E}_F$. However, if the carriers within a particular band are treated as being in a state of "quasi-equilibrium" with one another, it is possible to describe their density using an individual electrochemical potential (i.e. quasi-Fermi level) for each carrier type.[21]

$$n(x) = n_i \exp\left(\frac{\mathbf{E}_i - \mathbf{E}_{F,n}}{kT}\right) \tag{2.14}$$

$$p(x) = n_i \exp\left(\frac{\mathbf{E}_{F,p} - \mathbf{E}_i}{kT}\right) \tag{2.15}$$

In the preceding equations, $\mathbf{E}_{F,n}$ and $\mathbf{E}_{F,p}$, are the quasi-Fermi level of electrons and holes, respectively, and the subscript has been dropped from the carrier concentrations to indicate the existence of non-equilibrium conditions.

III. METHODS AND PROCEDURES

All samples, experimental methods, and measurement protocols have been described in previous publications.[2,9] Numerical device simulations were performed using the Two-dimensional SemiConductor Analysis (ToSCA) software package. ToSCA was developed by Gajewski and coworkers for numerical simulation of carrier transport in semiconductors.[26] The code is based upon van Roosbroeck's drift-diffusion model,[27] which consists of a differential equation system that includes Poisson's equation and the continuity equations for electrons and holes. ToSCA solves this system of equations numerically, and self-consistently calculates the potential distribution in the solid and the concentration profiles of charge carriers in accord with Fermi-Dirac statistics. Optical generation of carriers, as well as bulk and surface recombination, are incorporated explicitly into the ToSCA package. The simulation of specific electrical contacts (e.g., gate or ohmic) is accomplished by the imposition of suitable boundary conditions. A more detailed description of the mathematical and physical models used in ToSCA can be found in a previous publication and references therein.[28]

The interface between the semiconductor and the electrolyte was modeled by modifying the boundary conditions initially incorporated into the ToSCA package. The ToSCA boundary conditions representing a solid-state gate oxide contact were changed to reflect the physical properties of the Helmholtz double layer. Specifically, the gate was specified to be a leaky dielectric having a thickness of 0.3 nm and a dielectric constant of $6\varepsilon_0$ (as expected for directed water dipoles[29]) where ε_0 is the permittivity of free space. Charge transfer across this gate oxide represented the Faradaic current flow due to oxidation or reduction of the redox species in the electrolyte. Band edge shifts were computed self-consistently as a result of any change in surface charge produced across this dielectric layer.

Marcus-Gerischer theory, as specified by eqs 2.16a and 2.16b,[30-33] was used to calculate the interfacial charge transfer current densities across the modified gate gcontact.[34]

$$j_c = -qk_c^{max}N_c c_{red}\exp\left[-\frac{(\mathbf{E}_c - \mathbf{E}^{o'}_{redox} + \lambda)^2}{4kT\lambda}\right]\left(\frac{n_s}{n_{so}} - 1\right) \quad (2.16a)$$

$$j_v = qk_v^{max}N_v c_{ox}\exp\left[-\frac{(\mathbf{E}_v - \mathbf{E}^{o'}_{redox} - \lambda)^2}{4kT\lambda}\right]\left(\frac{p_s}{p_{so}} - 1\right) \quad (2.16b)$$

In these expressions, q denotes the elementary charge, k denotes the Boltzmann constant, T denotes the temperature, $\mathbf{E}_c$ and $\mathbf{E}_v$ denote the energies of the conduction band and valence band of the semiconductor, respectively, N_c and N_v are the effective densities of states in the conduction and valence band, respectively, n_s is the surface electron concentration (having an equilibrium value n_{so}), p_s is the surface hole concentration (having a value at equilibrium of p_{so}), and k_c^{max} and k_v^{max} (having units of $cm^4\ s^{-1}$)[35-37] are the charge transfer rate constants at optimal exoergicity for the conduction band and valence band processes, respectively. In these rate constant expressions, the concentrations of the redox species (c_{red}, c_{ox}) are multiplied by an exponential term, the so-called nuclear (or Franck-Condon) factor, that accounts for the fluctuation of the solvation shell around a redox species having a formal electrochemical potential $\mathbf{E}^{o'}_{redox}$ and a reorganization energy λ. Within the Gerischer formalism of semiconductor electrochemistry, this Franck-Condon term yields a measure of the overlap of occupied/empty states of the redox system with the states of the valence/conduction band of the solid.[38-41] The contribution of the semiconductor to the overall rate of charge transfer is determined by the effective density of states in the energy bands (N_C, N_V), and by the ratios of the carrier concentrations at the surface (n_s, p_s) to the interfacial carrier concentrations present under equilibrium conditions (n_{so}, p_{so}). The equilibrium carrier concentrations are determined by the barrier height of the semiconductor/liquid contact, which was known experimentally for the systems under study.[37,42-48] Thus, two parameters, k_{ct}^{max} ($k_c^{max} = k_v^{max}$ was always used in the simulations) and λ, were used to describe the exchange current densities resulting from charge transfer from the conduction and valence bands. While it is possible to infer the homogeneous reorganization free energy of these ions from NMR measurements of self-

exchange rate constants,[49] no experimental data for the reorganization energy of ions at the semiconductor/electrolyte interface appear to have been published.[48,50,51] Theoretical studies have suggested that λ for the oxidation/reduction of an outer sphere redox species at a metal electrode is approximately one-half that for the same ion in a homogeneous self-exchange process.[52,53] However, the reorganization energy for a semiconductor/liquid system is predicted to be approximately twice that of the corresponding value at a metal/liquid interface, when only static dielectric contributions to the reorganization energy are included.[53,54] Due to these uncertainties, the reorganization energy for all of the redox couples used in this study was approximated as 0.5 eV.[47,48,55-60] A drawback to the ToSCA code as presently formulated is the inability to account for concentration polarization and series resistance losses in the electrolyte; thus, the specified interfacial charge transfer rates were independent of time for given carrier concentrations in the solid, when in actuality the interfacial charge transfer rates change with stirring rate, time, etc. to reflect the changes during current flow in the steady-state concentration of donor and acceptor species in the region of the electrolyte adjacent to the electrode surface.

The simulated electrode had x-y-z dimensions of 120 μm x 60 μm x10 μm (with the 120 μm dimension corresponding to the sample thickness and the 60 μm dimension corresponding to the width of the exposed electrode). Simulations were performed for the x and y directions, and the carrier concentrations were assumed to be uniform in the other dimension (z), which was parallel to the electrode surface.

Two dimensional simulations were carried out in which the back had both n^+ and p^+ contacts, as in the actual sample (Figure 2.1a). The two degenerately doped regions were specified in the simulation to be separated by 20 μm and to have individual dimensions of 10 μm in the y direction. The dopant profiles for these ohmic-selective contacts were generated by specifying the presence of high dopant concentrations at the back contact. The highly-doped regions were specified to have dopant concentrations of 10^{18} cm^{-3} that were uniform over an x-range of 1 μm (from the back of the sample) and

then were allowed to decay into the bulk with a Gaussian distribution that reached 1/e of its maximum value in 8 μm. The background donor density was fixed at the experimentally measured value of $3x10^{13}$ cm^{-3} throughout the bulk of the sample. Figure 2.2a-c shows the potential distribution, as well as the carrier concentration profiles at equilibrium (in the dark), that result from these doping profiles for a Si/CH_3OH contact, which has a barrier height of 0.6 V.

For comparison to experimental data, a series of simulations was performed using this two-dimensional back contact geometry in which the electron quasi-Fermi level was controlled through the n^+ ohmic contact and the hole quasi-Fermi level ($qV_{p+,oc}$) was calculated at the edge of the p^+ ohmic contact. For numerical reasons ToSCA requires the current density through the p^+ contacts, J_{p+}, to be non-zero, so the open circuit condition at the p^+ contacts under such conditions was modeled by specifying that $|J_{p+}| \leq 10$ nA cm^{-2}. In another series of simulations, the hole quasi-Fermi level was controlled through the p^+ ohmic contact and the electron quasi-Fermi level was calculated at the edge of the n^+ ohmic contact. Under these conditions the simulation was constrained so that $|J_{n+}| \leq 10$ nA cm^{-2}, where J_{n+} is the current density through the n^+ points.

Some aspects of the experimentally observed behaviors were modeled by simulations in which the back contact geometry was simplified to be uniformly degenerately doped with either electrons or holes. In these simulations, an n^+ region (of donor density, N_d, equal to 10^{18} cm^{-3}) was created at the back surface of the electrode for simulation of experiments in which the electron quasi-Fermi level was being controlled potentiostatically, while a p^+ region (of acceptor density, N_a, equal to 10^{18} cm^{-3}) was generated to simulate experiments in which the hole quasi-Fermi level was maintained under potentiostatic control. When this procedure was used, the experimentally measured quasi-Fermi level value for the carrier being monitored at open-circuit was estimated as the simulated quasi-Fermi level value at the edge of the diffused back contacts ($x \approx 80$-100 μm from the solid/liquid contact). In other words, when the potential was being controlled at

the n^+ points, the hole quasi-Fermi level that would be measured at the p^+ points was taken to be the value of the hole quasi-Fermi level computed at the edge of a spatially uniform, diffused n^+ back contact region. The simplified and full two-dimensional simulations were compared in several representative cases, and, in each instance, the quasi-Fermi level positions calculated from the simplified sample were found to be virtually identical to those obtained from the simulations that contained the actual spatial distribution of the back point contacts.

Except for the charge transfer rate constants, essentially all of the input parameters (Table 2.1) used in the digital simulation program were determined experimentally or were known from the literature. The bulk low-level minority carrier lifetime of these Si samples was 1 ms, and this was represented in the simulation by setting the nonradiative (Shockley-Read-Hall) bulk lifetime $\tau_n = \tau_p = 1$ ms.[61] The front surface recombination velocity, describing recombination mediated by surface states, was chosen to be 100 cm s^{-1}, which corresponds to the experimentally measured value for these Si/CH_3OH contacts.[3,4,62,63] Other specific input parameters for the simulations of this work are provided in the appropriate sections of the chapter.

physical parameter	value	reference
intrinsic carrier concentration	$n_i = 1.45 \times 10^{10}$ cm^{-3}	24
dielectric constant	$\varepsilon/\varepsilon_o = 11.9$	24
energy gap	$E_g = 1.12$ eV	24
effective density of states in conduction band	$N_c = 2.8 \times 10^{19}$ cm^{-3}	24
effective density of states in valence band	$N_v = 1.04 \times 10^{19}$ cm^{-3}	24
electron mobility	$\mu_n = 1500$ cm^2 V^{-1} s^{-1}	24
hole mobility	$\mu_p = 450$ cm^2 V^{-1} s^{-1}	24
nonradiative bulk lifetime	$\tau_n = \tau_p = 1$ ms	61
coefficient of radiative recombination	$B = 6 \times 10^{-14}$ cm^3 s^{-1}	64
coefficient of Auger recombination	$C_n = C_p = 2 \times 10^{-31}$ cm^6 s^{-1}	65-68
absorption coefficient	$\alpha = 1.2 \times 10^4$ cm^{-1}	
reorganization energy	$\lambda = 0.5$ eV	47,48,55-60

Table 2.1: Physical input parameters of the ToSCA simulations

Figure 2.2: Results of the two-dimensional computer simulation of the initial condition in the dark (equilibrium) for an n-Si/liquid contact. The figures show the contact to the electrolyte at the left (front) side. The asymmetric back contact is situated at the right side of the figures. The Fermi level was set to be equal to the electrochemical potential of the solution, which was chosen to be zero. The rate constants for the electron and hole transfer were assumed to be equal, with $k_{ct}^{max} = 10^{-18}$ cm^4 s^{-1}. The concentrations were c_{red}=14 mM and c_{OX}=17 mM, and the barrier height of the contact was .6 V.[48] (a) Profile of the electric potential[69] , (b) profile of the electron concentration, and (c) profile of the hole concentration for this sample.

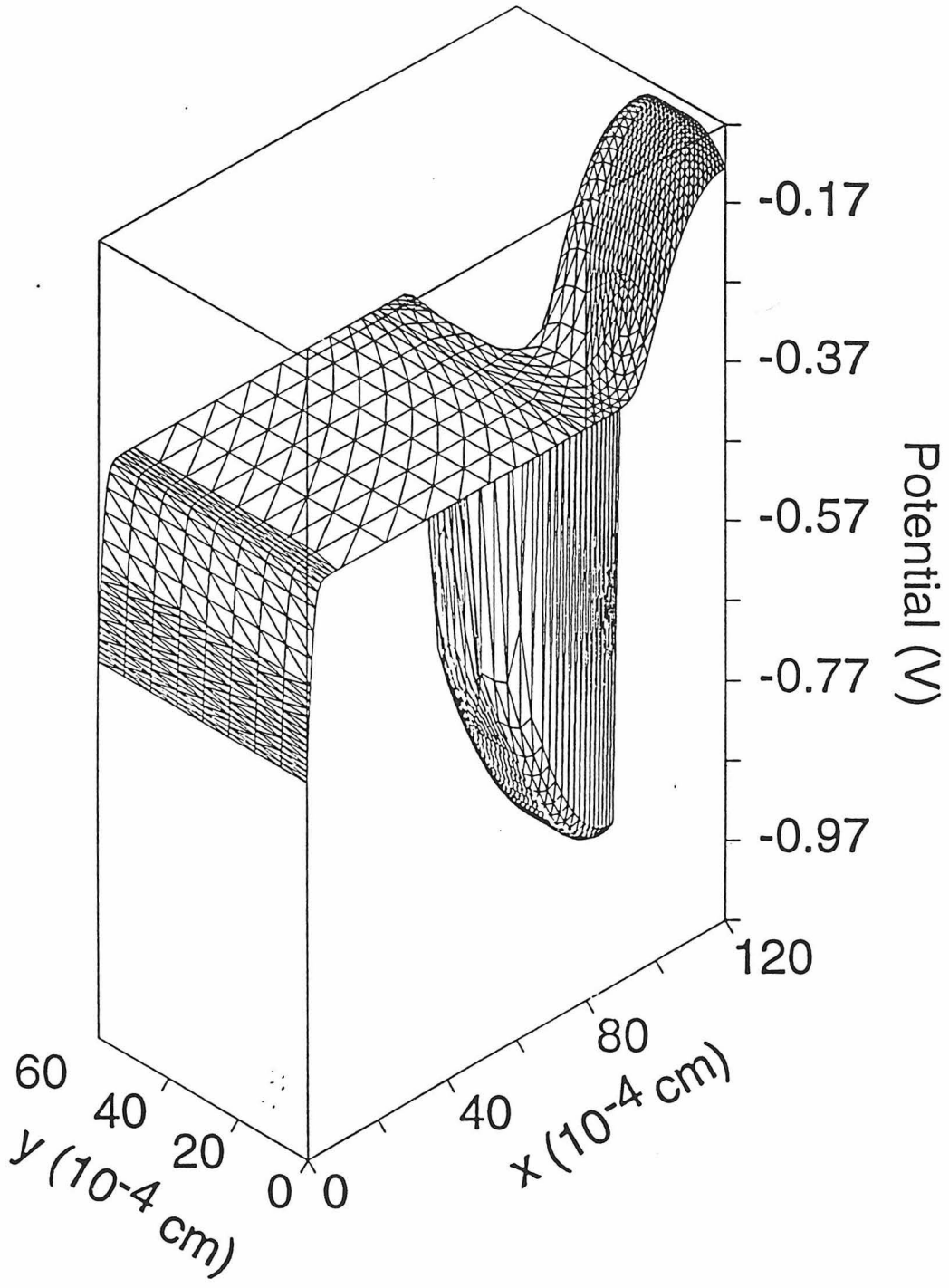
-0.17
-0.37
-0.57
-0.77
-0.97
Potential (V)
120
80
40
0
x (10-4 cm)
60
40
20
0
y (10-4 cm)

Figure 2.2a

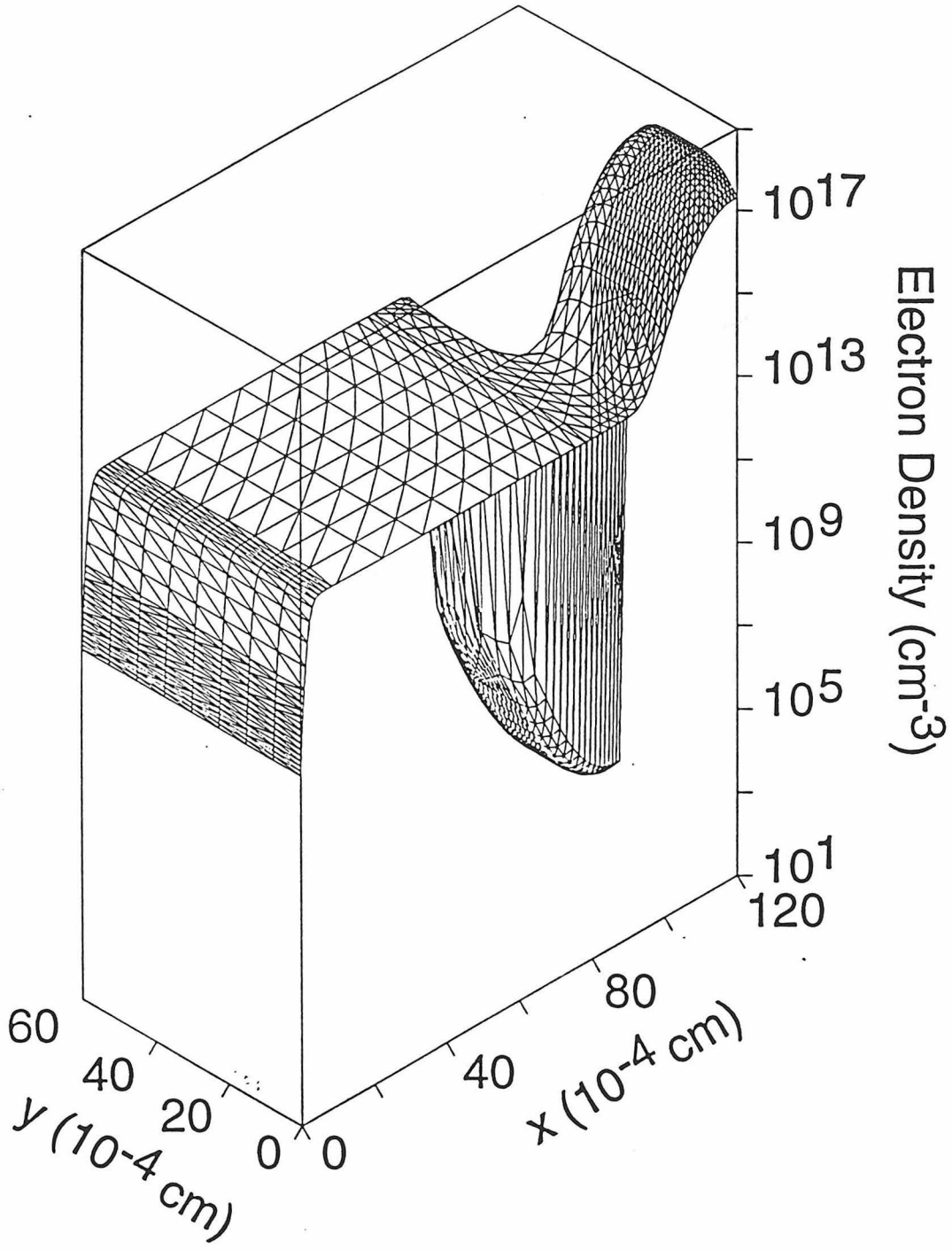
Electron Density (cm-3)
10^17
10^13
10^9
10^5
10^1
120
80
40
0
x (10-4 cm)
60
40
20
0
y (10-4 cm)

Figure 2.2b

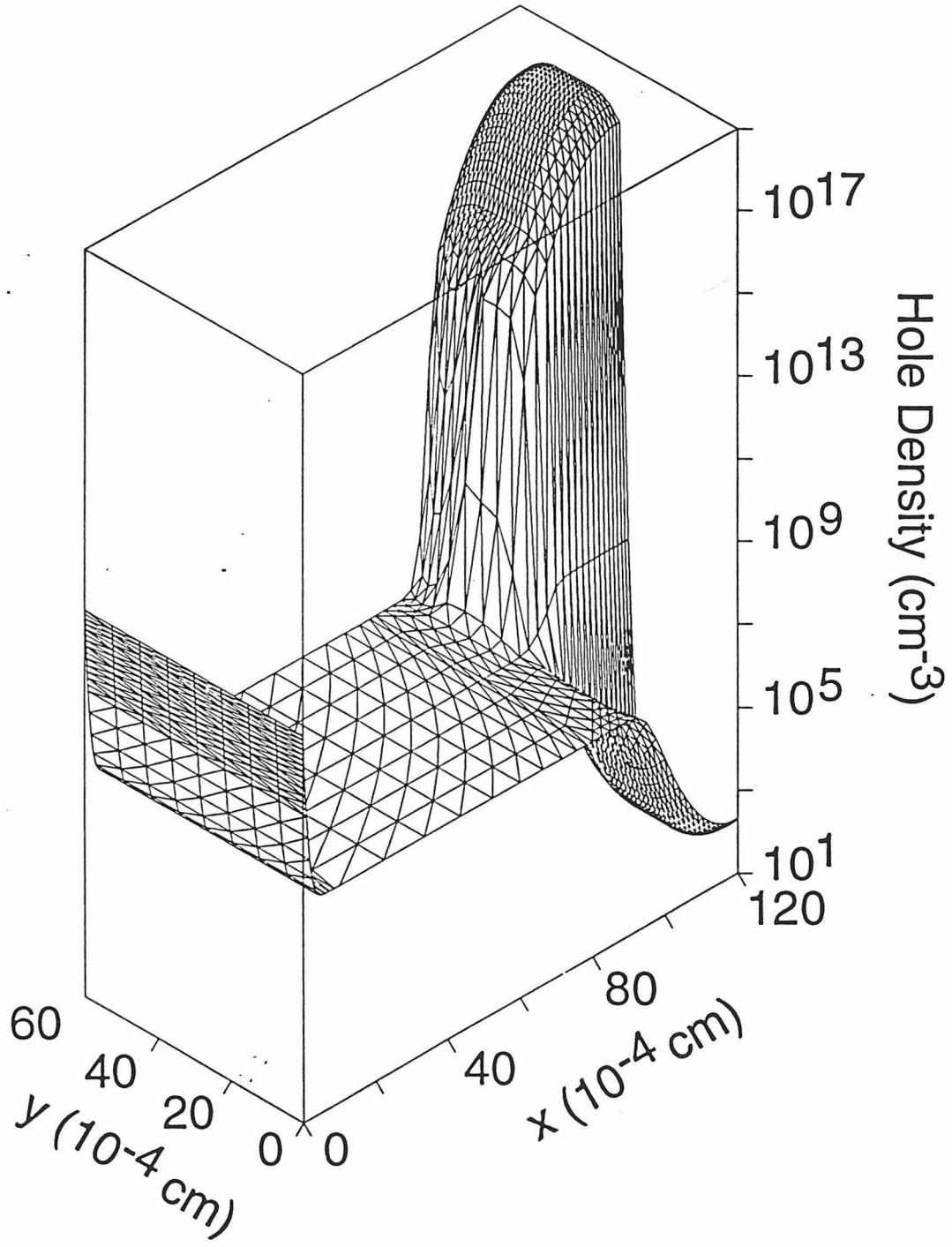
Hole Density (cm-3)
10^17
10^13
10^9
10^5
10^1
120
80
40
0
x (10-4 cm)
60
40
20
0
y (10-4 cm)

Figure 2.2c

IV. RESULTS AND DISCUSSION

1. DEPENDENCE OF THE PHOTOVOLTAGES AND PHOTOCURRENTS ON BACK CONTACT GEOMETRY AND ENERGETICS OF THE SOLID/LIQUID CONTACT

This section analyzes the principles governing the photocurrent and photovoltage behaviors of the Si samples studied in this work, as a function of the redox couple and the contact geometry. For these photoelectrodes, it was found that redox couples with very positive values of $\mathbf{E}(A/A^-)$ yielded large photovoltages for electron collection at the n^+ points and produced small photovoltages at the p^+ points, so that the illuminated electrode acted as if it were an n-type doped sample. In contrast, when the redox couple had a very negative electrochemical potential, the photoelectrode behaved as if it were a p-type doped electrode, producing large photovoltages at the p^+ points and small photovoltages at the n^+ points.[2,9] A superficial analysis would imply that this behavior was fortuitous, and that the $Me_2Fc^{+/0}$ redox couple, which has $\mathbf{E}(A/A^-)$ near the energy of the top of the valence band, $\mathbf{E}_v$, simply happened to have a relatively large capture rate constant for holes and a small capture rate constant for electrons, thereby producing a photoanodic current flow and also allowing the electron's effective electrochemical potential to deviate from equilibrium under illumination while not wasting energy in collection of the holes. A similar coincidence would then also be required for the $CoCp_2^{+/0}$ redox couple (having $\mathbf{E}(A/A^-)$ near the energy of the bottom of the conduction band, $\mathbf{E}_c$), except that this redox couple would need to collect electrons rapidly while fortuitously rejecting holes to produce a photocathodic current flow and a large photovoltage at the p^+ point contacts. Such preferential charge transfer of one carrier type or the other has been invoked previously to rationalize the photoelectrochemical behavior of nanocrystalline CdSe systems.[70] It is demonstrated below that a more fundamental principle governs the photoelectrochemical behavior of the Si-based systems, and by extension, is likely applicable to other related systems that use intrinsically-doped semiconductors under high level injection conditions.

A. Behavior of the Photovoltage

The open-circuit voltage was previously identified as determining the free energy available from an illuminated photoelectrochemical cell. In practice, this value is measured as the potential difference between the ohmic back contact of the semiconductor electrode and a metal electrode poised at the redox potential of the solution, $E(A/A^-)$. However, this does not necessarily correspond to the maximum photovoltage developed in the sample which is governed by the separation of the electron and hole quasi-Fermi levels. Figure 2.3 depicts a conventional n-type photoelectrode under low-level illumination and illustrates that the voltage corresponding to the quasi-Fermi level separation at the interface, $(\mathbf{E}_{F,p}-\mathbf{E}_{F,n})/q$, is larger than the V_{oc} value that would be measured. It is also shown that information on the actual quasi-Fermi level separation is not available for these contacts as the minority carrier quasi-Fermi level ($\mathbf{E}_{F,p}$ for n-type samples) collapses in the bulk of the semiconductor to that of the majority carrier, $\mathbf{E}_{F,n}$. The coalescence of the quasi-Fermi levels is brought about by the large excess of majority carriers in the bulk which effectively recombine with any minority carriers that diffuse into this region. Even if the minority carriers had a sufficiently long lifetime to be able to diffuse to the back of the sample, $\mathbf{E}_{F,p}$ could not be monitored as recombination at the single metallic back contact would force it to merge with $\mathbf{E}_{F,p}$.

In contrast to the behavior described above, information on the position of both the electron and hole quasi-Fermi level is available from the Si photoelectrodes used herein. The extremely long carrier lifetime of these Si samples permit $\mathbf{E}_{F,n}$ and $\mathbf{E}_{F,p}$ to remain separated throughout the sample, and the ohmic-selective n^+ and p^+ point contacts make possible the individual and simultaneous measurement of the two electrochemical potentials (Figure 2.1b). The quasi-Fermi level positions for these Si samples in contact with 1,1' dimethylferrocene$^{+/0}$ ($Me_2Fc^{+/0}$), cobaltocene$^{+/0}$ ($CoCp_2^{+/0}$), methyl viologen$^{2+/+}$ ($MV^{2+/+}$), and decamethylferrocene$^{+/0}$ ($Me_{10}Fc^{+/0}$) have been reported previously by Tan et al.[9,71] and are repeated for convenience in Table 2.2.

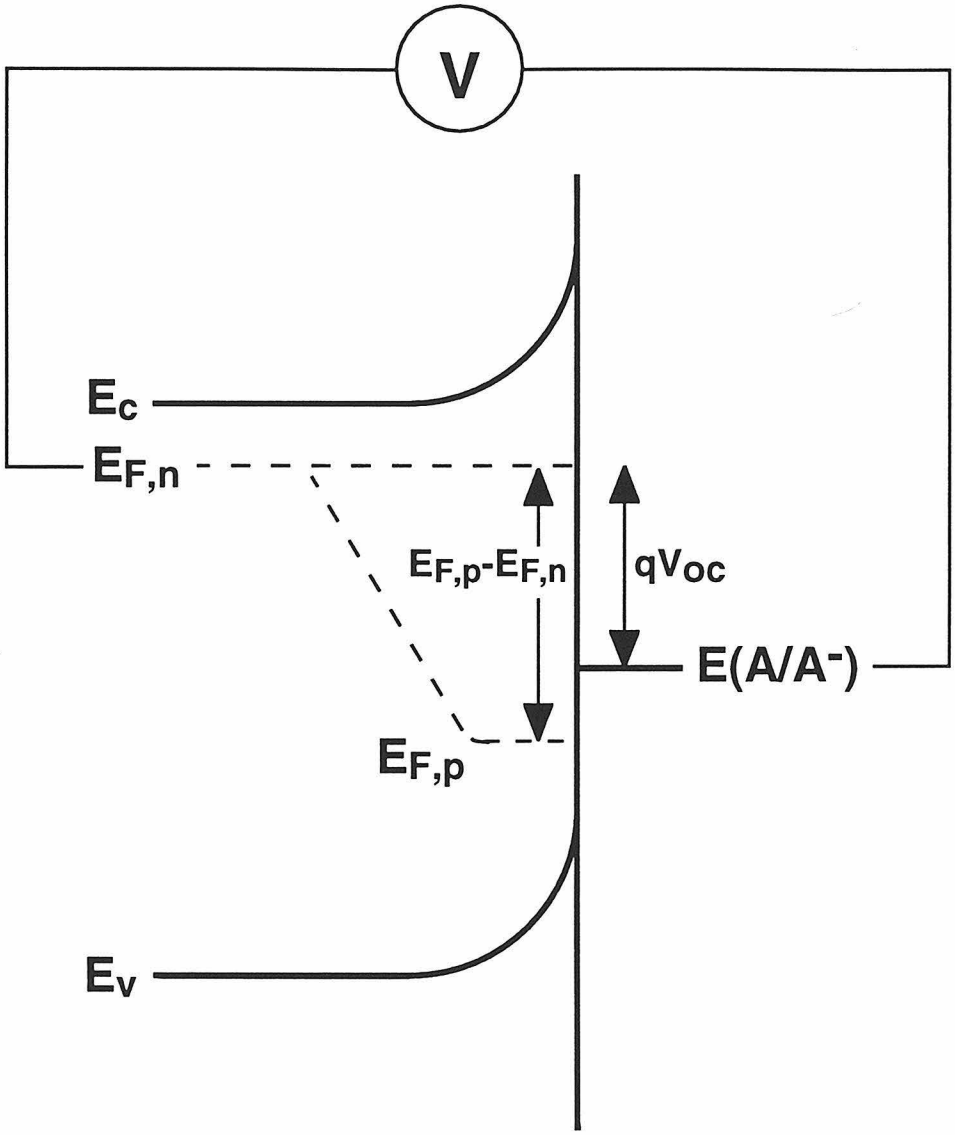

Figure 2.3: Energy band diagram for a conventional n-type photoelectrode under low-level illumination illustrating that the V_{oc} value measured is not necessarily equal to the maximum photovoltage developed in the semiconductor. Information on the minority carrier quasi-Fermi level position ($E_{F,p}$) cannot be obtained in this configuration.

Redox Couple	$V_{n+,oc}$ (mV)	$V_{p+,oc}$ (mV)
$Me_2Fc^{+/0}$	- 550	< 5
$Me_{10}Fc^{+/0}$	- 370	60
$MV^{2+/+}$	- 220	190
$CoCp_2^{+/0}$	< 5	500

Table 2.2: Representative values of the voltages measured at open circuit between the p^+ and n^+ point contacts and the solution potential ($V_{p+,oc}$ and $V_{n+,oc}$, respectively) at an illumination intensity sufficient to generate a photocurrent of 3.5 mA cm^{-2}. The quasi-Fermi level positions are obtained by multiplying the voltages by the elementary charge.

Since the photovoltage was influenced by the nature of the solid/liquid contact (Table 2.2), it is of interest to evaluate the factors controlling its behavior. The question involves the mechanism by which the sample appears to behave "n-type" when a system with a positive redox potential is present, and then appears to behave "p-type" when a system with a negative redox potential is present. A key point to explain this behavior is that the interfacial charge transfer fluxes obey equations of the following form[17,33,40]:

$$\text{hole flux} = k_p (p_s - p_{so}) \tag{2.17}$$

$$\text{electron flux} = k_n (n_s - n_{so}) \tag{2.18}$$

where k_p and k_n are the hole and electron capture rate constants, respectively, n_s and p_s are the electron and hole concentrations, respectively, at the semiconductor surface, p_{so} and n_{so} are the equilibrium hole and electron concentrations, respectively, at the semiconductor surface. These expressions are reasonable because at equilibrium they yield no net interfacial hole flux or electron flux. Away from equilibrium, these equations indicate that the interfacial flux of electrons or holes is proportional to the charge carrier capture coefficient in effect at equilibrium multiplied by any deviation from the equilibrium charge carrier concentration in the nonequilibrium state. This latter relationship can be deduced by

application of the principle of detailed balance to the semiconductor/liquid interface, with the simplifying assumption (used for the purposes of this discussion but not required for a general treatment) that the electrons and holes are thermalized to the lattice temperature under the non-equilibrium conditions of interest.

A second key point required to understand the observed behavior is that the electrochemical potential of electrons (i.e., the electron quasi-Fermi level), $\mathbf{E}_{F,n}(x)$, measured relative to the electrochemical potential of the solution ($\mathbf{E}_F=\mathbf{E}(A/A^-)= 0$ at equilibrium, by definition of the reference potential in this work) can be described at any position within the sample by:[12,32]

$$\mathbf{E}_{F,n}(x) = -(kT)\ \ln\ (n(x)/n_o(x)) \tag{2.19}$$

Similarly, the quasi-Fermi level of holes, $\mathbf{E}_{F,p}(x)$, is given as:

$$\mathbf{E}_{F,p}(x) = (kT)\ \ln\ (p(x)/p_o(x)) \tag{2.20}$$

The relations in eqs 2.17-2.20 are all that are needed in order to explain the photovoltage behavior observed experimentally for these photoelectrodes.

For the open-circuit condition to be met, no net current can flow across the solid liquid interface. Thus, eqs 2.17 and 2.18 yield:

$$k_p\ (p_s-p_{so}) = k_n\ (n_s-n_{so}) \tag{2.21}$$

Illumination creates excess electron and hole concentrations Δn and Δp, respectively, where $\Delta n \equiv n-n_o$ and $\Delta p \equiv p-p_o$ at any point in the solid. Using these definitions in a rearranged form of eq 2.21 yields the desired final relationships:

$$(p_s/p_{so}) = 1 + (k_n/k_p)(\Delta n_s/p_{so}) \tag{2.22}$$

$$(n_s/n_{so}) = 1 + (k_p/k_n)(\Delta p_s/n_{so}) \tag{2.23}$$

Eqs 2.21-2.23 act as constraints (in addition to any other recombination mechanisms that operate in the sample) that will dictate the carrier concentrations, and thus, the quasi-Fermi levels $\mathbf{E}_{F,n}(0)$ and $\mathbf{E}_{F,p}(0)$ at the solid/liquid interface, .

Although the hole and electron concentrations contain all of the fundamental information on the device, the experimental protocol used herein probes the voltages $V_{n+,oc}$

and $V_{p+,oc}$. It is therefore necessary to relate these quantities to the carrier concentrations. The potentials of the individual quasi-Fermi levels at the back of the sample, $E_{F,n}(d)$, $E_{F,p}(d)$ (with $E_{F,n}=\mathbf{E}_{F,n}/q$ and $E_{F,p}=\mathbf{E}_{F,p}/q$), are equal to the voltages measured between the point contacts and the solution potential, which are determined experimentally as $V_{n+,oc}$ and $V_{p+,oc}$. Assuming the quasi-Fermi levels are flat throughout the sample (as validated by digital simulations; see accompanying papers) implies that $\mathbf{E}_F(d)=\mathbf{E}_F(0)$. This equality can be combined with eqs 2.19 and 2.20 to yield:

$$V_{n+,oc} = - (kT/q) \ln (n_s/n_{so}) \tag{2.24}$$

$$V_{p+,oc} = (kT/q) \ln (p_s/p_{so}) \tag{2.25}$$

The implications of eqs 2.22-2.25 are first explored for a redox couple having $\mathbf{E}(A/A^-)$ near $\mathbf{E}_v$, such as $Me_2Fc^{+/0}$. For such a system, p_{so} is very large, and n_{so}, given by n_i^2/p_{so} where n_i is the intrinsic carrier concentration of the semiconductor, is correspondingly small. Consequently, it is expected that $\Delta n_s \leq p_{so}$, even under high level illumination. This implies that $p_s \approx p_{so}$, even for equal rate constants of electron and hole capture (eq 2.22). Under these conditions, eq 2.25 indicates that $V_{p+,oc} \approx 0$, and, thus, that the hole quasi-Fermi level will remain very close to the redox potential of the solution. However, since n_{so} is small, these same illumination conditions yield $n_s/n_{so} >> 1$, and eq 2.24 then predicts a large value for $V_{n+,oc}$. In other words, this scenario produces $V_{n+,oc} >> V_{p+,oc}$ and $V_{p+,oc} \approx 0$, in accord with the experimental observations for the $Si/CH_3OH\text{-}Me_2Fc^{+/0}$ junction (Table 2.2).[72]

A similar argument can be developed for redox couples having $\mathbf{E}(A/A^-)$ near $\mathbf{E}_c$. In this case, the analysis described above would yield $n_s/n_{so} \approx 1$ and $p_s/p_{so} >> 1$. This set of conditions would imply, according to eqs 2.24 and 2.25, that $V_{p+,oc} >> V_{n+,oc}$ and $V_{n+,oc} \approx 0$. This is precisely the situation observed for the $Si/CH_3OH\text{-}CoCp_2^{+/0}$ contact (Table 2.2). For $\mathbf{E}(A/A\text{-})$ in the middle of the semiconductor band gap, $n_s/n_{so} > 1$ and $p_s/p_{so} > 1$ at open circuit and therefore both $V_{n+,oc}$ and $V_{p+,oc}$ will be substantial. This is exactly the behavior observed experimentally for $Si/THF\text{-}CH_3OH\text{-}Me_{10}Fc^{+/0}$ and

Si/CH_3OH-$MV^{2+/+}$ contacts (Table 2.2). It is therefore seen that the underlying semiconductor statistics that control the available free energy of an illuminated photoelectrode account for the experimental observations that the intrinsic Si sample appears to adjust its photoelectrochemical behavior to respond optimally to the redox potential of the solution, regardless of the actual values of the charge transfer rate constants of the system under study.

B. Behavior of the Photocurrent

The directionality of the photocurrent observed for these Si samples was not a function of the charge transfer kinetics at the solid/liquid contact, but instead was governed entirely by the boundary conditions imposed by back contact.[2,9] When the n^+ points were contacted, the photocurrents were always anodic in sign, regardless of the concentrations, ratio of oxidized to reduced species, or redox potentials of the redox couple in the solution. This situation held for redox couples having electrochemical potentials near the conduction band, in the middle of the band gap, or near the valence band of the semiconductor, and therefore logically applies to contacts having a variety of electron/hole charge transfer rate constant ratios. Similarly, when the p^+ points were contacted, the photocurrents were cathodic in sign for all the types of solution contacts. This behavior is readily understood as electrons cannot pass through the back p^+-Si/intrinsic-Si junction. An ohmic back contact that collected both carrier types efficiently and simultaneously would simply lead to effective recombination and would produce small, if any, photocurrents or photovoltages for any type of redox couple. The data fully support the conclusions that the direction of current flow is dictated by the back contact conditions and that preferential charge transfer rates of one carrier type or the other at the solid/liquid interface can affect the photovoltage, but not the photocurrent directionality, of an efficient photoelectrochemical cell under high level injection.

C. Implications for Other Intrinsic Photoelectrodes

The treatment developed herein is also useful in explaining the behavior of intrinsically doped layers present in amorphous hydrogenated Si (Si:H) photoelectrodes. The photocurrent and photovoltage properties of such materials have been previously explained in terms of drift effects and the initial energetics of the solid/liquid and solid/back contacts.[73,74] In this explanation, the electric fields across such materials, produced by the energetic differences between the work functions of the liquid contact and the back contact, have been associated with the directionality of current flow and with the photovoltage properties of the system. In this approach, it is not apparent what the direction of the photocurrent flow, or what the magnitude of the photovoltage, should be for any particular system. For example, when only the relative energetics of the back and front contacts are considered, it is not clear whether the electric field under illumination of an intrinsically doped semiconductor should develop with respect to the position of the valence or conduction band edge, and it is also unclear whether the sample should behave as a photoanode or photocathode when contacting a particular redox couple.

In contrast, the framework described herein accounts for the experimentally observed behavior of such systems. The intrinsic a-Si:H layer behaves as an n-type photoanode in an n^+-i/liquid configuration because of the back contact metallurgy, which kinetically prevents collection of holes and therefore induces only photoanodic currents. This occurs regardless of the front contact energetics. The p^+-i/liquid configuration of amorphous Si photoelectrodes produces the opposite photocurrent because of its p^+ back contact boundary conditions, not because of the energetics of the back contact work function relative to the redox potential of the liquid phase. Additionally, as discussed above, the fundamental statistics of the front contact system can be used to explain the experimental observations that significant photovoltages are obtained from the electron quasi-Fermi level for redox couples with positive redox potentials and from the hole quasi-Fermi level for redox couples with negative redox potentials. This formalism thus provides

a unifying framework that not only can explain the observations to date on crystalline Si and amorphous hydrogenated Si, but which also allows the formulation of useful predictions for optimal energy conversion configurations from a variety of intrinsically-doped devices operated under high level injection conditions.

2. MEASUREMENT AND SIMULATION OF QUASI-FERMI LEVELS AT SI/LIQUID INTERFACES UNDER APPLIED BIAS

The preceding section presents a theoretical analysis of the factors that control the photovoltage and photocurrent directionality of Si photoelectrodes operated in high-level injection.[9] As discussed therein, this analysis have provided insight into the open circuit behavior of the quasi-Fermi levels at semiconductor/liquid contacts, and has led to a kinetic description of the photocurrent and photovoltage behavior of such systems.

The electrical junction configuration fabricated into these samples also offers the possibility of controlling electrically the potential at, and measuring the charge carrier flux through, one collection of contacts while monitoring the electrochemical potential (at open circuit) produced at the other set of contacts. Such measurements, described herein, allow investigation of the position of the quasi-Fermi level for a given carrier type in the presence of band gap excitation of the semiconductor, under a variety of bias conditions and for a variety of redox couples in the liquid phase. These results are relevant to the controversy regarding the thermodynamic interpretation of the quasi-Fermi levels in an operating, illuminated photoelectrochemical cell, and are of fundamental interest with respect to the behavior of the quasi-Fermi levels under an applied bias.[10-17] This section describes experimental data and digital simulations of the carrier generation, transport, and recombination processes in such systems. The simulations have been performed to confirm quantitatively some of the approximations advanced in the preceding and present papers,[2-4,9] and to provide insight into some unexpected aspects of the behavior of quasi-Fermi levels that have been observed during the course of this study.

A. Experimental Measurement of Quasi-Fermi Level Characteristics at Si/Liquid Interfaces Under Applied Bias

As depicted in Figure 2.1b, the contact geometry in these samples provided an opportunity to set the potential of one carrier type in the photoelectrode while monitoring the potential adopted by the other carrier type. For example, the potential at the n^+ points could be controlled using a potentiostat (with $V_{n+} = E(A/A^-)-E(n^+)$ where $E(A/A^-)$ is the redox potential of the solution), while the current density for electron collection (J_{n+}), and the open circuit potential of the p^+ points, $V_{p+,oc} = E(p^+)-E(A/A^-)$, were monitored. This type of experiment could be performed while the sample was under an arbitrary degree of illumination.

As a specific example, electron collection, accomplished through potentiostatic control of the n^+ points, is considered. The current density vs voltage data for electron collection at these points, J_{n+} vs V_{n+}, has been presented elsewhere.[2,9] Figure 2.4a presents additional data for the $Si/CH_3OH\text{-}Me_2Fc^{+/0}$ contact in which the potential of the holes, $V_{p+,oc}$, was measured as a function of the potential applied to the n^+ points, V_{n+}. Such data were recorded independently of, but simultaneously with, measurements of the electron flux through the n^+ points at various values of V_{n+}.

There were two distinct regions of such plots. In the rising portion of the J_{n+} vs V_{n+} plot, where the current density at the n^+ points depended on the applied bias to the system, $V_{p+,oc}$ was observed to be a function of the potentiostatically controlled voltage V_{n+}. In the region where J_{n+} was independent of V_{n+}, no change in $V_{p+,oc}$ was observed, even for significant variation of V_{n+}. Thus, in this region, the difference between $V_{p+,oc}$ and V_{n+} was linearly dependent on the value of V_{n+}, with more positive V_{n+} values producing smaller separations of the electron and hole quasi-Fermi levels at the back of the sample. Although not shown in the figure, a third region of behavior, in which $V_{p+,oc}$ again became dependent on V_{n+}, was observed at sufficiently positive biases.

$V_{p+,oc}$ vs V_{n+} data for the other two redox couples that displayed significant photovoltages in this contact configuration are presented in Figures 2.4b-c. Two distinct regimes were observed for all such data. As described above for Si/CH_3OH-$Me_2Fc^{+/0}$ contacts, when the J_{n+} vs V_{n+} data exhibited a dependence on applied potential, changes in the potential applied to one contact produced changes in the open circuit potential measured at the other contact. In the other regime, where the photocurrent density was limited either by mass transport or by the electron-hole pair generation rate, changing the voltage applied at the n^+ contact did not produce any changes in the open circuit potential measured at the p^+ contact. In this regime of behavior, the quasi-Fermi level separation became smaller as the sample was driven further into reverse bias. As was observed for the Si/CH_3OH-$Me_2Fc^{+/0}$ system, $V_{p+,oc}$ was found to again become dependent on the value of V_{n+} at strong reverse bias (not shown in figures).

As shown in Figure 2.4d, the Si/CH_3OH-$CoCp_2^{+/0}$ system exhibited ohmic behavior in this experiment. This behavior is expected theoretically since the electrochemical potential of the $CoCp_2^{+/0}$ system is close to the conduction band edge energy of the semiconductor.[75]

It was also possible to measure, for this same series of semiconductor/liquid contacts under identical illumination conditions, the current-voltage properties of holes while monitoring the quasi-Fermi level behavior of electrons. These data were obtained by applying a bias to the p^+ points and measuring J_{p+} as well as $V_{n+,oc}$. Figure 2.5a displays the J_{p+} vs V_{p+} data for the Si/CH_3OH-$Me_2Fc^{+/0}$ contact, showing that this system exhibited near-ohmic behavior under illumination. As was the case for the $CoCp_2^{+/0}$ system when the n^+ points were controlled potentiostatically, the behavior of the Si/CH_3OH-$Me_2Fc^{+/0}$ contact under control of the p^+ points is expected theoretically since the electrochemical potential of the redox couple is close to the energy of the valence band edge.[48] Figures 2.5b-d display the J_{p+} vs V_{p+} as well as $V_{n+,oc}$ vs V_{p+} relationships under illumination for redox couples that developed significant photovoltages in this contact

configuration. In all of these cases, in the potential range where the photocurrent was dependent upon the applied potential, the value of $-V_{n+,oc}$ increased as the forward bias, V_{p+}, decreased. In the region where J_{p+} was independent of V_{p+}, $V_{n+,oc}$ was essentially insensitive to changes in V_{p+}. Thus, in all respects, the behavior observed when holes were controlled potentiostatically corresponds to the observations made when the electrons were controlled potentiostatically (i.e., Figures 2.5b-d were analogous to Figures 2.4a-c).

Figure 2.4: Plot of the open-circuit potential measured at the p^+ points ($V_{p+,oc}$; open squares), and current collected at the n^+ points (J_{n+}; solid circles), as a function of the potential applied to the n^+ points (V_{n+}). (a) Si/CH_3OH-1.0 M $LiClO_4$-103 mM Me_2Fc-12 mM Me_2FcBF_4 ($E(A/A^-)$ = 170 mV vs SCE) (b) Si/75% THF-25% CH_3OH (v/v)-1.0 M $LiClO_4$-4.3±0.5 mM $Me_{10}Fc$-4.4±0.5 mM $Me_{10}FcBF_4$ ($E(A/A^-)$ = -23 mV vs SCE) (c) Si/CH_3OH-1.0 M LiCl-10. mM MV^+-21 mM $MVCl_2$ ($E(A/A^-)$ = -446 mV vs SCE) (d) Si/CH_3OH-0.90 M LiCl-2.3±0.2 mM $CoCp_2$-45 mM $CoCp_2Cl$ ($E(A/A^-)$ = -890 mV vs SCE).

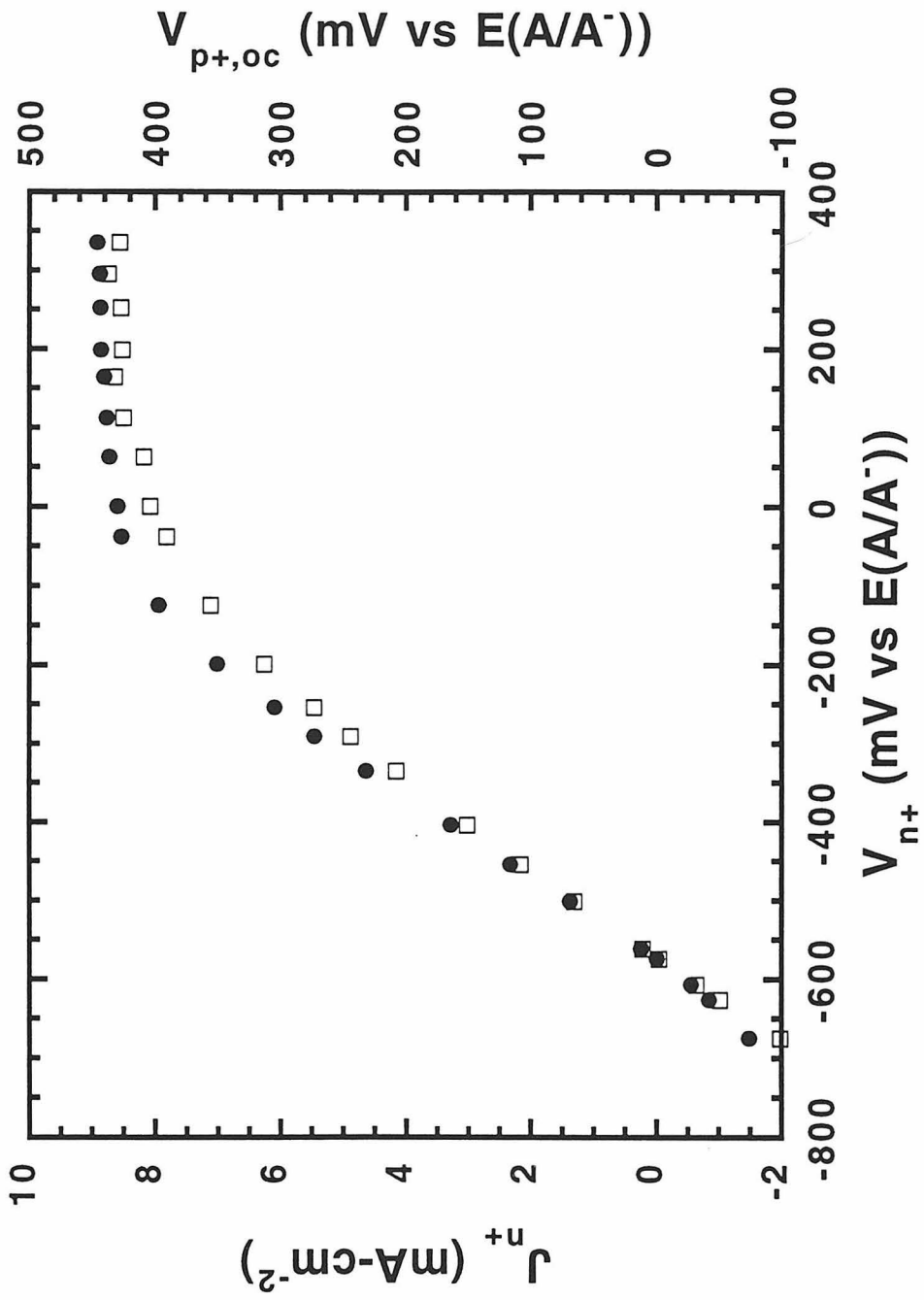
$V_{p+,oc}$ (mV vs E(A/A$^-$))
500
400
300
200
100
0
-100
400
200
0
-200
-400
-600
-800
V_{n+} (mV vs E(A/A$^-$))
10
8
6
4
2
0
-2
J_{n+} (mA-cm^{-2})

Figure 2.4a

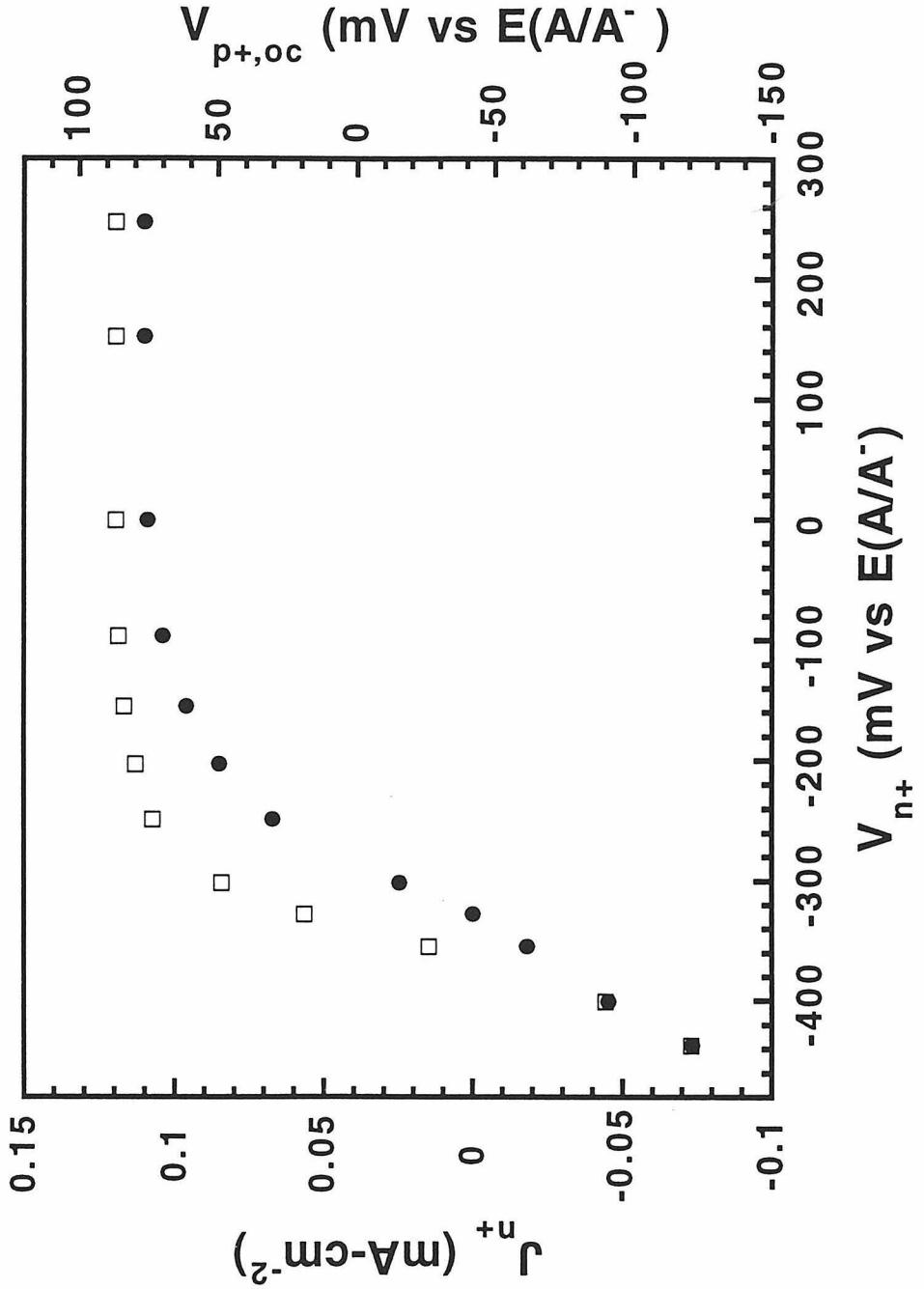
$V_{p+,oc}$ (mV vs E(A/A$^-$))
100
50
0
-50
-100
-150
0.15
0.1
0.05
0
-0.05
-0.1
J_{n+} (mA-cm^{-2})
-400
-300
-200
-100
0
100
200
300
V_{n+} (mV vs E(A/A$^-$))

Figure 2.4b

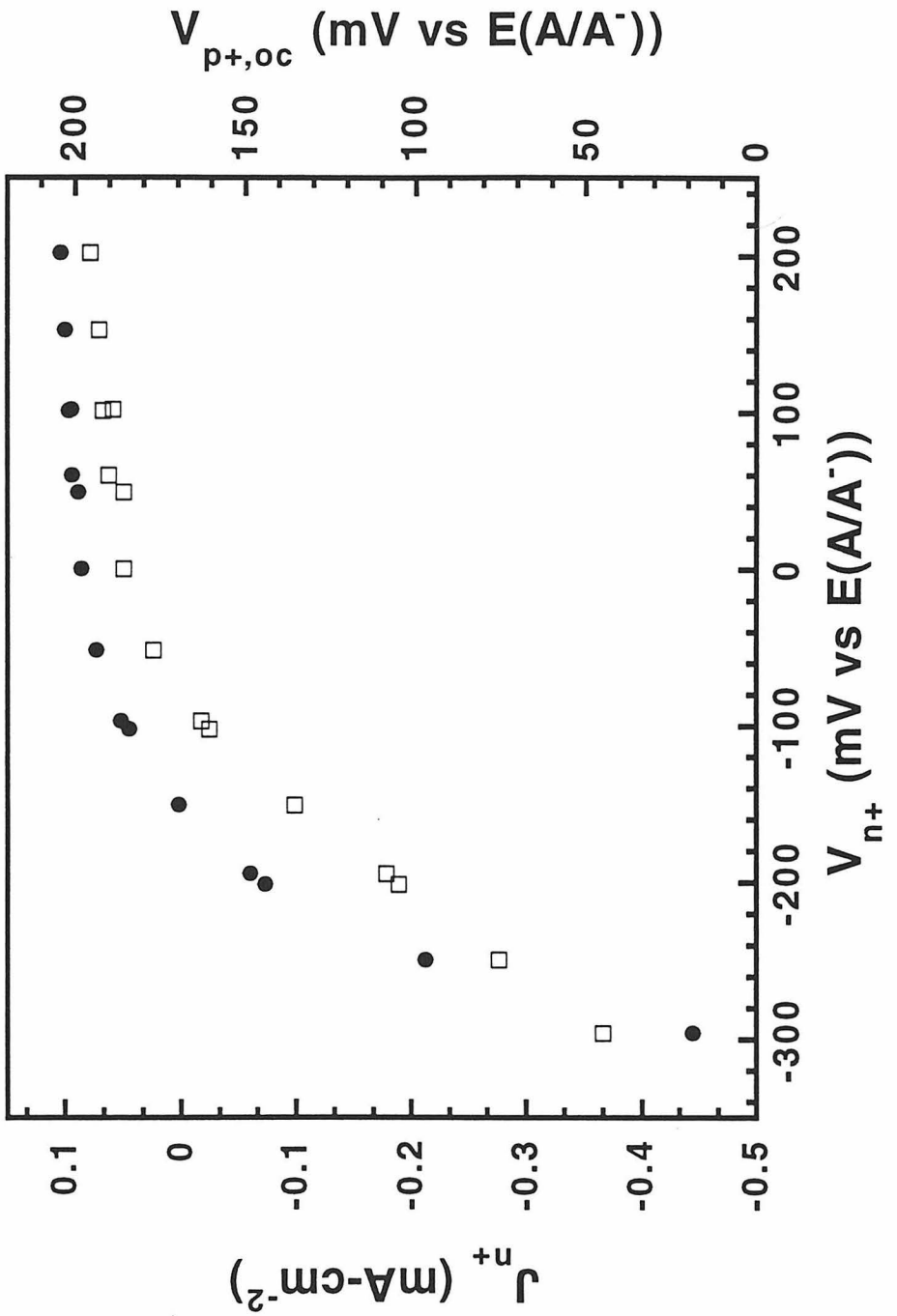
$V_{p+,oc}$ (mV vs E(A/A$^-$))
200
150
100
50
0
-300
-200
-100
0
100
200
V_{n+} (mV vs E(A/A$^-$))
0.1
0
-0.1
-0.2
-0.3
-0.4
-0.5
J_{n+} (mA-cm^{-2})

Figure 2.4c

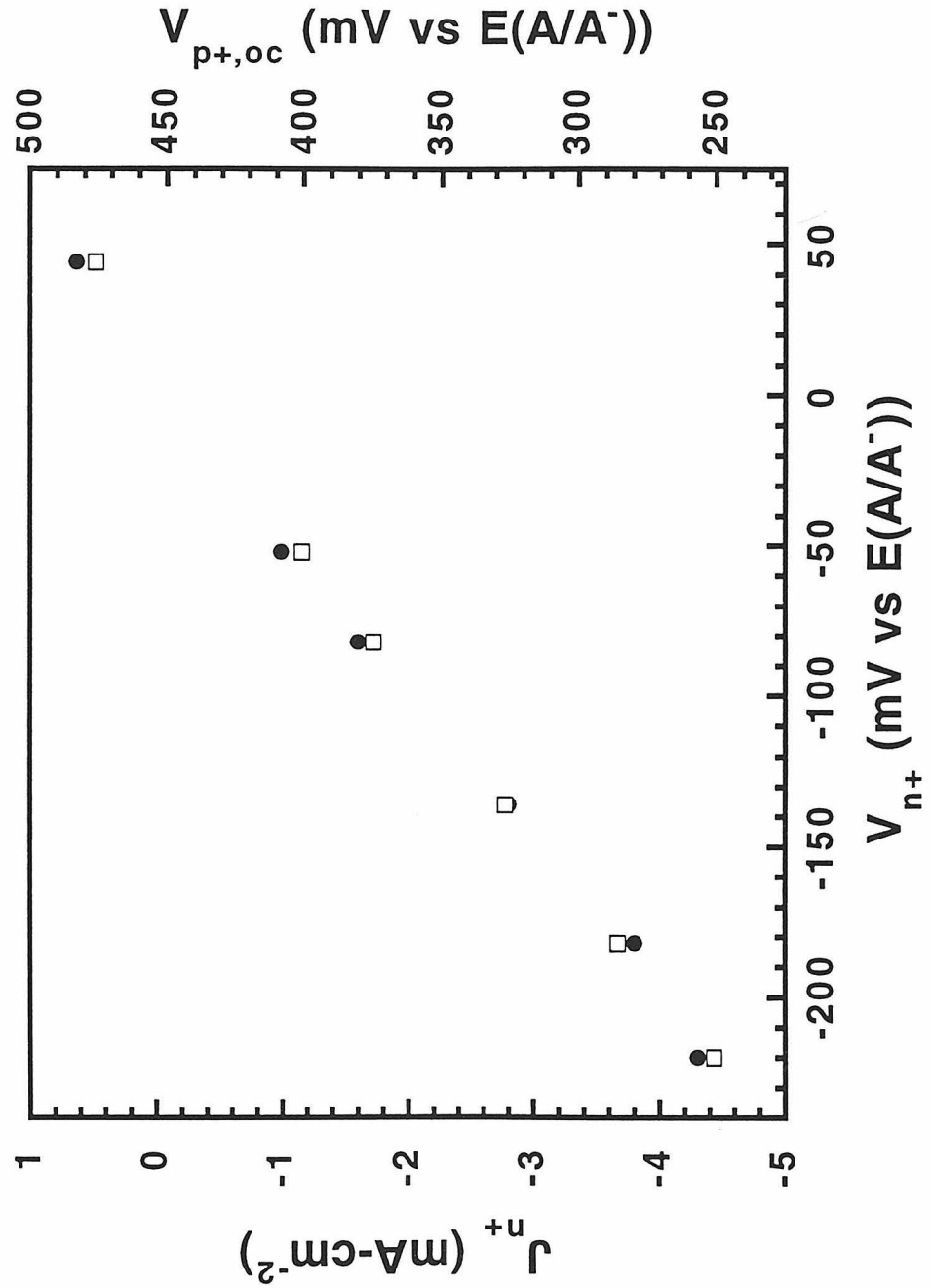
$V_{p+,oc}$ (mV vs E(A/A$^-$))
500
450
400
350
300
250
50
0
-50
-100
-150
-200
V_{n+} (mV vs E(A/A$^-$))
1
0
-1
-2
-3
-4
-5
J_{n+} (mA-cm^{-2})

Figure 2.4d

Figure 2.5: Plot of the open-circuit potential measured at n^+ points ($V_{n+,oc}$; open squares), and current collected at p^+ points (J_{p+}; solid circles), as a function of the potential applied to the n^+ points (V_{p+}). (a) Si/CH_3OH-1.0 M $LiClO_4$-103 mM Me_2Fc-12 mM Me_2FcBF_4 (E(A/A^-) = 170 mV vs SCE) (b) Si/80% THF-20% CH_3OH (v/v)-0.54 M $LiClO_4$-23 mM $Me_{10}Fc$-14 mM $Me_{10}FcBF_4$ (E(A/A^-) = -3 mV vs SCE) (c) Si/CH_3OH-1.0 M LiCl-6.0 mM MV^+-26 mM $MVCl_2$ (E(A/A^-) = -420 mV vs SCE) (d) Si/CH_3OH-0.90 M LiCl-2.3±0.2 mM $CoCp_2$-45 mM $CoCp_2Cl$ (E(A/A^-) = -890 mV vs SCE)

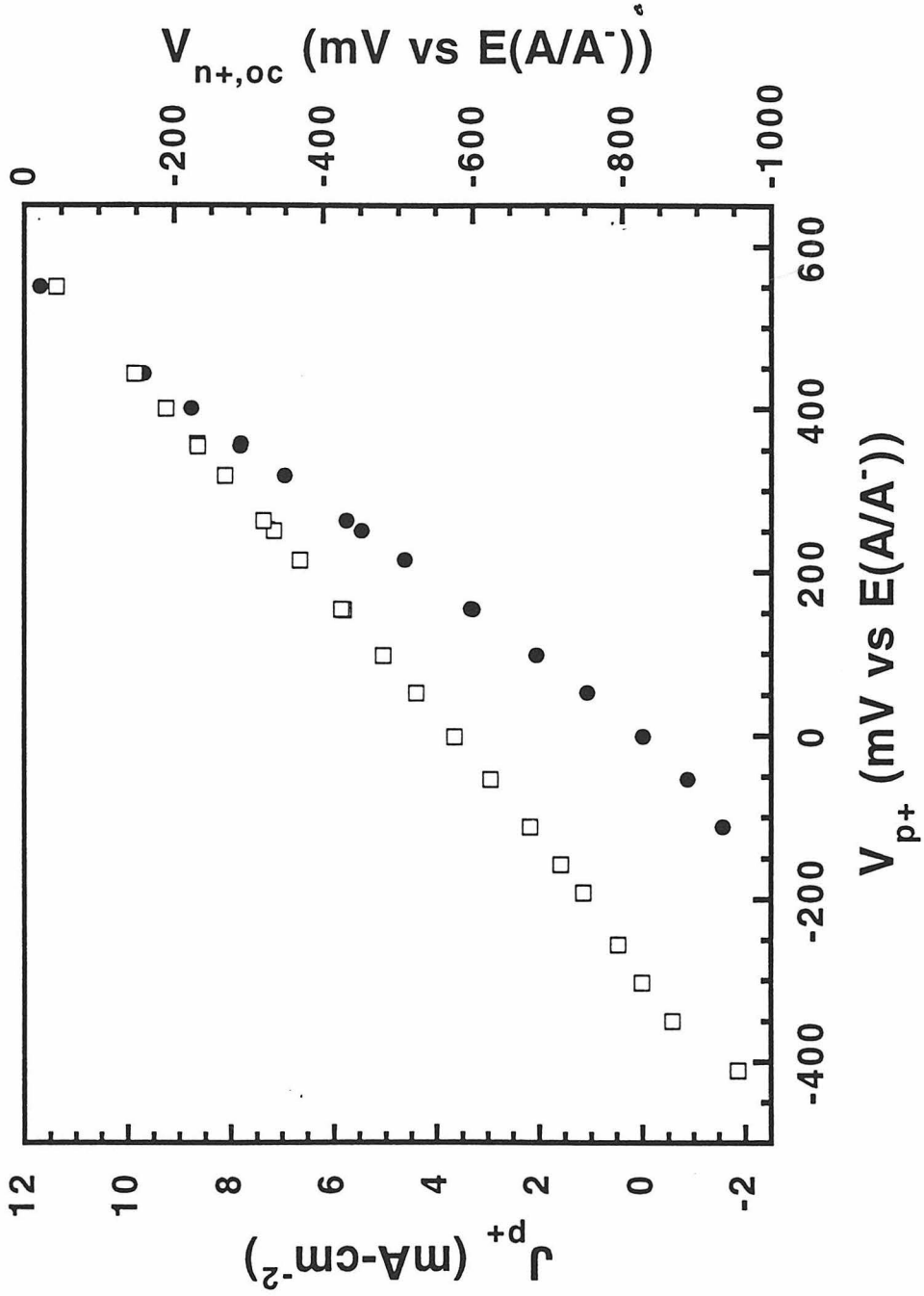
$V_{n+,oc}$ (mV vs E(A/A$^-$))
0
-200
-400
-600
-800
-1000
J_{p+} (mA-cm^{-2})
12
10
8
6
4
2
0
-2
V_{p+} (mV vs E(A/A$^-$))
-400
-200
0
200
400
600

Figure 2.5a

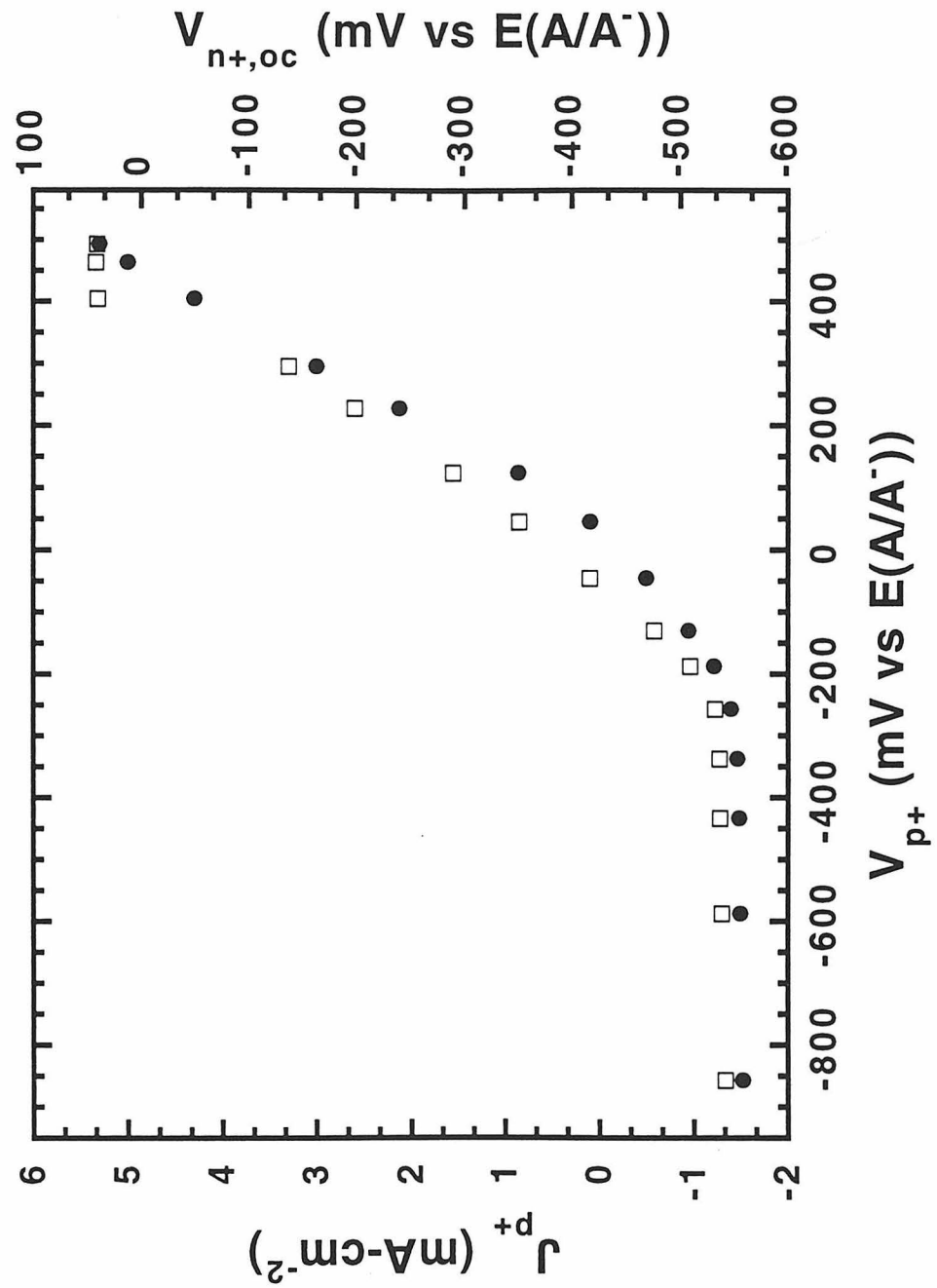
$V_{n+,oc}$ (mV vs E(A/A$^-$))
100
0
-100
-200
-300
-400
-500
-600
6
5
4
3
2
1
0
-1
-2
J_{p+} (mA-cm^{-2})
-800
-600
-400
-200
0
200
400
V_{p+} (mV vs E(A/A$^-$))

Figure 2.5b

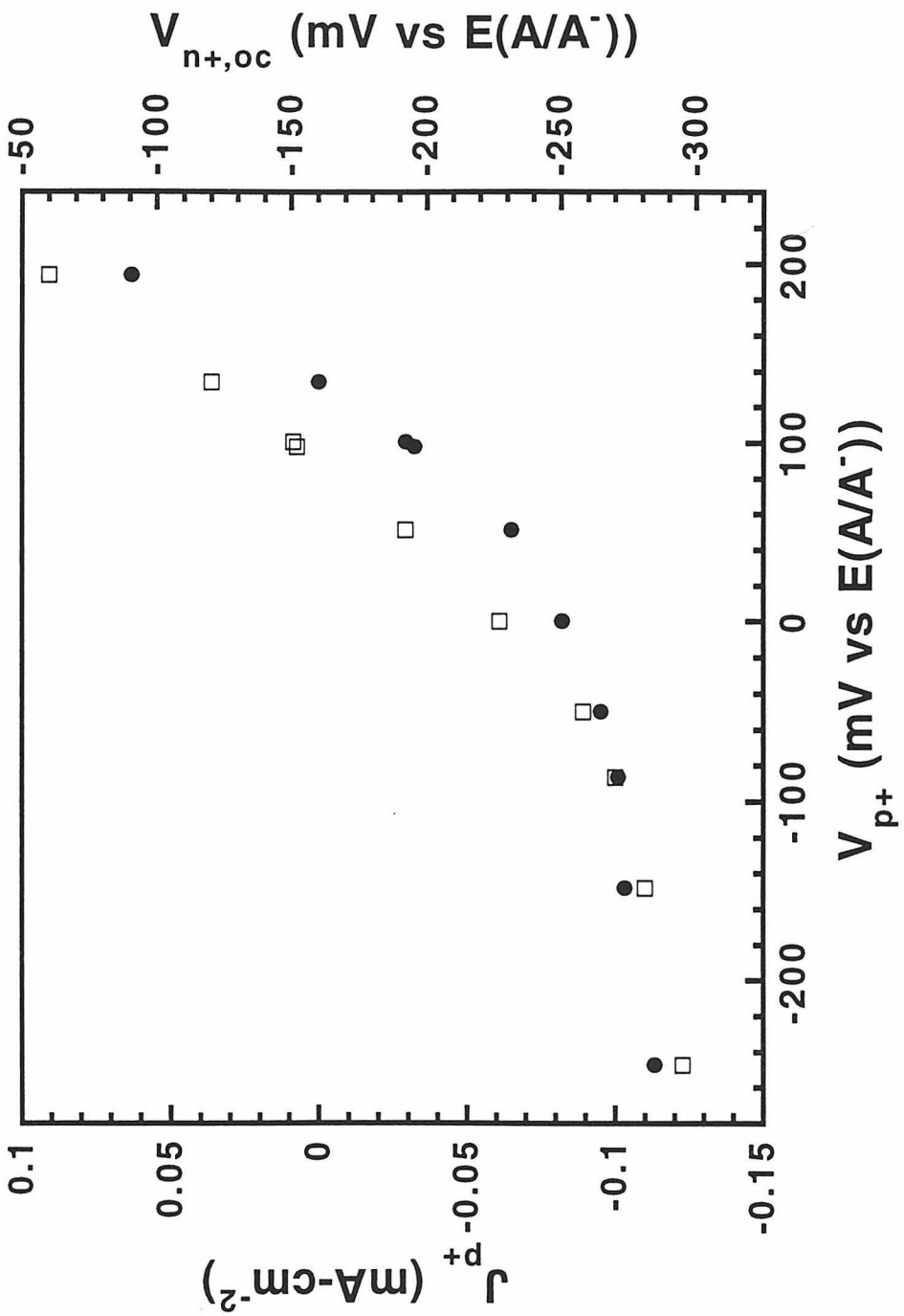
V n+,oc (mV vs E(A/A-))
-50
-100
-150
-200
-250
-300
200
100
0
-100
-200
V p+ (mV vs E(A/A-))
0.1
0.05
0
-0.05
-0.1
-0.15
J p+ (mA-cm-2)

Figure 2.5c

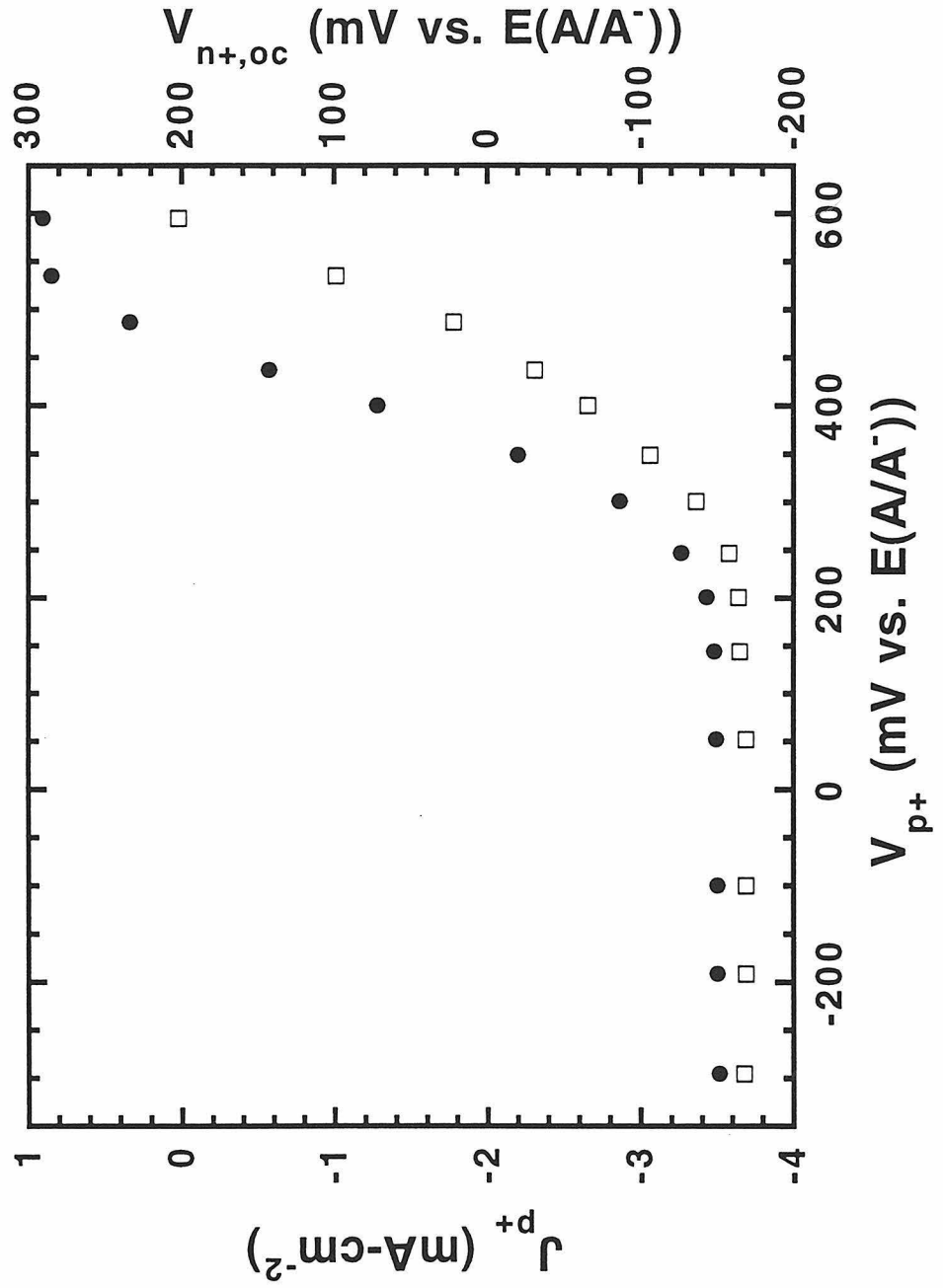
$V_{n+,oc}$ (mV vs. E(A/A$^-$))
300
200
100
0
-100
-200
600
400
200
0
-200
V_{p+} (mV vs. E(A/A$^-$))
1
0
-1
-2
-3
-4
J_{p+} (mA-cm^{-2})

Figure 2.5d

B. Qualitative Understanding of the Experimental Quasi-Fermi Level Behavior Under Applied Bias

The data described above show that the potential of the quasi-Fermi level of the carrier type not under potential control was a function of the current density of the carrier being collected through the back of the sample at the regions under potential control. This was true regardless of the energetic position of the electrochemical potential of the solution relative to the valence or conduction band edge energies, and regardless of the carrier type being collected at the back of the sample. Such data are especially important with respect to understanding the behavior of quasi-Fermi levels of illuminated semiconductor photoelectrodes as originally predicted by Gerischer[12] and as discussed extensively in several recent, elegant publications by Memming and co-workers.[13-15,32]

The behavior of the Si/CH_3OH-$Me_2Fc^{+/0}$ junctions with control of the n^+ points (Figure 2.4a) is readily understood. If collection of electrons at the n^+ contacts results in holes being collected at the solid/liquid interface, changes in V_{n+} should produce changes in the value of $V_{p+,oc}$. Specifically, as the hole flux increases across the solid/liquid contact, $V_{p+,oc}$ should increase to accommodate this increase in interfacial charge transfer. This is exactly the behavior observed experimentally for the Si/CH_3OH-$Me_2Fc^{+/0}$ contact. When the light-limited photocurrent density was reached in this system, the hole flux became constant with changes in the applied potential, and further increases in V_{n+} had no effect on the value of $V_{p+,oc}$. This is also in accord with theoretical expectations, since no further polarization of the hole quasi-Fermi level is required when the interfacial hole flux is constant with variations in potential.

An additional implication of this correlation between the electron and hole fluxes is that the potential necessary to produce a certain interfacial hole flux, measured as the J_{p+} vs V_{p+} relationship for this solid/liquid junction, should be related directly to the J_{n+} vs V_{n+} relationship of this contact. If removal of an electron at the back n^+ contact indeed produces injection of a hole from the valence band into the electrolyte, then the constraint

$J_{n+}=J_{p,f}$ (where $J_{p,f}$ is the interfacial hole current density at the solid/liquid interface) must apply. In other words, if establishing a certain current density of electrons at the back contact (J_{n+}) requires establishing an equal current density for holes across the front contact ($J_{p,f}$), then the hole quasi-Fermi level ($V_{p+,oc}$) must move positively at the solid/liquid contact in order to accommodate this specific interfacial hole flux.

This prediction is experimentally testable, because the relationship between the hole quasi-Fermi level and the interfacial hole flux can be experimentally determined from the behavior of J_{p+} vs V_{p+}. If the constraint $J_{n+}=J_{p,f}$ holds, then a plot of J_{p+} (established by controlling V_{p+}) vs the value of $V_{n+,oc}$ developed for that interfacial hole flux should map onto a plot of J_{n+} vs V_{n+}. As shown in Figure 2.6a, this is in excellent accord with the experimental data for the $Si/CH_3OH\text{-}Me_2Fc^{+/0}$ contact. Thus, for this system, holes obey the same interfacial current density vs quasi-Fermi level relationship regardless of whether their interfacial flux is dictated by biasing their potential directly at the back p^+ points (as "majority carriers") to produce an interfacial hole current at the solid/liquid contact or whether their interfacial flux is the "minority carrier" response to removal of the potentiostatically controlled "majority carrier" at the back contact through biasing the n^+ points and collecting electrons at the back contact. This relationship, which has been experimentally verified for the contacts studied herein, is essentially the underlying, enabling assumption in the quasi-Fermi level description of semiconductor electrochemistry.[12]

The same principles can also be applied to the behavior of $Si/CH_3OH\text{-}CoCp_2^{+/0}$ junctions. When the p^+ points are controlled potentiostatically, electron transfer with the conduction band dominates the interfacial current flow as discussed above. Thus, collection of holes at the back of the Si (J_{p+}), resulting from biasing the p^+ contact (V_{p+}), requires interfacial electron transfer ($J_{n,f}$) and therefore affects the electron quasi-Fermi level at the solid/liquid contact, in accord with the experimental observations (Figure 2.5d). As was the case for holes at $Si/CH_3OH\text{-}Me_2Fc^{+/0}$ contacts, it was possible to

independently determine the relationship between the electron quasi-Fermi level position and the interfacial electron flux (Figure 2.4d). Applying the constraint that $J_{n,f} = J_{p+}$, a plot of J_{n+} (established by controlling V_{n+}) vs the value of $V_{p+,oc}$ developed for that interfacial electron flux should map onto a plot of J_{p+} vs V_{p+}. Figure 2.6b show that this relationship is also borne out experimentally. Although not shown in the figures of this thesis, analogous results were also observed for the redox couples having energies in the middle of the semiconductor band gap, $MV^{2+/+}$ and $Me_{10}Fc^{+/0}$.

One potential confounding variable in these measurements is the degree to which the observed values of the quasi-Fermi levels at the back contact ($qV_{n+,oc}$, $qV_{p+,oc}$) reflect the positions of the quasi-Fermi levels at the solid/liquid interface. Since it can be shown both experimentally,[4] and through digital simulation methods of the steady state response (*vide infra*), that the potentials measured at the back of the sample are within <2 meV of those at the semiconductor/liquid contact under the experimental conditions used herein, it can be concluded that the data of Figures 2.4 and 2.5 yield direct measurements of the behavior of the quasi-Fermi levels at these semiconductor/liquid junctions.

Figure 2.6: (a) Comparison of the interfacial current density vs quasi-Fermi level relationships for the Si/CH_3OH-1.0 M $LiClO_4$-103 mM Me_2Fc-12 mM Me_2FcBF_4 ($E(A/A^-)$ = 170 mV vs SCE) contact. The solid circles depict the J_{n+} vs V_{n+} behavior while the open diamonds illustrate the relationship between a given interfacial hole flux, J_{p+}, (established by controlling V_{p+}) and the open-circuit potential developed at the n^+ points, $V_{n+,oc}$. Similarly, the solid squares represent the J_{p+} vs V_{p+} data while the open triangles show the J_{n+} vs $V_{p+,oc}$ relationship. (b) Plot analogous to (a) for the Si/CH_3OH-0.90 M LiCl-14 mM $CoCp_2$-8.0 mM $CoCp_2Cl$ ($E(A/A^-)$ = -915 mV vs SCE) contact. The symbols have the same meaning as in (a).

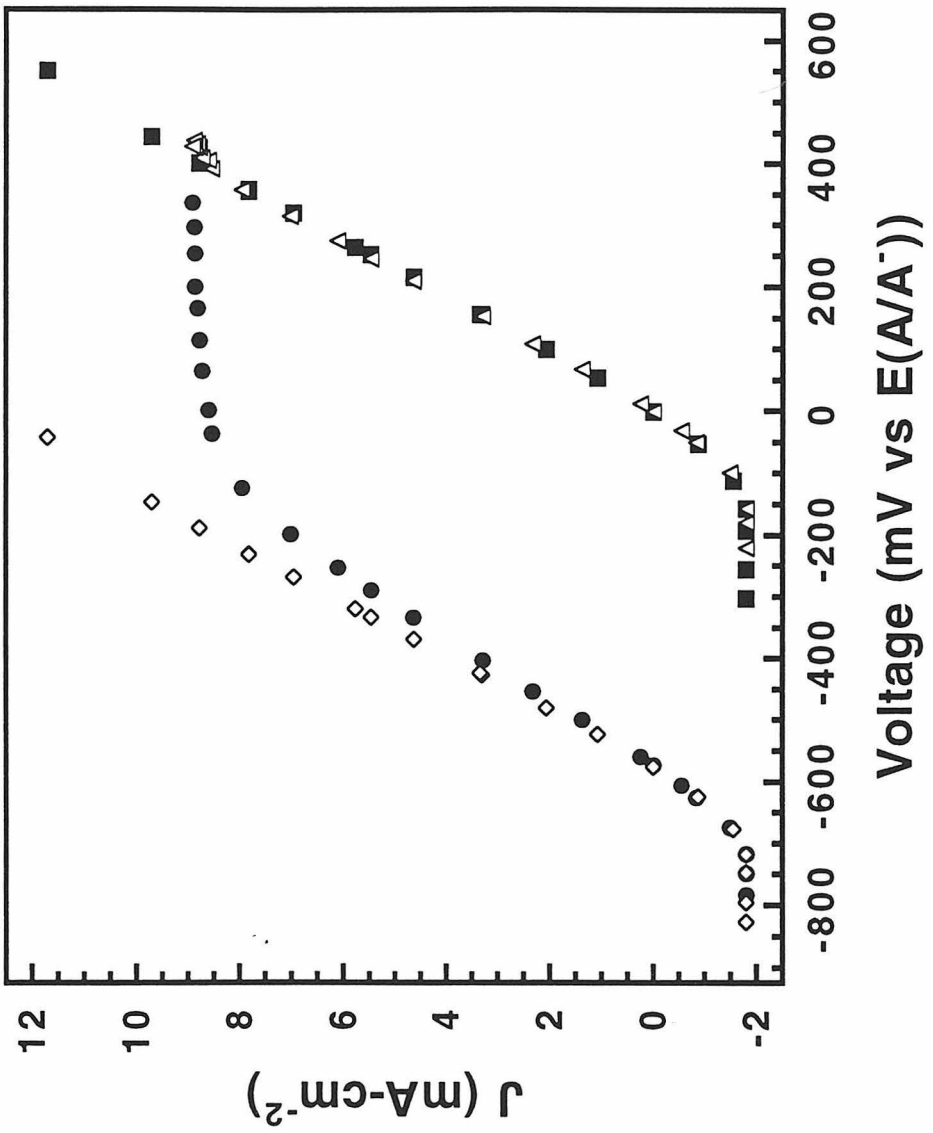
J (mA-cm⁻²)
12
10
8
6
4
2
0
-2
-800
-600
-400
-200
0
200
400
600
Voltage (mV vs E(A/A⁻))

Figure 2.6a

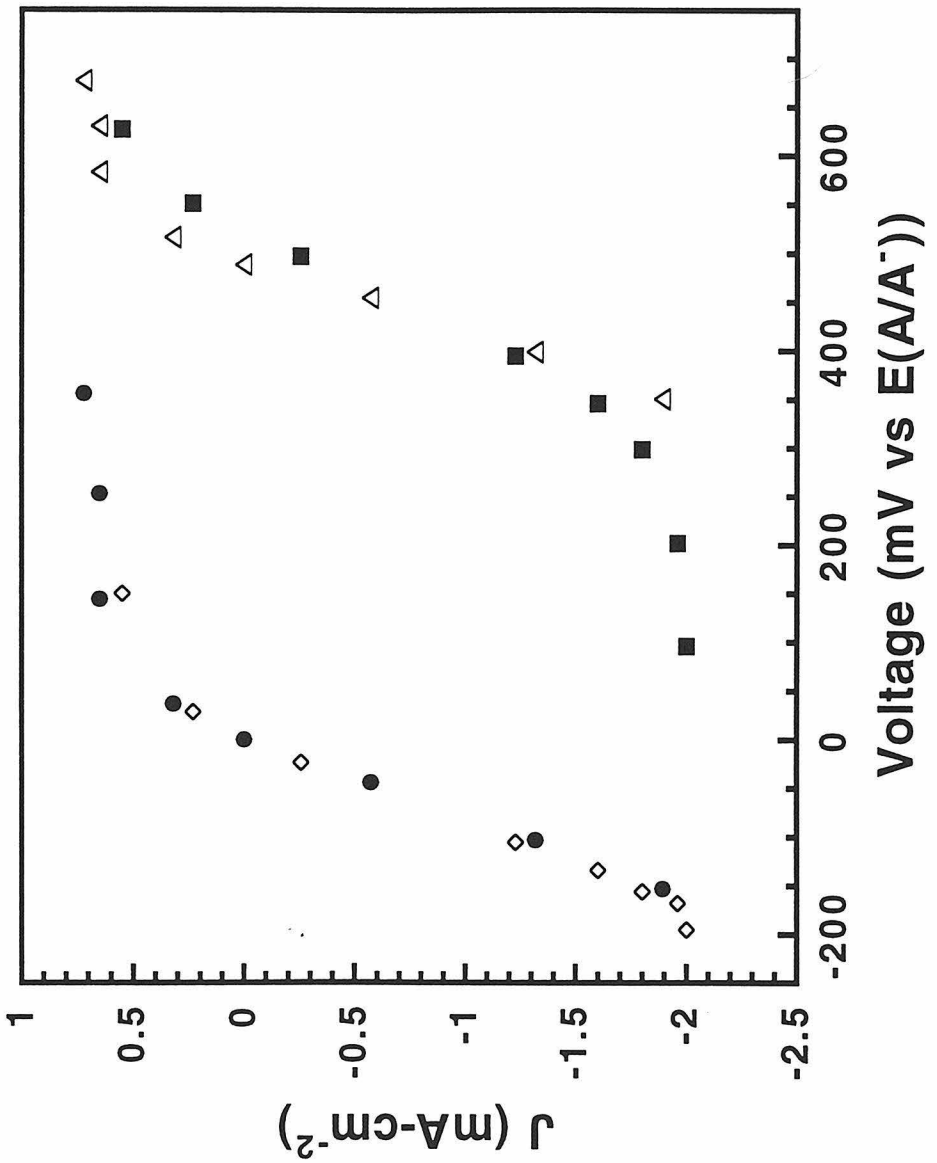

Figure 2.6b

C. Digital Simulation of the Quasi-Fermi Level Behavior of Si/Liquid Contacts Under Applied Bias

1. Simulations of the Quasi-Fermi Level Behavior of Si/CH_3OH-$Me_2Fc^{+/0}$ Contacts

A more complete, quantitative understanding of the data presented in Section IV.A.2 can be obtained by reference to the steady-state quasi-Fermi level profiles computed using a digital simulation of the solid/liquid junction. The ToSCA program provided an opportunity to perform a detailed simulation of the carrier generation, recombination, and transport processes in these samples, while incorporating constraints due to Poisson's equation along with boundary conditions that were appropriate for the back and front surfaces of the Si photoelectrodes studied experimentally in this work. Since the simulation program produced steady-state potentials and carrier concentration profiles as a function of distance from the solid/liquid interface (Figures 2.2a-c), it was used to confirm the qualitative arguments advanced above regarding the behavior of the quasi-Fermi levels under various combinations of applied bias and redox potential conditions. In addition, the simulations yielded insight into the behavior of the quasi-Fermi levels under strong reverse bias that were observed experimentally and into other aspects of the J-V data that have not been addressed in the preceding analysis.

Simulations were carried out for Si/$Me_2Fc^{+/0}$, Si/$MV^{2+/+}$ and Si/$CoCp_2^{+/0}$ solid/liquid contacts. The input photon intensity (i.e., the steady-state charge carrier generation rate) was chosen to produce good agreement between the simulated and experimentally measured steady-state current densities (3.5 mA cm^{-2}) and open circuit voltages. Simulations were performed for a series of applied voltages ranging from forward biases larger than V_{oc} to voltages well into reverse bias. At each potential, the carrier concentrations, semiconductor band edge energies, and quasi-Fermi levels were computed as a function of position in the semiconductor.

Figure 2.7a depicts the computed J_{n+} vs V_{n+} behavior of the Si/CH_3OH-$Me_2Fc^{+/0}$ contact along with the computed $V_{p+,oc}$ vs V_{n+} relationship of this system. This simulation

represented a limiting case in which $\mathbf{E}(A/A^-)$ was close to one of the band edge positions, ($\mathbf{E}(A/A^-)$ is near $\mathbf{E}_v$ in this particular situation). The simulations were able to reproduce the general form of the experimental data. At the open circuit potential, ($V_{n+} \approx$ -0.6 V) $V_{p+,oc}$ is calculated to be 0 V, in accord with experimental observations. As V_{n+} moved positively from $V_{n+,oc}$ towards reverse bias, the current density increased until it reached a plateau in which J_{n+} was limited by the photogenerated carrier flux. For this same potential regime, the simulations showed that the hole concentration at the electrode surface, and thus the interfacial hole flux into the solution ($J_{p,f}$), increased as J_{n+} increased. In this region of control over V_{n+}, the value of $V_{p+,oc}$ increased only slightly (3 mV) in the simulation relative to its value at open circuit (of 0 V vs the Nernstian potential of the cell, $E(A/A^-)$). In further reverse bias, the computed J_{n+} was independent of V_{n+}, and the computed $V_{p+,oc}$ also became independent of V_{n+}. The lack of change in $V_{p+,oc}$ when J_{n+} is constant is in accord with the experimental data. However, the experimental $V_{p+,oc}$ value for the $Si/CH_3OH\text{-}Me_2Fc^{+/0}$ contact increased monotonically with increasing reverse bias until reaching a value of $\approx$0.4 V vs $E(A/A^-)$ (Figure 2.4a). The difference between the simulated and observed plateau value of $V_{p+,oc}$ is readily explained by the lack of incorporation into the simulation routine of concentration polarization and series resistance losses in the solution, whereas the actual photoelectrochemical cell must experience these overpotentials in order to sustain a net interfacial current flow. The self-consistency between the independently measured concentration polarization/series resistance losses for holes evident in the J_{p+} vs V_{p+} plots and those reflected in the $V_{p+,oc}$ vs V_{n+} behavior (Figure 2.4a) clearly indicates that these factors are responsible for the difference between the simulated behavior and the experimental data.

Figures 2.7b,c display the quasi-Fermi level profiles of electrons and holes and the electric potential profiles vs distance that were computed for representative values of V_{n+} in each of these regions of $V_{p+,oc}$ vs V_{n+} behavior. These profiles represent two sections through the semiconductor, both of which are perpendicular to the surface and pass

through the center of the n^+ and p^+ contacts. In both cases, the simulations verified that the quasi-Fermi levels were essentially flat across the sample, so the values at the edges of the point contacts provided reliable estimates of the values of the quasi-Fermi levels at the solid/liquid interface. The simulations also verified the qualitative relationships discussed above between $V_{p+,oc}$ and V_{n+}. In essence, the value of n_s was set by the potentiostatically controlled value of V_{n+}, and the hole concentration at the electrode surface adjusted so that the condition $J_{p,f}=J_{n+}$ was met. In this fashion, changes in V_{n+} for the Si/CH_3OH-$Me_2Fc^{+/0}$ contact effected changes in $V_{p+,oc}$ through the constraint that $J_{p,f}=J_{n+}$, thereby linking the electron and hole quasi-Fermi levels and producing simulated electrode behavior in excellent accord with the experimental data.

The simulation of the Si/CH_3OH-$Me_2Fc^{+/0}$ contact also addressed another aspect of the $V_{p+,oc}$ vs V_{n+} properties in that it predicted a third region of $V_{p+,oc}$ vs V_{n+} behavior. As mentioned earlier, the experimental value of $V_{p+,oc}$ became linearly dependent on V_{n+} at large positive V_{n+} values. This is an interesting result because J_{n+} is constant in this region, so the interfacial hole flux should have remained constant as V_{n+} varied. The experimental behavior was indeed obtained from the digital simulation results. There are two possible reasons for such $V_{p+,oc}$ vs V_{n+} behavior: a) as V_{n+} is increased, a shift in the band edges occurs as excess holes are built up at the solid/liquid interface, producing a voltage drop that would be reflected in the value of $V_{p+,oc}$ measured at the back surface of the semiconductor, and/or b) the quasi-Fermi levels are no longer flat across the sample so that a change in $V_{p+,oc}$ does not necessarily correspond to a change in the surface concentration of holes (dictating $J_{p,f}$). The digital simulation clearly showed that the quasi-Fermi levels are no longer constant across the sample at large reverse biases (Figure 2.7d). Additionally, neither a significant change in the band edge position at the solid/liquid interface, nor a significant increase in the hole concentration at the semiconductor surface, was computed in the simulation. Thus, this third region of $V_{p+,oc}$ vs V_{n+} behavior is evidently an inherent feature of the samples and did not require an excess charge buildup or

slow interfacial kinetics to produce a large voltage drop across the Helmholtz layer. This aspect of the $V_{p+,oc}$ vs V_{n+} behavior required the detailed digital simulation to be evaluated quantitatively.

2. Simulations of the Quasi-Fermi Level Behavior of Si/CH_3OH-$MV^{2+/+}$ Contacts

Digital simulations were also performed on a representative Si/liquid contact for which the electrochemical potential of the solution was located near the middle of the Si band gap. Figure 2.7e shows the calculated J_{n+} vs V_{n+} behavior along with the $V_{p+,oc}$ vs V_{n+} data for the Si/CH_3OH-$MV^{2+/+}$ system. In Figures 2.7f-h, the quasi-Fermi level profiles and electric potential profiles along lines perpendicular to the surface and through the centers of the two selective ohmic back contacts are displayed for representative V_{n+} values for this junction. The computed behavior was similar to that of the Si/CH_3OH-$Me_2Fc^{+/0}$ system, but displayed a few significant differences. First, when the n^+ points were at their open circuit potential, the computed quasi-Fermi level for holes was not equal to the Nernstian potential of the solution ($V_{p+,oc} \neq 0$) (Figure 2.7e). This behavior is in accord with the experimental observations (Figure 2.4b above and Table 2.2), and indicates that the surface concentration of holes required to reach open circuit at the specified light intensity is larger than the equilibrium hole concentration at the surface ($p_s/p_{so} > 1$). This is in contrast to the situation for redox couples having $\mathbf{E}(A/A^-)$ close to one band edge, in which the current is almost completely due to the transfer of one carrier type.

A second difference between the simulated behavior of the Si/CH_3OH-$MV^{2+/+}$ and Si/CH_3OH-$Me_2Fc^{+/0}$ contacts was the delayed onset of the region at reverse bias in which $V_{p+,oc}$ increased with more positive values of V_{n+}. This change in the $V_{p+,oc}$ vs V_{n+} behavior occurred despite no change in the light-limited value of J_{n+} over this range of V_{n+} values. As shown in Figure 2.8, the simulations revealed that the value of V_{n+} at which this behavior occurred depended strongly on the value of the interfacial hole transfer rate constant in the system. This behavior is readily understood by reference to the quasi-Fermi level profiles depicted in Figure 2.7f-h. Relatively large interfacial charge transfer rate

constants required relatively low hole concentrations at the electrode surface to produce the desired interfacial hole flux. Thus, for large k_v^{max} values, the value of $V_{p+,oc}$ did not deviate greatly from its equilibrium value for moderate values of V_{n+}. However, further increases in V_{n+} resulted in the quasi-Fermi levels varying across the semiconductor sample, and this produced significant changes in $V_{p+,oc}$. In contrast, small k_v^{max} values required a significant increase in the concentration of holes at the surface as well as in the bulk, and thus (i) extended the range over which the $V_{p+,oc}$ increased with more positive V_{n+} values and (ii) increased the value of $V_{p+,oc}$ in the plateau region indicating that the surface concentration of holes is larger under such conditions than would be required with larger values of k_v^{max} .

3. Simulations of the Quasi-Fermi Level Behavior of Si/CH_3OH-$CoCp_2^{+/0}$ Contacts

An analogous set of simulations was performed for Si/CH_3OH-$CoCp_2^{+/0}$ contacts. For this system, the J_{p+} vs V_{p+} behavior under illumination was modeled along with the V_{p+} vs $V_{n+,oc}$ relationship (not shown). In almost all aspects, the simulated plots exhibited features that were analogous to those computed for Si/CH_3OH-$Me_2Fc^{+/0}$ contacts except that the currents were of opposite sign. In the region where the photocurrent was dependent on the applied potential, the value of $V_{n+,oc}$ was calculated to be linearly dependent on V_{p+}. In the region where the photocurrent was constant with potential, no further increase in the surface electron concentration was required to fulfill the constraint $J_{n,f} = J_{p+}$, and, therefore, no further negative shift in $V_{n+,oc}$ was calculated until the value of the V_{p+} was negative enough that the quasi-Fermi levels start to bend.

The digital simulations also reproduced the experimentally observed behavior that at a constant light intensity, the quasi-Fermi level separation, $qV_{p+,oc} - qV_{n+,oc}$, was greatest for systems having a redox potential near either the conduction band edge or valence band edge. Smaller $V_{p+,oc} - V_{n+,oc}$ values, and therefore more total recombination, were observed for the two redox couples having $E(A/A^-)$ nearer the middle of the semiconductor band gap (Table 2.2). The computer simulations also showed that the energy bands were

flat at V_{oc} for redox couples having electrochemical potentials near the middle of the band gap. On the other hand, if the electrochemical potential of the solution is close to one of the energy band edges, the simulations showed a residual electrical field at V_{oc} even under the high level injection conditions applied in the experiments.

Figure 2.7: Results of 2-dimensional computer simulations for the n-Si/$Me_2Fc^{+/0}$ (a)-(d) and n-Si/$MV^{2+/+}$ systems (e)-(h).

(a) The current density-voltage curve (solid circles) for the $Me_2Fc^{+/0}$ contact is shown along with the calculated open circuit voltages at the p^+-points (open squares) when the potential is applied to the n^+ points. The rate constants for the electron and hole transfer were assumed to be equal, with $k_{ct}^{max} = 10^{-18}$ cm^4 s^{-1}. The concentrations were c_{red}=110 mM and c_{ox}=16 mM, and the barrier height of the contact was 1.0 V.[37,42-47] (b)-(d) Profiles of the quasi-Fermi levels (open circles depict $\mathbf{E}_{F,n}$ and open diamonds depict $\mathbf{E}_{F,p}$) and of the conduction and valence band (solid squares depict $\mathbf{E}_c$ and solid triangles depict $\mathbf{E}_v$) along a cut perpendicular to the surface and passing through the center of the n^+ points. The solid lines represent a corresponding cut through the center of the p^+ points.

(e) The current density-voltage curve for the $MV^{2+/+}$ contact is shown along with the calculated open circuit voltages at the p^+ points when the potential is applied to the n^+ points. The rate constants for the electron and hole transfer were assumed to be equal, with $k_{ct}^{max} = 10^{-18}$ cm^4 s^{-1}. The concentrations were c_{red}=10 mM and c_{ox}=21 mM, and the barrier height of the contact was 0.5 V.[48] (f)-(h) Profiles of the quasi-Fermi levels and of the conduction and valence band along a cut perpendicular to the surface and passing through the center of the n^+ points. The symbols have the same meaning as in (b)-(d), and the solid lines represent a corresponding cut through the center of the p^+ points.

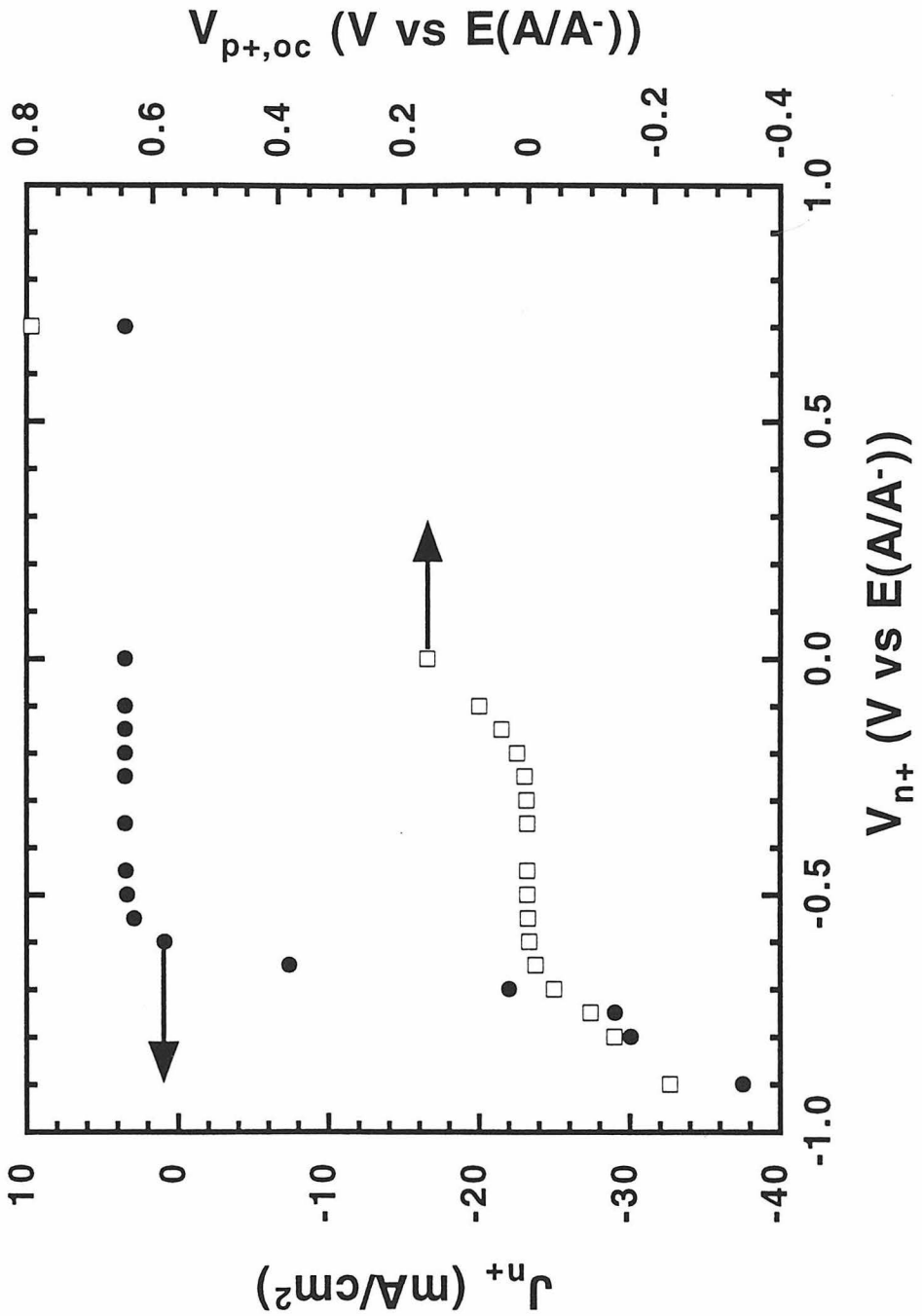
$V_{p+,oc}$ (V vs E(A/A$^-$))
0.8
0.6
0.4
0.2
0
-0.2
-0.4
10
0
-10
-20
-30
-40
J_{n+} (mA/cm^2)
-1.0
-0.5
0.0
0.5
1.0
V_{n+} (V vs E(A/A$^-$))

Figure 2.7a

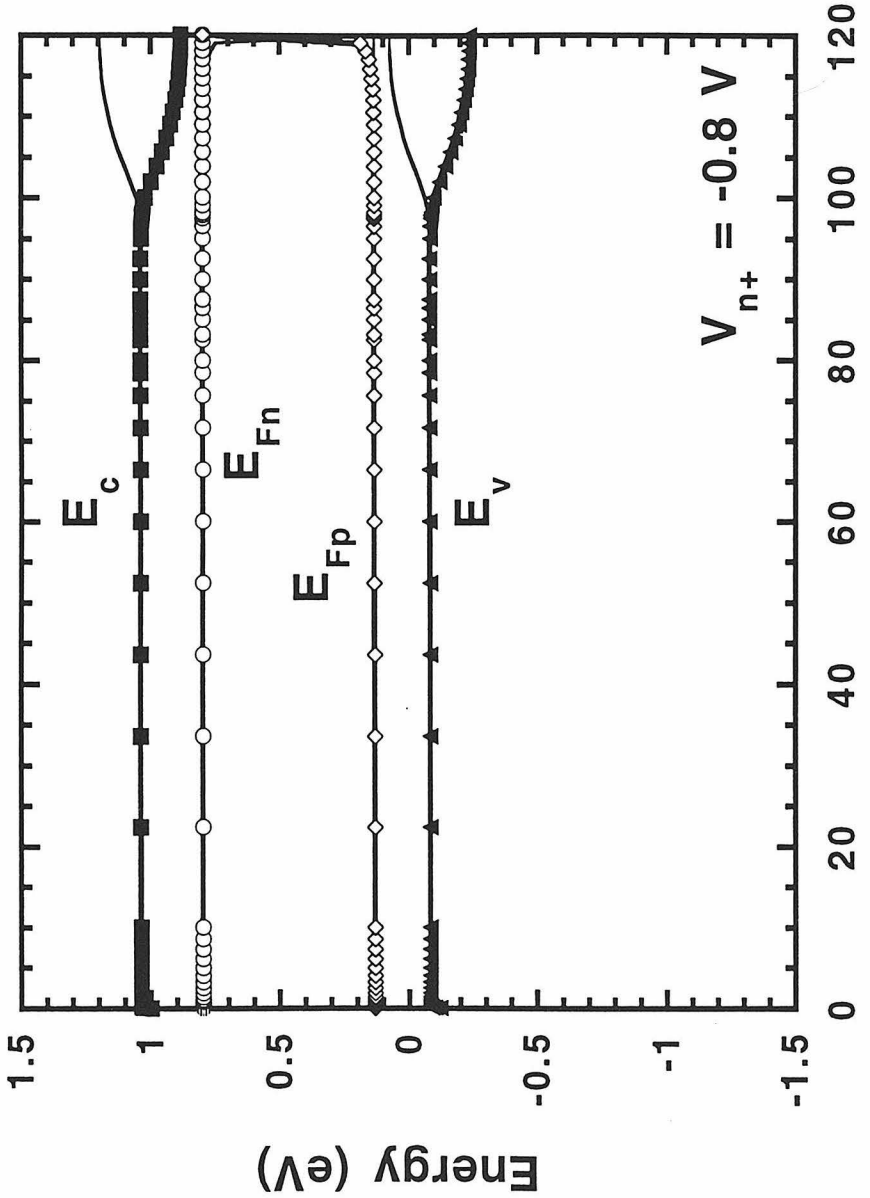
Energy (eV)
1.5
1
0.5
0
-0.5
-1
-1.5
0
20
40
60
80
100
120
Distance (10^{-4} cm)
E_c
E_{Fn}
E_{Fp}
E_v
V_{n+} = -0.8 V

Figure 2.7b

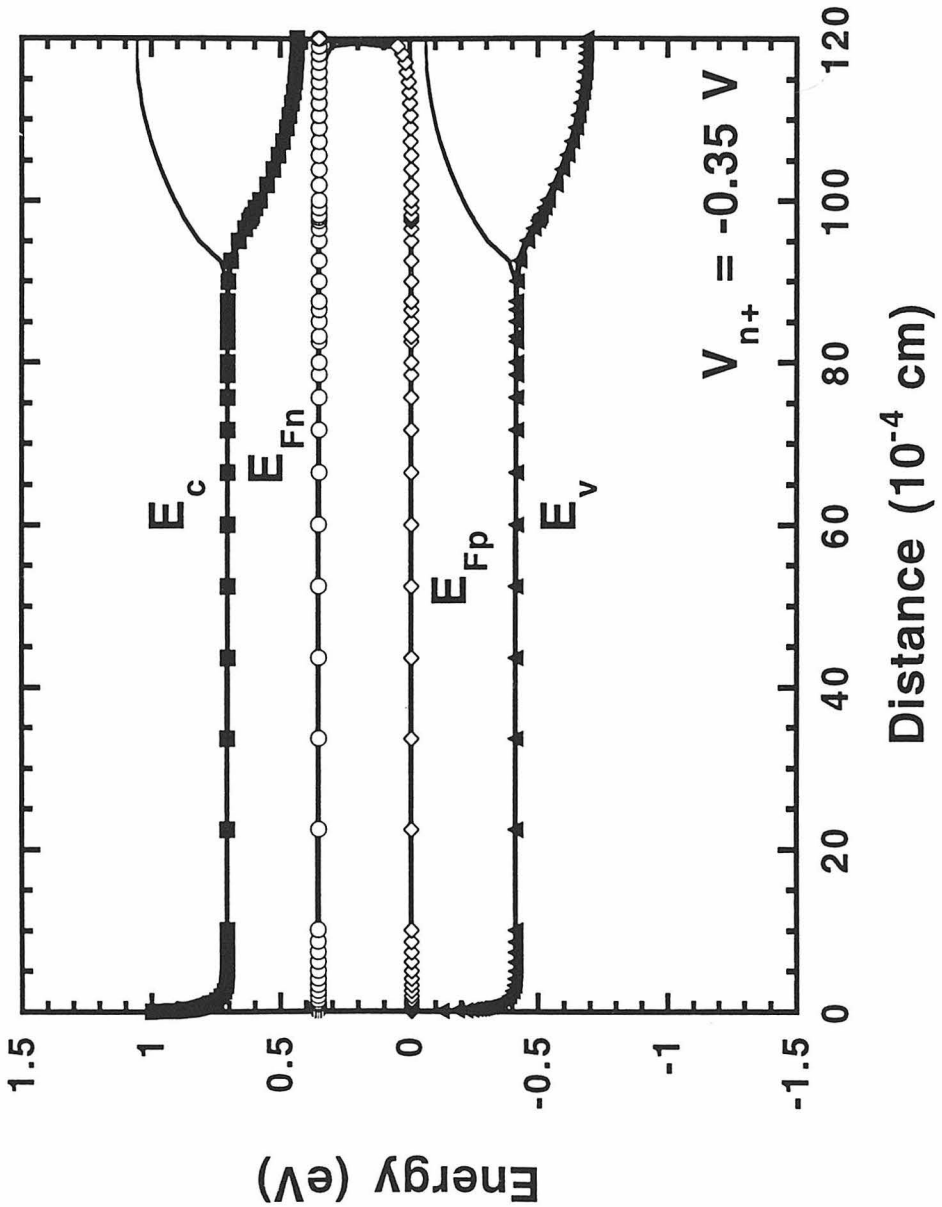
Energy (eV)
1.5
1
0.5
0
-0.5
-1
-1.5
0
20
40
60
80
100
120
Distance (10^{-4} cm)
E_c
E_{Fn}
E_{Fp}
E_v
V_{n+} = -0.35 V

Figure 2.7c

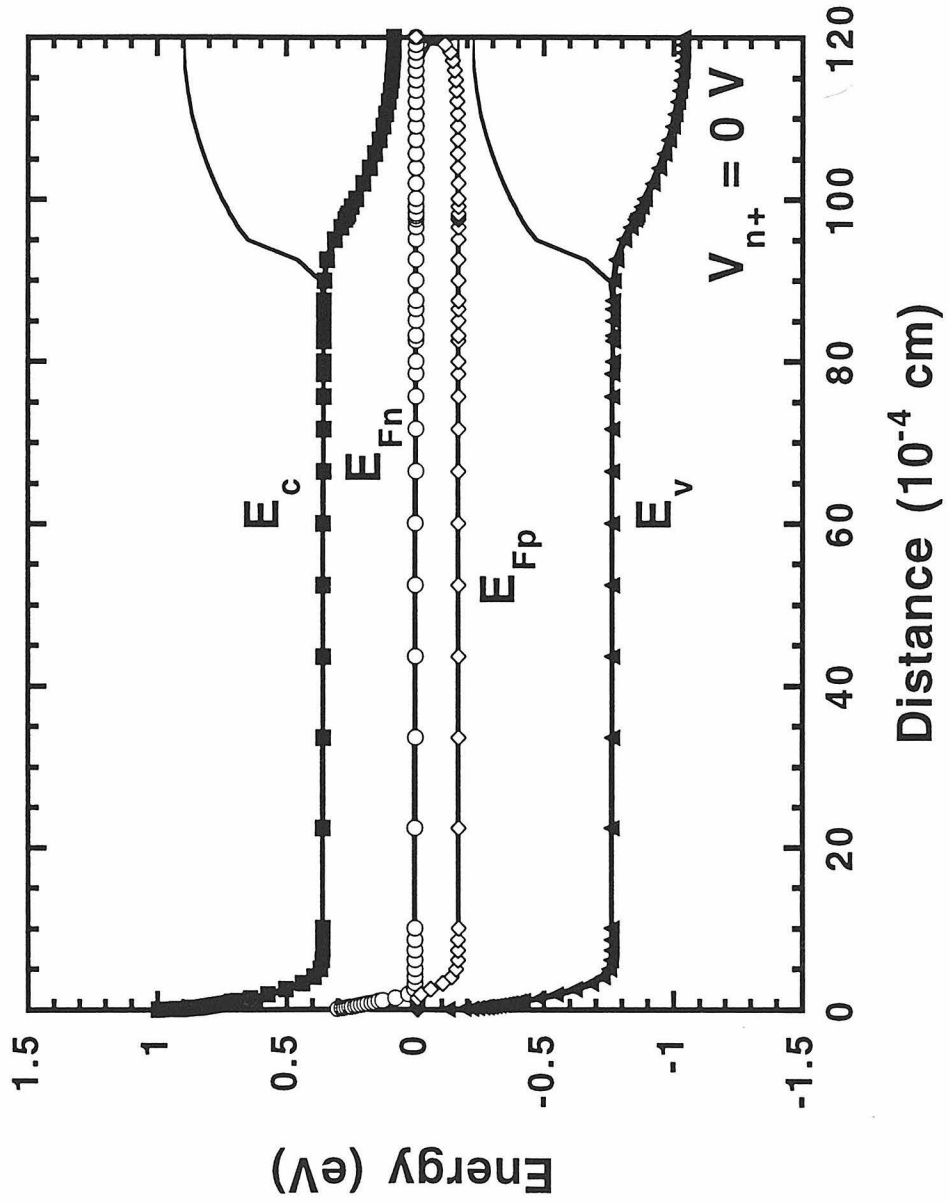
Energy (eV)
1.5
1
0.5
0
-0.5
-1
-1.5
0
20
40
60
80
100
120
Distance (10^{-4} cm)
E_c
E_{Fn}
E_{Fp}
E_v
V_{n+} = 0 V

Figure 2.7d

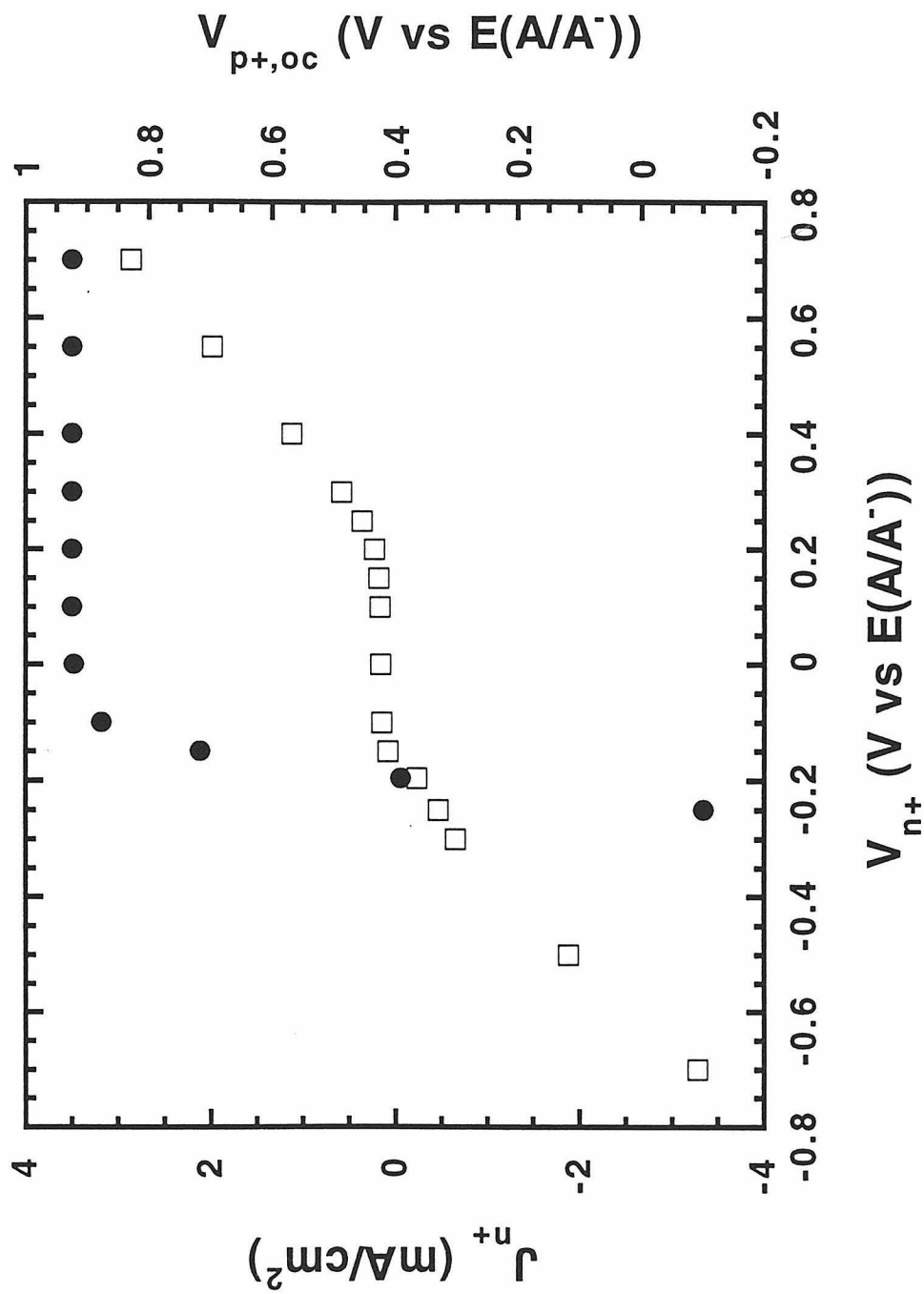
$V_{p+,oc}$ (V vs E(A/A$^-$))
1
0.8
0.6
0.4
0.2
0
-0.2
4
2
0
-2
-4
J_{n+} (mA/cm^2)
-0.8
-0.6
-0.4
-0.2
0
0.2
0.4
0.6
0.8
V_{n+} (V vs E(A/A$^-$))

Figure 2.7e

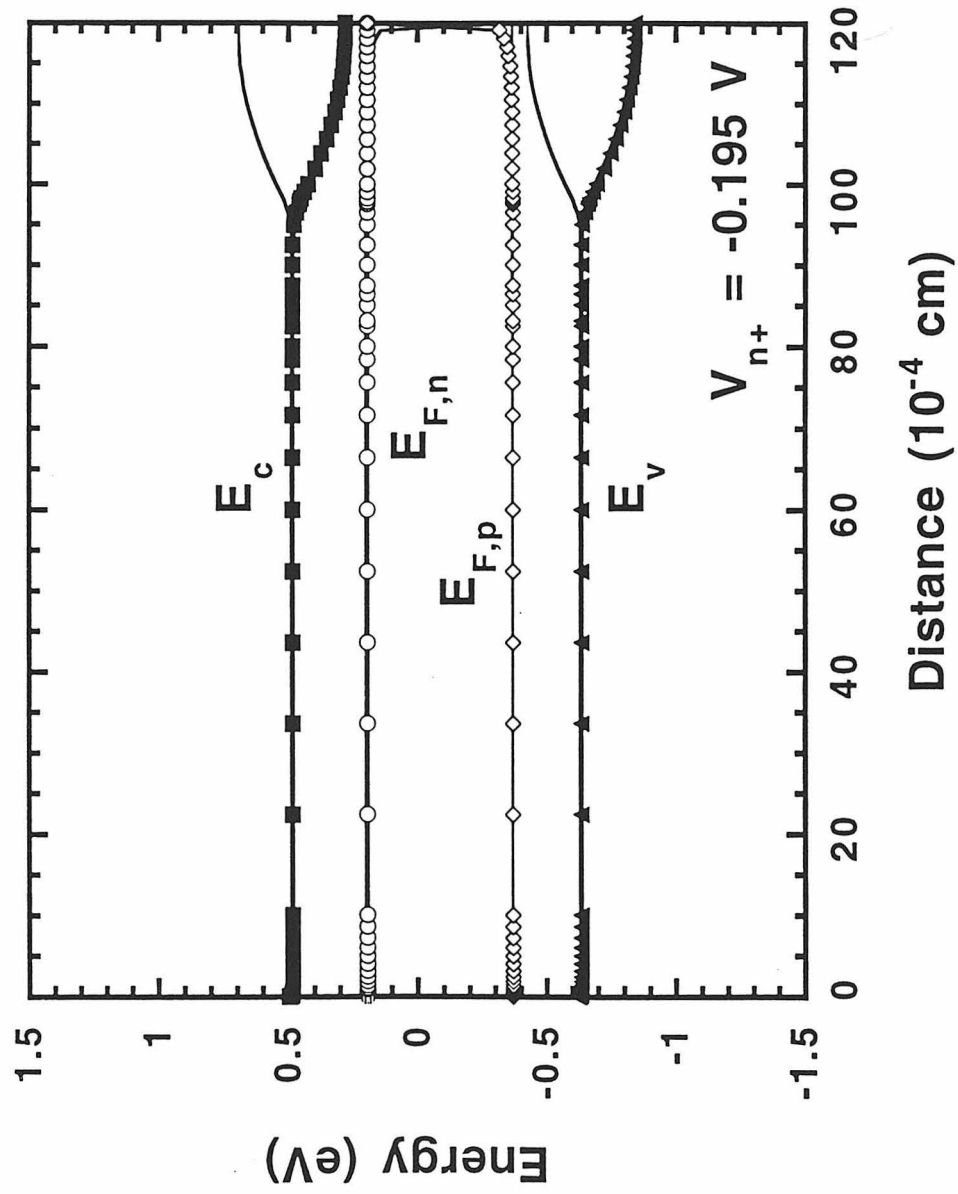
Energy (eV)
1.5
1
0.5
0
-0.5
-1
-1.5
0
20
40
60
80
100
120
Distance (10^{-4} cm)
E_c
$E_{F,n}$
$E_{F,p}$
E_v
V_{n+} = -0.195 V

Figure 2.7f

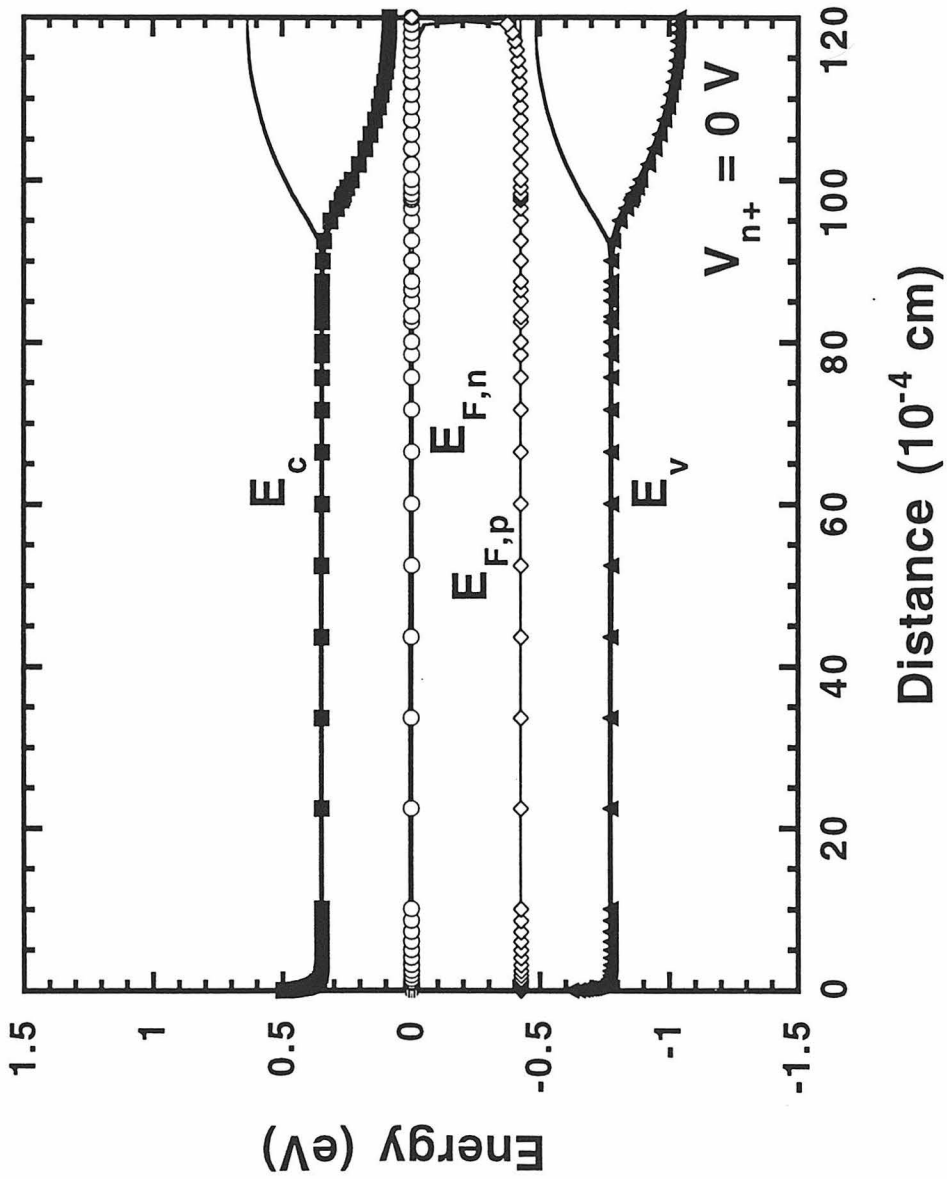
Energy (eV)
1.5
1
0.5
0
-0.5
-1
-1.5
0
20
40
60
80
100
120
Distance (10^{-4} cm)
E_c
$E_{F,n}$
$E_{F,p}$
E_v
V_{n+} = 0 V

Figure 2.7g

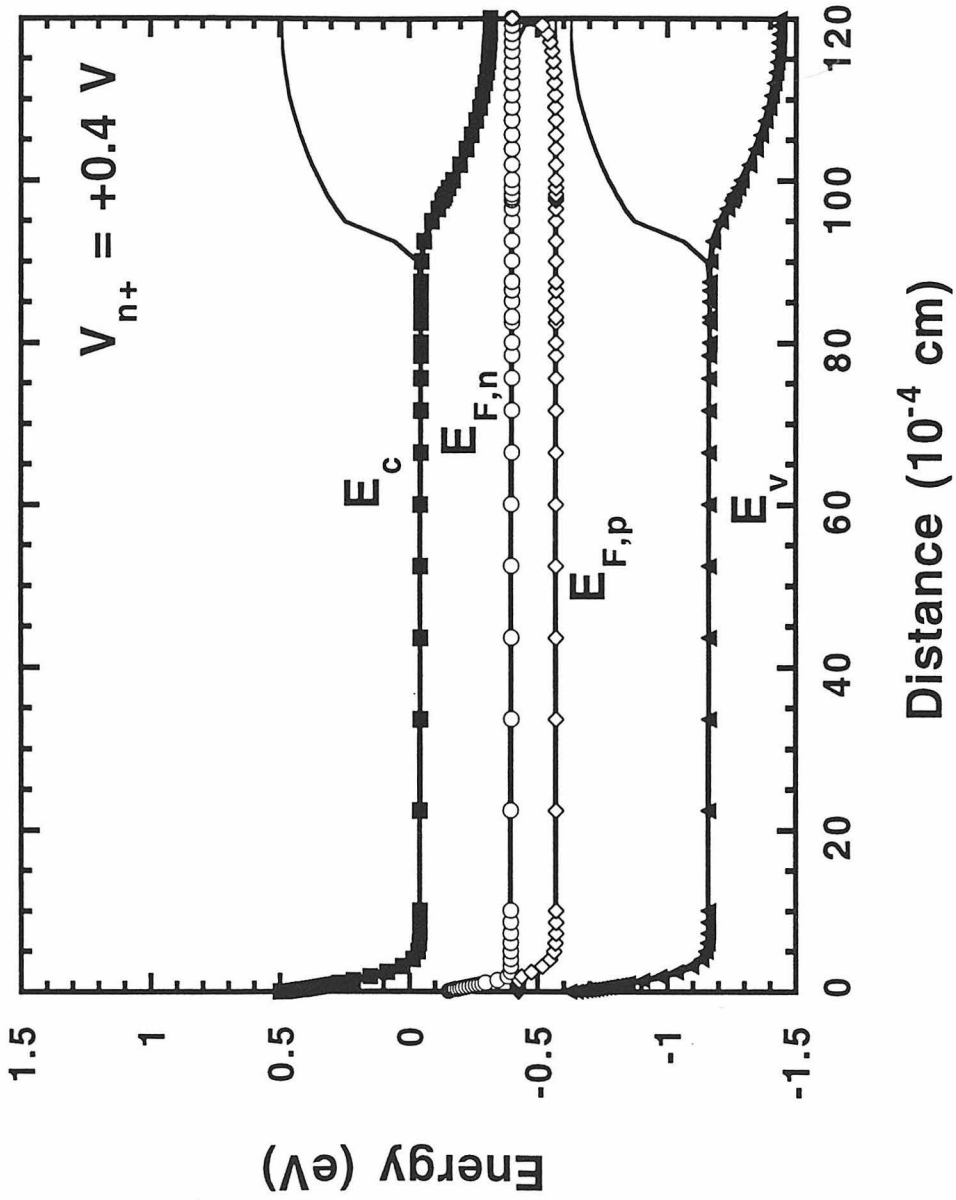
V_n+ = +0.4 V
E_c
E_F,n
E_F,p
E_v
Energy (eV)
Distance (10^-4 cm)
1.5
1
0.5
0
-0.5
-1
-1.5
0
20
40
60
80
100
120

Figure 2.7h

Figure 2.8: Results of one-dimensional computer simulations for the n-Si/$MV^{2+/+}$ system demonstrating the dependence of the quasi-Fermi level of the holes (open circuit potential at the p^+ points) on the quasi-Fermi level of electrons (potential is applied at the n^+ points) for three different charge transfer rate constants, k_{ct}^{max} (filled circles: 10^{-16} cm^4 s^{-1}, open squares: 10^{-18} cm^4 s^{-1}, filled triangles: 10^{-20} cm^4 s^{-1}). It should be noted that in ToSCA the physicists' definition of the electric potential is used. In each case the rate constants for the electron and hole transfer were assumed to be equal (k_{ct}^{max}). The concentrations were c_{ox}=21 mM and c_{red}=10 mM, and the barrier height of the contact was Φ_b= 0.5 eV.[48]

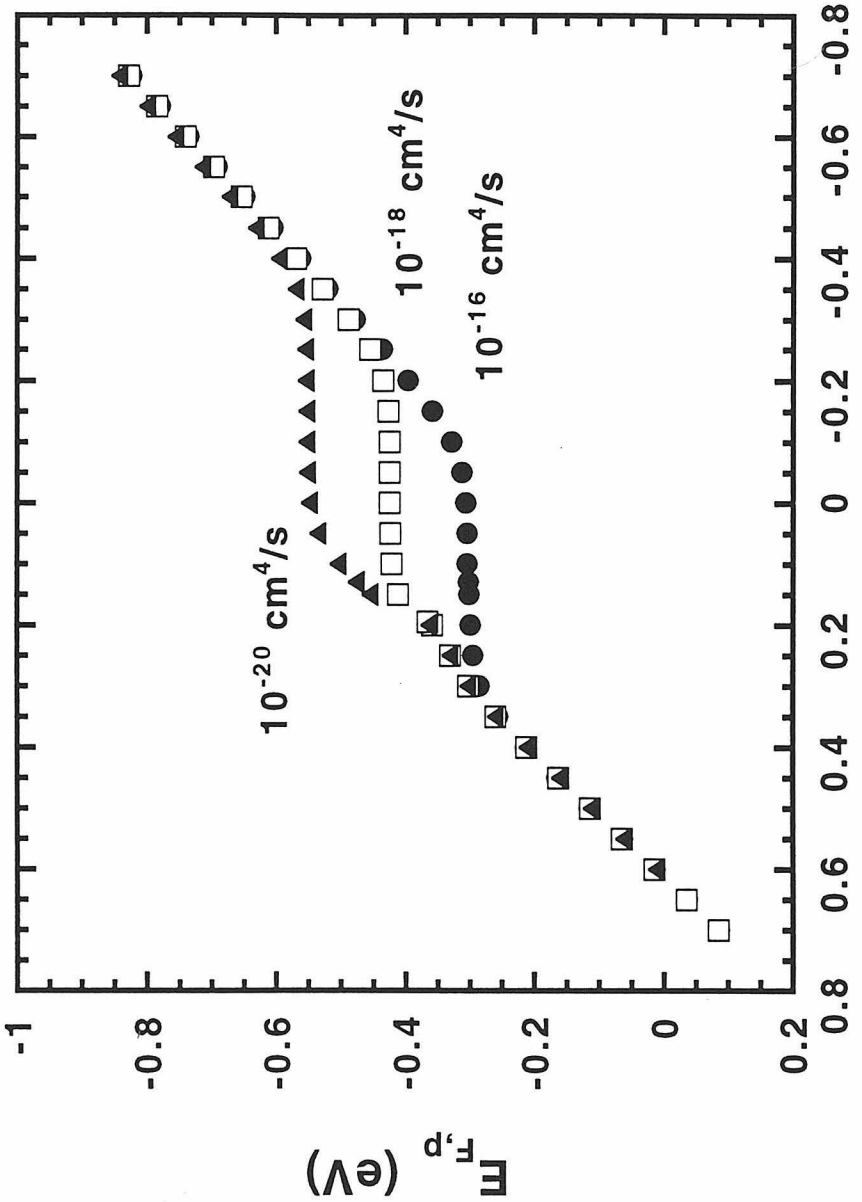
10^{-20} cm^4/s
10^{-18} cm^4/s
10^{-16} cm^4/s
$E_{F,p}$ (eV)
$E_{F,n}$ (eV)
-1
-0.8
-0.6
-0.4
-0.2
0
0.2
0.4
0.6
0.8

Figure 2.8

4. The Quasi-Fermi Level Behavior of Systems Exhibiting Nonrectifying J-V Behavior Under Illumination

The quasi-Fermi level behavior observed at the n^+ points during potentiostatic control over the p^+ potential at Si/CH_3OH-$Me_2Fc^{+/0}$ interfaces (Figure 2.5a), and at the p^+ points during potentiostatic control of the n^+ points for Si/CH_3OH-$CoCp_2^{+/0}$ contacts (Figure 2.4d), was also revealed by the digital simulations. Hole transfer with the valence band has already been identified as the dominant interfacial current flow at the Si/CH_3OH-$Me_2Fc^{+/0}$ contact.[7,76] Thus, removing an electron from the back of these intrinsic Si samples results in hole transfer into the solution at this solid/liquid interface. Nevertheless, when holes are removed at the back p^+ contact, the value of the electron quasi-Fermi level was observed to shift, even though holes, not electrons, were injected across the solid/liquid contact. The digital simulation revealed that this unexpected behavior arose because, under these specific circumstances, the quasi-Fermi levels were not flat across the sample. Instead, the measured value of V_{n+} at the back of the sample did not accurately reflect the potential corresponding to the electron quasi-Fermi level position at the solid/liquid contact. Thus, the dependence of $V_{n+,oc}$ on the value of V_{p+} is a consequence of the experimental contact geometry in the sample, and does not imply that manipulation of the hole concentration at the p^+ points produced interfacial electron transfer or a change in the value of the electron quasi-Fermi level at the Si/CH_3OH-$Me_2Fc^{+/0}$ contact.

The behavior observed at the p^+ points during potentiostatic control of the n^+ points for the Si/CH_3OH-$CoCp_2^{+/0}$ system was analogous to that seen in the reverse contact configuration for Si/CH_3OH-$Me_2Fc^{+/0}$ contact. The hole quasi-Fermi level position was affected by changes in bias at the n^+ points even though the interfacial current in this system is completely dominated by electron transfer with the conduction band. While this behavior is similar to that observed for Si/CH_3OH-$Me_2Fc^{+/0}$ interfaces, digital simulations revealed the underlying physical phenomena to be different. For the Si/CH_3OH-$CoCp_2^{+/0}$ system, the quasi-Fermi levels were calculated to remain flat across the sample but a

monotonic shift was predicted to occur in the band edge positions as a function of the applied potential. This information was both interesting and satisfying because such shifts in V_{n+} as V_{p+} was varied were unexpected but were correctly accounted for by the simulation package. This agreement between experiment and simulation provided confidence that the properties of the semiconductor/liquid contact were being accounted for correctly by the simulation routine.

5. Correlations Between the Back Contact Fluxes and Fluxes at the Semiconductor/Liquid Junction

The simulations for the systems having $\mathbf{E}(A/A^-)$ close to one of the energy band edges of the semiconductor are summarized in Figure 2.9. The results confirm the experimental observations presented in Figure 2.6. If the overall charge transfer at the solid/liquid interface is dominated by one carrier type (e.g. electron transfer between the $CoCp_2^{+/0}$ redox couple and the silicon conduction band) the potential at the corresponding (n^+) point back contact represents a measure of the concentration of that carrier at the electrode surface, and thus is directly related to the current density at the front contact ($J_{n,f} >> J_{p,f}$, eqs 2.17 and 2.18). The observations and simulations presented herein therefore confirm that the current density of each carrier type at the solid/liquid contact is identical for a given carrier potential, regardless of whether the potential of interest is obtained by applying a bias to the back of the semiconductor, and thus directly influencing the carrier of concern, or whether the other carrier type is controlled potentiostatically, indirectly producing a flux of the probed carrier type at the solid/liquid contact.

These results are fully consistent with the quasi-Fermi level concept that has been used by Memming and co-workers previously to describe processes in semiconductor photoelectrochemistry.[13,14,77] In earlier work, a comparison between reaction rates at n-type and p-type electrodes was required in order to investigate experimentally the applicability of the quasi-Fermi level concept. In the present study, the use of high purity, low dopant density Si electrodes with ohmic selective back contacts has allowed the direct

measurement of the quasi-Fermi levels individually and simultaneously for a single semiconductor/liquid junction. This feature has allowed us to explore several aspects of quasi-Fermi level behavior that have not been probed previously. In general, the results described herein have validated the basic applications of the quasi-Fermi level concepts, at open circuit and under applied bias conditions, for both carrier types, in these Si/CH_3OH junctions photoelectrochemical cell.

Figure 2.9: (a) Results of two-dimensional computer simulations for the n-Si/$Me_2Fc^{+/0}$ system: Comparison of the interfacial current density vs quasi-Fermi level relationships. The rate constants for the electron and hole transfer were assumed to be equal k_{ct}^{max} = 10^{-18} cm^4 s^{-1}. The concentrations were c_{ox}=16 mM and c_{red}=110 mM, and the barrier height of the contact was 1.0 V.[37,42-47] The meanings of the symbols are given in the inset.

(b) Plot analogous to (a) for the n-Si/$CoCp2^{+/0}$ system: The rate constants for the electron and hole transfer were assumed to be equal, with k_{ct}^{max} = 10^{-18} cm^4 s^{-1}. The concentrations were c_{red}=2 mM and c_{ox}=45 mM, and the energy difference between the conduction band and the electrochemical potential of the solution was taken to be 0.12 eV.[48]

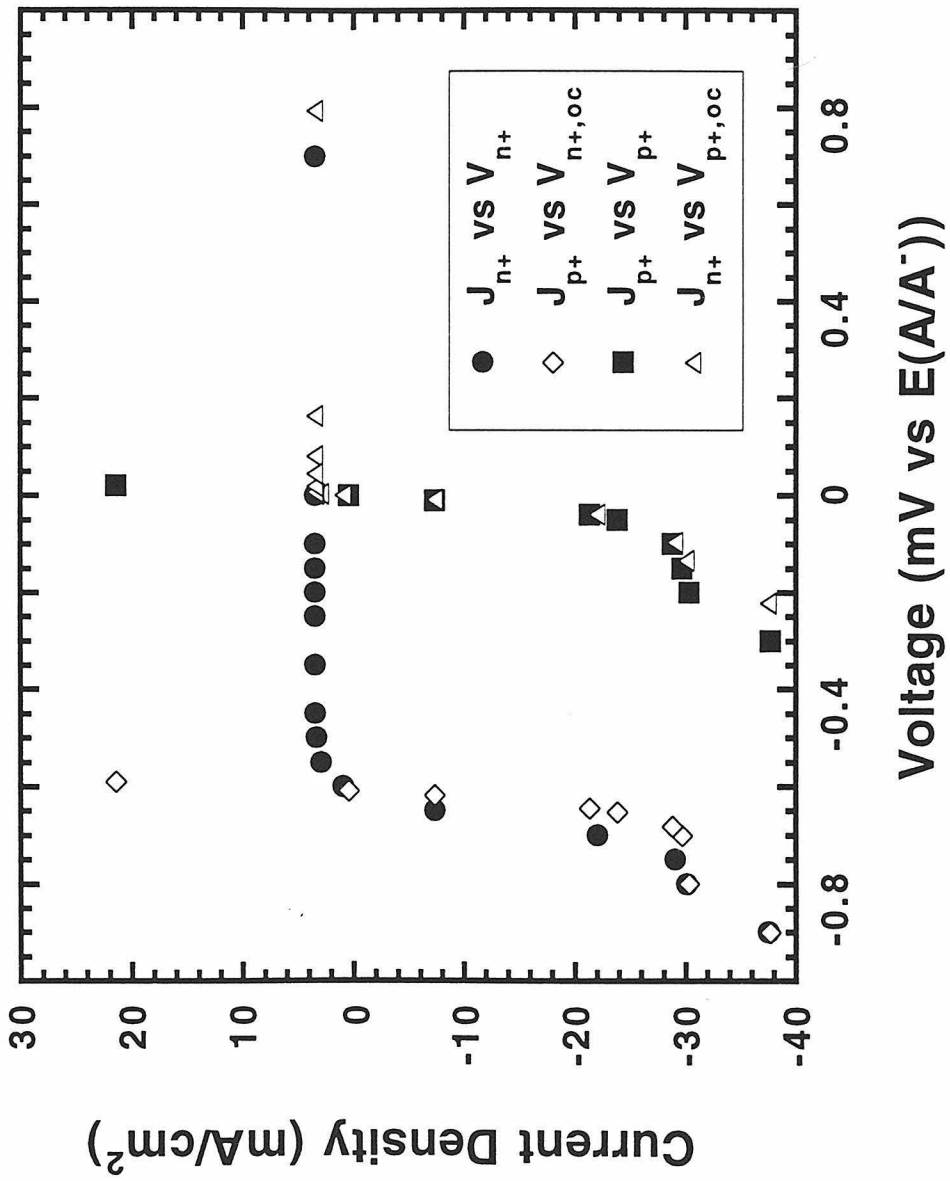
Current Density (mA/cm²)
30
20
10
0
-10
-20
-30
-40
-0.8
-0.4
0
0.4
0.8
Voltage (mV vs E(A/A⁻))
J n+ vs V n+
J p+ vs V n+,oc
J p+ vs V p+
J n+ vs V p+,oc

Figure 2.9a

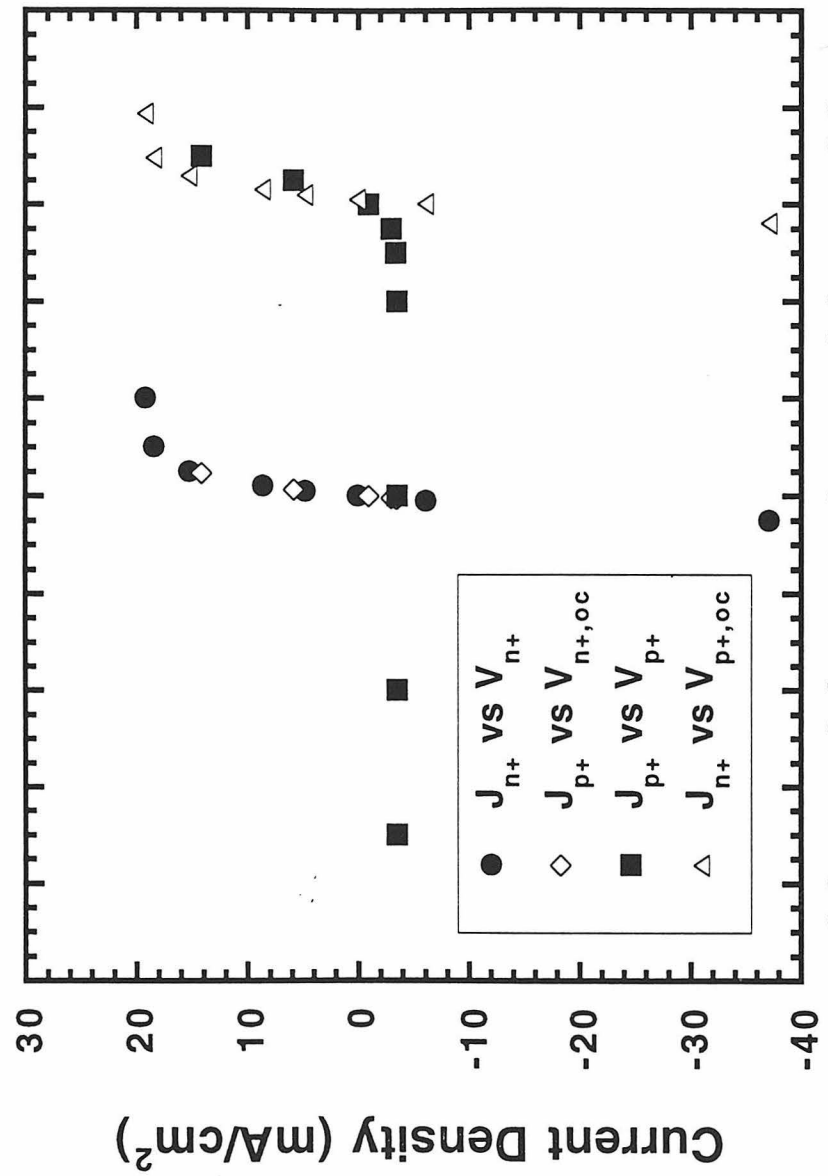
Current Density (mA/cm²)
30
20
10
0
-10
-20
-30
-40
-0.8
-0.4
0
0.4
0.8
Voltage (mV vs E(A/A⁻))
J_n+ vs V_n+
J_p+ vs V_n+,oc
J_p+ vs V_p+
J_n+ vs V_p+,oc

Figure 2.9b

V. SUMMARY

This chapter has described experimental studies and theoretical analysis of the behaviors of Si/liquid contacts under high level injection conditions. Photocurrents in such samples can be either anodic or cathodic in sign, and this behavior is dictated exclusively by the kinetic charge carrier collection properties established by the metallurgy at the back (non-liquid) side of the semiconductor electrode. The interfacial charge carrier kinetics at the solid/liquid interface primarily affect the photovoltage and energy conversion efficiency of these junctions. The fundamental semiconductor statistics of junction equilibration have been shown to provide a simple explanation of the photovoltage properties of these samples, and to explain which junctions will have the proper initial energetic differences to produce optimal energy conversion devices for a given contact configuration. These principles are of importance to understanding the photoelectrochemical behavior of bulk intrinsic semiconductor photoelectrodes, particulate semiconductor photoelectrode systems, and of other photoelectrodes that are operated under high level injection conditions.

In addition to the analysis of Section IV.1, experiments have been presented exploiting the unique contact geometry of these samples to obtain previously unavailable insight into the behavior of quasi-Fermi levels at illuminated semiconductor/liquid contacts. In this study, the quasi-Fermi levels were probed experimentally and exhibited behavior that was consistent with the predictions of the basic model for semiconductor electrochemistry. The current density-voltage behavior of a specific charge carrier in these samples was observed to be the same regardless of whether it was a "majority" carrier, whose flux was specified by an applied potential at the back of the sample, or a "minority" carrier, whose interfacial flux was generated by optical absorption of band gap illumination in the photostationary state of a biased semiconductor/liquid contact. The general behavior of these quasi-Fermi levels can be understood based on simple principles, but certain aspects required a detailed analysis of the generation, recombination, and transport properties of the specific sample geometry of concern. Digital simulations provided by the

ToSCA package were in excellent accord with all of the essential aspects of the experimental behavior. These nearly intrinsic photoelectrodes, operated under high level injection, thus offer a unique opportunity to investigate the behavior of kinetically controlled charge separation processes in a semiconductor photoelectrode. The experimental behavior and digital simulations described herein serve to advance, both qualitatively and quantitatively, the analytical description of charge separation and collection events at illuminated semiconductor/liquid contacts.

VI. REFERENCES

(1) Kumar, A.; Lewis, N.S. *Appl. Phys. Lett.* **1990**, *57*, 2730.

(2) Tan, M.X.; Kenyon, C.N.; Wilisch, W.C.A.; Lewis, N.S. *J. Electrochem. Soc.* **1995**, *142*, L62.

(3) Tan, M.X.; Kenyon, C.N.; Lewis, N.S. *J. Phys. Chem.* **1994**, *98*, 4959.

(4) Kenyon, C.N.; Tan, M.X.; Krüger, O.; Lewis, N.S. *J. Phys. Chem.* submitted for publication.

(5) Fahrenbruch, A.L.; Bube, R.H. *Fundamentals of Solar Cells: Photovoltaic Solar Energy Conversion*; Academic: New York, 1983.

(6) Lewis, N.S.; Rosenbluth, M. In *Photocatalysis: Fundamentals and Applications*; Serpone, N., Pelizzetti, E. Eds.; John Wiley & Sons: New York, 1989; p 45.

(7) Rosenbluth, M.L.; Lewis, N.S. *J. Am. Chem. Soc.* **1986**, *108*, 4689.

(8) Fonash, S.J. *Solar Cell Device Physics*; Academic: New York, 1981.

(9) Tan, M.X.; Kenyon, C.N.; Krüger, O.; Lewis, N.S. *J. Phys. Chem.* submitted for publication.

(10) Nozik, A.J. *Annu. Rev. Phys. Chem.* **1978**, *29*, 189.

(11) Williams, F.; Nozik, A.J. *Nature* **1978**, *271*, 137.

(12) Gerischer, H. In *Solar Energy Conversion. Solid-State Physics Aspects*; Seraphin, B.O. Ed.; Topics in Applied Physics; Springer-Verlag: Berlin, 1979; Vol. 31; p 115.

(13) Reineke, R.; Memming, R. *J. Phys. Chem.* **1992**, *96*, 1310.

(14) Reineke, R.; Memming, R. *J. Phys. Chem.* **1992**, *96*, 1317.

(15) Meissner, D.; Memming, R. *Electrochim. Acta* **1992**, *37*, 799.

(16) Gregg, B.A.; Nozik, A.J. *J. Phys. Chem.* **1993**, *97*, 13441.

(17) Shreve, G.A.; Lewis, N.S. *J. Electrochem. Soc.* **1995**, *142*, 112.

(18) Wang, S. *Fundamentals of Semiconductor Theory and Device Physics*, Prentice Hall Series in Electrical and Computer Engineering; Chua, L.O. Ed.; Prentice Hall: Englewood Cliffs, NJ, 1989.

(19) Pleskov, Y.V.; Gurevich, Y.Y. *Semiconductor Photolectrochemistry*; Consultants Bureau: New York, 1986.

(20) Shockley, W. *Electrons and Holes in Semiconductors*; Van Nostrand: New York, 1950.

(21) Blakemore, J.S. *Semiconductor Statistics*; Dover: New York, 1987.

(22) Bard, A.J.; Faulkner, L.R. *Electrochemical Methods: Fundamentals and Applications*; John Wiley & Sons: New York, 1980.

(23) Pierret, R.F. *Advanced Semiconductor Fundamentals*, Modular Series on Solid State Devices; Pierret, R.F., Neudeck, G.W. Eds.; Addison-Wesley: Reading, MA, 1987.

(24) Sze, S.M. *The Physics of Semiconductor Devices*, 2nd ed.; John Wiley and Sons: New York, 1981.

(25) Kittel, C. *Introduction to Solid State Physics*, 6th ed.; John Wiley and Sons: New York, 1986.

(26) Gajewski, H. *GAMM (Gesellschaft für Angewandte Mathematik und Mechanik) Mitteilungen* **1993**, *16*, 35.

(27) van Roosbroeck, W. *Bell Syst. Tech. J.* **1950**, *29*, 560.

(28) Krüger, O.; Jung, C.; Gajewski, H. *J. Phys. Chem.* **1994**, *98*, 12653.

(29) Forker, W. *Elektrochemische Kinetik*; Akademie-Verlag: Berlin, 1989.

(30) Marcus, R.A. *Annu. Rev. Phys. Chem.* **1964**, *15*, 155.

(31) Gerischer, H. In *Physical Chemistry: An Advanced Treatise*; Eyring, H.; Henderson, D., Yost, W. Eds.; Academic: New York, 1970; Vol. IXA; p 463.

(32) Memming, R. In *Electron Transfer I*; Mattay, J. Ed.; Topics in Current Chemistry; Springer-Verlag: Berlin, 1994; Vol. 169; p 105.

(33) Tan, M.X.; Laibinis, P.E.; Nguyen, S.T.; Kesselman, J.M.; Stanton, C.E.; Lewis, N.S. *Prog. Inorg. Chem.* **1994**, *41*, 21.

(34) The normalization factor $(4\pi\lambda kT)^{-1/2}$ for the distribution of energy states in a redox system is included in the quoted charge transfer rate constants, as specified in ref. 39.

(35) Lewis, N.S. *Annu. Rev. Phys. Chem.* **1991**, *42*, 543.

(36) Koval, C.A.; Howard, J.N. *Chem. Rev.* **1992**, *92*, 411.

(37) Pomykal, K.E.; Fajardo, A.M.; Lewis, N.S. *J. Phys. Chem.* **1996**, *100*, 3652.

(38) Gerischer, H. *Z. Phys. Chem.* **1960**, *26*, 223.

(39) Memming, R. In *Electroanalytical Chemistry*; Bard, A.J. Ed.; Marcel Dekker, Inc.: New York, 1979; Vol. 11; p 1.

(40) Morrison, S.R. *Electrochemistry at Semiconductor and Oxidized Metal Electrodes*; Plenum: New York, 1980.

(41) Williams, F.; Nozik, A.J. *Nature* **1984**, *312*, 21.

(42) Tomkiewicz, M. *Electrochim. Acta* **1990**, *35*, 1631.

(43) Kobayashi, H.; Chigami, A.; Takeda, N.; Tsubomura, H. *J. Electroanal. Chem.* **1990**, *287*, 239.

(44) Kobayashi, H.; Takeda, N.; Sugahara, H.; Tsubomura, H. *J. Phys. Chem.* **1991**, *95*, 813.

(45) Kobayashi, H.; Ono, J.; Ishida, T.; Okamoto, M.; Kawanaka, H.; Tsubomura, H. *J. Electroanal. Chem.* **1991**, *312*, 57.

(46) Laibinis, P.E.; Stanton, C.E.; Lewis, N.S. *J. Phys. Chem.* **1994**, *98*, 8765.

(47) Pomykal, K.E.; Fajardo, A.M.; Lewis, N.S. *J. Phys. Chem.* **1995**, *99*, 8302.

(48) Fajardo, A.M.; Lewis, N.S. *Science* submitted for publication.

(49) Marcus, R.A. *J. Phys. Chem.* **1963**, *67*, 853.

(50) Howard, J.N.; Koval, C.A. *Anal. Chem.* **1994**, *66*, 4525.

(51) Watts, D.K.; C.A., K. *J. Phys. Chem.* **1996**, *100*, 5509.

(52) Marcus, R.A. *J. Chem. Phys.* **1965**, *43*, 679.

(53) Marcus, R.A. *J. Phys. Chem.* **1990**, *94*, 1050.

(54) Smith, B.B.; Koval, C.A. *J. Electroanal. Chem.* **1990**, *277*, 43.

(55) Yang, E.S.; Chan, M.; Wahl, A.C. *J. Phys. Chem.* **1975**, *79*, 2049.

(56) Bock, C.R.; Connor, J.A.; Gutierrez, A.R.; Meyer, T.J.; Whitten, D.G.; Sullivan, B.P.; Nagle, J.K. *Chem. Phys. Lett.* **1979**, *61*, 522.

(57) Yang, E.S.; Chan, M.S.; Wahl, A.C. *J. Phys. Chem.* **1980**, *84*, 3094.

(58) Nielson, R.M.; McManis, G., E.; Golovin, M.N.; Weaver, M.J. *J. Phys. Chem.* **1988**, *92*, 3441.

(59) Nielson, R.M.; McManis, G.E.; Safford, L.K.; Weaver, M.J. *J. Phys. Chem.* **1989**, *93*, 2152.

(60) McManis, G.E.; Nielson, R.M.; Gochev, A.; Weaver, M.J. *J. Am. Chem. Soc.* **1989**, *111*, 5533.

(61) Sinton, R.A.; Kwark, Y.; Gan, J.Y.; Swanson, R.M. *IEEE Electron Device Lett.* **1986**, *EDL-7*, 567.

(62) Forbes, M.D.E.; Lewis, N.S. *J. Am. Chem. Soc.* **1990**, *112*, 3682.

(63) Fajardo, A.M.; Karp, C.D.; Kenyon, C.N.; Pomykal, K.E.; Shreve, G.A.; Tan, M.X.; Lewis, N.S. *Solar Energy Mater. Solar Cells* **1995**, *38*, 279.

(64) Blinov, L.M.; Bobrova, E.A.; Vavilov, V.S.; Galkin, G.N. *Fiz. Tverd. Tela* **1967**, *9*, 3221.

(65) Nilsson, N.G.; Svantesson, K.G. *Solid State Comm.* **1972**, *11*, 155.

(66) Dziewior, J.; Schmid, W. *Appl. Phys. Lett.* **1977**, *31*, 346.

(67) Fossum, J.G.; Mertens, R.P.; Lee, D.S.; Nijs, J.F. *Solid-State Electron.* **1983**, *26*, 569.

(68) Tyagi, M.S.; Van Overstraeten, R. *Solid-State Electron.* **1983**, *26*, 577.

(69) Internally, ToSCA utilizes the physics convention for the sign of the electric potential, i.e. a positively charged space charge region is a region having more negative potential. This convention is opposite to the IUPAC convention traditionally used in electrochemistry. For consistency, all equations in the present thesis have been specified using the IUPAC convention (see Section 1.II).

(70) Hodes, G.; Howell, I.D.J.; Peter, L.M. *J. Electrochem. Soc.* **1992**, *139*, 3136.

(71) Tan, M.X. Ph. D. Thesis, California Institute of Technology, 1994.

(72) Even if $\Delta n \geq p_{so}$, V_{n+} is very large, but V_{p+} deviates from zero because holes must build up relative to their equilibrium values in order to achieve an open-circuit condition.

(73) Calabrese, G.S.; Lin, M.-S.; Dresner, J.; Wrighton, M.S. *J. Am. Chem. Soc.* **1982**, *104*, 2412.

(74) Harrison, D.J.; Calabrese, G.S.; Ricco, A.J.; Dresner, J.; Wrighton, M.S. *J. Am. Chem. Soc.* **1983**, *105*, 4212.

(75) Tan, M.X.; Lewis, N.S. *Inorg. Chim. Acta* **1996**, *242*, 311.

(76) Rosenbluth, M.L.; Lieber, C.M.; Lewis, N.S. *Appl. Phys. Lett.* **1984**, *45*, 423.

(77) Reineke, R. Ph. D. Thesis, Hamburg, 1988.

VI. APPENDIX

Before simulations using the ToSCA package were available, an understanding of the steady-state data of Section IV.2 was sought through use of a numerical finite-difference algorithm for calculating the carrier concentration profiles. This program, historically known as nllum, was originally written by N. S. Lewis for modeling time-resolved experiments, and was translated to C and presented in detail by G. N. Ryba (Ph. D. Thesis, California Institute of Technology, 1992.). The program is capable of describing generation, recombination, diffusion, and charge transfer, but cannot account for the effects of electric potential. The simulations performed using this program were able to explain some elements of the observed behaviors, and provided insight into the coupling of the carrier concentrations through recombination. However, their inability to include effects due to electric fields mandated that these computations would fail to reproduce many of the key features of the quasi-Fermi level behavior presented in this work. Nonetheless, a brief description of these efforts is given since during their course new functionality was incorporated into the program and other existing aspects (such as how pulse widths greater than the time interval are treated) were significantly refined.

To approximate steady-state conditions, the pulse width of the excitation was chosen to be 1 sec and simulations were performed for some fraction of this until the following conditions were satisfied: i) the carrier concentrations were invariant between successive iterations; ii) generation was equal to recombination (as determined by examining output using FileType = 2). Simulations were first performed to yield open-circuit concentration profiles and trap occupancies (FileType = 1). Subsequent simulations were then initiated using these data and applied potentials were treated as perturbations from this open-circuit condition. The voltages were converted to concentrations through use of the quasi-Fermi level relationship for electrons, and the concentration in the last (nboxes-1) box was set to this value before each iteration. Iterations were performed until a new steady state, as defined by the earlier criteria, was reached.

Input File Syntax:

The syntax for the input file is given below. It must be a text file containing only the specified variables. A value of zero for certain parameters results in unpredictable (or predictably bad) behavior and these are designated by (≠0). If it is desired to turn off one of the non-radiative recombination processes, simply set the trap density to a very low value such as 1. Additionally, the flag -1 should be used to disable storing of concentration files or luminescence points.

```
ket             /* Electron transfer rate constant (cm^4 sec^-1)
kht             /* Hole transfer rate constant (cm^4 sec^-1)
Ca              /* Concentration of oxidized species in solution (cm^-3)
Cd              /* Concentration of reduced species in solution (cm^-3)
ntf             /* Surface state density at the front surface (cm^-2)  (≠0)
ntbulk          /* Trap density in the semiconductor back (cm^-3)  (≠0)
ntback          /* Surface state density at the back surface (cm^-2) (≠0)
kr              /* Radiative rate constant (B; cm^-3 sec^-1)
neq             /* Equilibrium electron concentration (N_d; (cm^-3))
izero           /* Number of photons in pulse per unit area (cm^-2)
pulsewidth      /* Temporal width of pulse (sec)
invalpha        /* Penetration depth of excitation wavelength (cm)
invalphalum     /* Penetration depth of luminescence wavelength (cm)
                   -not implemented -
tmax            /* Length of time to be simulated (sec)
thick           /* Thickness of sample (cm)
Vapp            /* Applied voltage (Volts)
iterations      /* Number of iterations
NumConcFiles    /* Number of concentration files to be stored
                        -1 = zero files stored
NumLumPts       /* Number of luminescence points to be stored (≤200)
                        -1 = zero points and no luminescence file stored
LumTimeChange   /* Fraction of decay at which to change frequency for storing
                   luminescence points - not implemented -
FileType        /* Type of output file desired
                        0 = concentrations only
                        1 = trap occupancies and concentrations
                            (this option creates files which can be read by getconc())
                        2 = recombination statistics, trap occupancies and
                            concentrations
outputfilename  /* Prefix for output files
```

Computer Code:

The ANSI C computer code is contained in the file nlcnk.c. It must be compiled with a header file containing parameters specific to the semiconductor material. The following is an example for Si having traps located at the intrinsic level.

Siparm.h

```
#define ni          1.45e10
#define mue         1350
#define mup         480
#define p1bulk      ni
#define n1bulk      ni
#define p1ss        ni
#define n1ss        ni
#define kpbulk      1e-8
#define knbulk      1e-8
#define knss        1e-8
#define pnss        1e-8
```

nlcnk.c

```
/*  nlcnk.c encodes the algorithm for the finite difference calculation. */

#include <math.h>
#include <stdio.h>
#include <stdlib.h>
#include <string.h>
#include "Siparm.h"   /* Parameters dependent on the semiconductor material */

#define DEFAULT 0

int nboxes;
char outfname[20];
float pold[1000], nold[1000], ftblk[1000], ftblk_mt[1000], lum[1001][2];

int main(void)
{

  int getparms(char * , float *, long *, int *, float *, int *, int *);
  int getconc(char *, float *[]);
  int writeconc(int, int, float *[], float *[]);
  int writelum(int);
  char parmfname[20], input[20];
  void nllum(char *);     /* finite difference algorithm */

  printf("\n\nInput the filename to be read: ");
  gets(input);
  sscanf(input, "%s", parmfname);

  nllum(parmfname);
  printf("\n\n");
  return(0);
}
```

```
void nllum(char *infname)
{
 int NumConcFiles, NumLumPts;
 int i,j,k, boxFlag, startFlag, FileType;
 long iterations;
 float parameters[30],kht,ket,Ca,Cd,ntf,ntback,ntbulk,kr,neq,izero;
 float pulsewidth,invalpha,invalphalum,tmax,thick, Vapp, LumTimeChange;
 float De,Dp,D,dx,Dstar;
 float peq,nisq,alpha,inject,in_pulse[1000];
 float khtCddt,ketCadt,krdt,NtCn,NtCp,ftfCh,ftfCe,ftbCe,ftbCh;
 float ftbulk,ftbulk_mt,ftfss,ftfss_mt,ftbss,ftbss_mt;
 float hbsurftrp,ebsurftrp,hfsurftrp,efsurftrp,dsurftrp;
 float etransfer,htransfer;
 float dt,delta,time;
 float dp[1000],dn[1000],sump, sumn,*recombination_ptrs[8];
 float drad[1000],htrapped[1000],etrapped[1000],dtrapped,*trap_ptrs[4];
 char  answer[10],concfname[20];

 getparms(infname,parameters,&iterations,&NumConcFiles,&NumLumPts,\
          &LumTimeChange,&FileType);

 ket     = parameters[0];
 kht   = parameters[1];
 Ca      = parameters[2];
 Cd      = parameters[3];
 ntf   = parameters[4];
 ntbulk   = parameters[5];
 ntback   = parameters[6];
 kr      = parameters[7];
 neq   = parameters[8];
 izero = parameters[9];
 pulsewidth = parameters[10];
 invalpha  = parameters[11];
 invalphalum = parameters[12];          /* not yet implemented */
 tmax = parameters[13];
 thick = parameters[14];
 Vapp = parameters[15];

 trap_ptrs[0] = &ftfss;
 trap_ptrs[1] = &ftfss_mt;
 trap_ptrs[2] = &ftbss;
 trap_ptrs[3] = &ftbss_mt;

 recombination_ptrs[0] = &etransfer;
 recombination_ptrs[1] = &htransfer;
 recombination_ptrs[2] = &hfsurftrp;
 recombination_ptrs[3] = &efsurftrp;
 recombination_ptrs[4] = &hbsurftrp;
 recombination_ptrs[5] = &ebsurftrp;
 recombination_ptrs[6] = &sump;
 recombination_ptrs[7] = &sumn;

/*  Initialize parameters  */
```

```
alpha = 1.0/invalpha;
nisq = ni*ni;
peq = nisq/neq;

/* Diffusion constants */
De =.0257*mue;
Dp =.0257*mup;
Dstar = 2.0*De*Dp/(De + Dp);

boxFlag = 99;
do{
 dt = tmax/iterations;
 delta = dt*Dstar/.4;
 dx = sqrt(delta);
 nboxes = itrunc(thick/dx);
 dx = thick/nboxes;            /* recalculate dx based on nboxes */
 D = Dstar*dt/(dx*dx);          /* recalculate the dimensionless D */

 printf("\nThis yields %d boxes (≤1000) and a time interval of %g.", nboxes,dt);
 printf("\nIf this is unacceptable, enter (1) otherwise enter [0]:");
 while(1==1){
  gets(answer);
  if (sscanf(answer, "%d", &boxFlag) == EOF)
      boxFlag = DEFAULT;
  if (boxFlag == 0)
      break;
  else if (boxFlag == 1){
      printf("\nInput new number of iterations: ");
      gets(answer);
      sscanf(answer, "%ld", &iterations);
      break;
  }
  else{
      fprintf(stderr, "\nPlease answer (1) or [0]: ");
      continue;
  }
 }
}while (boxFlag != 0);

/*  consolidate constants:*/

krdt=kr*dt;
khtCddt=kht*Cd*dt;
ketCadt=ket*Ca*dt;
NtCp=ntbulk*kpbulk*dt;
NtCn=ntbulk*knbulk*dt;
ftfCh=ntf*kpss*dt;
ftfCe=ntf*knss*dt;
ftbCh=ntback*kpss*dt;
ftbCe=ntback*knss*dt;

/* Initialize carrier concentrations and trap occupancy */

startFlag = 99;
```

```
printf("\n\nDo you wish to start from Voc (1) or equilibrium [0]? ");
while(1==1){
 gets(answer);
 if (sscanf(answer, "%d", &startFlag) == EOF)
  startFlag = DEFAULT;

 if (startFlag == 0){

  ftbulk = 1/(1+n1bulk/neq);            /* bulk fraction occupied */
  ftbulk_mt = 1/(1+ p1bulk/peq);   /* bulk fraction empty */
  ftfss = 1/(1+n1ss/neq);       /* front surface occupied */
  ftfss_mt = 1/(1+ p1ss/peq);    /* front surface empty */
  ftbss = ftfss;             /* back surface occupied */
  ftbss_mt = ftfss_mt;       /* back surface empty */

  for(i=0; i<nboxes; i++){
      pold[i] = peq;
      nold[i] = neq;                    /* concentrations */
      ftblk[i] = ftbulk;
      ftblk_mt[i] = ftbulk_mt;            /* trap occupancy */
  }
  break;
 }

 else if (startFlag == 1){
  printf("\nInput the name of the initial concentrations file: ");
  while(1==1){
      gets(answer);
      if ((sscanf(answer, "%s", concfname) == EOF)){
       fprintf(stderr, "\nPlease enter a filename: ");
       continue;
      }
      else
       break;
  }

  getconc(concfname, trap_ptrs);
  break;
 }
 else{
  fprintf(stderr, "\nPlease enter (1) or [0]");
  continue;
 }
}

/*  **********TOP OF time LOOP in k *********
    Changes due to each process in the model are
    calculated and stored as "dp" or "dn", then they are
    added to pold or nold at the end.  */

time = 0;

for (k=1; k<=iterations; k++){
```

```
time += dt;

if (Vapp != 0)
 nold[nboxes-1] = ni*exp(-Vapp/.0256);

if ((time <= pulsewidth) || (k == 1)){
 if (pulsewidth < dt)
     inject = izero;
 else
     inject = izero/itrunc(pulsewidth/dt);

 for (i=0; i<nboxes; i++){
     in_pulse[i] = (inject/dx)*(exp(-alpha*(i)*dx) - exp(-alpha*(i+1)*dx));
     pold[i] = pold[i] + in_pulse[i];
     nold[i] = nold[i] + in_pulse[i];
 }
}

                    /* First Process:  Diffusion: */

dp[0]=D*(pold[1]-pold[0]);          /* first (i.e. [0]) box */
dn[0]=D*(nold[1]-nold[0]);

for(i=1; i<=nboxes-2; i++){
 dp[i] = D*(pold[i+1] - 2.0*pold[i] + pold[i-1]);
 dn[i]=  D*(nold[i+1] - 2.0*nold[i] + nold[i-1]);
}

        /* last (i.e [nboxes-1]) box */
dp[nboxes-1]=D*(pold[nboxes-2]-pold[nboxes-1]);
dn[nboxes-1]=D*(nold[nboxes-2]-nold[nboxes-1]);


for (i=0; i<nboxes; i++){       /* update concentrations */
 pold[i]=pold[i]+dp[i];
 nold[i]=nold[i]+dn[i];
}

for (i=0; i<nboxes; i++){

 /* 2nd Process: bulk radiative recombination */
 drad[i] = (krdt*pold[i]*nold[i] - nisq*krdt);

 /* 3rd Process: bulk trapping */
 htrapped[i] = (ftblk[i]*pold[i] - p1bulk*ftblk_mt[i])*NtCp;
 etrapped[i] = (ftblk_mt[i]*nold[i] - n1bulk*ftblk[i])*NtCn;


 dtrapped = (etrapped[i] - htrapped[i])/ntbulk;  /* update trap filling: */
 ftblk[i] = ftblk[i] + dtrapped;
 ftblk_mt[i] = ftblk_mt[i] - dtrapped;
}

/* 4th Process: surface trapping */
```

```
hfsurftrp = (pold[0]*ftfss - ftfss_mt*p1ss)*ftfCh;
efsurftrp = (nold[0]*ftfss_mt - ftfss*n1ss)*ftfCe;
dsurftrp = (efsurftrp - hfsurftrp)/ntf;
ftfss = ftfss + dsurftrp;
ftfss_mt = ftfss_mt - dsurftrp;

hbsurftrp = (pold[nboxes-1]*ftbss - ftbss_mt*p1ss)*ftbCh;
ebsurftrp = (nold[nboxes-1]*ftbss_mt - ftbss*n1ss)*ftbCe;
dsurftrp = (ebsurftrp - hbsurftrp)/ntback;
ftbss = ftbss + dsurftrp;
ftbss_mt = ftbss_mt - dsurftrp;

/* 5th Process: charge transfer */
htransfer = (pold[0] - peq)*khtCddt;
etransfer = (nold[0] - neq)*ketCadt;


/* Calculate total change */

                    /* first [0] box */
dp[0] = -htransfer/dx - htrapped[0] - hfsurftrp/dx - drad[0];
dn[0] = -etransfer/dx - etrapped[0] - efsurftrp/dx - drad[0];

                    /* 2nd [1] to penultimate [nboxes-2] boxes */
for(i=1; i<=nboxes-2; i++){
  dp[i] = -htrapped[i] - drad[i];
  dn[i] = -etrapped[i] - drad[i];
}

                    /* last [nboxes-1] box */
dp[nboxes-1] = -htrapped[nboxes-1] - hbsurftrp/dx - drad[nboxes-1];
dn[nboxes-1] = -etrapped[nboxes-1] - ebsurftrp/dx - drad[nboxes-1];

                      /* update pold, nold */
for(i=0; i<nboxes; i++){
  pold[i] += dp[i];
  nold[i] += dn[i];
}

if(NumConcFiles != -1){
  if(k==1 || ((k % itrunc(iterations/NumConcFiles)) == 0)){
       for(i=0,sumn=0,sump=0; i<nboxes; i++){
         sump += htrapped[i];
         sumn += etrapped[i];
       }
       writeconc(k, FileType, trap_ptrs, recombination_ptrs);
  }
}
if(NumLumPts != -1){
  if(k==1 || ((k % itrunc(iterations/NumLumPts)) == 0)){
       if(k==1)
         j=0;
       lum[j][0] = time;
       j++;
```

```
        for(i=0; i<nboxes; i++)
          lum[j][1] += drad[i];
      }
     }
  }
  if(NumLumPts != -1)
    writelum(NumLumPts);
}
int getparms(char *fname,float *parms,long *iter,int *NumCfiles, \
             float *NumLpoints, int *LumTchange, int *fType)
{
  FILE *sourcefile;
  int i;
  if((sourcefile = fopen(fname, "r")) == NULL){
    fprintf(stderr, "\nCannot open input file.\n");
    exit(1);
  }
  for(i=0; i<16; i++){
    while((fscanf(sourcefile, "%g", parms+i)) != 1){
      fprintf(stderr, "\nError reading input file.\n");
      exit(1);
    }
  }
  if (fscanf(sourcefile, "%ld %d %d %f %d %s", iter,NumCfiles,NumLpoints,\
            LumTchange,fType,outfname) != 6){
    fprintf(stderr, "\nError reading input file.\n");
    exit(1);
  }
  fclose(sourcefile);
  return(i);
}

getconc(char *fname, float *trap_stats[])
{
  FILE *in;
  int i;
  if((in = fopen(fname, "r")) == NULL){
    fprintf(stderr,  "\nCannot open input file.\n");
    exit(1);
  }

  fscanf(in, "%g %g", trap_stats[0], trap_stats[1]);
  fscanf(in, "%g %g", trap_stats[2], trap_stats[3]);
  for(i=0; i<nboxes; i++)
    fscanf(in, "%g %g %g %g", pold+i, nold+i, ftblk+i, ftblk_mt+i);
  fclose(in);
  return(i);
}

int writeconc(int IterationNum, int FileType, float *trap_stats[], float *rec_stats[])
{
  FILE *out;
  int i,file_num;
  char current_fname[20], file_suffix[3];
```

```
 static char permanent_name[20];
 if (IterationNum == 1){
  strcpy(permanent_name, outfname);
  file_num = 0;
 }
 else
  file_num++;

 sprintf(file_suffix, "_%d", file_num);
 strcpy(current_fname, permanent_name);
 strcat(current_fname, file_suffix);

 if((out = fopen(current_fname, "w+")) == NULL){
  fprintf(stderr, "\nCannot open output file.\n");
  exit(1);
 }
 if (FileType > 1){
  fprintf(out, "%-#11.5e %-#11.5e\n", *rec_stats[0], *rec_stats[1]);
  fprintf(out, "%-#11.5e %-#11.5e %-#11.5e %-#11.5e\n", *rec_stats[2],\
          *rec_stats[3],*rec_stats[4],*rec_stats[5]);
  fprintf(out, "%-#11.5e %-#11.5e\n\n", *rec_stats[6], *rec_stats[7]);
 }
 if (FileType > 0){
  fprintf(out, "%-7.5f %-7.5f\n", *trap_stats[0], *trap_stats[1]);
  fprintf(out, "%-7.5f %-7.5f\n\n", *trap_stats[2], *trap_stats[3]);
  for (i=0; i<nboxes; i++)
    fprintf(out, "%-#11.5e %-#11.5e %-#7.5f %-#7.5f\n", pold[i], nold[i], ftblk[i],
ftblk_mt[i]);
 }
 else  for (i=0; i<nboxes; i++)
    fprintf(out, "%-#11.5e %-#11.5e\n", pold[i], nold[i]);
 fclose(out);
 printf("\nJust wrote %s on iteration %d", current_fname, IterationNum);
 return(0);
}

int writelum(int NumLpoints)
{
 FILE *out;
 int i;
 char lum_fname[20];
 strcpy(lum_fname, outfname);
 strcat(lum_fname, "_lum");
 if((out = fopen(lum_fname, "w+")) == NULL){
  fprintf(stderr, "\nCannot open output file.\n");
  exit(1);
 }
 for (i=0; i<NumLpoints; i++)
  fprintf(out, "%e %e\n", lum[i][0], lum[i][1]);
 fclose(out);
 return(0);
}
```

Chapter 3

Time-Resolved Photoluminescence Studies of InP/Liquid Interfaces

I. INTRODUCTION

Time-resolved photoluminescence (TRPL) has found increasing favor as a technique for investigating carrier transport and charge transfer at the semiconductor/electrolyte interface.[1-6] TRPL is a contactless, non-destructive method having good sensitivity and capable of excellent time resolution. This last feature makes possible the observation of recombination dynamics on the time scale on which they occur, and gives TRPL a significant advantage over steady-state methods where such kinetic information must be inferred. This chapter describes the application of TRPL to the study of indium phosphide (InP) in contact with a series of outer-sphere redox couples. Although the results are largely qualitative, they do provide an estimate of the upper limit for charge transfer at these interfaces and suggest which InP/liquid contacts are good candidates for further study.

Many features of the TRPL technique and were originally developed by solid-state physicists for measuring carrier lifetime and the rate at which carriers are consumed at the surface through recombination.[7,8] It is the accessibility of information on the latter rate, usually quantified as the surface recombination velocity (SRV), that makes TRPL useful in semiconductor/liquid charge transfer studies. Although the mechanism of electron-hole recombination through a surface defect site is fundamentally different from that of charge capture by a molecular species in solution, they can be treated in a similar mathematical fashion.

One limitation of TRPL is that it is only applicable to direct band gap semiconductors, a classification that includes the III-V materials GaAs and InP and the II-VI compounds CdS and CdSe. The majority of TRPL studies of semiconductor/liquid junctions have been performed on GaAs.[2-4,9-11] A number of factors have contributed to this predominance including interest stimulated by the success of GaAs in photoelectrochemical solar energy conversion schemes[12-14] and practical considerations such as the availability of high quality bulk and epilayer samples. While it has received the

most attention, GaAs is not an optimal choice for the study of charge transfer to well-defined outer-sphere redox couples which are those necessary for verifying key elements of the theories of Marcus and Gerischer.[15-18] This is because the intrinsic SRV of GaAs surfaces is very high,[19,20] and as this surface process competes with charge transfer, its predominance makes it is difficult to observe effects due to the surface process of interest. To circumvent this problem, studies of GaAs/liquid junctions have often relied on passivation of the semiconductor surface by strongly adsorbed chalcogenides.[3,6,21] While these studies have provided some useful information on the timescale for charge transfer at semiconductor/liquid interfaces, they are difficult to evaluate theoretically.

The problems associated with studying charge transfer at GaAs/liquid interfaces generated interest in performing time-resolved PL studies of InP. Earlier investigations comparing the steady-state PL intensity of n-InP to that of n-GaAs had indicated the intrinsic SRV of n-InP to be low ($\leq 10^3$ cm sec^{-1}),[22] and this conclusion has been supported by recent luminescence decay measurements of the semiconductor in contact with air.[23] Additional criteria also indicated InP to be an attractive material for charge transfer studies. In particular, n-InP had been demonstrated to form the basis of stable semiconductor/liquid junctions in contact with a variety of outer-sphere redox couples.[24,25]

Despite its apparent suitability, the number of time-resolved studies of InP/liquid interfaces is very small, the published work being limited to two reports.[26,27] This paucity is not restricted to studies of the semiconductor in contact with electrolytes. There is also surprisingly few studies of InP in the solid-state literature reporting direct measurements of carrier lifetime and SRV.[28,29] This stands in contrast to the extensive data available on GaAs.

Although the amount of TRPL data on InP/liquid interfaces is limited, some extraordinary claims have been made regarding it. Photoluminescence decays collected for the p-InP/H_2O-$Fe(CN)^{3-/4-}$ contact as a function of applied bias have been interpreted as evidence of charge transfer occurring with rate constants as high 10^{-12} cm^4 sec^{-1}.[27] This

analysis was based on a computer model purported to be able to differentiate the effects on the PL decay rate due to simple field-driven charge separation from that attributable to electron transfer.[30,31] A charge transfer rate constant of that magnitude implies that carriers must be transported from the semiconductor bulk to the surface at a velocity in excess of 10^7 cm sec^{-1} (roughly equal to the saturation drift velocity of electrons in InP[32]) and is inconsistent with estimates for the maximum charge transfer rate of 10^{-16}-10^{-17} cm^4 sec^{-1} that are based on the classical theories of Marcus and Gerischer.[33] The reported value of k_{et} is also much greater than values which have been determined recently for n-InP/CH_3OH junctions using steady-state current voltage techniques.[25] To explain this discrepancy, a new model of electron transfer at the semiconductor/liquid interface has been presented.[34] This controversy underscores the need for more time-resolved studies of stable well-defined InP/liquid junctions.

II. BACKGROUND

The principle underlying the use of time-resolved photoluminescence as a probe of charge transfer kinetics is that the rate of radiative recombination, observable as the PL intensity, is proportional to the carrier concentrations in the semiconductor.[35,36] Knowledge of these concentrations as a function of time can provide the desired information on interfacial rates. However, interpretation of TRPL decay data is not facile as there are a number of mechanisms capable of determining its form, the most common of which are introduced below. As has been done elsewhere in this thesis, where it is necessary to make a distinction, the treatment is given for an n-type semiconductor.

A. Bulk Mechanisms

1. Radiative Recombination

Photoluminescence, the observable in TRPL experiments, is the result of band to band radiative recombination of an electron-hole pair. Although the physical origin of this phenomenon is complex, and requires a detailed understanding of the band structure, it is relatively straightforward to treat on a statistical basis.[37] The photoluminescence intensity, I_{PL}, is equal to net rate of radiative recombination integrated over the sample volume (V).[35] This rate has a familiar bimolecular form and, in one dimension (x), is proportional to the product of the electron and hole concentrations integrated over the sample thickness (d).

$$I_{PL} = -\int \left.\frac{\partial n}{\partial t}\right|_{rad} dV = B\int_0^d \left[n(x,t)p(x,t) - n_i^2\right]dx \qquad (3.1)$$

All the details of the coupling between the conduction and valence bands are contained in the proportionality constant, B, known as the radiative rate coefficient.[38] As simple as eq 3.1 appears, extraction of interfacial rates from TRPL data can be problematic. The calculation requires knowledge of the spatial profiles of carriers within the solid, and the PL intensity does not contain any direct information on these distributions. A general description of the time-dependent carrier concentrations following pulsed laser excitation requires solving the electron and hole continuity equations which are coupled through

Poisson's equation. No complete analytical solution to this system of differential equations exists, and this has resulted in the development of numerous models including both analytical, approximate solutions[39-44] and entirely numerical approaches of varying complexity.[1,31,45] Although a thorough comparison of the predictions of these models would be useful, none have appeared to date, and it is fair to say that no model has gained general acceptance.

Along with the difficulty in evaluating which model is correct or appropriate, interpretation of TRPL data is further complicated by the numerous factors besides radiative recombination which can dominate the form of the decay. Figure 3.1 illustrates some of the most important mechanisms that influence the temporal and spatial profiles of the photogenerated carrier concentrations following pulsed illumination. To facilitate the interpretation of TRPL data, experiments are typically conducted under either high-level or low-level injection conditions where certain approximations can be made.[35]

In high-level injection, the excess carrier concentrations, Δn, Δp, are much greater than either of the equilibrium carrier concentrations n_o, p_o. As discussed in Chapter 2, these large and equal excess carrier densities screen any space charge fields in the semiconductor and thereby minimize the effects of drift on carrier motion. This is the situation depicted in Figure 3.1 where the bands have been drawn as flat to indicate the neglect of terms attributable to the presence of an electric field in the solid.[46] An additional consequence is that the rate of radiative recombination should exhibit an approximately quadratic dependence on the number of photogenerated carriers. This can be understood by separating the concentrations in eq 3.1 into sums of equilibrium and excess contributions.

$$-\left.\frac{\partial n}{\partial t}\right|_{rad} = -\left.\frac{\partial \Delta n}{\partial t}\right|_{rad} = B\left[(n_o + \Delta n)(p_o + \Delta p) - n_i^2\right] \qquad (3.2)$$

Using the inequalities $\Delta n \Delta p >> \Delta p n_o$ and recalling that $n_o p_o = n_i^2$, eq 3.2 can be simplified to:

$$-\left.\frac{\partial \Delta n}{\partial t}\right|_{rad} = B(\Delta n + n_o)\Delta p = B\left[\Delta n^2 + n_o \Delta n\right] \qquad (3.3)$$

where the nonlinearity is made explicit using the fact that $\Delta n = \Delta p$ by injection. A consequence of eq 3.3 is that if radiative recombination is the dominant mechanism of carrier loss, the PL should decay faster as the injection level is increased.[36]

At the other limit of injection $\Delta n << (n_o + p_o)$, the majority carrier concentration is essentially unchanged by photogeneration and the radiative rate becomes linear in the excess minority carrier density, Δp. Under these conditions, eq 3.2 assumes the simple form of a first order rate law.

$$-\left.\frac{\partial \Delta n}{\partial t}\right|_{rad} = B n_o \Delta p \qquad (3.4)$$

Combining this result with eq 3.1 reveals that when radiative recombination dominates the carrier decay, an exponential PL decay with a lifetime $1/Bn_o$ should be observed.

2. Diffusion

The familiar process of diffusion acts to redistribute the carriers in the solid so as to flatten the concentration profiles. It is always operative and can dominate the form of the PL decay in certain situations, especially at short times following excitation when strongly absorbed wavelengths, which create steep initial carrier profiles, are employed. A strategy that has been exploited to minimize the effects of diffusion is to perform TRPL experiments on thin epilayer samples where the time for spreading of the carrier concentrations is short relative to the timescale of interest. Confining the carriers to the epilayer requires the use of a heterostructure geometry where the active layer is grown on a lattice-matched substrate having a larger band gap. The best example of this is the AlGaAs/GaAs heterostructure which has been employed in both solid-state[47,48] and semiconductor/liquid studies.[6]

3. Non-Radiative Bulk Recombination

The other important process occurring in the semiconductor bulk is non-radiative recombination through states in the energy gap (traps). Shockley, Read, and Hall initially

described this process and it is sometimes referred to as SRH recombination.[49,50] The change in carrier concentrations as a function of time (units of cm^{-3} sec^{-1}) due to bulk non-radiative recombination is given for electrons and holes by the following expressions:

$$\left.\frac{\partial n}{\partial t}\right|_{SRH} = c_n(n_1 f_T N_T - n(1-f_T)N_T) \tag{3.5}$$

$$\left.\frac{\partial p}{\partial t}\right|_{SRH} = c_p(p_1(1-f_T)N_T - p f_T N_T) \tag{3.6}$$

where N_T is the number of traps per unit volume, n_1, p_1 are constants dependent upon the energy of the trap, f_T is the fraction of traps that are occupied and c_n, c_p are the capture coefficients (rate constants) for electrons and holes, respectively. Eqs 3.5 and 3.6 are arrived at using detailed balance arguments and their derivation can be found in introductory books on semiconductor physics.[38,51] These expressions are quite general and are valid for a range of experimental conditions subject to the assumption that c_n, c_p remain constant.

Although the experiments described herein are performed under transient condition, it is worthwhile to examine the situation at steady-state as it more clearly reveals the coupling between the individual capture rates. At steady-state, the net rate of electron and hole capture must be equal, and this makes it possible to solve for the rate of non-radiative bulk recombination, R_{SRH}.

$$R_{SRH} = \frac{np - n_i^2}{\frac{1}{c_p N_T}(n+n_1) + \frac{1}{c_n N_T}(p+p_1)} \tag{3.7}$$

The reciprocals in the denominator are the hole and electron bulk non-radiative lifetimes, τ_{po}, τ_{no}, respectively. Under low-level injection conditions, this simplifies to eq 3.8 where the rate is dictated by the minority carrier lifetime.[51]

$$R_{SRH} = \frac{\Delta p}{\tau_{po}} \qquad \Delta p << (n_o + p_o) \tag{3.8}$$

If SRH recombination is the dominant mechanism of carrier decay, an exponential PL decay with a lifetime, $\tau_{po,}$ will be observed. At higher injection levels, the rate asymptotically approaches that given by eq 3.9, and is dominated by whichever capture rate is smaller.[23,36,52]

$$R_{SRH} = \frac{\Delta p}{\tau_p + \tau_n} = \frac{\Delta n}{\tau_p + \tau_n} \qquad \Delta p >> (n_o + p_o) \qquad (3.9)$$

Comparison of eqs 3.8 and 3.9 reveals that SRH recombination is expected to be slower in high-level injection than in low-level injection. Consequently, PL decays dominated by SRH recombination should become slower as the injection level is increased, which is opposite the behavior predicted for a radiatively limited decay.

4. Auger Recombination

One final bulk mechanism to be mentioned is Auger recombination.[38] At very high carrier densities, band-to-band recombination of electron-hole pairs can occur non-radiatively, with the excess energy being transferred to another carrier in the band. This process is not expected to contribute significantly at the carrier concentrations attained in the present work.

B. Surface Processes

While it is necessary to consider effects on the PL decay due to processes occurring in the semiconductor bulk, it is the influence of carrier recombination at the surface that is of interest in these experiments. There are two principal mechanisms which can consume carriers at the surface, surface state recombination and charge transfer. Their contributions are always additive although they do not have the same functional dependence on certain parameters such as potential.

1. Surface State Recombination

Surface state recombination, as its name implies, is a mechanism by which electron-hole pairs recombine through states localized at the surface.[53] It is a non-radiative process that is similar both conceptually, and in its mathematical treatment, to the analogous bulk

pathway. General equations of the form of eqs 3.5 and 3.6 can be written to describe the individual rates of electron and hold capture by surface states and, under steady-state conditions, they can be solved to yield an expression for the net rate of surface recombination, R_{ss}.

$$R_{ss} = \frac{n_s p_s - n_i^2}{\frac{1}{c_{ps} N_{Ts}}(n_s + n_{1s}) + \frac{1}{c_{ns} N_{Ts}}(p_s + p_{1s})} \tag{3.10}$$

Terms in the eq 3.10 have the same meaning as in eq 3.7 (subscript *s* added to indicate the quantities are evaluated at the surface), except that the state density is specified per unit area, and Rs, as a surface rate, has the units of flux (cm^{-2} sec^{-1}). Eq 3.10 simplifies as did the corresponding expression for the bulk rate, and in high-level injection is given by:

$$R_{ss} = \frac{\Delta p_s}{\frac{1}{s_p} + \frac{1}{s_n}} = \frac{\Delta n_s}{\frac{1}{s_p} + \frac{1}{s_n}} \tag{3.11}$$

where substitutions of s_p for $c_{ps}N_{Ts}$, and s_n for $c_{ns}N_{Ts}$, have been made. These two individual values, s_p, s_n, are referred to as the hole and electron surface recombination velocity, respectively, and have units of cm sec^{-1}. It is again evident that the overall rate will be dominated by the larger term in the denominator (smaller s value) and it is common to combine the two reciprocals into a single surface recombination velocity, S_{ss}.[8]

$$\frac{1}{S_{ss}} = \frac{1}{s_p} + \frac{1}{s_n} \tag{3.12}$$

2. Charge Transfer

The final process to be considered is the one for which kinetic information is sought in these TRPL experiments. Charge transfer operates in parallel with surface state recombination and under the open-circuit, high-level injection condition, an equation similar to eq 3.10 can be used to express its rate. Carrier loss at the surface due to hole and electron transfer to molecular acceptors in solution can be described by inserting into eq 3.10, the hole and electron heterogeneous rate constants (k_{ht} and k_{et} in units of cm^4 sec^{-1})

in place of c_{ps}, c_{ns} and replacing N_{Ts} with the acceptor concentration in solution. Simplifying for the high-level injection condition, and combining the interfacial rate constants and acceptor concentrations into hole and electron charge transfer collection rate constants, k_p, k_n, respectively,[33] gives the following.

$$R_{ct} = \frac{\Delta p_s}{\frac{1}{k_p} + \frac{1}{k_n}} = \frac{\Delta n_s}{\frac{1}{k_p} + \frac{1}{k_n}} \tag{3.13}$$

The charge transfer collection rate constants have the same units (cm sec^{-1}) as s_n and s_p in eq 3.11 and can also be combined into a net velocity.[1]

$$\frac{1}{S_{ct}} = \frac{1}{k_p} + \frac{1}{k_n} \tag{3.14}$$

The total effect of surface processes on the time resolved photoluminescence from a semiconductor/liquid contact is given by the sum of S_{ct} and S_{ss}. For this reason, even when a PL decay can be identified as dominated by carrier loss at the surface, calculating a charge transfer rate requires prior knowledge of the magnitude of S_{ss} or additional information such as that obtained from concentration studies. Unless otherwise specified, references to the surface recombination velocity refer to the composite value.

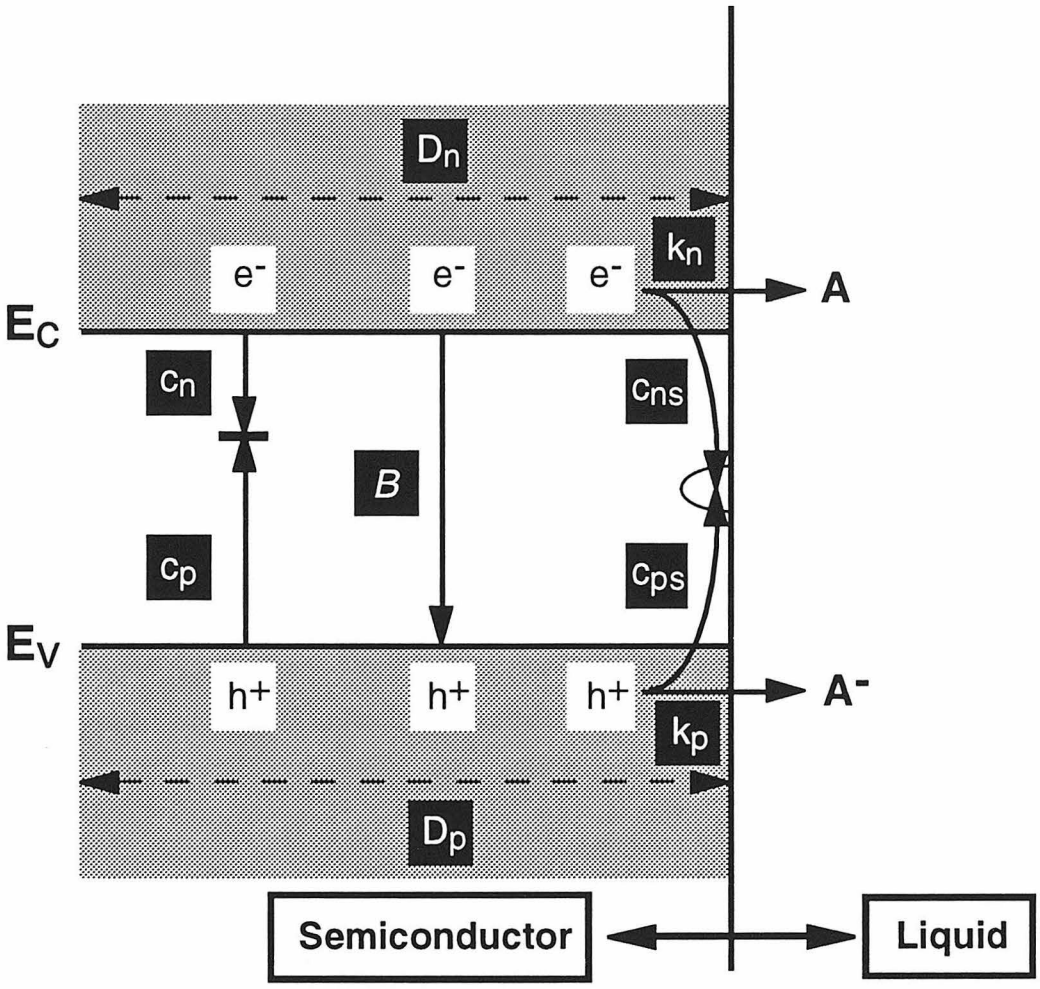

Figure 3.1: Illustration of the mechanisms which affect the time-dependent carrier concentration profiles following band gap illumination of the semiconductor. They can be identified by their rate constants which are described in the text. An exception is the process of diffusion which is indicated by double-ended arrows and the diffusion coefficients for electrons (D_n) and holes (D_p).

III. EXPERIMENTAL

A. Materials and Preparation

The samples used in the work presented herein were prepared from two single crystal InP wafers, both of which were purchased from CrystaComm. Initial experiments were performed on (100)-oriented p-type (Zn doped) samples while later studies were done using samples prepared from a nominally undoped (111)B-oriented InP wafer.

For use in the PL experiments, small pieces of the InP wafer (3-5 mm on a side) were cut from the wafers and mounted onto the flattened end of a glass rod using epoxy (Dexter). Prior to use in an experiment, the electrodes were etched following a procedure outlined by Aspnes and Studna.[54] The method typically involved cycling three times between a .05% solution (by volume) of Br_2 (Aldrich) in CH_3OH and a 1:1 (v:v) mixture of concentrated NH_4OH (Mallinckrodt) and deionized water. Making the very dilute solutions of $Br:CH_3OH$ was accomplished most efficiently by transferring 10 µl of Br_2 into 20 ml of CH_3OH using a micropipettor (Drummond Scientific). The samples would be stirred in the $Br:CH_3OH$ solution for 15 s and then stirred for an equal length of time in $NH_4OH:H_2O$. As a final step, the surface was thoroughly rinsed with deionzied water and then blown dry in a stream of N_2.

B. Solvents and Chemicals

The redox compounds and solvents used in these experiments used in these studies were purchased from various sources. Solvents were dried according to published procedures. Me_2Fc (PolySciences or Strem) was purified by sublimation and dried in vacuo while $Me_{10}Fc$ (Strem) was simply dried. Methyl viologen hexafluorophosphate ($MV(PF_6)_2$), cobaltocenium hexafluorophosphate ($CoCp_2PF_6$), and tetrabutylammonium hexaflurophosphate (TBAPF6) were prepared according to published procedures[55] by metathesis of the halide salts, $MVCl_2$ (Aldrich), $CoCp_2Cl$ (Alfa) and TBABr (Aldrich), with hexafluorophosphoric acid (Aldrich).

C. Optics and Electronics

The TRPL experiments presented in this chapter were performed using the time-correlated single photon counting (TCSPC) technique.[56] Many elements of the laser configuration and the TCSPC apparatus used in this work have been described in detail previously and will not be repeated here.[9] Instead, emphasis is placed on specifics relevant to the present studies as well as any changes or refinements that have been implemented since the earlier report.

1. Laser Configuration

Excitation for these experiments was provided by a Coherent Inc. Model 701 Dye laser equipped with a Model 7200 cavity dumper. DCM (Exciton) and Rhodamine 6G (Exciton) dyes were used in the dye laser and the specific excitation wavelengths are given in Tables 3.1-3.3. Wavelengths were determined using the "Wavelength-O-Matic", a monochromator/photomultiplier combination assembled from salvaged components, and calibrated using known He:Ne and He:Cd laser lines. Pulse widths were measured and optimized during the course of experiments using an Inrad Model 5-14B autocorrelator (equipped with the optional picosecond delay blocks) and a Kikisui Model 5020 oscilloscope. Unless otherwise noted the dye laser repetition rate was set at 190 kHz by a Coherent Inc. Model 7200-38 cavity dumper driver. The delay between pulses at this repetition rate is greater than 5 μs, which is substantially longer than the timescale for the observed decays.

The dye laser was synchronously pumped by the frequency-doubled pulse train (532 nm; 76 MHz; ~70 ps FWHM) of a Coherent Inc. Antares 76-S Nd:YAG laser equipped with a Model 7600 mode locker. The second harmonic output utilized in early studies was generated as described previously, by passing the fundamental 1064 nm pulses through a KTP crystal assembly.[6] Later experiments were performed using 532 nm light generated in a temperature-controlled LBO crystal (CSK Optronics SPIA-5). This latter

configuration is capable of higher conversion efficiencies which reduces the performance demands on the Nd:YAG laser.

2. Excitation Intensity

A key parameter in time-resolved photoluminescence studies of semiconductor interfaces is the injection level, the ratio of the number of excess carriers created per unit volume to the equilibrium majority carrier concentration. Unfortunately, it is also one of the most difficult to quantify accurately. In the semiconductor/liquid PL experiments presented herein, sources of error in calculating the injection level include difficulty in determining the number of photons in each laser pulse, reflection at the various interfaces, light absorption by the electrolyte, and uncertainty in the illuminated area. To obtain estimates of the average number of photons per pulse, the dye laser power was measured with a Coherent Inc. LabMaster equipped with a Model LM-10 power meter. It was necessary to take these readings at a repetition rate of 3.8 MHz as the average power produced at 190 kHz (the rate employed in the experiments) was too low to be determined accurately. Readings were also taken periodically at 380 kHz and the power was found to scale roughly linearly if the fine delay on the cavity dumper driver was reoptimized.

Calculations were performed using the Fresnel equations[57] to provide an estimate of the total amount of light lost to reflection at air/glass, glass/solution and solution/semiconductor interfaces. Figure 3.2a shows the fraction of the incident power reflected as a function of the angle of incidence. Some attempts were made to exploit the somewhat higher transmission of p-polarized light, but the gains were partially offset by losses introduced by the polarization compensator used to rotate the inherently s-polarized output of the dye laser.

For experiments in which it was desirable to have as high an injection level as possible, the laser beam was focused onto the sample surface using a 25.4 mm focal length (f.l.) achromatic lens. For a 600 nm laser beam having a diameter of 1.3 mm, the diffraction limited spot obtainable using this lens is approximately 30 μm in diameter. To

calculate the photon flux at the semiconductor surface, the effect of the non-zero angle of incidence must also be considered (Figure 3.2b). This angle was originally reported to be 45° (as measured from normal),[9] but a more optimized configuration reduced this to 35°, which decreases the calculated area of the illuminated ellipse to ~8 x 10^{-6} cm^2.

3. Photon Detection

The luminescence from the sample was imaged onto the entrance slit of a monochromator at *f*/4 using a 25.4 mm diameter, 5 mm f.l. lens placed between the sample and the monochromator, and 10 mm from each. The monochromator was set to pass luminescence at 920 nm, which was determined empirically to be near the center of the broad InP emission. This wavelength agrees well with the value of 918 nm predicted by the InP room temperature band gap of 1.35 eV. Photons were detected using an S-1 photocathode in conjunction with a Hamamatsu Model R1564U-05 2-stage proximity-focused microchannel plate/photomultiplier tube (MCP/PMT) biased at -3030 V and maintained at -40 C using a Products for Research Model TE335 refrigerated housing. Ambient and scattered laser light were discriminated against by placing long-pass cutoff filters in front of the monochromator.

4. Timing

The basic layout of the experiment is shown in Figure 3.3. Timing is accomplished by the time-to-amplitude converter (TAC) (Tennelec Model TC864), which accepts start and stop pulses and outputs a voltage pulse proportional to the time elapsed between the two. Experimentally, the start pulse is produced by splitting off a small portion of the excitation beam prior to the sample and directing it to a fast photodiode (Thor labs; rise time ~300 ps). The stop pulse is the (amplified) current pulse generated by the MCP/PMT when an incident photon strikes the photocathode. In order to minimize errors in timing brought about by variations in the input pulse heights, both the start and stop pulses are passed through a constant fraction discriminator (EG&G Ortec Model 934). Because the CFD only accepts negative pulses, the photodiode was reconfigured by attaching the signal lead

to the cathode (n-type region of p-i-n diode), and reversing the polarity of the bias by simply inserting the 22 V battery opposite to its specified orientation.

The overall instrument response function (IRF) was obtained by setting the monochromator to the laser wavelength and scattering a small amount of the incident light off a piece of Teflon or a cuvette of distilled water. While the temporal width of the IRF exhibited some variation, it was typically 70-80 ps FWHM after autocorrelation of the dye laser pulses. In an attempt to shorten the time response of the system, experiments were performed using photodiodes having shorter rise times, but these did not yield an improved IRF. This was true even after the external delay of the CFD channel accepting the photodiode pulses was bypassed by soldering a very short delay cable onto the breadboard. This modification makes the CFD, designed for detecting slower nuclear events, more compatible with the picosecond pulses, and had previously produced substantial benefits when done for the MCP/PMT input channel.[9]

The overall response of the system and calibration of the multi-channel analyzer, which converts and bins the output pulses from the TAC, was checked periodically by recording PL decays for laser dyes and other compounds for which the lifetime was known.

Figure 3.2: Plots of the effect of the angle of incidence on the excitation intensity at the semiconductor surface. (a) Fraction of incident power reflected as a function of the angle of incidence (degrees from normal). The calculation was performed using indices of refraction of 1.0 for air, 1.47 for the Pyrex sample holder, 1.34 for CH_3CN, and 3.57 for InP. A minimum in the fraction reflected occurs at about 65°. (b) Calculation of the relative power density at the surface as a function of the angle of incidence. This figure was produced by dividing the data of (a) by the relative geometric area of an ellipse formed by the intersection of a plane with a cylinder, as a function of the angle of intersection. A relative power of density of 1.0 in this calculation corresponds to a completely transmitted beam at normal incidence. This figure indicates that the relative area is the dominant term in determining the power density; the increase in transmitted power at large angles of incidence (p-polarized light) is overwhelmed by an increase in the illuminated area. Consequently, angles as close to normal as experimentally feasible are desirable for obtaining high excitation intensities.

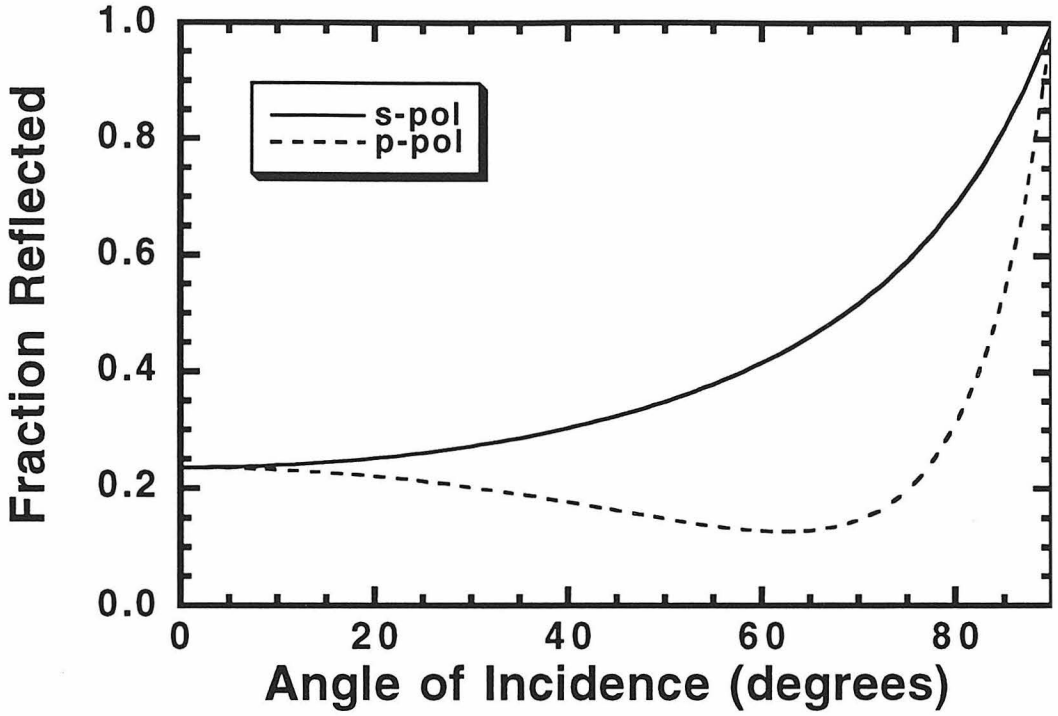

Figure 3.2a

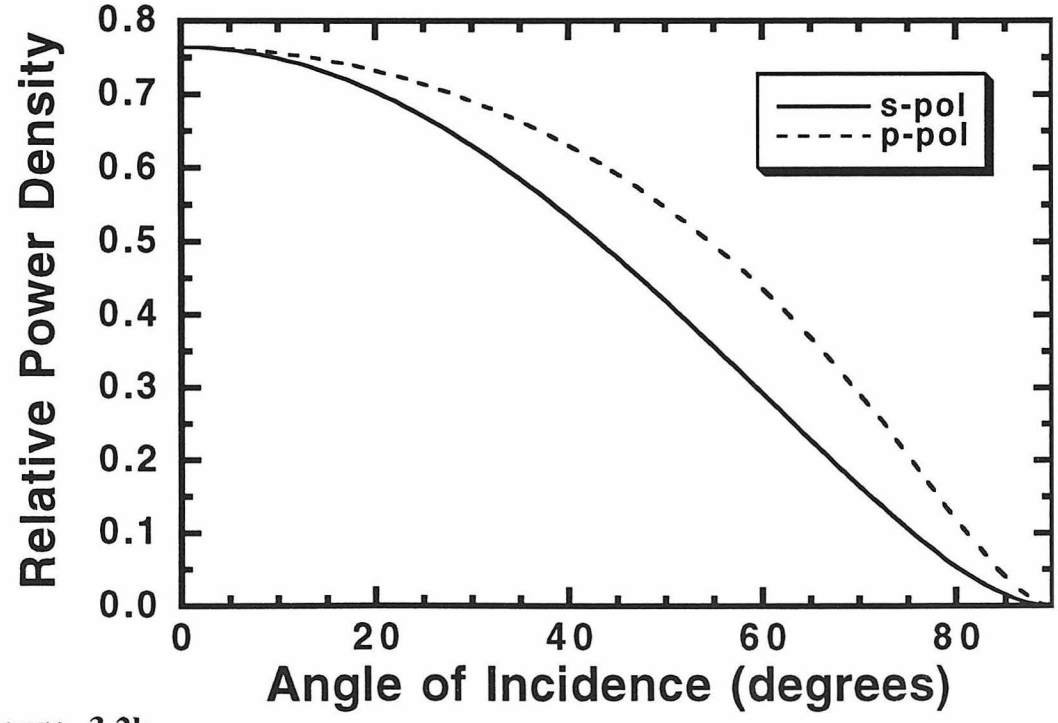

Figure 3.2b

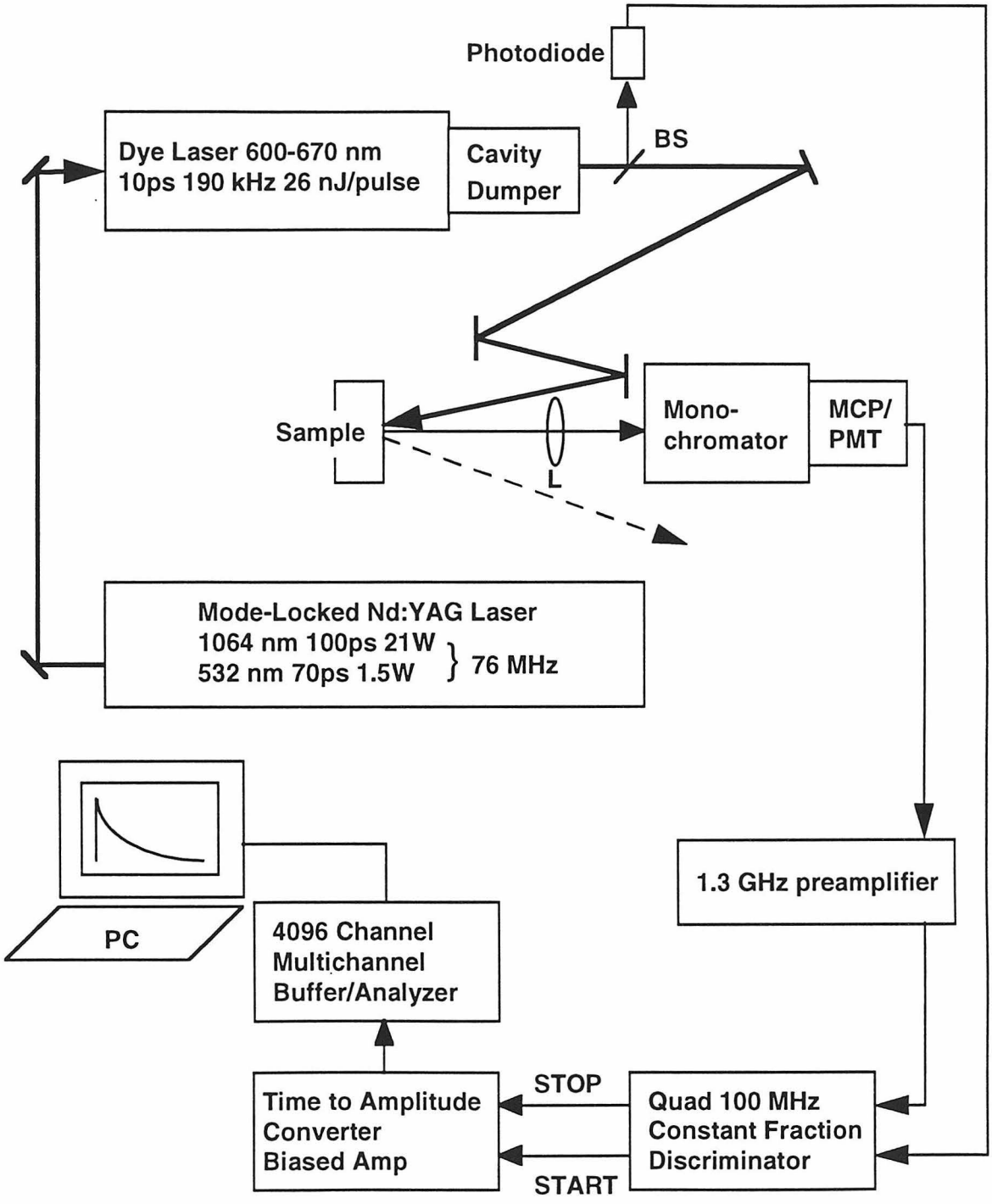

Figure 3.3: Schematic of the TCSPC experiment.

IV. RESULTS

It is evident from Section II that extraction of charge transfer rate information from TRPL studies requires attention to the various mechanisms which can determine the form of the data. The experiments on semiconductor/liquid interfaces described herein were performed on semi-infinite InP samples using excitation designed to produce initial high-level injection conditions. It was desirable to use employ high-level illumination as the strong electric field present at the semiconductor/liquid interface under low-level injection conditions leads to rapid quenching of the photoluminescence that is not dependent on the charge transfer kinetics. Only one form of the redox couple was added initially (whichever had the lower extinction coefficient at the excitation wavelength), but it is expected that concentrations of both the oxidized and reduced species will be present at the surface following pulsed illumination. This is because the open-circuit conditions employed herein require that carrier loss through interfacial charge transfer involve capture of both carrier types by molecular species in solution.

The experimental conditions employed in the present work have been utilized in other TRPL studies of semiconductor/liquid interfaces.[1,26,58] However, there are several points that should be addressed regarding these conditions. The thickness of the semiconductor samples is such that diffusion of photogenerated carriers into the bulk will continue throughout the carrier decay. Secondly, there will be regions of the semiconductor in different injection regimes, and this will be true even initially due to the exponential absorption of the light. In the past it has been argued that the PL signal is dominated by regions in high-level injection since the rate of radiative recombination is greatest where the concentration of excess carriers is largest. A final point, which applies generally to experiments performed under high-level injection conditions, is that all decays must eventually pass through the low-level injection regime such that decays collected at both limits will assume the same form at longer times. Additionally, as the transition into low-level injection occurs, electric fields in the solid will again become important so it is

desirable to focus analysis on the earlier portions of the PL decay profiles, where high-level injection conditions prevail.

A. Luminescence Decay Profiles for Etched Samples

Before time-resolved photoluminescence data were recorded for InP samples in contact with electrolytes, decay profiles were obtained for etched samples under an inert (N_2) atmosphere. These data provided necessary information on the intrinsic photoluminescence properties of the material. In addition to serving as a reference point for the later studies on InP/liquid contacts, the data are interesting simply because the number of time-resolved PL studies of InP, especially p-type InP, is very small.[23,28] Decays at several light intensities were collected for both (100) p-type InP (N_a=5x10^{16} cm^{-3}) and (111) n-type InP (unintentionally doped; N_d=5x10^{15} cm^{-3}).

1. p-InP

The normalized PL intensity as a function of time for an etched p-InP sample is presented on a linear scale in Figure 3.4a and in semilogarithmic form in Figure 3.4b to elucidate the later time behavior. These initial results were discouraging as the short timescale for the decays meant the dynamic range available for observation of effects due to interfacial charge transfer would be small. This was the situation that frustrated earlier time-resolved PL studies of n-GaAs in contact with CH_3CN-Fc; intrinsic surface recombination processes were sufficiently fast to preclude a significant increase in the rate of carrier decay upon addition of the redox species.[9]

Although the decays presented in Figure 3.4 were faster than what was hoped for originally, they are in agreement with earlier picosecond photoluminescence studies of p-InP samples having dopant densities comparable to that of the material used in the present work.[59] Interestingly, the authors reported that numerical simulations of their data indicate the rapid decays to be a result of a low non-radiative bulk lifetime, and not a high surface recombination velocity.[59] Their claim opposed the generally accepted view that the intrinsic SRV of p-InP is very high (10^5-10^7 cm sec^{-1}), unlike n-InP which was believed to

have a low SRV.[28] This earlier conclusion was based largely on steady-state PL measurements that found the PL intensity of p-InP to be two orders of magnitude lower than that of n-InP, and comparable to that obtained for GaAs.[22]

Also in accord with the earlier photoluminescence study is the observation that the PL decay became slower as the injection level was increased.[3,26] For a radiatively limited decays, the lifetime is expected to decrease with increasing illumination intensity; thus, the observed behavior is an indication that another process is dominant. This was previously explained as being the result of the injection dependence of the non-radiative bulk lifetime originally predicted by Shockley and Read (Section II.A.3).[49] Further support for this interpretation is provided by Figure 3.4b which reveals that decays taken at the higher injection levels became more rapid as they progressed and entered low-level injection.

2. n-InP

Photoluminescence decay profiles for a representative sample made from the n-type (111)B-oriented InP wafer are presented in Figure 3.5a. It is apparent that the timescale is substantially longer than that on which decays for the p-type wafer were recorded. This large discrepancy between the PL lifetime of n-type and p-type InP has also been observed previously, but a definitive explanation of its origin is still lacking.[23,59] It has been proposed that the PL decays for n-type material are radiatively limited, while those of p-InP are limited by SRH recombination. As evidence for a radiatively limited decay in n-InP, the authors reported a quadratic increase of the PL intensity, and a shortening of the PL decay, as the injection level was increased.[23] The data of Figure 3.5 reveal that an increased rate of PL decay at higher excitation intensities was also found in the present studies.

Filename	Sample	Wavelength (nm)	Photons/Pulse (10^{10} photons)	Injection Parameters
b01901	B02	640	7.6	[a]
b01902	B02	640	8.0	ND[b] 40
b01903	B02	640	8.0	ND 25,40
b03702	B02	600	5.6	loosely focused
b03703	B04	600	5.2	
b03704	B04	600	5.4	unfocused
b03705	B04	600	5.6	unfocused ND 25
b03705	B04	600	5.7	unfocused ND 25,40

Table 3.1: Experimental parameters for the data presented in Figures 3.4 and 3.5. The number of photons per pulse was calculated from laser power measurements performed at 3.8 MHz.

[a] Unless otherwise specified, the beam was tightly focused as described in Section III.

[b] Neutral density (ND) filters placed in the beam path to attenuate the intensity. The numbers specify the nominal percent transmission at the laser wavelength.

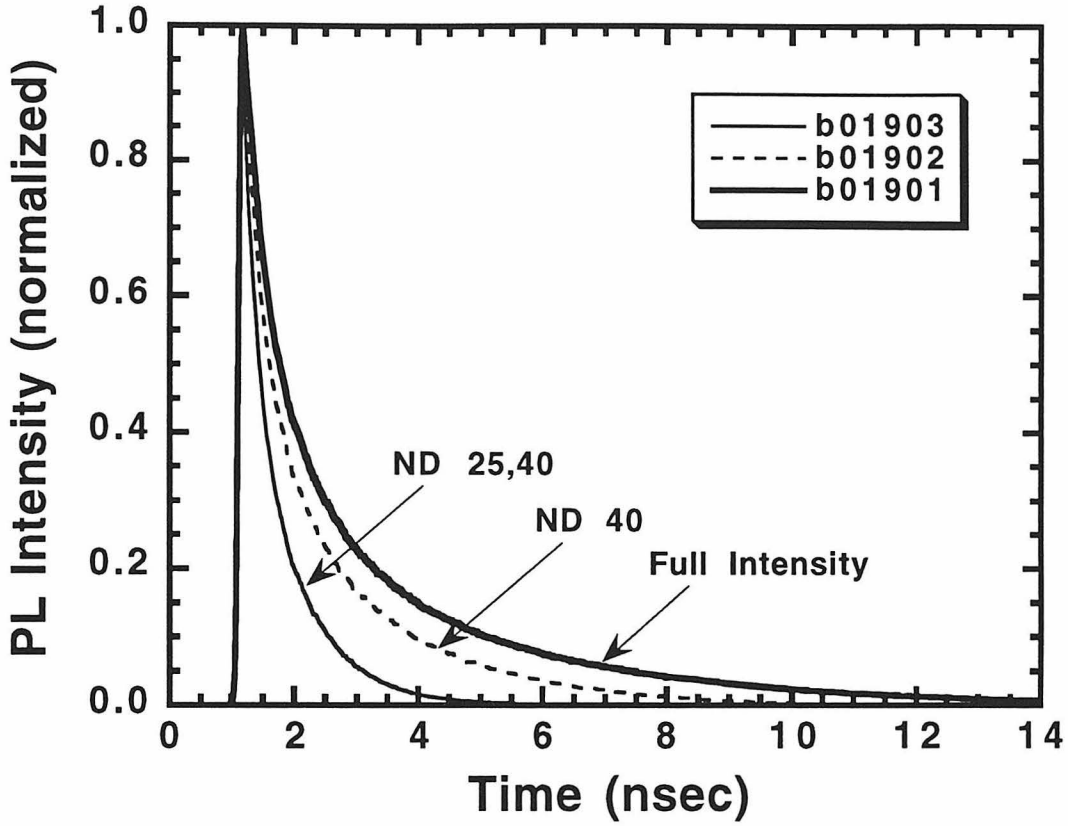

Figure 3.4a: Photoluminescence decay profiles for (100) p-type InP at several light intensities. The decays are observed to be slower at higher injection levels (Table 3.1), indicative of a mechanism other than radiative recombination being dominant.

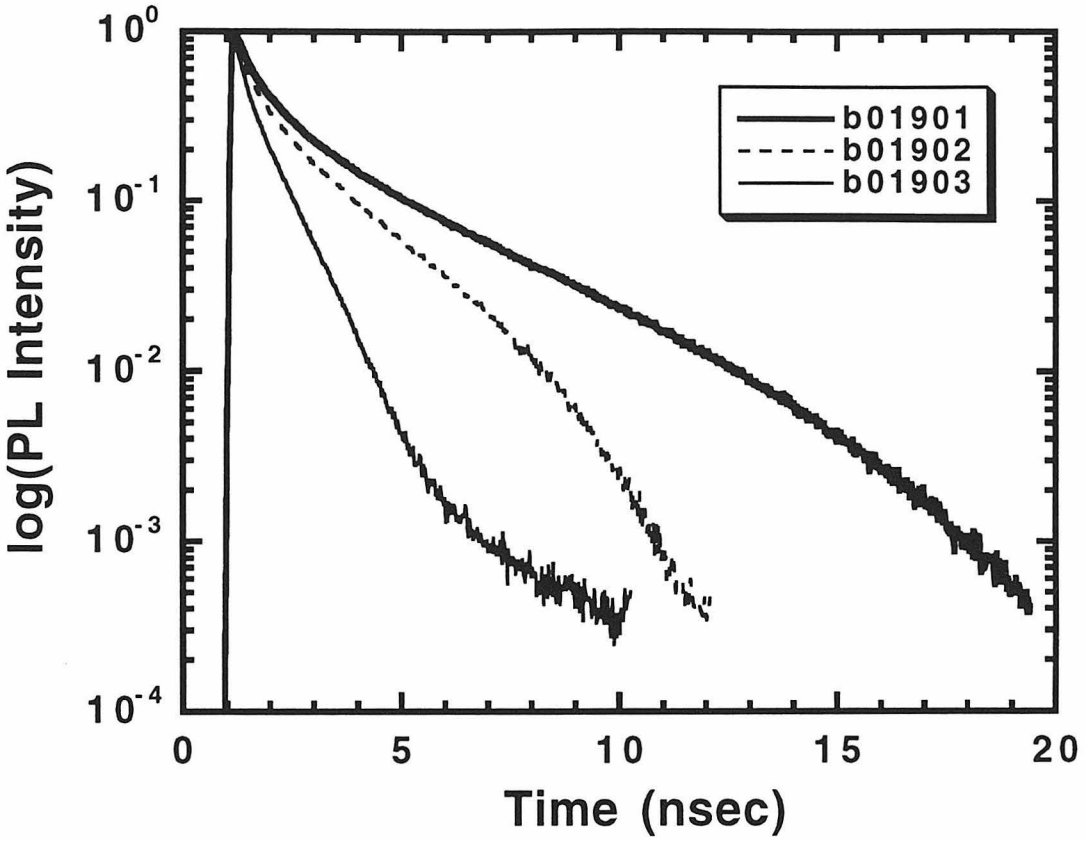

Figure 3.4b: Natural logarithm of the data in (a) showing the decays at the higher light intensities became more rapid as they proceeded. This is consistent with the rate of decay being dictated by non-radiative bulk recombination.

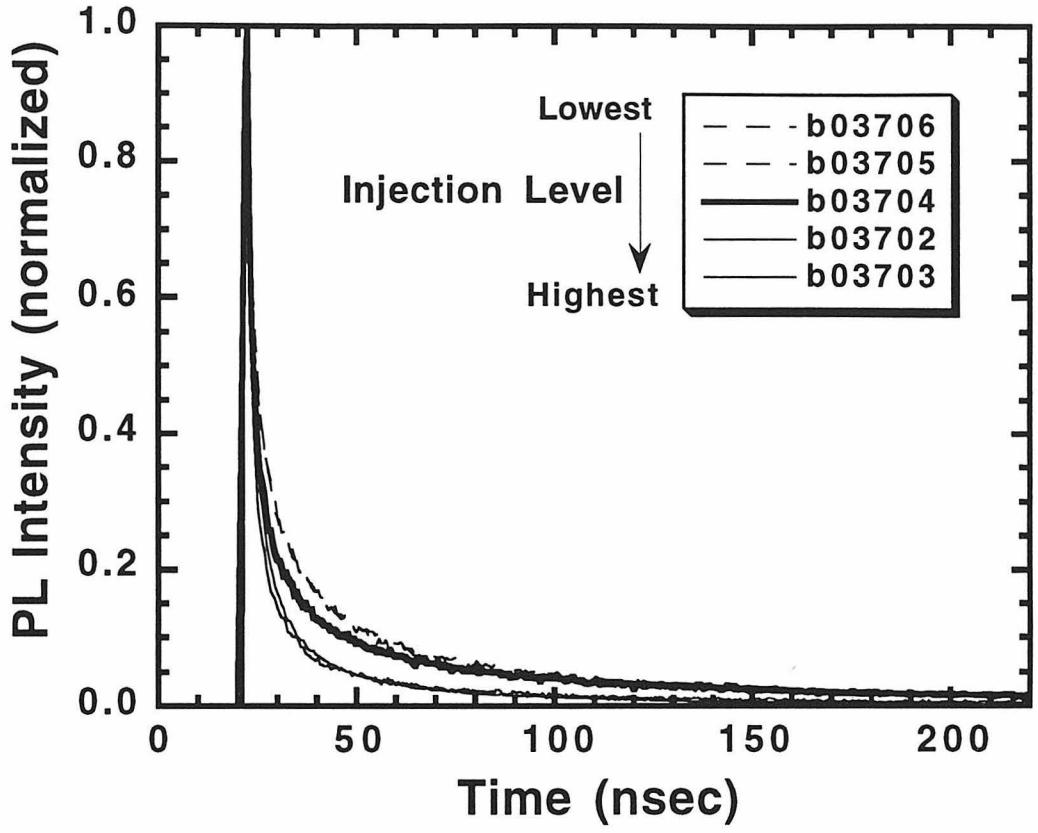

Figure 3.5: Photoluminescence decay profiles for (111)B n-type InP at several light intensities. Contrary to the behavior observed for p-InP (Figure 3.4), the decays were more rapid at higher injection levels. This has been interpreted as evidence of a radiatively limited PL lifetime. Limiting decays were observed at both the low (dashed curves) and high (thin solid lines) extremes of the injection level range that was probed.

B. Luminescence Decay Profiles of InP/CH_3CN Contacts

1. InP/MV^{2+} Contacts

The first TRPL decay experiments on InP samples in contact with an electrolyte were performed for the p-InP/CH_3CN-MV^{2+} system. These experiments were originally undertaken to examine the suitability of this contact for study by transient absorption spectroscopy. It has been desired for some time to perform a time-resolved study in which the products of electron transfer from a semiconductor electrode to molecular species in solution are observed directly. This experiment has not been accomplished to date due to the substantial difficulties associated with detecting the small number of species produced at the surface by a single laser pulse. The p-InP/CH_3CN-MV^{2+} system fulfilled many of the criteria for such an experiment, and a new transient absorption technique employed to monitor electron injection into SnS_2 appeared to have the required sensitivity.[60] However, an instrumental limitation sets the maximum time window available using this technique to ~300 ps, and the success of the experiment therefore hinged on a significant quantum yield for charge transfer on this timescale. The TRPL experiments were designed to probe if such rapid charge transfer, observable as a dramatic increase in the rate of PL decay, was characteristic of the p-InP/CH_3CN-MV^{2+} contact.

The TRPL experiments were initially performed on p-type (100)-oriented InP samples as it would have been necessary to employ p-type electrodes in the transient absorption experiments. Figure 3.6 presents data for the p-InP sample both in neat CH_3CN and in contact with CH_3CN-$MV(PF_6)_2$. Even at the relatively high concentration of MV^{2+} employed (.28 M), the decays observed were virtually identical to that recorded for the etched electrode at the highest light intensity (Figure 3.4). While it was encouraging that the solvent itself did not produce large changes in the PL decay, the invariance of the decay upon addition of MV^{2+} was not. The similarity indicated that charge transfer to the solution was unable to compete kinetically with recombination and transport processes intrinsic to the solid, and the latter were controlling the rate of PL decay. These results

suggested that the prospects for success of the transient absorption experiment using this system were poor.

Given the marked similarity of the observed decays, it became interesting to see if an increase in the rate of PL decay for InP could be observed under other experimental conditions. To increase the time window available, a switch was made to InP samples made from the (111)B n-type material. Figure 3.7a shows a decay for a representative sample both in contact with N_2 and with CH_3CN-$MV(PF_6)_2$. Contrary to the results seen with p-InP, addition of the redox species did produce an observable shortening of the PL lifetime, although the effect is not dramatic. One confounding issue is that the effect persisted when a decay was recorded subsequently for the sample in neat CH_3CN, even after thorough washing of the InP surface. This was observed for different experiments using individually prepared samples, and could only be reversed by etching of the semiconductor. The origin of this is still unclear at this time.

2. Photoluminescence Decay Profiles in Contact with Other Redox Species

To see if a pronounced increase in the rate of PL decay for InP could be produced by other outer-sphere redox species, TRPL experiments were also performed for InP in contact with CH_3CN-Me_2Fc, CH_3CN-$CoCp_2^+$ and CH_3CN-THF-$Me_{10}Fc$. An estimate of the energetics of these relative to the band edges of InP can be obtained from Figure 3.8 in which the corresponding formal potentials are compared with the conduction and valence band positions reported for n-InP in CH_3CN.[61] The time-resolved PL decay data are presented in Figures 3.7b-d. To maximize the available time window, all experiments were performed on the longer lifetime n-type (111) material. The PL decays recorded employing Me_2Fc (Figure 3.7b) and $CoCp_2$ (Figure 3.7c) as the acceptor species exhibited little or no change relative to that recorded for the etched sample. The decay for n-InP did show an increased rate upon addition of CH_3CN-THF-$Me_{10}Fc$ (Figure 3.7d), although the effect is again not very large.

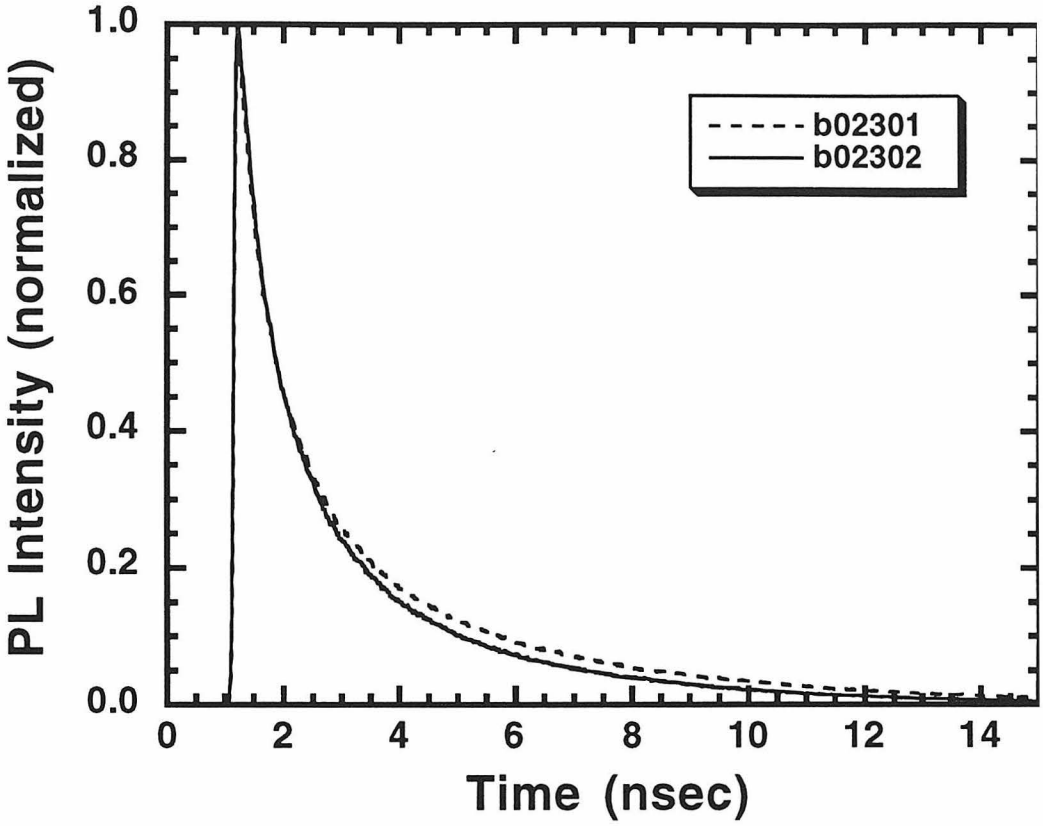

Figure 3.6: Photoluminescence decay profiles for a (100) p-InP sample in CH_3CN (solid line) and in contact with CH_3CN-.28 M $MV(PF_6)_2$ (dashed line).

Filename	Sample	Wavelength (nm)	Photons/Pulse (10^{10} photons)
b02301	B02	640	6.8
b02302	B02	640	7.7

Table 3.2: Experimental parameters for the TRPL experiment performed on the p-InP/CH_3CN-MV^{2+} contact. Data are presented above in Figure 3.6.

Filename	Sample	Wavelength (nm)	Photons/Pulse (10^{10} photons)	Experiment
b04301	B04	600	5.1	MV
b04304	B04	600	4.9	
b04502	B04	600	4.9	Me_2Fc
b04503	B04	600	4.8	
b04901	B04	600	5.2	$CoCp_2$
b04902	B04	600	5.2	
c01501	B05	630	5.4	$Me_{10}Fc$
c01504	B05	630	5.8	

Table 3.3: Experimental parameters for the TRPL experiments performed on n-InP in contact with CH_3CN-MV, CH_3CN-Me_2Fc, CH_3CN-$CoCp_2$, and CH_3CN-$Me_{10}Fc$. Data are presented in Figures 3.7a-7d.

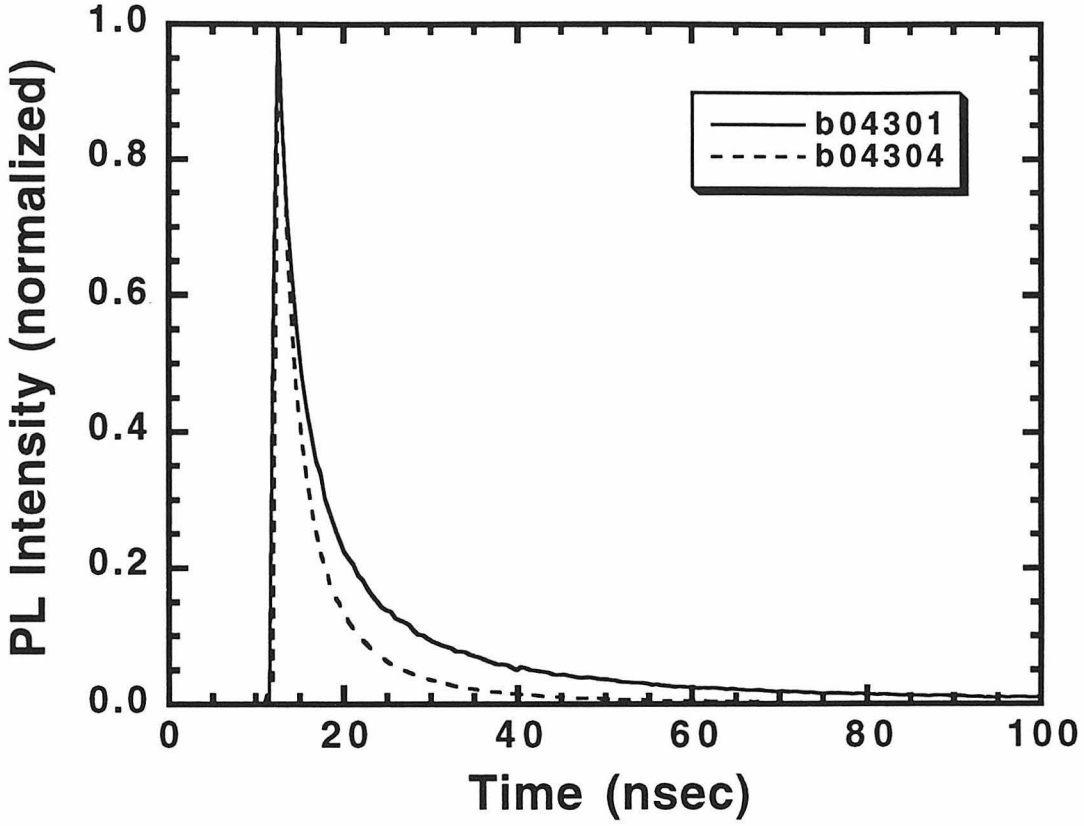

Figure 3.7a: Photoluminescence decay profiles for (111)B n-InP samples as etched (solid line) and in contact with CH_3CN-.2 M $MV(PF_6)_2$ (dashed line).

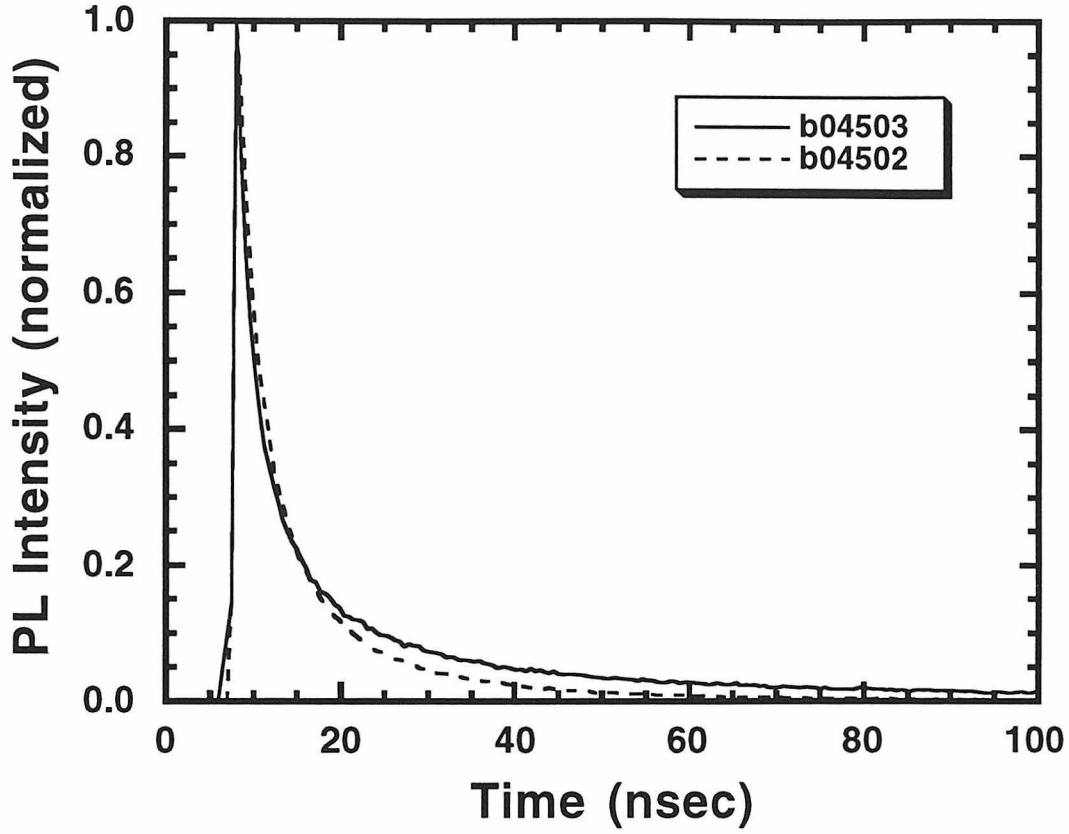

Figure 3.7b: Photoluminescence decay profiles for (111)B n-InP samples as etched (solid lines) and in contact with CH_3CN-.5 M $TBAPF_6$-.1 M Me_2Fc (dashed line).

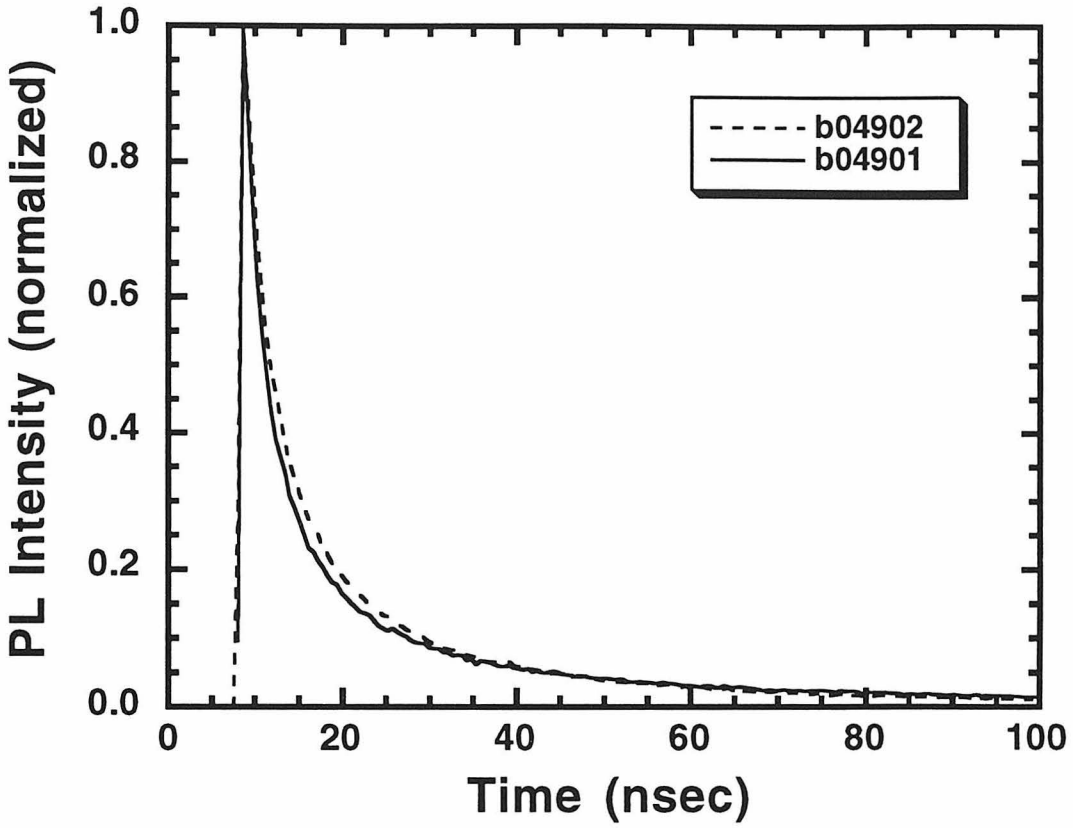

Figure 3.7c: Photoluminescence decay profiles for (111)B n-InP samples as etched (solid lines) and in contact with CH_3CN-.3 M $TBAPF_6$-.05 M $CoCp_2PF_6$ (dashed line).

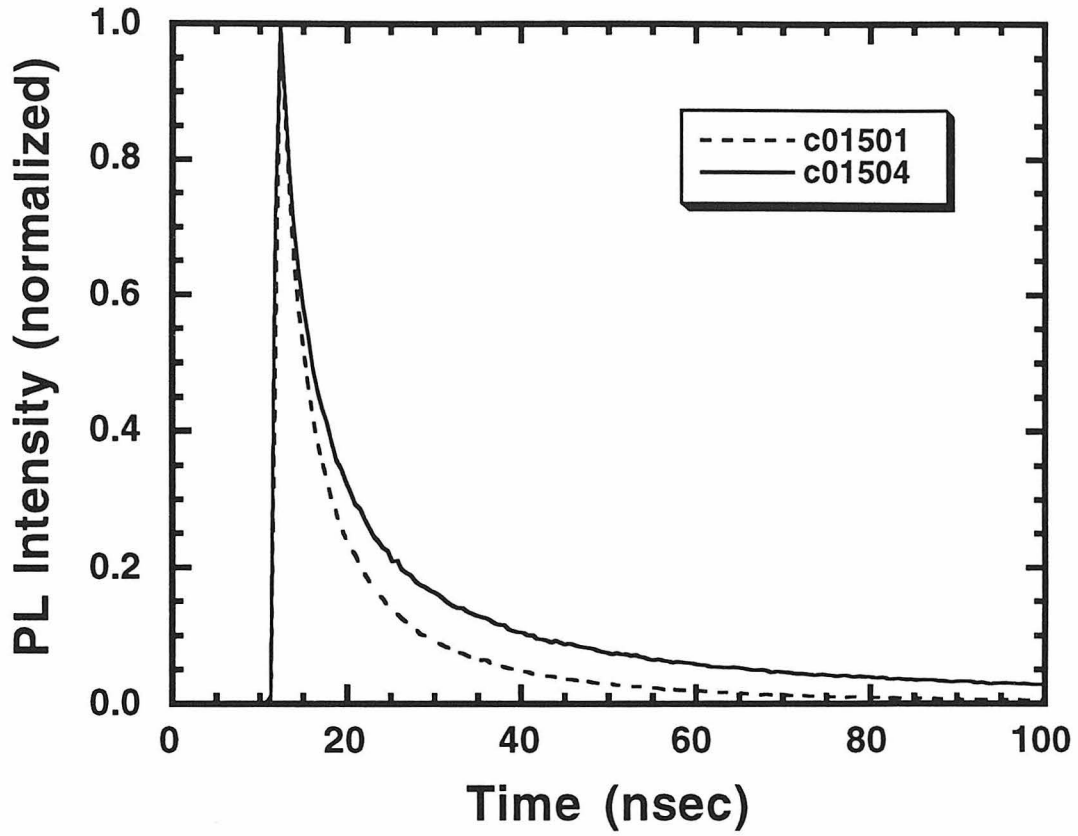

Figure 3.7d: Photoluminescence decay profiles for (111)B n-InP samples as etched (solid lines) and in contact with 50% CH_3CN-50% THF (v:v)-.2 M $TBAPF_6$-.025 M $Me_{10}Fc$ (dashed line).

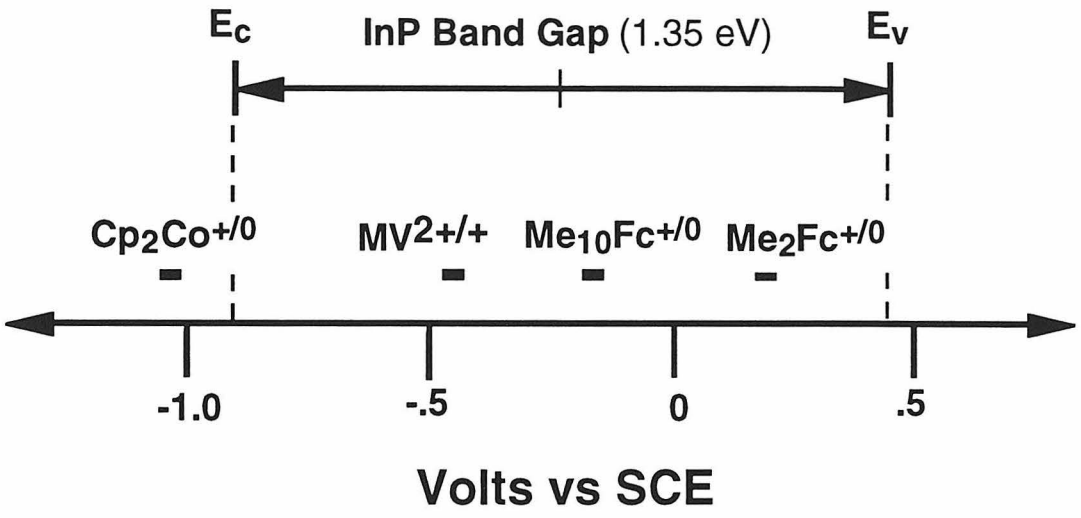

Figure 3.8 Band edge positions of InP relative to the formal potentials for the redox couples employed in this study. The formal potentials shown are published values determined in CH_3CN by cyclic voltammetry,[62] and the band edge positions in CH_3CN are those reported by Koval and coworkers.[61,63] It should be noted that a recent determination of $\mathbf{E_c}$, $\mathbf{E_v}$ in CH_3OH places the potentials corresponding to the band edges ~.3 V more positive.[25]

V. DISCUSSION

A. General Observations

Perhaps the most obvious feature of the PL decay profiles is the initial rapid decay which follows the rise of the signal. This behavior is strongly influenced by diffusion, and the similarity of this portion of the decay for all contacts highlights one of the difficulties associated with the use of bulk samples in these studies. Observation of effects at short times following excitation (when the high-level injection condition is most rigorously satisfied) is typically precluded by the dominance of bulk mechanisms

The second observation is that none of the electrolytes were successful in producing large increases in the PL decay rate. Evidence that such effects are observable in experiments of this type is provided by a TRPL study of InP in which dramatically enhanced PL decay rates were produced by evaporation of certain metals onto the semiconductor surface.[64] The only redox species which induced an appreciable shortening of the n-InP PL decay are MV^{2+} and $Me_{10}Fc$. It is necessary to consider possible sources of the shortening other than carrier loss through interfacial charge transfer. One possibility for the increased rate of decay is an increase in the injection level (a decrease would lead to a longer decay). A variety of factors could produce such a change, but as the laser powers were similar (Table 3.3), and the excitation focus was reoptimized before each experiment, this is not believed to be the cause. Another argument against this explanation is that the decays were faster than the most rapid observed in studies examining the intensity dependence of the PL decay for the etched samples (such as Figure 3.5). A second possibility for the shortening is that the equilibrium electric fields produced in the solid by addition of the electrolyte were not adequately screened by the photogenerated carriers and the increased rates of decay simply reflect field-driven charge separation. This is certainly a concern in experiments such as those described herein, but if this were the underlying mechanism, it would be expected that such an effect would be at least as pronounced for

Me_2Fc which has the most positive redox potential (Figure 3.8) and would be therefore expected to produce the largest equilibrium fields and depletion widths.

B. Comparison with Existing Data and Models

Even though the data of Section IV are not quantitative, they do provide some estimate of the timescale for charge transfer at InP/liquid interfaces and it is, therefore, worthwhile to compare the results with existing data and models. In interpreting this data, it is important to recall the points made above regarding the experimental conditions.

As was mentioned previously, there is very little time-resolved data available on InP/liquid interfaces collected using any technique. However, much of what has been presented is from TRPL studies performed on semi-infinite samples under open-circuit, high-level injection conditions similar to those employed in the present studies. Consequently, fairly direct comparisons with the data of Section IV can be made. Rosenwaks et al. reported TRPL decay data for n-type and p-type InP in contact with a series of metal ion solutions.[26] The authors present photoluminescence profiles indicating they were able to produce obvious increases in the rate of PL decay, even on the short timescale for such data on p-InP. For a p-InP (N_a $5x10^{16}$) sample in distilled water, the authors concluded the surface recombination velocity to be ~500 cm sec^{-1}. For the contact having a decay most similar to that in distilled water, while still exhibiting decidedly faster decay kinetics, they assigned an SRV of $6x10^3$ cm sec^{-1}. Visual comparison of the data places the decay profiles of Figure 3.6 on the timescale of these two curves and certainly not on that of solutions for which SRV values of $>10^4$ cm sec^{-1} were claimed. Therefore, application of the analysis and modeling of these workers would set an upper limit of ~$6x10^3$ cm sec^{-1}, and likely closer to $1x10^3$ cm sec^{-1}, on the charge transfer velocity at the p-InP/CH_3CN-MV^{2+} contact.

Large effects on the PL decay rate similar to those seen for p-InP were also observed in experiments performed on n-InP in metal ion solutions, and in another study examining the effects of metal deposition on the TRPL from n-InP.[26,64] Although it is

more difficult to compare these data due to the restricted portion of the decays presented, it is apparent that none of the data of Figure 3.7 are consistent with the published decays for which an SRV of $\geq 10^4$ cm sec^{-1} was assigned. Instead the data observed in the present work for n-InP in contact with outer-sphere redox species would, according to the reported analysis, be more consistent with an upper limit on the SRV of a few thousand.

While the comparisons described above are intriguing, little confidence is assigned to the actual SRV values because of problems associated with the earlier analysis. One such complication is the use of the Vaitkus solution[39] to calculate the carrier concentration profiles. This model is acknowledged to not be valid when radiative recombination has to be considered.[26] Considering that other studies (one of which is by the same authors) have concluded the PL decay of n-InP to be radiatively limited, the use of such a model is problematic.[23,65]

A final note of interest is that the two redox species for which an increase in the PL decay rate was recorded have energies corresponding to their formal potentials that are closer to the middle of the InP band gap than those of the molecules for which little change was observed. For open-circuit conditions such as those employed in this study, both the Marcus-Gerischer and Shockley-Read-Hall models predict that states in the middle of the band gap are the most efficient at consuming carriers. The data are hardly proof that these principles are operative, but they are at least consistent with the predictions.

VI. REFERENCES

(1) Evenor, M.; Gottesfeld, S.; Harzion, Z.; Huppert, D.; Feldberg, S.W. *J. Phys. Chem.* **1984**, *88*, 6213.

(2) Krüger, O.; Jung, C. *Ber. Bunsenges. Phys. Chem* **1994**, *98*, 1022.

(3) Rosenwaks, Y.; Thacker, B.R.; Ahrenkiel, R.K.; Nozik, A.J. *J. Phys. Chem.* **1992**, *96*, 10096.

(4) Kauffman, J.F.; Balko, B.A.; Richmond, G.L. *J. Phys. Chem* **1992**, *96*, 6371.

(5) Shumaker, M.L.; Dollard, W.J.; Waldeck, D.H. *J. Phys. Chem.* **1992**, *96*, 10371.

(6) Ryba, G.N.; Kenyon, C.N.; Lewis, N.S. *J. Phys. Chem.* **1993**, *97*, 13814.

(7) Orton, J.W.; Blood, P. *The Electrical Characterization of Semiconductors: Measurement of Minority Carrier Properties*, Techniques of Physics; March, N.H. Ed.; Academic: London, 1990; Vol. 13.

(8) Schroder, D.K. *Semiconductor Material and Device Characterization*; Wiley: New York, 1990.

(9) Ryba, G.N. Ph. D. Thesis, California Institute of Technology, 1992.

(10) Balko, B.A.; Richmond, G.L. *J. Phys. Chem.* **1993**, *97*, 9002.

(11) Kauffman, J.F.; Richmond, G.L. *J. Appl. Phys.* **1993**, *73*, 1912.

(12) Ellis, A.B.; Bolts, J.M.; Kaiser, S.W.; Wrighton, M.S. *J. Am. Chem. Soc.* **1977**, *99*, 2848.

(13) Parkinson, B.A.; Heller, A.; Miller, B. *Appl. Phys. Lett.* **1978**, *33*, 521.

(14) Tufts, B.J.; Abrahams, I.L.; Santangelo, P.G.; Ryba, G.N.; Casagrande, L.G.; Lewis, N.S. *Nature* **1987**, *326*, 861.

(15) Gerischer, H. *Electrochim. Acta* **1990**, *35*, 1677.

(16) Gerischer, H. In *Physical Chemistry: An Advanced Treatise*; Eyring, H.; Henderson, D., Yost, W. Eds.; Academic: New York, 1970; Vol. IXA; p 463.

(17) Marcus, R.A. *Annu. Rev. Phys. Chem.* **1964**, *15*, 155.

(18) Marcus, R.A. *J. Phys. Chem.* **1990**, *94*, 1050.

(19) Nelson, R.J.; Williams, J.S.; Leamy, H.J.; Miller, B.; Casey, H.C., Jr.; Parkinson, B.A.; Heller, A. *Appl. Phys. Lett.* **1980**, *36*, 76.

(20) Yablonovitch, E.; Sandroff, C.J.; Bhat, R.; Gmitter, T. *Appl. Phys. Lett.* **1987**, *51*, 439.

(21) Balko, B.A.; Miller, E.A.; Richmond, G.L. *J. Phys. Chem.* **1995**, *99*, 4124.

(22) Casey, H.C., Jr.; Buehler, E. *Appl. Phys. Lett.* **1977**, *30*, 247.

(23) Rosenwaks, Y.; Shapira, Y.; Huppert, D. *Phys. Rev. B* **1992**, *45*, 9108.

(24) Heben, M.J.; Kumar, A.; Zheng, C.; Lewis, N.S. *Nature* **1989**, *340*, 621.

(25) Pomykal, K.E.; Lewis, N.S. *J. Phys. Chem.* submitted for publication.

(26) Rosenwaks, Y.; Thacker, B.R.; Nozik, A.J.; Shapira, Y.; Huppert, D. *J. Phys. Chem.* **1993**, *97*, 10421.

(27) Rosenwaks, Y.; Thacker, B.R.; Nozik, A.J.; Ellingson, R.J.; Burr, K.C.; Tang, C.L. *J. Phys. Chem.* **1994**, *98*, 2739.

(28) Ahrenkiel, R.K. In *Properties of InP*; INSPEC: London, 1991; p 77.

(29) Bothra, S.; Tyagi, S.; Ghandhi, S.K.; Borrego, J.M. *Solid-State Electron.* **1991**, *34*, 47.

(30) Rosenwaks, Y.; Nozik, A.J.; Yavneh, I. *J. Appl. Phys.* **1994**, *75*, 4255.

(31) Rosenwaks, Y.; Thacker, B.R.; Ahrenkiel, R.K.; Nozik, A.J.; Yavneh, I. *Phys. Rev. B* **1994**, *50*, 1746.

(32) Adachi, S. *Physical Properties of III-V Semiconductor Compounds*; John Wiley and Sons: New York, 1992.

(33) Lewis, N.S. *Annu. Rev. Phys. Chem.* **1991**, *42*, 543.

(34) Smith, B.B.; Halley, J.W.; Nozik, A.J. *Chem. Phys.* **1996**, *205*, 245.

(35) Ahrenkiel, R.K. In *Minority Carries In III-V Semiconductors: Physics and Applications*; Ahrenkiel, R.K., Lundstrom, M.S. Eds.; Semiconductors and Semimetals; Academic: New York, 1993; Vol. 39; p 409.

(36) Blakemore, J.S. *Semiconductor Statistics*; Dover: New York, 1987.

(37) Wang, S. *Fundamentals of Semiconductor Theory and Device Physics*, Prentice Hall Series in Electrical and Computer Engineering; Chua, L.O. Ed.; Prentice Hall: Englewood Cliffs, NJ, 1989.

(38) Sze, S.M. *The Physics of Semiconductor Devices*, 2nd ed.; John Wiley and Sons: New York, 1981.

(39) Vaitkus, J. *Phys. Stat. Solidi A* **1976**, *34*, 769.

(40) t'Hooft, G.W.; van Opdorp, C. *J. Appl. Phys.* **1986**, *60*, 1065.

(41) Wilson, T.; Pester, P.D. *J. Appl. Phys.* **1988**, *63*, 871.

(42) Ioannou, D.E.; Gledhill, R.J. *J. Appl. Phys.* **1984**, *56*, 1797.

(43) Ramakrishna, S.; Rangarajan, S.K. *J. Phys. Chem.* **1995**, *99*, 12631.

(44) Tyagi, M.S.; Nus, J.F.; van Overstraeten, R.J. *Solid-State Electron.* **1982**, *25*, 411.

(45) Krüger, O.; Jung, C.; Gajewski, H. *J. Phys. Chem.* **1994**, *98*, 12653.

(46) Other workers have sought flat band conditions in TRPL experiments by the application of a bias to the semiconductor. However, these experiments were performed in electrolytes containing no deliberately added redox species.

(47) Ahrenkiel, R.K. *Solid-State Electron.* **1992**, *35*, 239.

(48) Nelson, R.J.; Sobers, R.G. *Appl. Phys. Lett.* **1978**, *32*, 761.

(49) Shockley, W.; Read, W.T. *Phys. Rev.* **1952**, *87*, 835.

(50) Hall, R.N. *Phys. Rev.* **1952**, *87*, 387.

(51) Pierret, R.F. *Advanced Semiconductor Fundamentals*, Modular Series on Solid State Devices; Pierret, R.F., Neudeck, G.W. Eds.; Addison-Wesley: Reading, MA, 1987.

(52) This analysis is subject to some assumptions and is valid for traps having energies near the middle of the band gap. A detailed discussion of the non-radiative lifetime can be found in the other references.

(53) Many, A.; Goldstein, Y.; Grover, N.B. *Semiconductor Surfaces*; North-Holland: Amsterdam, 1965.

(54) Aspnes, D.E.; Studna, A.A. *Appl. Phys. Lett.* **1981**, *39*, 316.

(55) Bansal, A.; Tan, M.X.; Tufts, B.J.; Lewis, N.S. *J. Phys. Chem.* **1993**, *97*, 7309.

(56) O'Connor, D.V.; Phillips, D. *Time-correlated Single Photon Counting*; Academic: London, 1984.

(57) Hecht, E. *Optics*, 2nd ed.; Addison Wesley: Reading, MA, 1987.

(58) Besslerpodorowski, P.; Huppert, D.; Rosenwaks, Y.; Shapira, Y. *J. Phys. Chem.* **1991**, *95*, 4370.

(59) Rosenwaks, Y.; Shapira, Y.; Huppert, D. *Phys. Rev. B* **1991**, *44*, 13097.

(60) Lanzafame, J.M.; Miller, R.J.D.; Muenter, A.A.; Parkinson, B.A. *J. Phys. Chem.* **1992**, *96*, 2820.

(61) Koval, C.; Austermann, R. *J. Electrochem. Soc.* **1985**, *132*, 2656.

(62) Schneemeyer, L.F.; Wrighton, M.S. *J. Am. Chem. Soc.* **1980**, *102*, 6964.

(63) Segar, P.R.; Koval, C.A.; Koel, B.E.; Gebhard, S.C. *J. Electrochem. Soc.* **1990**, *137*, 544.

(64) Rosenwaks, Y.; Shapira, Y.; Huppert, D. *Appl. Phys. Lett.* **1990**, *57*, 2552.

(65) Keyes, B.M.; Dunlavy, D.J.; Ahrenkiel, R.K.; Shaw, G.; Summers, G.P.; Tzafaras, N.; Lentz, C. *J. Appl. Phys.* **1994**, *75*, 4249.

(66) Nelson, R.J. *J. Vac. Sci. Technol.* **1978**, *15*, 1475.

(67) Hybertsen, M.S. *Appl. Phys. Lett.* **1991**, *58*, 1759.

(68) This is subject to the same caveat noted in ref. 45 of Chapter 1. The steady-state PL vs bias technique that is discussed probes the minority carrier charge transfer rate while the open-circuit TRPL experiment is most sensitive to whichever of the electron and hole rates is smaller.

(69) Mettler, K. *Appl. Phys.* **1977**, *12*, 75.

(70) Burk, J., A. A.; Johnson, P.B.; Hobson, W.S.; Ellis, A.B. *J. Appl. Phys.* **1986**, *59*, 1621.

(71) Smandek, B.; Chmiel, G.; Gerischer, H. *Ber. Bunsenges. Phys. Chem.* **1989**, *93*, 1094.

(72) Wittry, D.B.; Kyser, D.F. *J. Appl. Phys.* **1967**, *38*, 375.

(73) Ellis, A.B. In *Chemistry and Structure at Interfaces: New Laser and Optical Techniques*; Hall, R.B., Ellis, A.B. Eds.; VCH: Deerfield Beach, FL, 1986; p 245.

(74) Albery, W.J.; Bartlett, P.N.; Hamnett, A.; Dare-Edwards, M.P. *J. Electrochem. Soc.* **1981**, *128*, 1492.

(75) Schlichthorl, G.; Tributsch, H. *Electrochim. Acta* **1992**, *37*, 919.

VII. APPENDIX

A. Other Photoluminescence Studies of InP/Liquid Interfaces

As the TRPL studies of semi-infinite InP samples described in Section IV could only provide qualitative information on charge transfer rate constants at InP/liquid interfaces, other approaches based on photoluminescence were pursued. While these were largely unsuccessful, they are summarized below as it is hoped the latter (VII.A.2) will be revisited. Possible improvements are suggested.

1. Double Heterostructure Samples

It was mentioned earlier that double heterostructure (DH) samples, in which a thin active layer is placed between two larger band gap cladding layers, have been successfully employed in TRPL studies of semiconductor interfaces. In addition to minimizing the effects of diffusion, the use of epilayers instead of bulk samples enhances the sensitivity of the observed PL decays to surface processes by virtue of an increased surface to volume ratio. Furthermore, the finite width and symmetric nature of the DH permit some particularly simple expressions for $I_{PL}(t)$ to be obtained.[47] As discussed in the literature, a radiatively limited PL decay for a DH sample under low-level injection conditions is predicted to occur with an exponential lifetime given by 2S/d, where d is the thickness of the epilayer.[48] Elegant solid-state studies of a series of heterostructures having active layers of different thickness have verified this behavior for the AlGaAs/GaAs system.[66] In high-level injection, a radiatively limited PL decay should proceed such that a plot of $I_{PL}(t)^{-1/2}$ vs t will yield a straight line.[6] Verification of these predicted behaviors allows greater confidence in interpreting changes in the PL decay profiles upon addition of the electrolyte.

Given the advantages of DH samples in TRPL studies, an obvious extension is to employ them in charge transfer studies of InP. Towards this end, two different heterostructure samples were obtained that are based on $In_{.52}Al_{.48}As$ lattice matched to InP. InAlAs does have a larger band gap than InP but the difference is only .1 eV. The bands have a staggered lineup such that there is an approximately .35 eV barrier for

conduction band electrons to travel from InP to InAlAs but no barrier for valence band holes.[67] Neither of the samples exhibited useful or meaningful behavior. One structure had such a short carrier lifetime that it was completely unusable while the other failed to exhibit either of the predicted dependencies on injection level described above. Based on these experiences, it appears that heterostructures comparable in quality to the AlGaAs/GaAs system are not currently available for InP, an opinion that is shared by other workers in the field.[28]

2. Bias Dependence of Steady-State Photoluminescence

The time-resolved data presented in Section III suggested the rate of charge transfer from InP to outer-sphere redox couples to be relatively slow and this raised the possibility of accessing the kinetic information using other techniques.[68] One method explored was an analysis of the potential dependence of the InP steady-state photoluminescence according to the dead-layer model.[69-71]

The basic principle of the dead-layer model is an assertion that all carriers photogenerated in the space charge region are separated by the electric field before being able to recombine radiatively, and this region is, thus, "dead" for PL.[72] As the width of the space charge region is varied in response to some perturbation (applied bias, surface charge), the number of carriers generated in this layer will change, and this will be observed as a change in the PL intensity. The dead-layer model has been applied in a qualitative fashion to explain to a variety of PL phenomenon at semiconductor/liquid interfaces.[73] Of greater interest was a more quantitative formulation suggesting that if the barrier height of a semiconductor/liquid contact is known, information on the minority carrier charge transfer rate is available from the ratio of the PL intensity observed at the flat band potential to that extrapolated from measurements at reverse bias.[71] As reliable barrier heights for InP/CH_3OH interfaces had recently been determined, this appeared a promising approach. However, difficulties associated with biasing a semiconductor electrode at the

flat band potential without experiencing mass transfer limitations or band edge shifts, prompted the development of a more detailed protocol.

An analytical solution to the minority carrier continuity equation under low-level injection, steady-state conditions had been presented in the literature.[74] Based on this model, preliminary calculations were performed evaluating the carrier concentration profiles at different potentials, and calculating the PL that would be observed by multiplying the minority profiles by the majority carrier profile at each potential. The results indicated that differences in the PL vs bias behavior should be observable at potentials away from the flat band potential. This prediction was supported by numerical results from ToSCA calculated using the same input parameters. However, attempts made to fit data generated by ToSCA using a routine based on the analytical equations failed to accurately reproduce certain input parameters. One possible source of the discrepancy is that the analytical model treats the consumption of minority carriers at the surface through charge transfer and surface recombination in the same manner. While this is adequate under open-circuit conditions (Section II) it is not appropriate in the presence of faradaic charge flow. To rectify this problem, the contribution due to surface state recombination could be weighted by the potential dependence of the surface majority carrier concentration. Such an approach was used in computing the PL intensity, and has been employed by Schlichthörl and Tributsch in modeling steady-state microwave conductivity data.[75] Alternatively, an entirely numerical approach based on the results of ToSCA could be adopted, although agreement between two models would be satisfying.

Experimentally the n-InP/CH_3OH-$Me_2Fc^{+/0}$ was examined as it had recently been found that its flat band potential could be determined accurately, and previous studies had shown it to be a stable and well-behaved contact.[24,25] Consistent with the earlier studies, excellent current density-voltage characteristics were observed for the photoelectrochemical cells constructed in this work. A cw Ti:sapphire laser was used as the illumination source as it is capable of providing monochromatic light across a broad range of wavelength in the

near infrared where the absorption coefficients guarantee that a significant fraction of the light will be absorbed at the edge of the space charge region. Unfortunately the PL vs bias data were not very reproducible and do not merit inclusion, but the possibilities for success of this project are not exhausted. One aspect of the experiment which might be improved upon is the extent to which the low-level injection condition is satisfied. More highly doped InP samples (those employed were lightly n-type) would relax the restrictions on excitation level, and the use of a charge-coupled device (CCD) for photon detection would permit the use of lower illumination levels by virtue of an enhanced signal-to-noise ratio.